# Probing and changing polymersome morphologies in magnetic fields

Roger S.M. Rikken

# Probing and changing polymersome morphologies in magnetic fields

## Proefschrift

Promotoren:           Prof. dr. P.C.M. Christianen

Prof. dr. ir. J.C.M. van Hest

Copromotoren:       Dr. D.A. Wilson

Dr. H. Engelkamp

Manuscriptcommissie: Prof. dr. A.P.M. Kentgens

Prof. dr. ir. P.P.A.M. van der Schoot
(Technische Universiteit Eindhoven)

Dr. D.J. Kraft
(Universiteit Leiden)

# Contents

# Chapter 1

# Introduction

**Polymersomes: artificial vesicles**

Polymersomes are nanostructures consisting of polymers. They are interesting candidates for novel applications in nanochemistry, -physics and - medicine. As often is the case, inspiration for the design, construction and functionality of polymersomes is found in Nature, where processes like compartmentalization, (self-)replication and self-assembly are widely found [1, 2]. Compartmentalization is not only important for shielding certain components from their environment, it is also useful in the transport of compounds (i.e. drug delivery) [3, 4].

In biology, the components of a cell are contained by a closed cell membrane, which consists of many phospholipid molecules which are all ordered in a bilayer sheet [5]. The first biomimetic aggregates made from these phospholipids were created by Bangham [6]. It was found that by suspending the phospholipids in water, vesicles spontaneously assembled from their molecular constituents [6–9]. This is due to the amphiphilic nature of the phospholipids: one part is hydrophilic while the other part is hydrophobic. In a polar solvent, they arrange in such a way that all the hydrophobic parts are shielded from the solvent which reduces the internal energy. For phospholipids, this leads to assembly into a bilayer vesicle structure (see Figure 1.1a) which are often called phospholipid vesicles or liposomes [8, 9]

The principle of self-assembly is not limited to biological components. There are many examples in which synthetic molecules self-assemble into large aggregates. One particular class are the amphiphilic block-copolymers (ABCP's) [10–17]. These molecules consist of two different polymer blocks, covalently attached to each other. Since the block-copolymers are amphiphilic, one block is hydrophilic while the other is hydrophobic. Dispersion of these ABCP's in water or a mix of polar solvents leads to self-assembly into a variety of different
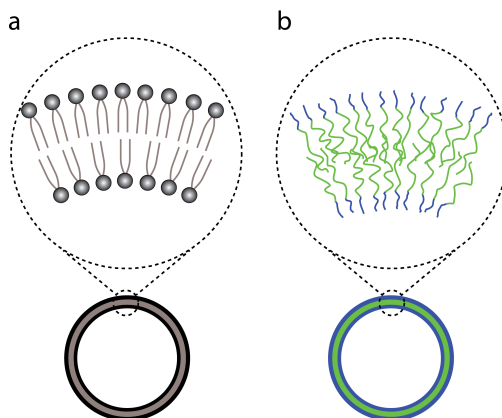
**Figure 1.1:** *(a) Schematic overview of a phospholipid membrane. The two monolayers are clearly separated. (b) In a polymersome membrane the polymers of both monolayers are entangled to some degree which does not allow for the two monolayers to move with respect to each other. The two membranes are not drawn to scale. A polymersome membrane is usually thicker than a phospholipid membrane.*

structures, depending on the (relative) length of both blocks and the chemical composition of the solvent mix [11, 12]. Micellar spheres, micellar rods and vesicles have all been reported to be formed out of ABCP's [12]. Vesicles in particular are of interest since they consist of a bilayer membrane and therefore resemble biological membranes to a certain extent (see Figure 1.1b). Since these vesicles are made from polymers rather than phospholipids, they are often called polymer vesicles or polymersomes. Compared to liposomes, polymersomes have the following advantages [18–20]:

- One can choose from a variety of different hydrophobic or hydrophilic blocks, each with its own properties.

- The length of each block can easily be tuned. Increasing polymer length often means a thicker membrane and therefore a higher rigidity and a lower permeability.

- It is much easier to modify polymers than phospholipids via addition of chemical groups. This makes it very convenient to change their properties or add functionality before or after self-assembly.

A disadvantage of polymersomes is that not all block copolymers are biological compatible, which somewhat limits their possible use in medical applications.

## Applications and the importance of shape

The applications of polymersomes can generally be divided into two categories. First of all, they can be used as a nano-container [21]. This means that one can load the vesicle with cargo, be it molecular components or nanoparticles. The second category is that of scaffolds. By adding chemical or biological functional groups to the outside of a polymersome, one uses the polymersome as a scaffold to display the moieties attached to the surface. For both types of applications, physical properties such as size and shape are important as well. This is shown in Figure 1.2. In Figure 1.2a, one can see a spherical and a bowl-shaped polymersome, the latter often being called a stomatocyte, which both are holding cargo. In case of the spherical polymersome, the cargo cannot escape the vesicle since there is no opening and the cargo is too large to diffuse through the membrane. In case of the stomatocyte, the cargo can still go through the small opening of the stomatocyte. The size of the opening of a stomatocyte can be tuned, and therefore this determines if the cargo can be released or not. From this example one can see that the shape of the container matters for its functionality. An example of polymersomes as a scaffold is given in Figure 1.2b [22]. An immune response can be provoked by adding antigens to the bloodstream which are presented individually to the cells in the immune system. By placing many antigens on a polymersome, these antigens can be presented to a surface simultaneously, increasing the effectiveness of the immune response as is also the case in real life when viruses and bacteria are presented
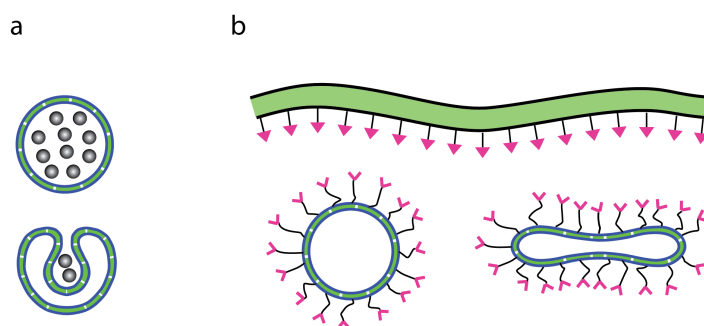


**Figure 1.2:** *(a) Polymersomes as a nano-container. A spherical and a bowl-shaped polymersome (a stomatocyte) have different properties: a stomatocyte can release its cargo via an opening while a polymersome cannot. (b) Polymersomes as a scaffold. Antigens have been linked to both a sphere and a disc of similar surface area. The disc can attach to a surface (shown on top) over a larger contact area than the sphere.*

to the cells of the immune system. It is also expected that a flat scaffold has a larger contact area with a larger cell than a spherical scaffold, as can be seen in the figure. From this it is expected that the efficiency of the immune response is strongly depending on the shape of the scaffold.

Since for both kind of applications the polymer shape is of importance, one ideally would like to be able to control its shape. To have full control over shape, one also needs to understand which factors and processes determine the assembly of amphiphiles into aggregates of a particular shape.

**Aim and approach**

In this thesis we describe our results in understanding and manipulating polymersome shape changes by applying magnetic fields. As was demonstrated already before, magnetic fields are a valuable tool in inducing small reversible shape changes in polymersome stomatocytes if the stomatocyte is made flexible and the field is sufficiently high [23]. Since these stomatocytes respond so well to magnetic fields, we envisioned that it might even be possible to use low magnetic fields to probe polymersome shape changes *in situ*.

Many of the polymersome shape changes reported in literature so far have been rather empirical and phenomenological in nature. Therefore, a good underlying theoretical framework is still lacking. The experiments described in this thesis are not only meant to provide new methods of making polymersomes of different shapes, they are also meant to provide a better understanding of the mechanisms that govern these shape changes. *In situ* tracking of the shape changes allows to follow the changes in time so one can stop the shape change process at well-defined points (by quenching of the shapes). This will allow one to describe the shapes mathematically (i.e. by means of parametrization) which then makes it possible to calculate all kinds of vesicle properties, which is necessary for understanding the physics behind the shape changes.

For our studies, we have chosen to use poly(ethylene glycol)-polystyrene ($PEG_n$-$PS_m$) as our block copolymer. For all experiments the length of the PEG was fixed at 44 units while the length of the PS segment ranged between 133 and 200 units. The advantage of PEG is that, although hydrophilic, it does not have a single electric charge at any position. Therefore, electrical interactions between adjacent polymers are not to be expected as is the case for other hydrophilic polymers like poly(acrylic acid) [12]. This reduces the interactions and forces involved in the shape changes which simplifies the system.

Polystyrene has been chosen as the hydrophobic block since it has a rather high glass transition temperature (between 70 and 97 °C, depending on the thickness of the PS layer [24]). This means that a PEG-PS polymersome in

**Figure 1.3:** *(a) Schematic picture showing the control over the flexibility of a PEG-PS polymersome membrane (green-blue chains) in water/organic solvent mixtures. The membrane swells in organic solvents (red dots) making it flexible. In water (blue dots) the membrane is glassy and rigid. Any polymersome shape can be fixated by a fast injecting in water, leading to a fast expulsion of the organic solvents and a kinetically trapped polymersome shape. (b) Schematic picture showing several examples of possible polymersome shapes, namely spheres, stomatocytes, rods and discs. All these shapes are cylindrically symmetric, with the axes of symmetry indicated by the dashed arrows.*

water is very rigid (glassy) at room temperature. The flexibility can be tuned by the addition of plasticizing agents, such as THF, which basically lowers the glass transition temperature. Since PEG-PS is self-assembled in a mixture of organic solvents and water, the polymersomes are initially flexible. By injecting the sample quickly in water, the polymersomes become rigid almost instantly, as is schematically shown in Figure 1.3a. This allows any shape (for example the ones shown in Figure 1.3b) to be fixated, as has been demonstrated before [20,25,26]. As we will demonstrate in the coming chapters, polystyrene has also very good

magnetic properties that allow polymersome shape changes to be probed in a magnetic field. This is due to the magnetic anisotropy of the polystyrene in the polymersome membrane, which leads to a shape dependent magnetic alignment of the polymersomes.

All the above mentioned properties of PEG and PS make the polymersomes self-assembled out of PEG-PS block copolymers an ideal model system for the investigation of polymersome shapes and shape changes.

**Outline of this thesis**

The thesis is structured as follows. In chapter 2, we review the different approaches that have been followed to manipulate nano- and microparticles with magnetic fields. Its focus is on the various combinations of magnetic materials (ferromagnets, paramagnets and diamagnets) and magnetic fields (homogeneous, inhomogeneous, rotating and oscillating). Besides the necessary theory, examples from literature are mentioned and discussed to illustrate the possibilities. This chapter is meant to place the rest of the thesis in a broader perspective.

The actual research on polymersomes begins in chapter 3. In this chapter, a mathematical description of cylindrically symmetric vesicle shapes is formulated in terms of a Fourier-based parametrization. Terms like magnetic energy and bending energy are formulated and subsequently expressed in terms of this parametrization. This allows one to describe experimentally found shapes and calculate their properties such as volume, surface area, area difference between the inner and outer part of the membrane, bending energy and magnetic anisotropy. Also, the contribution of a single PS monomer to the magnetic anisotropy of a vesicle as function of the average extensiveness in the membrane is given.

Shape changes in polymersomes can also be induced by dialysis, where the solvent composition is slowly changed over time by exchange of solvents over a synthetic membrane. In chapter 4 we show how a small dialysis cell, which is designed to fit inside a 2 T electromagnet and a 20 T Bitter magnet, can be used to probe the shape changes induced by dialysis over time. This cell, which was designed and built in-house, allows the birefringence to be measured over time while exposing the sample to magnetic fields up to 20 T. Changes in birefringence were measured, which are in accordance with electron microscopy images. The experimentally observed shapes are parameterized and their position in a geometrical phase diagram is determined.

In chapter 5 we demonstrate experimentally how initially spherical polymersomes can be molded into a variety of different shapes, such as rods, discs and

stomatocytes, by out-of-equilibrium self-assembly. All encountered shapes are fitted, using the parametrization stated in chapter 3, which allows their position in a geometrical phase diagram to be determined. They are all located near a local minimum in the bending energy which is the first time Seifert's bending energy model, initially used for phospholipid vesicles, is proven to apply to polymersomes as well.

Low magnetic fields up to 2 T are sufficient to partially align anisotropic polymersomes, which enables us to determine in real-time if shape changes are occurring. However, high magnetic fields up to 30 T allow the polymersomes to be aligned to such extent that their magnetic anisotropy can be determined as will be demonstrated in chapter 6. We have measured the magnetic birefringence of spheres, stomatocytes and discs, all made from the same block copolymer and used the magnetic birefringence in combination with cryo-TEM and cryo-SEM to determine the contributions of a single repeating unit of polystyrene to the magnetic anisotropy of the vesicles.

In chapter 7 we will describe some experiments in which initially spherical polymersomes were disturbed by a specific pipetting process in order to change their shape into prolates (rods and spheroids). When enclosing them in a cuvette, their shape slowly returned to a spherical morphology over time, which we measured with magnetic birefringence. The influence of polymer length on the relaxation time is investigated. This chapter also clearly demonstrates how carefully one must be in handling flexible polymersome samples which are self-assembled in a mixture of organic solvents and water. In some cases, pipetting the solution from one container to another can already induce a change in morphology which seems to be dependent on the solvent composition and the methods and materials used in pipetting.

In chapter 8 we describe our progress in the development of a new setup that allows one to perform dynamic light scattering (DLS) inside the wide-bore Bitter magnet of the HFML. DLS is a technique which is used to determine the diffusion coefficients of particles in solution. We attempted to probe changes in the diffusion coefficients in anisotropic polymersomes induced by magnetic alignment. Initial results already show some clear shape dependent effects.

Finally, in chapter 9, we provide the reader with an outlook, where we will address remaining questions and possible interesting directions for further research.

# References

[1] A. Vidonne and D. Philp, *Eur. J. Org. Chem.*, **2009**, 593 (2009)

[2] R.J.R.W. Peters, M. Marguet, S. Marais, M.W. Fraaije, J.C.M. van Hest and S. Lecommandoux, *Angew. Chem. Int. Ed.*, **53**, 146 (2014)

[3] A. Rössler, G.W.M. Vandermeulen and H.-A. Klok, *Adv. Drug Deliv. Rev.*, **53**, 95 (2001)

[4] A. Mahapatro and D.K. Singh, *J. Nanobiotechnol.*, **9**, 55 (2011)

[5] M. Edidin, *Nat. Rev. Mol. Cell Biol.*, **4**, 414 (2003)

[6] A.D. Bangham, M.M. Standish and J.C. Watkins, *J. Mol. Biol.*, **13**, 238 (1965)

[7] S. Vemuri and C.T. Rhodes, *Pharm. Acta Helv.*, **70**, 95 (1995)

[8] Y. Barenholz, D. Gibbes, B.J. Litman, J. Goll, T.E. Thompson and F.D. Carlson, *Biochemistry*, **16**, 2806 (1977)

[9] F. Szoka Jr. and D. Papahadjopoulos, *Ann. Rev. Biophys. Bioeng.*, **9**, 467 (1980)

[10] A. Choucair, C. Lavigueur and A. Eisenberg, *Langmuir*, **20**, 3894 (2004)

[11] Y. Mai and A. Eisenberg, *Chem. Soc. Rev.*, **41**, 5969 (2012)

[12] D.E. Discher and A. Eisenberg, *Science*, **297**, 967 (2002)

[13] B.M. Discher, Y.-Y. Won, D.S. Ege, J.C.-M. Lee, F.S. Bates, D.E. Discher and D.A. Hammer, *Science*, **284**, (1999)

[14] J.F. Le Meins, O. Sandre and S. Lecommandoux, *Eur. Phys. J. E*, **34**, (2011)

[15] J.A. Opsteen, J.J.L.M. Cornelissen and J.C.M. van Hest, *Pure Appl. Chem.*, **76**, 1309 (2004)

[16] R. Rodríguez-García, M. Mell, I. López-Montero, J. Netzel, T. Hellweg and F. Monroy, *Soft Matter*, **7**, 1532 (2011)

[17] D.E. Discher and F. Ahmed, *Annu. Rev. Biomed. Eng.*, **8**, 323 (2006)

[18] H. Bermúdez, A.K. Brannan, D.A. Hammer, F.S. Bates and D.E. Discher, *Macromol.*, **35**, 8203 (2002)

[19] H. Bermúdez, D.A. Hammer and D.E. Discher, *Langmuir*, **20**, 540 (2004)

[20] M.C.M. van Oers, F.P.J.T. Rutjes and J.C.M. van Hest, *J. Am. Chem. Soc.*, **135**, 16308 (2013)

[21] D.A. Wilson, R.J.M. Nolte and J.C.M. van Hest, *J. Am. Chem. Soc.*, **134**, 9894 (2012)

[22] J. van der Weijden, L.E. Paulis, M. Verdoes, J.C.M. van Hest and C.G. Figdor, *Chem. Sci.*, **5**, 3355 (2014)

[23] P.G. van Rhee, R.S.M. Rikken, L.K.E.A. Abdelmohsen, J.C. Maan, R.J.M. Nolte, J.C.M. van Hest, P.C.M. Christianen and D.A. Wilson, *Nat. Commun.*, **5**, 5010 (2014)

[24] J.L. Keddie, R.A.L. Jones and R.A. Cory, *Europhys. Lett.*, **27**, 59 (1994)

[25] K.T. Kim, J. Zhu, S.A. Meeuwissen, J.J.L.M. Cornelissen, D.J. Pochan, R.J.M. Nolte and J.C.M. van Hest, *J. Am. Chem. Soc.*, **132**, 12522 (2010)

[26] S.A. Meeuwissen, K.T. Kim, Y. Chen, D.J. Pochanand and J.C.M. van Hest, *Angew. Chem. Int. Edit.*, **50**, 7070 (2011)

# Chapter 2

# A review: manipulation of micro- and nanostructure motion with magnetic fields

## Abstract

This chapter will focus on how magnetic fields can be used to manipulate the motion of various micro- and nanostructures in solution. We will distinguish between ferromagnetic, paramagnetic and diamagnetic materials. Furthermore, the use of various kinds of magnetic fields, such as homogeneous, inhomogeneous and rotating magnetic fields is discussed. To date, most research has focused on the use of ferro- and paramagnetic materials, but here also the possibilities of magnetic manipulation of diamagnetic materials will be discussed. Since the vast majority of soft matter is diamagnetic, this paves the way for many new applications to manipulate the motion of micro- and nanostructures.

Controlled motion of micro- and nanostructures in solution is a key ingredient for transport and assembly of nanomaterials in various applications. For instance, in drug delivery it is important that carriers can be accurately manoeuvred to pick up drugs at one location and release it at another [1]. Another example is the separation of blood cells, bacteria or cancer cells from blood samples in microfluidics, which is crucial for diagnosing diseases or infections [2–5] Influencing motion and orientation of micro-objects also gives the ability to control their self-assembly in larger structures [6] or induce nematic phases in suspensions of spheroidal particles [7].

To master movement at the micro- and nanoscale, different concepts can be utilized, many of which are also found in nature. For instance, micro- and nanostructures can be moved along a predefined path. In cells this is done by kinesis proteins, which transport biomolecules by moving along tubulin fibers [8, 9]. Another example is the conversion of rotational motion into linear translation. This concept is applied by flagella, the rotating tail that bacteria use for propulsion [8]. Motion can also be induced by an external field gradient. For example, a proton gradient is necessary for inducing rotational movement in ATP-synthase, the protein responsible for ATP synthysis [8]. Finally, steering of micro- and nanostructures can be achieved by aligning them along an external vector field, such as electric and magnetic fields. This property is exploited by organisms that use the Earths magnetic field for orientation, like certain birds, fish and magnetotactic bacteria [10]. With such a diversity of examples, it is not surprising that many synthetic nanomotors are inspired by those found in nature.

Several review articles have been published over the years that discuss various nanomotors, for instance, molecular [11] and nanomotors with [12] or without [13] moving parts. The motion of these nanomotors was induced by various stimuli such as electromagnetic radiation, ultrasound, chemical reactions and electric or magnetic fields [14–16]. In this chapter we will discuss propulsion and steering of micro- and nanostructures induced by external magnetic fields. Using magnetic fields for manipulation has several advantages. First of all, the response can be varied by choosing the type of magnetism of the material, ranging from ferromagnetism and paramagnetism to diamagnetism. Secondly, for each of these magnetic materials, the field strength and orientation can be varied, or kept constant, in space, time or both. We can distinguish homogeneous magnetic fields (field strength and direction constant in space and time), inhomogeneous magnetic fields (strength changes with position but not with time), rotating magnetic fields (direction changes with time), and oscillating magnetic fields (strength changes with time). Thirdly, magnetic fields are a non-invasive way of manipulating matter, because magnetic forces are contactless, volume

forces and no chemical alteration is induced. Fourthly, when a magnetic field is used for propulsion, no depletion of fuel can occur. Fifthly, strong permanent magnets and (superconducting) electromagnets are nowadays readily commercially available. Finally, compared to electric fields magnetic fields do not induce currents by linearly accelerating charged particles in solution [17] and are not as sensitive to surface charges and pH [2].

Although some excellent reviews on magnetic manipulation of nanostructures have been published in the past [17–19], most of them have focussed on micro- and nanostructures containing ferromagnetic or paramagnetic particles, since these only require magnetic fields up to several tenths of mT. Here, we also include the magnetic manipulation of diamagnetic materials, which normally requires magnetic fields in the order of 1 T or more. The ability to magnetically manipulate seemingly nonmagnetic (diamagnetic) materials can lead to new opportunities to control and steer (biocompatible) soft matter. It is our goal to inform the reader about the possibilities of these different types of magnetic materials and magnetic fields for propulsion and steering of micro- and nanostructures.

## 2.1 Magnetism

In principle, magnetic fields can be produced by free electric currents or by magnetic materials, like permanent magnets. In electromagnetism these two different sources of magnetic field $\vec{B}$ are distinguished [20]:

$$\vec{B} = \mu_0 \left( \vec{H} + \vec{M} \right).$$ 

(2.1)

The field as a result of $\vec{H}$ is generated by a *free* (externally controllable) current[1] like in the coil of an electromagnet. Magnetic fields produced by magnetic materials are the result of the so-called magnetization $\vec{M}$ (magnetic moment per volume) inside the material. $\mu_0$ is the magnetic permeability of vacuum.

Magnetic materials can be divided into several different classes of which the most common are paramagnets, diamagnets and ferromagnets [20]. In this chapter we will focus mainly on these three classes. We shall begin with defining paramagnetism and diamagnetism, since they can be described in a similar formalism. After that, ferromagnetism and, shortly, superparamagnetism will be introduced.

---

[1]Actually, $\vec{H}$ is determined by the free electric current according to: $\oint \vec{H} \cdot \vec{dl} = I_f$. The integral of $\vec{H}$ along path $\vec{dl}$ is equal to the enclosed free current $I_f$.

### 2.1.1    Basic formalism of paramagnetism and diamagnetism

We consider para- and diamagnets at experimental conditions (ambient temperature) in which a magnetization is induced that is linear with an applied magnetic field [20]:

$$\vec{M} = \chi\vec{H}. \tag{2.2}$$

Here $\chi$ is the dimensionless (volume) magnetic susceptibility, where the sign of $\chi$ depends on whether the material is para- or diamagnetic: $\chi > 0$ for paramagnetic and $\chi < 0$ for diamagnetic materials. This means that the direction of $\vec{M}$ is parallel to $\vec{H}$ for paramagnetic materials and antiparallel to $\vec{H}$ for diamagnetic materials. Note that the magnetization is induced by the external field and reduces to zero when this field is removed, unlike the ferromagnetic case, which will be discussed in paragraph 2.3. Combining equations 2.1 and 2.2 gives:

$$\vec{B} = \mu\vec{H}, \tag{2.3}$$

with $\mu \equiv \mu_0 \left(1 + \chi\right)$ the magnetic permeability of the material. For paramagnetic materials $\mu > \mu_0$, while for diamagnetic materials $\mu < \mu_0$. However, in general para- and diamagnetism are weak effects and typically $|\chi| \ll 1$, which implies that the effect of $\vec{M}$ on the total field is small: $\vec{B} \approx \mu_0\vec{H}$. Nevertheless, quite some interesting effects can occur when a para- or diamagnetic object is placed in an external field.

The magnetic energy $E$ of an object with volume $V$ is given by [21]:

$$E = -\frac{1}{2\mu_0}\chi V B^2. \tag{2.4}$$

This equation shows that the energy of a paramagnet decreases with magnetic field, while that of a diamagnet increases with magnetic field. Since force and energy are related by $\vec{F} = -\vec{\nabla}E$, the magnetic force can be written as [21]:

$$\vec{F} = \frac{\chi}{\mu_0}V \left(\vec{B} \cdot \vec{\nabla}\right) \vec{B}, \tag{2.5}$$

with $\vec{\nabla} \cdot \vec{B}$ the magnetic field gradient. From this equation it follows that paramagnets are attracted to regions of high magnetic field strength (high field seekers), while diamagnets are expelled from them (low field seekers). This is the main difference between para- and diamagnets. The most common cause for paramagnetism is the presence of unpaired electrons in atomic or molecular orbitals [22]. Since electrons have a fundamental property called spin, which can be considered as a magnetic dipole having a permanent magnetic moment

$\vec{m}$, these spins will orient parallel to the magnetic field to minimize their energy, given by [23]:

$$E = -\frac{1}{\mu_0}\vec{m} \cdot \vec{B}. \qquad (2.6)$$

In materials where all electrons are paired in atomic or molecular orbitals (spin up and spin down), all spins cancel at all times and no net magnetization can be induced. Unpaired electrons however do not have this restriction and can, therefore, contribute to the magnetization of the material. In the absence of an external magnetic field the unpaired spins point in random directions, thereby cancelling each other on a macroscopic level and the total magnetization is zero. When an external magnetic field is applied, the unpaired spins will start to align, leading to a net magnetization. This alignment competes with thermal motion that tends to randomize the spin orientations, which indicates that the paramagnetic response strongly depends on temperature. At low temperatures it is possible to fully align the spins at high magnetic fields and saturate the magnetization. However, at room temperature and for magnetic field strengths typically applied in the research described in this chapter, the magnetization remains linear with the applied magnetic field, following equation 2.2.

A historic overview of diamagnetism and its discovery by Anton Brugmans is given by Küstler [24]. Most often, diamagnetism is caused by the tiny distortion of the electron orbits within atoms or molecules by the applied magnetic field. Magnetic dipoles are induced that oppose the external field [25]. This quantum mechanical effect occurs in all materials but its absolute value is typically smaller than para- and ferromagnetism. A diamagnetic response is, therefore, observed for materials that do not exhibit para- and ferromagnetism, which is roughly 95% of all matter. It also means that stronger magnetic fields ($>$ 1 T) are necessary to efficiently manipulate (steer, align or propel) diamagnetic structures in a diamagnetic solution. Although historically this has been relatively hard to achieve, producing such high magnetic fields is no longer a limiting factor. Superconducting magnets up to 20 T are commercially available and in many cases permanent neodymium-iron-boron magnets are also sufficient [2, 24, 26–28]. Since the vast majority of (soft) materials are diamagnetic, this creates new opportunities to manipulate those materials with magnetic fields, including many biomolecules, such as DNA, RNA, peptides and the majority of cells and tissues [29], indicating that diamagnetic manipulation can be employed in biological and medical research.

### 2.1.2 Manipulation of paramagnets and diamagnets

Manipulation of para- and diamagnets can be done in homogeneous or inhomogeneous magnetic fields. Homogeneous magnetic fields are frequently used to align these magnetic materials. Two mechanisms are available that allow magnetic orientation of paramagnetic and diamagnetic particles [21]. The first one is due to an intrinsic anisotropy of the magnetic susceptibility of the material, which occurs when $\chi$ differs for at least two axes. The most simple case is an uniaxial material, with a susceptibility difference of $\Delta\chi(= \chi_{parallel} - \chi_{bot})$ for the two main axes, leading to the following angle dependence of the magnetic energy [25]:

$$E\left(\theta\right) = -\frac{1}{2\mu_0}\Delta\chi V B^2 \cos^2\left(\theta\right).\tag{2.7}$$

Here, $\theta$ is the angle between the axis of the lowest susceptibility and the applied magnetic field. These materials will orient in such a way that their axis corresponding to the highest susceptibility is parallel to the magnetic field. Magnetic alignment of anisotropic structures can lead to a change in refractive index between the directions parallel and perpendicular to the applied magnetic field. This magnetic field induced difference in refractive index is called magnetic birefringence and is often used to measure the degree of alignment. The relation between magnetic alignment and magnetic birefringence will be derived in chapter 3.

The second method to align para- and diamagnetic materials is via so-called shape anisotropy [21]. The induced magnetic moment (magnetization integrated over volume) not only depends on the magnetic susceptibility, but also on the shape of the object, due to the so-called demagnetization effect (see Figure 2.1). As a consequence, it is energetically favorable to align the object with its longest axis parallel to the magnetic field [21].

Inhomogeneous magnetic fields can be used to propel micro- and nanostructures in solution as indicated by equation 2.5. Since such structures are moving through a solution, one has to account for the magnetic susceptibility of the solvent as well. In this case, it is the difference in magnetic susceptibility between solvent and the object that determines the magnetic force [30]:

$$\vec{F} = \frac{1}{\mu_0}\left(\chi_{\mathrm{obj}} - \chi_{\mathrm{sol}}\right) V \left(\vec{B} \cdot \vec{\nabla}\right) \vec{B},\tag{2.8}$$

with $\chi_{\mathrm{obj}} - \chi_{\mathrm{sol}}$ the difference in magnetic susceptibility between the object and the solvent. From this equation it follows that the force on a diamagnetic object (negative $\chi$) can be enhanced by placing it in a paramagnetic solution (positive $\chi$) [26, 27, 31–34].
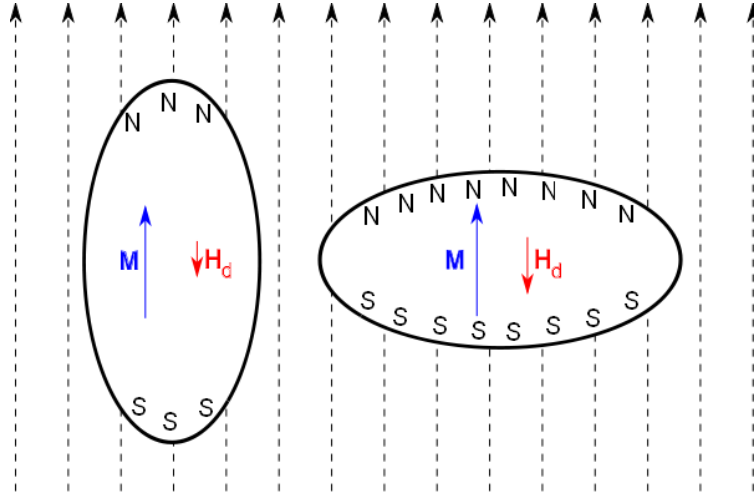
**Figure 2.1:** *Two identical pieces of paramagnetic material that are magnetized along two different axes by an external magnetic field (dashed arrows). Left: the long axis of the paramagnet is aligned along the external field. At the ends magnetic dipole charges (indicated by N and S) are induced leading to a demagnetizing magnetic field $H_d$ antiparallel to the induced magnetization. Right: when the paramagnet is aligned with its long axis perpendicular to the external field, the induced demagnetizing field is larger, due to the enhanced magnet surface charges. Alignment along the long axis results in the smallest demagnetizing field and is therefore energetically favourable.*

Diamagnetic materials are repelled by a magnetic field, which allows stable magnetic levitation in a field gradient, at a position in the magnet where the magnetic force balances the gravitational force [35]. Braunbek was the first to demonstrate diamagnetic levitation by placing graphite and bismuth in an inhomogeneous magnetic field created by an electromagnet [24]. Fifty years later, Beaugnon and Tournier demonstrated the levitation of other weaker diamagnetic materials such as water, wood and plastics using a hybrid magnet, composed of a Bitter-type electromagnet and a superconducting magnet [36]. Strong Bitter and hybrid magnets can provide these gradients over volumes in the order of cm$^3$. Indeed, it was demonstrated that (bio)matter containing large amounts of water (such as a living frog) could be levitated [37]. Water microdroplets have also been levitated using permanent neodymium-iron-boron magnets, which proves that these strong gradients can also be created by permanent magnets albeit over much smaller volumes [28]. Paramagnetic solutions or gasses have been used to lower the necessary $\left( \vec{B} \cdot \vec{\nabla} \right) \vec{B}$ required for levita-

tion [31, 33, 34, 38]. In this case, the forces acting on the diamagnetic particles are determined by the buoyancy and the difference in magnetic susceptibility per unit of volume between the diamagnetic object and the paramagnetic solution [21]:

$$\frac{\vec{F}}{V} = - \left( \rho_{\text{dia}} - \rho_{\text{sol}} \right) \vec{g} + \frac{1}{\mu_0} \left( \chi_{\text{dia}} - \chi_{\text{sol}} \right) \left( \vec{B} \cdot \vec{\nabla} \right) \vec{B}, \tag{2.9}$$

with $\frac{\vec{F}}{V}$ the force on the diamagnetic object per unit of volume, $\rho_{\text{dia}} - \rho_{\text{sol}}$ the difference in density between the diamagnetic object and the solvent, $\vec{g}$ the specific gravity and $\chi_{\text{dia}} - \chi_{\text{sol}}$ the difference between the magnetic susceptibilities of the diamagnetic object and the solvent. Levitation occurs when $\frac{\vec{F}}{V}$ equals zero and is known as Magneto-Archimedes levitation when a paramagnetic solution is employed to facilitate the levitation.

### 2.1.3 Ferromagnetism

Ferromagnetism is the most familiar type of magnetism, since it is responsible for permanent magnetism. It occurs for materials with unpaired electrons, which have a strong mutual interaction and a positive exchange energy [22]. As a consequence it is energetically favourable for adjacent spins to align parallel and form domains. Within each domain the spins point in the same direction, but this direction varies amongst different domains. In an unmagnetized sample the domains are randomly oriented, so the net magnetization is zero. By applying a magnetic field the domains tend to align along the field direction: the domains that are originally aligned along the field grow at the expense of the others. When the external field is removed the net magnetization does not return to zero, which is exploited in the fabrication of permanent magnets.

The magnetization of a ferromagnet is thus highly non-linear and depends on the history of the sample and the applied fields (*magnetic hysteresis*), as is shown in Figure 2.2. The figure shows the applied magnetic field $\mu_0 H$ on the x-axis and the total magnetic field $B$ or magnetization $M$ on the y-axis. For ferromagnets, $B$ is predominantly given by $M$, which is much larger than $H$.

When starting with unmagnetized material ($B = \mu_0 H = 0$), applying a magnetic field leads to the dashed curve in Figure 2.2. The magnetization saturates (beyond $\mu_0 H_{\text{S}}$) when all domains point in the same direction. When the applied field is reduced to zero, the ferromagnet will retain a net magnetization. To bring the magnetization back to zero, one can either heat the material above its Curie temperature, or one can apply a magnetic field in the opposite direction. The field necessary to flip the direction of magnetization is called
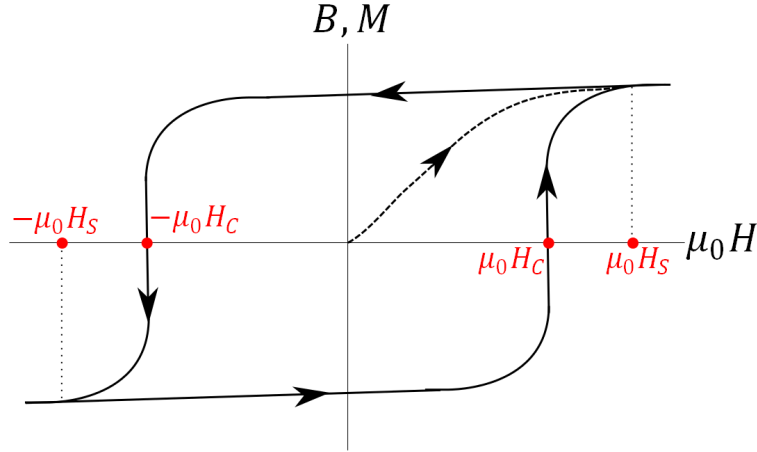
**Figure 2.2:** *Representation of a typical magnetization hysteresis loop for a ferromagnet. $\mu_0 H_C$ is the coercive magnetic field, which is the applied field at which the total magnetic field B or magnetization M changes sign. $\mu_0 H_S$ is the applied magnetic field at which the magnetization saturates.*

the *coercive field* $H_C$. A magnetized ferromagnet maintains its magnetization as long as the applied magnetic field is smaller than this coercive field. In this case, a ferromagnet will orient with its magnetic moment parallel to the applied magnetic field (equation 2.6). Note the difference with the magnetization of para- and diamagnets that are linear with the applied magnetic field at ambient temperatures (equation 2.3).

According to equation 2.6, the energy of a permanent magnetic dipole decreases with increasing magnetic field. Since force and energy are related by $\vec{F} = -\vec{\nabla}E$, the magnetic force in an inhomogeneous field can be written as [3]:

$$\vec{F} = \frac{1}{\mu_0} \left( \vec{m} \cdot \vec{\nabla} \right) \vec{B}. \tag{2.10}$$

Equation 2.10 shows that a ferromagnetic particle in an inhomogeneous field will experience a force towards regions of higher magnetic field. The strength of this force scales linearly with the size of both the magnetic dipole moment and the field gradient. Again it must be noted that equation 2.10, like equation 2.6, is valid as long as the applied magnetic field is below the coercive field of the material.

|  | Static magnetic fields | | Dynamic magnetic fields | |
|  | Homogeneous | Inhomogeneous | Rotating | Oscillating |
|---|---|---|---|---|
| **Ferromagnetic materials** | Alignment and steering | Alignment and propulsion | Induce rotational movement of structures with permanent magnetic moment | Create heat to induce motion (thermophoresis) |
| **Paramagnetic materials** | Alignment and steering | Alignment and propulsion. Guidance of paramagnetic particles over magnetic garnet films. Magnetic trapping | Rotational movement of paramagnetic beads in microfluidics | Manipulate the self-assembly of paramagnetic beads |
| **Diamagnetic materials** | Alignment and deformation | Magnetic levitation and separation. Magnetic trapping | Alignment along multiple axes | No known examples so far |

**Table 2.1:** *Overview of magnetic materials, magnetic fields and applications.*

### 2.1.4   Superparamagnetism

Superparamagnetism occurs for very small single domain ferromagnets (or fer-rimagnets[2]). In this case, the thermal energy is able to constantly turn over the direction of the magnetization. As a result, the average magnetization is zero and the material behaves as a paramagnet. However, since the particle still consists of a single domain, its susceptibility for magnetic fields is much larger than that of a normal paramagnet, hence its classification as a super-paramagnet. Since superparamagnets behave similarly to normal paramagnets, we discuss superparamagnetic particles in the paramagnetism section. A more elaborate discussion on superparamagnetic particles can be found in ref. [39].

In the remainder of this chapter, we will focus on the three introduced

---

[2]Ferrimagnets consist of domains like ferromagnets, but within each domain the spins have an alternating up and down orientation. Since the up and down spins are created by different species or ions within the crystal lattice, the magnetic moments of the two are not of equal size and hence do not cancel completely. Each domain therefore maintains a total magnetic moment unequal to zero.

classes of magnetic materials. For each, we will discuss how homogeneous, inhomogeneous, rotating and oscillating magnetic fields can be used to manipulate the motion of micro- and nanostructures. Manipulation of motion consists of propulsion, steering, or a combination of the two. An overview of these combinations is shown in Table 2.1.

## 2.2 Structures containing ferromagnetic materials

### 2.2.1 Homogeneous magnetic fields and ferromagnets

Several groups have used ferromagnetic particles to enable steering of their micro- and nanostructures. Kline *et al.* have fabricated 1.5 micron long rods consisting of alternating nickel and gold domains, which were capped by a platinum domain at one end [40]. Propulsion was achieved chemically by catalytic decomposition of hydrogen peroxide on the platinum surface. This led to the formation of oxygen bubbles, which gave the rod a recoil upon dissociation from the platinum surface and hence led to the desired propulsion [41]. The nickel sections were magnetized perpendicularly to the rod, ensuring a perpendicular alignment of the rod relative to the magnetic field direction (see Figure 2.3). Steering was achieved by changing the direction of an applied magnetic field of only 55 mT.
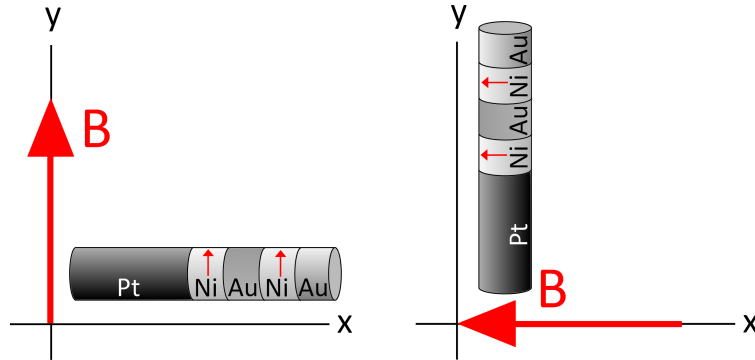


**Figure 2.3:** *Magnetic steering of rods consisting of Pt, Ni and Au segments. Rotation of the magnetic field leads to the rotation of the nanorod, such that the long axis of the rod is perpendicular to the field direction. The magnetic moments in the nickel segments are indicated by the small arrows. Adapted from ref. [41].*

This combination of magnetic steering and chemical propulsion has been

explored further by other groups. Baraban *et al.* made so-called Janus motors by partly capping 5 $\mu$m silica particles with a cobalt layer used for magnetization, which was topped with a platinum layer for catalysis of hydrogen peroxide decomposition [42]. The Janus motors were steered by magnetic fields below 1 mT. Other examples include microtubes made of rolled-up titanium-iron-platinum films, which decomposed hydrogen peroxide inside the tube [6]. The propulsion resulted from the expulsion of oxygen bubbles at the largest opening of the microtube. The presence of the ferromagnetic iron provided the advantage of facile manipulation and steering of the tubes by magnetic fields of 5 mT. Furthermore these tubes were able to transport and organise nanoplates.

### 2.2.2 Inhomogeneous magnetic fields and ferromagnets

Gradient magnetic fields were used in many occasions to propel ferromagnetic micro- and nanostructures. For instance, it was shown that polymer beads coated with ferromagnetic nickel could be moved in a horizontal direction by a magnetic field gradient [43]. Movement in the vertical direction was determined by buoyancy created by oxygen bubbles upon hydrogen peroxide decomposition on the nickel surface.

Similar experiments were also performed with cobalt ferrite microparticles, which were doped with palladium [44]. In a solution of hydrogen peroxide, propulsion of the particles was determined by oxygen formation on the particle surface. The authors demonstrated that small magnetic fields could be used to align and hence steer the ferromagnetic particles. However, higher magnetic fields also led to higher magnetic field gradients, which caused the microparticles to aggregate at the magnetic poles, where the magnetic field was strongest. It was also mentioned that relatively large particles, up to 150 $\mu$m in diameter, were used in order to track their movement with optical microscopy. Many examples in literature use micrometer-sized structures to allow for observation using optical microscopy and to avoid motion disruptions caused by Brownian motion, which occurs when the structures become so small that their magnetic energy becomes smaller than the thermal energy. Besides optical microscopy, only a few other *in situ* techniques are available to track magnetic particles. Dynamic light scattering [45] or confocal microscopy [46] are suitable alternatives, which also have the potential of tracking nanometer-sized objects. The problem of decreasing magnetic energy upon miniaturization of magnetic objects is resolved by the employment of higher magnetic fields (i.e. superconducting or Bitter magnets) [47].

The use of magnetic field gradients has also shown promising for applications in drug delivery. Mathieu *et al.* have investigated the possibility whether

ferromagnetic particles can be steered through blood vessels by the magnetic field gradients in a MRI machine [48–50]. For this purpose, carbon steel spheres (with 2.38 and 3.18 mm diameters) were forced to move against a water flow by a magnetic field gradient of 18 mT/m created within an MRI magnet. The flow properties were chosen to be close to those in real arteries. Since the employed particles are rather large (mm range) they can only find potential applications in the larger blood vessels like the aorta. The authors underlined that for propulsion of smaller particles through real mice capillaries gradients of several T/m would be needed. Since MRI systems cannot provide such large gradients additional gradient coils are needed. A coil providing a gradient of 0.443 T/m proved to be sufficient to move and steer 10.82 $\mu$m iron oxide microparticles in a simple artificial Y-shaped channel [50].

More examples on biomedical applications of inhomogeneous magnetic fields are summarized in the reviews by Pankhurst *et al.* [51, 52]. They offer an excellent overview on topics like magnetic separation, using magnetic particles, and magnetically guided drug delivery.

### 2.2.3 Rotating magnetic fields and ferromagnets

When a magnetic dipole is exposed to a magnetic field, it will align along the magnetic field as described by equation 2.6. This principle can be utilized to induce rotational motion in a structure containing a permanent magnetic dipole by rotating the applied magnetic field. This can be achieved by rotating a bar magnet or by setting up two perpendicular coils through which an oscillating current is fed. The strength of the rotating field should be smaller than the coercive field of the ferromagnet. Fields of a few mT are usually sufficient [53–59].

Magnetically induced rotations are often converted into translational motion [53–58], but also the investigation of the rotation itself has been reported [59]. Translational movements of micro- and nanostructures induced by rotating magnetic fields are often inspired by bacterial flagella [53–56]. Honda *et al.* were the first to investigate if a helical structure coupled to a permanent magnet could be propelled by a rotating magnetic field in the micro world [53]. Their construct consisted of a 1 mm$^3$ magnet coupled to a thin helical copper wire of several centimetres long. Rotation of the applied magnetic field resulted in the rotation of the small magnet and the helix attached to it, which propelled the whole structure forward. The direction of the motion inverted by reversing the rotation direction of the magnetic field. The structure was placed inside a high viscosity silicone oil to emulate low Reynolds numbers, similar to the condition for microstructures in water, and operated at frequencies between 2-5 Hz for

the most viscous oil used.

A similar structure, but on the micron scale, was made by Zhang *et al.* [54]. An artificial bacterial flagella (ABF), 47 $\mu$m long, was fabricated by connecting a magnetic head consisting of a Cr/Ni/Au trilayer square plate to a helical tail made of an InGaAs/GaAs bilayer or an InGaAs/GaAs/Cr trilayer. Three pairs of orthogonal coils were used to be able to rotate a magnetic field in all possible directions. Rotation of the applied magnetic field at 1-1.67 Hz resulted in rotation of the magnetic square plate and hence the helical tail as shown in Figure 2.4. Rotation of the helical tail propelled the ABF forward or backward, depending on the chirality of the helix. Furthermore, the direction of propulsion could be inverted by rotating the magnetic field in the opposite direction. Steering of the ABF was achieved by alignment of one of the magnetic plate diagonals with the magnetic field. Other examples utilizing rotating magnetic fields to induce linear movement include the linkage of a polystyrene microbead to a magnetic nanoparticle with an actual flagellar filament [55], planar ferromagnetic polymer structures, which deformed into helical structures when a rotating magnetic field was applied [56] and DNA-linked paramagnetic particles on glass surfaces [57].
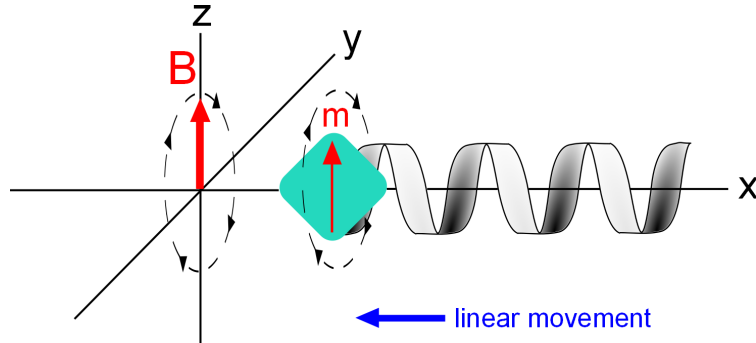


**Figure 2.4:** *Helix attached to a ferromagnet in a rotating magnetic field. The magnetic moment of the ferromagnet constantly aligns along the magnetic field, leading to rotation of the ferromagnet and the helix. Rotation of the helix will induce linear motion, in this case along the $\hat{x}$ direction. Adapted from ref. [54]*

A 7 $\mu$m long rodlike hybrid motor was reported by Gao *et al.*, which consisted of sequential nickel, silver, gold and platinum domains [58]. The nanowire could be propelled either by decomposition of hydrogen peroxide at the gold/platinum end, or by applying a rotating magnetic field which led to the rotation of the ferromagnetic nickel (see Figure 2.5). The silver was made

flexible by partly dissolving it in a hydrogen peroxide solution, which allowed the breaking of the symmetry of the rod, enabling the transfer of rotation into translational motion. Since the two forms of propulsion acted in opposite directions, a change in propulsion method also led to a change in direction.
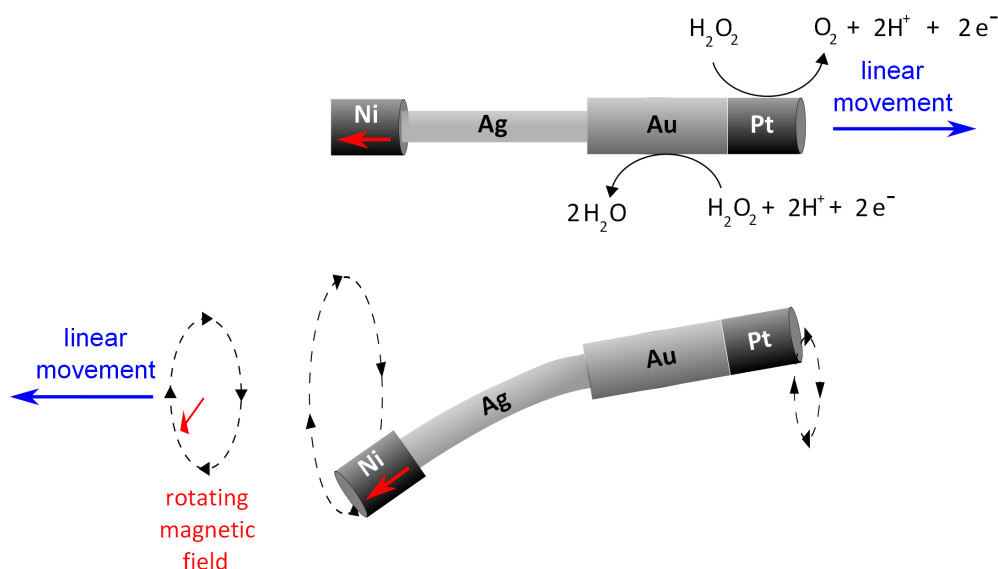


**Figure 2.5:** *Hybrid nanowire showing the two methods of propulsion. Top: catalytic propulsion by hydrogen peroxide decomposition. Bottom: magnetic propulsion by a rotating magnetic field. The magnetic moments in the nickel segments are indicated by the small arrows. Adapted from ref. [58]*

### 2.2.4   Oscillating magnetic fields and ferromagnets

While rotating magnetic fields are widely used to induce direct rotational motion, which is often transformed into translational motion, oscillating magnetic fields are used to induce heat in ferromagnetic materials. This technique is investigated in the medical world as a possible treatment for cancer, where it is known as magnetic hyperthermia [60–63]. The magnitude of magnetic hyperthermia is related to the energy needed to change the magnetization, which is equal to the area under the magnetization hysteresis curve. By applying an oscillating magnetic field, the magnetization will change continuously in direction and magnitude, following the magnetization hysteresis curve like the one shown in Figure 2.2. The energy of the oscillating magnetic field, which is essentially electromagnetic radiation, is absorbed in this process by the ferromagnet and is

dissipated in the form of heat. The amount of heat generated can be controlled by both the frequency and the amplitude of the oscillating magnetic field [62].

Propulsion of microstructures using the concept of magnetic hyperthermia has recently been demonstrated by Baraban *et al.* [63]. Micron sized silica particles were coated on one side with a magnetic permalloy. Frequencies of 400-6000 Hz with an amplitude of 7.5 mT were applied by a solenoid coil. Local heating of the magnetic cap provided a temperature gradient in the solvent, which propelled the Janus particle in the direction opposite to the magnetic cap by thermophoresis.

## 2.3 Structures containing paramagnetic materials

### 2.3.1 Homogeneous magnetic fields and paramagnets

Butykai *et al.* showed that paramagnetic anisotropic rod-like triclinic heme crystals, called hemozoin, can be magnetically aligned, using magnetic fields up to 5 T [64]. The heme crystals consist of hematin dimers linked via an iron-oxygen bond of adjacent hematin molecules, which are assembled via hydrogen bonding. Hemozion crystals are aligned with their long axis perpendicular to the magnetic field, since that axis has the highest paramagnetic susceptibility.

Alignment of particles based on shape anisotropy has been demonstrated by Tierno *et al.* [65]. Ellipsoid polystyrene particles, doped with superparamagnetic iron oxide, were oriented with their long axis parallel to the magnetic field. By coating part of the particle surfaces with platinum, the ellipsoids were propelled by the catalytic decomposition of hydrogen peroxide into water and oxygen. Steering of the ellipsoid particles was successfully achieved by changing the orientation of the magnetic field as shown in Figure 2.6. Steering of similar particles of spherical shapes could not be achieved, indicating that the shape anisotropy was indeed responsible for the alignment.

Doublet microparticles, consisting of silver and superparamagnetic Dynabead microspheres were demonstrated by Chaturvedi *et al.* to form long chains aligned by magnetic fields generated by neodymium-iron-boron bar magnets [66]. Furthermore, the chains could be decoupled from each other by activating the propulsion of the doublet particles. The propulsion of the doublet particles was not based on oxygen formation as in previously reported systems but the result of diffusiophoresis, which, besides the presence of hydrogen peroxide, also required irradiation with UV light to form silver and $OOH^-$ ions.

Since homogeneous magnetic fields do not propel ferro- and paramagnetic particles, the use of such fields is normally limited to orienting and steering. However, recent experiments have shown that a homogeneous magnetic field
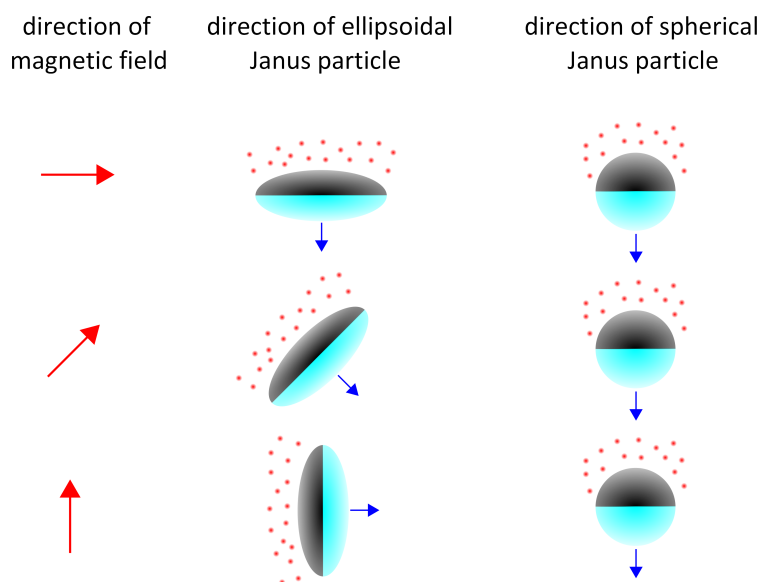
**Figure 2.6:** *Alignment of paramagnetic Janus particle coated partly with platinum (black) for decomposition of hydrogen peroxide. Formation of oxygen (small spheres) propelled the Janus particles in the direction indicated by the small arrows. Magnetic steering occurred only when shape anisotropy was present. Adapted from ref. [65].*

can alter not only the direction but also the speed of Janus particles partially covered with a cobalt/platinum layer topped by palladium [67]. In a hydrogen peroxide solution, the palladium catalyzes the decomposition of hydrogen peroxide into oxygen and water. During this process $OH^-$ and $H^+$ ions are formed as intermediates, which recombine into water. The authors claimed that these ions, which are only produced on the palladium side of the Janus particle, created an electric field responsible for polarization of the Janus particle and forced it to move towards the palladium side. This self-electrophoresis counteracts the propulsion created by the oxygen dissociation. The authors suggest that the magnetic field is responsible for an increase in recombination time of the $OH^-$ and $H^+$ ions by giving the ions a helical component. The helical component is induced by the Lorentz force, acting on moving charged particles in a magnetic field and directed perpendicular to the velocity of the particle and the magnetic field. This then leads to a decrease in the scattering cross-section and hence an increase in the ion lifetimes.

### 2.3.2   Inhomogeneous magnetic fields and paramagnets

The effect of gradient magnetic field forces on different kinds of paramagnetic transition metal ions have been studied by Tanimoto and co-workers [68–71]. In a gradient of 0.41 T$^2$/m, $\left(\vec{B} \cdot \vec{\nabla}\right) \vec{B}$, paramagnetic ions like Fe$^{3+}$, Co$^{2+}$, Ni$^{2+}$ and Cu$^{2+}$ were deposited in droplets on a silica gel plate. The droplets followed the direction of the gradient towards higher magnetic fields. The authors showed that the extent of displacement depended on the value of the paramagnetic susceptibility, the adsorption to the silica gel and the ion concentration of the droplets [69–71]. Also, the amount of displacement was much larger than could be explained by the drift velocity of a single ion induced by the magnetic field gradient. These latter results indicate that the ions do not move separately in a magnetic field gradient but rather in an orchestrated cluster consisting of both ions and water molecules. It was suggested that the magnetic force on individual ions was conveyed to ions and the surrounding water molecules by collisions resulting in a collective behaviour of paramagnetic ions and water molecules. For Cu$^{2+}$ the diameter of such a cluster was calculated to be 4.6 $\mu$m. The movement of paramagnetic particles does furthermore depend on the concentration gradient of these particles. Effectively, in an inhomogeneous solution of paramagnetic particles, the susceptibility of the solution as a whole will consequently be inhomogeneous as well. This will lead to *magnetoconvection*, in which regions of high susceptibility move towards higher fields, replacing regions of lower susceptibility.

Magnetic field gradients of a permanent magnet have also been used to accumulate superparamagnetic iron oxide at one side of ellipsoidal polystyrene particles, leading to the formation of ellipsoidal Janus particles [72]. The authors further showed that the interaction between such Janus particles differed from the interaction between ellipsoids with homogeneous distributions of iron oxide.

Magnetic field gradients can also be created by magnetic garnet films [73,74]. These ferromagnetic films contain magnetic domains which have their magnetic moments directed perpendicularly to the plane, pointing either up or down. At the boundary of two domains with opposite magnetic moments, a strong magnetic field gradient exists. Dhar *et al.* have shown that superparamagnetic particles can easily be guided along such boundaries as shown in Figure 2.7 [73]. Since the domain sizes and their magnetic orientation (up/down) can be manipulated beforehand, it is possible to create predefined magnetic paths along which paramagnetic particles can be moved [74].

Superparamagnetic particles in combination with inhomogeneous magnetic fields are also frequently employed in microfluidic applications, often for sepa-
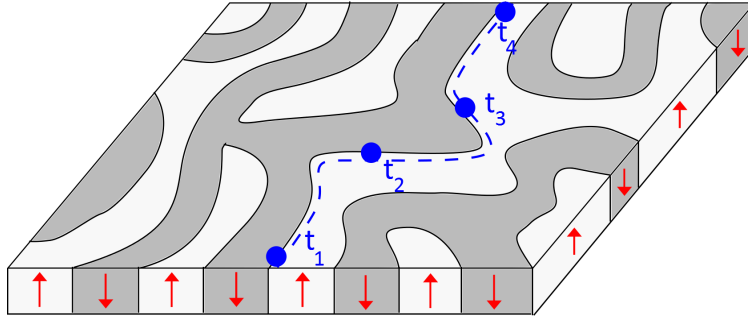
**Figure 2.7:** *Representation of a magnetic garnet film. The arrows at the sides show the direction of the magnetic moments. A paramagnetic particle (spheres) can be directed along boundaries of regions with opposite magnetic moments. Adapted from [73].*

rations, mixing, and biochemical procedures. For an extensive review on this specific topic we direct the reader to refs. [2–4].

### 2.3.3 Rotating magnetic fields and paramagnets

It was demonstrated that superparamagnetic microparticles (polystyrene spheres doped with iron oxide), form chains when a magnetic field is applied [75]. This is caused by the dipole-dipole interactions between the induced dipoles of each microparticle. Since these chains are of anisotropic shape, they can be rotated with a rotating magnetic field. Vuppu *et al.* achieved this for rotating fields of 4.5 to 7 mT [76,77]. At very low frequencies (5 rpm), growth of the chains was observed. This was explained by the fact that rotation increases encounters between different chains. Higher frequencies led to a breakage of chains, induced by viscous forces.

To prevent the breakage of the chains, Biswal *et al.* chemically linked the beads with glutaraldehyde to create rigid chains and with poly(ethylene glycol) (PEG) to create flexible chains [78,79]. The stiffness of the PEG-linked chains was adjusted by varying the length of the PEG linker. Flexible chains were shown to deform under rotating fields into a bent or even folded conformation (see Figure 2.8).

Rotating magnetic fields were not only used to induce rotation of paramagnetic chains. Karle *et al.* used a rotating permanent magnet to pull superparamagnetic beads labelled with DNA from one channel to the other in a microfluidic device [80]. The rotating magnet created an alternating strong and weak magnetic field. While the strong (inhomogeneous) field was respon-
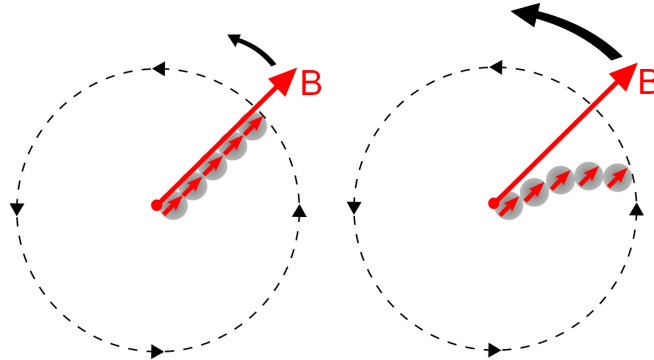
**Figure 2.8:** *Rotation of a chain of paramagnetic particles (PEG-linked) induced by a rotating magnetic field. Left: at low rotation frequencies the chain of particles will follow the magnetic field without a lag phase. Right: at high rotation frequencies there will be a phase lag between the chain and the magnetic field. At sufficiently high frequencies the chain will break. The small arrows in the paramagnetic particles represent the induced magnetization. Adapted from ref. [78].*

sible for pulling the paramagnetic particles from one channel to the other, the weak field was necessary to prevent the particles from sticking to the channels surface, which would have prevented further movement along with the flow.

The same group also demonstrated how a rotating magnetic field can be used to allow a superparamagnetic bead chain to walk over a microchannels inner surface [81]. Walking of bead chains was based on alignment of the bead chain by the magnet (which changed its orientation by rotation) and friction on the channels surface caused by attraction of the bead chain by the inhomogeneous magnetic field. The authors demonstrated that the bead chain could even walk against flows of up to 7.9 mm/s.

### 2.3.4 Oscillating magnetic fields and paramagnets

Dreyfus *et al.* have attached paramagnetic beads chains, interconnected with DNA linkers, to red blood cells [82]. These structures were exposed to a combination of a static homogeneous magnetic field and a perpendicular oscillating magnetic field, both in the order of 10 mT. The total magnetic field therefore changes orientation as function of time and this led to an induced beating pattern of the paramagnetic bead chain similar to that of a eukaryotic flagella. This induced beating pattern propelled the red blood cell in the direction of the paramagnetic chain. The authors demonstrated that the velocity of the red

blood cell depends on parameters like the length and rigidity of the bead chain, the oscillation frequency and strength of the static magnetic field component.

A combination of an oscillating magnetic field with a static homogenous magnetic field was also used to influence the self-assembly of superparamagnetic beads [83]. The authors demonstrated that at frequencies below 3 Hz, bead chains in the shape of the letters L and T were created. The distance between junctions could be increased by increasing the frequency. Above 3 Hz, the changing of the induced magnetic dipole in the beads was too fast compared to the translational movement. This led to the formation of disclike structures, originating at the places of highest bead concentration, which was near the junctions.

## 2.4 Diamagnetic structures

### 2.4.1 Homogeneous magnetic fields and diamagnets

Alignment of diamagnetic materials in magnetic fields has already been demonstrated for several molecules and molecular structures [84–88]. Magnetic alignment can greatly enhance the orientational order in a material, thereby improving several of its properties. Depending on the diamagnetic molecules or clusters used, magnetic alignment has for instance already been used to improve optical [85], transport [86] and electrical properties [87, 88].

A well-known example of steering diamagnetic materials is the alignment of Paramecium Caudatum, a unicellar organism which is diamagnetically anisotropic [89]. It was demonstrated that in fields larger than 3 T, swimming paramecium could be aligned, and hence their motion could be steered. The authors emphasised the difference with magnetotactic bacteria, which contains permanent magnetic structures called magnetosomes that allow to sense the Earths magnetic field of $5 \cdot 10^{-5}$ T.

Alignment of diamagnetic molecules has also been used to deform structures assembled from diamagnetic molecules [25]. An example is the deformation of liposomes. Phospholipids are diamagnetically anisotropic and tend to align perpendicular to a magnetic field. Since liposomes are made of phospholipids, a magnetic field is forcing the molecules to reorient, deforming the spherical liposome. This magnetic deformation force is balanced by the increasing bending force in the phospholipid membrane. Helfrich was the first to develop a model for the deformation of lipid bilayer vesicles [90, 91]. Helfrich's original idea was to use the magnetically induced deformation to determine the flexibility of these vesicles. The model assumed deformation of spheres into ellipsoids.

Helfrich's models have been used by other groups to carry out actual exper-

iments to deform diamagnetic vesicles in homogeneous magnetic fields [92–95]. For example, it has been shown that liposomes made from dipalmitoylphosphatidyl choline (DPPC) can be deformed at fields of 3.8 T as a function of temperature [92]. A transformation in shape from spherical to an elongated sphere (spheroid) was observed at temperatures higher than the glass transition temperature by measuring the magnetically induced birefringence. These kinds of liposomes were also reported to fuse under the influence of magnetic fields of up to 28 T [93].

Deformation is not limited to DPPC liposomes. For instance, an NMR study on dimyristoylphosphatidylcholine (DMPC) vesicles also showed deformation at 11.7 T [94]. With small angle neutron scattering, deformation was even already observed at magnetic fields up to 4 T [95]. In both cases, the extent of deformation was increased significantly above the glass transition temperature.

Tan *et al.* have shown that the orientation of phospholipid bicelles in a magnetic field can be switched from a parallel to a perpendicular orientation by adding biphenyl moieties to the phospholipids [96]. This is based on the fact that single bonds have a negative diamagnetic anisotropy, while that of multiple bonds is positive [29]. Adding a biphenyl group along the alkyl chains significantly increases the $\Delta\chi$ of the phospholipids, such that the total anisotropy goes from negative to positive. Consequently, the alignment of the bicelle changes from parallel to perpendicular to the field. The magnetic anisotropy of phospholipid molecules can also be modified by incorporation of certain paramagnetic lanthanide ions. It has been experimentally demonstrated that doping of phospholipids with $Eu^{3+}$, $Er^{3+}$, $Tm^{3+}$, and $Yb^{3+}$ changes the magnetic anisotropy from negative to positive [97]. Incorporation of certain other paramagnetic lanthanide ions like $Dy^{3+}$ leads to a more negative anisotropy [98, 99].

Magnetic deformation has also been shown to occur for non-biological structures. Spherical sexithiophene nanocapsules were deformed into oblate spheroids in magnetic fields up to 20 T [100, 101]. The deformation was visualized by magnetic birefringence and scanning electron microscope imaging of the deformed capsules trapped in a gel (see Figure 2.9). Since the $\Delta\chi$ of sexithiophenes is positive, deformation leads to oblate structures rather than prolate as was the case for liposomes.

Deformation of spherical nano-objects into spheroids could find some interesting applications in the manipulation of their motion. Firstly, a spheroid breaks spherical symmetry and hence the diffusion coefficient decreases along the long axis while it increases along the short axis [102–104]. Secondly, by tuning the sign of $\Delta\chi$, one can differentiate between a prolate ($\Delta\chi < 0$) or oblate ($\Delta\chi > 0$) spheroid, where the first is a sphere elongated along one axis while the second is a sphere which is contracted along one axis. This differentiation
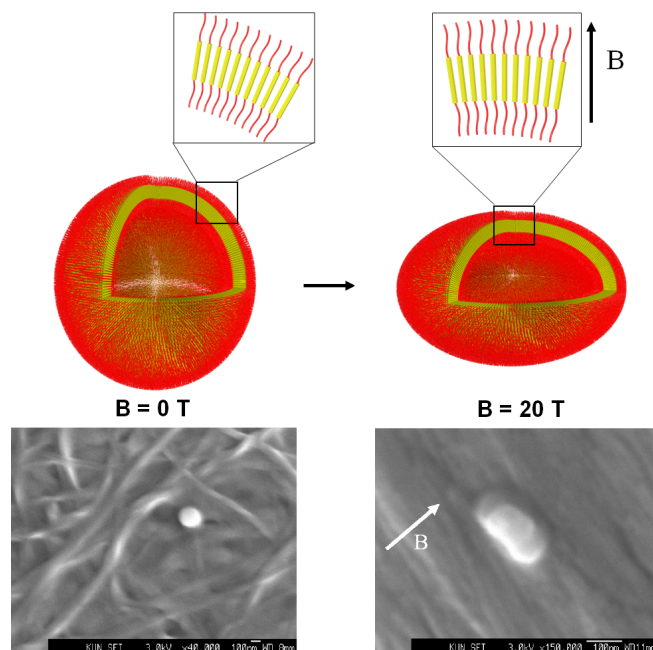
**Figure 2.9:** *Left: a sexithiophene nanocapsule stored in a gel at 0 T. Right: a nanocapsule stored in a gel at 20 T. The figure shows how the individual molecules are oriented with respect to the magnetic field. Adapted from ref. [100].*

made it possible to choose the direction of least drag.

In our group, we used diamagnetic amphiphilic block co-polymers to create several supramolecular morphologies like micelles, rods, vesicles and so-called stomatocytes [105–111]. The latter architectures were filled with platinum spheres to construct nanomotors. Since the block co-polymers exhibit diamagnetic anisotropy, we expect that high magnetic fields will form an interesting tool to controllably and reversibly modify the conformations and alignment of these structures. Indeed we have recently shown that bowl-shaped polymersomes called stomatocytes, self-assembled from (polyethylene glycol)-polystyrene (PEG-PS) block copolymers, are deformed by magnetic fields of 20 T, as is shown in Figure 2.10 [111]. Deformation is expected since the individual polymers within the polymersome membrane tend to align in a magnetic field, leading to tension in the membrane and hence a deformation of the stomatocyte. This deformation was only possible if organic solvents were present to plasticize the PS part of the membrane to make it more flexible. Interestingly,
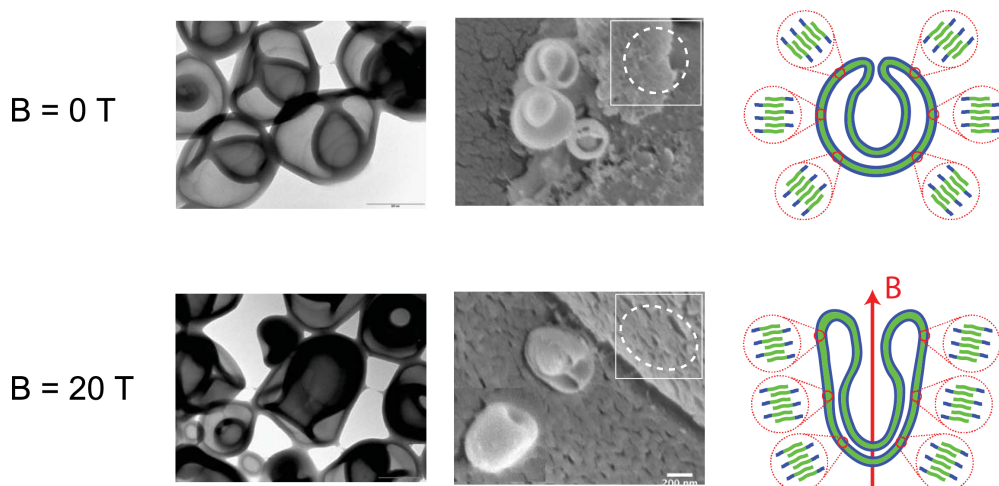
**Figure 2.10:** *Top: Electron microscope images of stomatocytes at 0 T. The stomatocytes are almost completely spherical and the opening is very small. Bottom: Electron microscope images of stomatocytes at 20 T. The stomatocytes are more elongated at this field and the opening is visibly larger. The cartoon on the right shows that at 20 T more polymers are almost perpendicular to the applied magnetic field. Adapted from ref [111].*

the deformation caused the stomatocyte opening to increase in diameter. This deformation was found to be reversible, allowing us to capture nanoparticles at 20 T and trap them by removing the field. The particles were released again when bringing the magnetic field back to 20 T.

## 2.4.2 Inhomogeneous magnetic fields and diamagnets

Magneto-Archimedes levitation was used to separate mixtures of diamagnetic matter [31–34] or mixtures of diamagnetic and paramagnetic matter [112]. Winkleman *et al.* showed that polystyrene particles differing in the amount of added $CH_2Cl$ groups could be separated by a pair of permanent magnets when placed inside a paramagnetic solution of gadolinium salts [32]. Another example is the levitation and separation of diamagnetic sodium chloride and potassium chloride particles inside pressurized paramagnetic gas (oxygen) at magnetic field gradients of 410 $T^2/m$ [24]. Pressurized oxygen has also been used to separate different biological materials such as DNA and cholesterol [33,34].

In the area of microfluidics, diamagnetic manipulation can be performed with permanent magnets, since they can be positioned very closely to mi-

crochannels or they can be integrated in microfluidic chips [113]. This can create relatively strong magnetic field gradients over small volumes. Zhu *et al.* used this principle to repulse diamagnetic polystyrene particles in a paramagnetic magnesium chloride solution [112]. The group of Pamme also experimented with repulsion of diamagnetic microparticles in microfluidic chips [114, 115]. Diamagnetic polymer microspheres were placed in paramagnetic manganese chloride solutions and exposed to an inhomogeneous magnetic field created by a superconducting magnet to create a repelling force leading to repulsion of the diamagnetic particles.

Another example is the trapping of diamagnetic polystyrene beads and living cells in a paramagnetic buffer between two permanent magnets placed 30 $\mu$m apart [27]. The two magnets faced each other with their north poles, creating a large magnetic field gradient. The diamagnetic particles were trapped in the midst between the two magnets where the magnetic field strength was lowest. The authors described this technique as a viable alternative to optical tweezers, being able to trap a wide variety of materials with larger sizes than those held by optical traps.

### 2.4.3  Rotating magnetic fields and diamagnets

In the previous sections, it was discussed that static magnetic fields can be used to align particles with their axis of highest magnetic susceptibility parallel to the magnetic field. The drawback of this type of alignment is that it leaves the other two axes free to rotate perpendicular to the magnetic field [116].

Kimura *et al.* have shown that it is also possible to align diamagnetic particles along their axis of lowest magnetic susceptibility by using a rotating magnetic field. Nylon fibers were used with $\chi_z < \chi_y = \chi_x < 0$ [117]. In a static magnetic field, the fibers aligned perpendicular to the magnetic field, but were still able to rotate in a plane perpendicular to the field. The authors showed, both experimentally and theoretically, that the use of a rotating magnetic field led to alignment of the fibers along the molecular $z$-axis. This was achieved by first aligning the fibers by a static magnetic field, followed by exposure to a rotating magnetic field. An alternative method used alternating exposure to a homogeneous magnetic field in two perpendicular directions (see Figure 2.11). Although the fiber dimensions were in the order of millimetres, the authors calculated that this procedure would also work for smaller particles (dimensions in the order of tenths of nanometers) if magnetic fields of 10 T or more are used. Rotating magnetic fields have also been used to align chiral cellulosic microfibers that form a nematic liquid crystal phase uniaxially which resulted in the unwinding of the helical structure [118]. Theoretical research

1. No magnetic field    2. Magnetic field    3. Switch magnetic
                   along z-direction     field to x-direction

$$\chi_z < \chi_y = \chi_x < 0$$

**Figure 2.11:** *Alignment of a nylon fiber can be achieved by an alternating magnetic field. When no field is present the fiber is free to rotate along all three axes (1). A field along the z-axis aligns the fiber on the xyplane, but the fiber is still free to rotate within this plane (2). A subsequent switch of the magnetic field to the x-direction will align the fiber in the xy-plane along the y-axis. Adapted from ref. [117].*

has also predicted that it will be possible to align molecules with a diamagnetic anisotropy of $\chi_z < \chi_y < \chi_x < 0$ by a rotating elliptic magnetic field [116]. These techniques also apply to paramagnetic particles with similar magnetic anisotropy.

## 2.5   Conclusions

Most research on the magnetic propulsion and steering of micro- and nanostructures has been performed with ferro- and paramagnetic (nano)particles. The most important reason for this is their relatively strong response to magnetic fields compared to diamagnetic matter. Manipulation of movement was achieved with homogeneous, inhomogeneous, rotating and oscillating magnetic fields.

Exposure of diamagnetic materials to (strong) magnetic fields can be used to

align them, and/or to induce shape changes that make them anisotropic. This allows for reversible modifications and, therefore, creates new opportunities to control the motion of novel micro- and nanostructures. Diamagnetic manipulation with permanent magnets has already been employed in microfluidics where magnetic repulsion of diamagnetic particles is enhanced by placing them in paramagnetic solutions. Deformation of supramolecular structures built from diamagnetic molecules still requires magnetic fields up to several Tesla, depending on the diamagnetic anisotropy of the molecules used.

Most research, for all magnetic materials, has been performed on microstructures rather than nanostructures. One reason for this is that smaller structures experience smaller magnetic forces, meaning that they are more easily disturbed by Brownian motion. This problem could be addressed by the use of higher magnetic fields. A second reason is the lack of *in situ* techniques that allow velocity determination and tracking of nanoparticles while exposing them to controllable magnetic fields. Optical microscopes are easily adapted with small bar or electromagnets but their resolution is usually limited to the micron size. Possible techniques that could be developed are *in situ* confocal microscopy or *in situ* Dynamic Light Scattering in stronger magnetic fields of 2 T or more. This could allow for miniaturization of para-, dia- and ferromagnetic nanostructures that can still compete with Brownian motion and whose movements can be tracked.

# References

[1] D. Kagan, R. Laocharoensuk, M. Zimmerman, C. Clawson, S. Balasubramanian, D. Kang, D. Bishop, S. Sattayasamitsathit, L. Zhang and J. Wang, *Small*, **6**, 2741 (2010)

[2] N. Pamme, *Lab Chip*, **6**, 24 (2006)

[3] M.A.M. Gijs, F. Lacharme and U. Lehmann, *Chem. Rev.*, **110**, 1518 (2010)

[4] M.A.M. Gijs, *Microfluid. Nanofluid.*, **1**, 22 (2004)

[5] N. Xia, T.P. Hunt, B.T. Mayers, E. Alsberg, G.M. Whitesides, R.M. Westervelt and D.E. Ingber. *Biomed. Microdevices.* **8**, 299 (2006)

[6] A.A. Solovev, S. Sanchez, M. Pumera, Y.F. Mei, and O.G. Schmidt, *Adv. Funct. Mater.*, **20**, 2430 (2010)

[7] A.A. Shah, H. Kang, K.L. Kohlstedt, K.H. Ahn, S.C. Glotzer, C.W. Monroe and M.J. Solomon, *Small*, **8**, 1551 (2012)

[8] P.D. Vogel, Eur. J. Pharm. Biopharm., **60**, 267 (2005)

[9] K. Svoboda, C.F. Schmidt, B. J. Schnapp and S.M. Block, *Nature*, **365**, 721 (1993)

[10] Y. Lu, L. Dong, L.-C. Zhang, Y.-D. Su, S.-H. Yu, *Nano Today*, **7**, 297 (2012)

[11] B.L. Feringa, *J. Org. Chem.*, **72**, 6635 (2007)

[12] W.R. Browne and B.L. Feringa, *Nat. Nanotechnol.*, **1**, 25 (2006)

[13] R. Kapral, *J. Chem. Phys.*, **138**, 020901 (2013)

[14] J. Wang and K.M. Manesh, *Small*, **6**, 338 (2010)

[15] J. Wang and W Gao, *ACS Nano*, **6**, 5745 (2012)

[16] S.J. Ebbens and J.R. Howse, *Soft Matter*, **6**, 726 (2010)

[17] P. Fischer and A. Ghosh, *Nanoscale*, **3**, 557 (2011)

[18] N.-T. Nguyen, *Microfluid Nanofluid*, **12**, 1 (2012)

[19] G. Friedman and B. Yellen, *Curr. Opin. Colloid Interface Sci.*, **10**, 158 (2005)

[20] D.J. Griffiths, *Introduction to Electrodynamics*, Benjamin Cummings 3th Ed. 2008, Chapter 6

[21] M. Yamaguchi and Y. Tanimoto (Ed.). *Magneto-Science*, 2006, Kodansha Springer. 1st Ed. Chapter 1.

[22] C. Kittel, *Introduction to Solid State Physics*, Wiley 8th Ed. 2005, Chapter 11

[23] P.W. Atkins, J. De Paula, *Physical Chemistry*, Oxford 8th Ed. 2006, Chapter 15

[24] G. Küstler, *Rev. Roum. Sci. Tech.-El.*, **52**, 265 (2007)

[25] A. Sakaguchi, A. Hamasaki and S. Ozeki, *Chem. Lett.*, **41**, 342 (2012)

[26] M. Suwa and H. Watarai, *Anal. Chim. Acta.*, **690**, 137 (2011)

[27] A. Winkleman, K.L. Gudiksen, D. Ryan and G.M. Whitesides, *Appl. Phys. Lett.*, **85**, 2411 (2004)

[28] I.F. Lyuksyutov, D.G. Naugle and K.D.D. Rathnayaka, *Appl. Phys. Lett.*, **85**, 1817 (2004)

[29] G. Maret and K. Dransfeld, *Top. Appl. Phys.*, **57**, 143 (1985)

[30] A.R. Urbach, J.C. Love, M.G. Prentiss and G.M. Whitesides, *J. Am. Chem. Soc.*, **125**, 12704 (2003)

[31] Y. Ikezoe, T. Kaihatsu, S. Sakae, H. Uetake, N. Hirota and K. Kitazawa, *Energ. Convers. Manage.*, **43**, 417 (2002)

[32] A. Winkleman, R. Perez-Castillejos, K.L. Gudiksen, S.T. Phillips, M. Prentiss and G.M. Whitesides, *Anal. Chem.*, **79**, 6542 (2007)

[33] N. Hirota, M. Kurashige, M. Iwasaka, M. Ikehata, H. Uetake, T. Takayama, H. Nakamura, Y. Ikezoe, S. Ueno and K. Kitazawa, *Physica B*, **346**, 267 (2004)

[34] K. Yokoyama, N. Hirota and M. Iwasaka, *IEEE Trans. Appl. Supercond.*, **17**, 2181 (2007)

[35] M.V. Berry and A.K. Geim, *Eur. J. Phys.*, **18**, 307 (1997)

[36] E. Beaugnon and R. Tournier, *Nature*, **349**, 470 (1991)

[37]  M.D. Simon and A.K. Geim, *J. Appl. Phys.*, **87**, 6200 (2000)

[38]  K.A. Mirica, S.T. Phillips, C.R. Mace and G.M. Whitesides, *J. Agric. Food Chem.*, **58**, 6565 (2010)

[39]  S.S. Shevkoplyas, A.C. Siegel, R.M. Westervelt, M.G. Prentiss and G.M. Whitesides, *Lab Chip*, **7**, 1294 (2007)

[40]  T.R. Kline, W.F. Paxton, T.E. Mallouk and A. Sen, *Angew. Chem. Int. Ed.*, **44**, 744 (2005)

[41]  R.F. Ismagilov, A.Schwartz, N. Bowden and G.M. Whitesides, *Angew. Chem.Int. Ed.*, **41**, 652 (2002)

[42]  L. Baraban, D. Makarov, R. Streubel, I. Mnch, D. Grimm, S. Sanchez and O.G. Schmidt, *ACS Nano*, **6**, 3383 (2012)

[43]  K.K. Dey, D. Sharma, S. Basu and A. Chattopadhyay, *J. Chem. Phys.*, **129**, 121101 (2008)

[44]  K.K. Dey, K.K. Senapati, P. Phukan, S. Basu and A Chattopadhyay, *J. Phys. Chem C.*, **115**, 12708 (2011)

[45]  P.K. Challa, O. Curtiss,J.C. Williams, R. Twieg, J. Toth, S. McGill, A. Jkli, J.T. Gleeson and S.N. Sprunt, *Phys. Rev. E.*, **86**, 011708 (2012)

[46]  N. Hirota and T. Ode, *Rev. Sci. Instrum.*, **77**, 036107 (2006)

[47]  S. Foner, *IEEE Trans. Appl. Supercond.*, **5**, 121 (1995)

[48]  J.-B. Mathieu, S. Martel, L. Yahia, G. Soulez and G. Beaudoin, *Biomed. Mater. Eng.*, **15**, 367 (2005)

[49]  J.-P. Mathieu, G. Beaudoin and S. Martel, *IEEE Trans. Biomed. Eng.*, **53**, 292 (2006)

[50]  J.-P. Mathieu and S. Martel, *Conf. Proc. IEEE Eng. Med. Biol. Soc.*, **1**, 472 (2006)

[51]  Q.A. Pankhurst, J. Connolly, S.K. Jones and J. Dobson. *J. Phys. D: Appl. Phys.*, **36**, R167 (2003)

[52]  Q.A. Pankhurst, N.T.K. Thanh, S.K. Jones and J. Dobson, *J. Phys. D: Appl. Phys.*, **42**, 224001 (2009)

[53]  T. Honda, K.I. Arai and K. Ishiyama, *IEEE Trans. Mag.*, **32**, 5085 (1996)

[54]  L. Zhang, J.J. Abbott, L. Dong, B.E. Kratochvil, D. Bell and B.J. Nelson, *Appl. Phys. Lett.*, **94**, 064107 (2009)

[55]  U.K.Cheang, D. Roy, J.H. Lee and M.J. Kim, *Appl. Phys. Lett.*, **97**, 213704 (2010)

[56]  P. Garstecki, P. Tierno, D.B. Weibel, F. Sagus and G.M. Whitesides, *J. Phys:. Condens. Matter*, **21** 204110 (2009)

[57]  P. Tierno, R. Golestanian, I. Pagonabarraga and F. Sagus, *J. Phys. Chem. B*, **112**, 16525 (2008)

[58]  W. Gao, K.M. Manesh, J. Hua, S. Sattayasamitsathit and J. Wang, *Small*, **7**, 2047 (2011)

[59] P. Dhar, C.D. Swayne, T.M. Fisher, T. Kline and A. Sen, *Nano, Lett.*, **7**, 1010 (2007)

[60] A. Jordan, R. Scholz, P. Wust, H. Fhling and R. Felix, *J. Magn. Magn. Mater.*, **201**, 413 (1999)

[61] C.S. Kumar and F. Mohammad, Adv. Drug Deliv. Rev, 2011, 63, 789

[62] B. Mehdaoui, J. Carrey, M. Stadler, A. Cornejo, C. Nayral, F. Delpech, B. Chaudret, and M. Respaud, *Appl. Phys. Lett.*, **100**, 052403 (2012)

[63] L. Baraban, R. Streubel, D. Makarov, L. Han, D. Karnaushenko, O.G. Schmidt and G. Cuniberti, *ACS Nano*, **7**, 1360 (2013)

[64] A. Butykai, A. Orbn, V. Kocsis, D. Szaller, S. Bordcs, E. Ttrai-Szekeres, L.F. Kiss, A. Bta, B.G. Vrtessy, T.Zelles and I. Kzsmrki, *Scientific Reports*, **3**, 1431 (2013)

[65] P. Tierno, R. Albalat and F. Sagus, *Small*, **6**, 1749 (2010)

[66] N. Chaturvedi, Y. Hong, A. Sen and D. Velegol, *Langmuir*, **26**, 6308 (2010)

[67] L. Baraban, D. Makarov, O. Schmidt, G. Cuniberti, P. Leiderer and A. Erbe, *Nanoscale*, **5**, 1332 (2013)

[68] M. Fujiwara, D.Kodoi, W. Duan and Y. Tanimoto, *J. Phys. Chem. B*, **105**, 3343 (2001)

[69] K. Chie, M. Fujiwara, Y. Fujiwara and Y. Tanimoto, *J. Phys. Chem. B*, **107**, 14374 (2003)

[70] M. Fujiwara, K. Chie, J. Sawai, D. Shimizu and Y. Tanimoto, *J. Phys. Chem. B*, **108**, 3531 (2004)

[71] M. Fujiwara, K. Mitsuda and Y. Tanimoto, *J. Phys. Chem. B*, **110**, 13965 (2006)

[72] O. Güell, F. Sagus and P. Tierno, *Adv. Mater.*, **23**, 3674 (2011)

[73] P. Dhar, Y.Cao, T. Kline, P. Pal, C. Swayne, T.M. Fischer, B. Miller, T.E. Mallouk, A. Sen and T.H. Johansen, *J. Phys. Chem. C*, **111**, 3607 (2007)

[74] P. Tierno, F. Sagus, T.H. Johansen and T.M. Fischer, *Phys. Chem. Chem. Phys.*, **11**, 9615 (2009)

[75] E.M. Furst, C. Suzuki, M. Fermigier and A.P. Gast, *Langmuir*, **14**, 7334 (1998)

[76] A.K. Vuppu, A.A. Garcia and M.A. Hayes, *Langmuir*, **19**, 8646 (2003)

[77] S. Krishnamurthy, A. Yadav, P.E. Phelen, R. Calhoun, A.K. Vuppu, A.A. Garcia and M.A. Hayes, *Microfluid. Nanofluid.*, **5**, 33 (2008)

[78] S.L. Biswal and A.P. Gast, *Phys. Rev. E*, **69**, 041406 (2004)

[79] S.L. Biswal and A.P. Gast, *Anal. Chem.*, **76**, 6448 (2004)

[80] M. Karle, J. Miwa, G. Czilwik, V. Auwrter, G. Roth, R. Zengerle and F. Von Stetten, *Lab Chip*, **10**, 3284 (2010)

[81] M. Karle, J. Whrle, J. Miwa, N. Paust, G. Roth, R. Zengerle and F. Von Stetten, *Microfluid. Nanofluid.*, **10**, 935 (2011)

[82] R. Dreyfus, J. Baudry, M.L. Roper, M. Fermigier, H.A. Stone and J. Bibette, *Nature*, **437**, 862 (2005)

[83] Y. Nagaoka, H. Morimoto and T. Maekawa, *Langmuir*, **27**, 9160 (2011)

[84] P.C.M. Christianen, I.O. Shklyarevskiy, M.I. Boamfa, J.C. Maan, *Physica B*, **346-347**, 255 (2004)

[85] I. O. Shklyarevskiy, M. I. Boamfa, P. C. M. Christianen, F. Touhari, H. van Kempen, G. Deroover, P. Callant and J.C. Maan, *J. Chem. Phys.*, **116**, 8407 (2002)

[86] I.O. Shklyarevskiy, P. Jonkheijm, P.C.M. Christianen, A.P.H.J. Schenning, A. Del Guerzo, J.-P. Desvergne, E.W. Meijer and J.C. Maan, *Langmuir*, **21**, 2108 (2005)

[87] I.O. Shklyarevskiy, P. Jonkheijm, N. Stutzmann, D. Wasserberg, H.J. Wondergem, P.C.M. Christianen, A.P.H.J. Schenning, D.M. de Leeuw, Z. Tomovi, J. Wu, K. Mllen and J.C. Maan, *J. Am. Chem. Soc.*, **127**, 16233 (2005)

[88] J.C. Gielen, M. Wolffs, G. Portale, W. Bras, O. Henze, A.F.M. Kilbinger, W.J Feast, J.C. Maan, A.P.H.J. Schenning and P.C.M. Christianen, *Langmuir*, **25**, 1272 (2009)

[89] K. Guevorkian and J.M. Valles Jr. *Biophys. J.*, **90**, 3004 (2006)

[90] W. Helfrich, *Phys. Lett.*, **43A**, 409 (1973)

[91] W. Helfrich, *Z Naturforsch C.*, **28**, 693 (1973)

[92] T.S. Tenforde and R.P. Liburdy, *J. Theor. Biol.*, **133**, 385 (1988)

[93] S. Ozeki, H. Kurashima and H. Abe, *J. Phys. Chem. B*, **104**, 5657 (2000)

[94] X. Qiu, P.A. Mirau and C. Pidgeon, *Biochim. Biophys Act.*, **1147**, 59 (1993)

[95] M.A.Kiselev, M. Janich, P. Lesieur, A. Hoell, J. Oberdisse, G. Pepy, A.M. Kisselev, I.V. Gapienko, T. Gutberlet and V.L. Aksenov, *Appl. Phys. A*, **74**, 1239 (2002)

[96] C. Tan, B.M. Fung and G. Cho, *J. Am. Chem. Soc.*, **124**, 11827 (2002)

[97] R.S. Prosser, S.A. Hunt, J.A. DiNatale and R.R. Vold, *J. Am. Chem. Soc.*, **118**, 269 (1996)

[98] P. Beck, M. Liebi, J. Kohlbrecher, T. Ishikawa, H. Rüegger, H. Zepik, P. Fischer, P. Walde and E. Windhab., *J. Phys. Chem. B*, **114**, 174 (2010)

[99] M. Liebi, P.G. van Rhee, P.C.M. Christianen, J. Kohlbrecher, P. Fischer, P. Walde and E.J. Windhab, *Langmuir*, **29**, 3467 (2013)

[100] I.O. Shklyarevski, P. Jonkheijm, P.C.M. Christianen, A.P.H.J. Schenning, E.W. Meijer, O. Henze, A.F.M Kilbinger, W.J. Feast, A. Del Guerzo, J.-P. Desvergne and J.C. Maan, *J. Am. Chem. Soc.*, **127**, 1112 (2005)

[101] O.V. Manyuhina, I.O. Shklyarevski, P. Jonkheim, P.C.M. Christianen, A. Fasolino, Mi.I. Katnelson, A.P.H.J. Schenning, E.W. Meijer, O. Henze, A.F.M. Kilbinger, W.J. Feast and J.C. Maan, *Phys. Rev. Lett.*, **98**, 146101 (2007)

[102] F. Perrin, *Le Journal de Physique et le Radium*, **7**, 497 (1934)

[103] H. Shimiuzu, *J. Chem. Phys.*, **37**, 765 (1962)

[104] R. Vasanthi, S. Bhattacharyya and B. Bagchi, *J. Chem. Phys.*, **116**, 1092 (2002)

[105] J.A. Opsteen, J.J.L.M. Cornelissen, and J.C.M. van Hest, *Pure Appl. Chem.*, **76**, 1309 (2004)

[106] M.G. Jeong, J.C.M. van Hest and K.T. Kim, *Chem. Comm.*, **48**, 359069 (2012)

[107] K,T. Kim, J. Zhu, S.A. Meeuwissen, J.J.L.M. Cornelissen, D.J. Pochan, R.J.M. Nolte and J.C.M. van Hest, *J. Am. Chem. Soc.*, **132**, 12522 (2010)

[108] S.A. Meeuwissen, K. Kim, Y. Chen, D.J. Pochan, and J.C.M. van Hest, *Angew. Chem. Int. Ed.*, **50**, 7070 (2011)

[109] D.A. Wilson, R.J.M. Nolte and J.C.M. van Hest, *Nat. Chem.*, **4**, 268 (2012)

[110] D.A. Wilson, R.J.M. Nolte and J.C.M. van Hest, *J. Am. Chem. Soc.*, **134**, 9894 (2012)

[111] P.G. van Rhee, R.S.M. Rikken, L.K.E.A. Abdelmohsen, J.C. Maan, R.J.M. Nolte, J.C.M. van Hest, P.C.M. Christianen and D.A. Wilson, *Nat. Commun.*, **5**, 5010 (2014)

[112] F. Mishima, T. Terada, Y. Akiyama and S. Nishijima, *IEE Trans. Appl. Supercond.*, **21**, 2059 (2011)

[113] J. Zhu, L. Liang and X. Xuan, *Microfluid. Nanofluid.*, **12**, 65 (2012)

[114] M.D. Tarn, N. Hirota, A. Iles and N. Pamme, *Sci. Technol. Adv. Mater.*, **10**, 014611 (2009)

[115] M.Vojtek, M.D. Tarn, N.Hirota and N. Pamme, *Microfluid. Nanofluid.*, **13**, 625 (2012)

[116] T. Kimura and M. Yoshino, *Langmuir*, **21**, 4805 (2005)

[117] T. Kimura, M. Yoshino, T. Yamane, M. Yamato and M. Tobita, *Langmuir*, **20**, 5669 (2004)

[118] F. Kimura, T. Kimura, M. Tamura, A. Hirai, M. Ikuno and F. Horii, *Langmuir*, **21**, 2034 (2005)

# Chapter 3

# Calculations on polymers and polymer vesicles

## Abstract

A parametrization is introduced to describe the shape of any cylindrically symmetric polymersome. Its geometrical properties, like surface area, area difference and volume are expressed in terms of this parametrization. For PEG-PS polymers, the magnetic anisotropy is calculated based on the anisotropies of single chemical bonds and groups and the degree of extension of the polymer. The magnetic anisotropy of a vesicle as a whole is found to be proportional to the magnetic anisotropy of a single polymer chain, the number of polymers in a vesicle and a shape dependent parameter which can be calculated in terms of the proposed parametrization. Finally, the total magnetic energy of a polymersome in a magnetic field is defined in terms of bending, osmotic and magnetic energy.

## 3.1   Introduction

In order to acquire a deeper understanding of (changes in) polymersome morphologies, one ideally would like to calculate their geometrical or physical properties such as volume, surface area and bending energy. The first step towards this goal is to describe the surface of a vesicle mathematically. In principle, there are two ways to this [1]:

- *Parametrization* [2–6]. Parametrization involves the description of all points $\vec{r}$ lying on a surface $S$ by a set of equations containing a number of adjustable parameters. In Cartesian coordinates, $\vec{r}$ is defined as: $\vec{r} = (x, y, z)$, which means that three equations, one for $x$, $y$ and $z$ each, are enough to describe the whole surface. The main advantage is that only a limited amount of parameters is needed to describe the entire surface. The disadvantage is that one is bound to only those shapes that can be described by the chosen parametrization. For instance, if a parametrization describes cylindrically symmetric shapes, one can never obtain a non-cylindrically symmetric shape by changing any of the parameters.

- *Triangulation* [7–9]. Another frequently used method used to describe a surface is triangulation. This is done by defining a large number of points which are positioned on the surface. These points can be connected, creating small triangular surface patches, hence the name triangulation. The advantage is that any arbitrary shape can be described, as long as one takes into account enough points. However, since every point has three coordinates $(x, y, z)$, the number of variables is three times the number of points, which, for an accurate description of a surface, can become quite numerous.

Either method allows one to calculate vesicle properties like surface area, volume and bending energy. In this chapter, we will introduce a parametrization that describes any cylindrically symmetric vesicle. The magnetic anisotropy of a PEG-PS block-copolymer is calculated and an equation is derived that relates the magnetic properties of a single vesicle to its shape. Finally, we will conclude by stating the total energy of a polymersome in a magnetic field, which can be calculated numerically using the proposed parametrization.

## 3.2 Parametrization of vesicle shapes

### 3.2.1 Parametrization and fitting of cylindrically symmetric vesicles

In order to obtain a useful, yet not too complicated, parametrization, we will assume that the vesicles are always cylindrically symmetric around the $z$-axis, an assumption which seem to have hold so far [1]. A requisite is that the parametrization should not only describe many different vesicle shapes, such as rods, discs, stomatocytes and spheroids, but it should also allow for variations within these different shapes. Another requisite is that both the surface and its slope are continuous. A discontinuous slope would lead to physical anomalies like infinite local bending energy. Because the shapes are cylindrically symmetric, this means that the slope of the shape at the symmetry axis must always be zero, otherwise there would appear a discontinuity in the slope of the surface at the symmetry axis.

To fulfill the first requisite, a Fourier-based approach seems a straightforward choice since, in principle, any shape can be described by the sum of many subsequent terms in sine or cosine. To address the second requisite, the direction parallel to the symmetry axis (which we will define as the z-axis) should be described in terms of cosine only while the directions perpendicular to the symmetry axis (the x and y-axes) should be described only in terms of sines. This means that the cross section of any cylindrically symmetric shape can be described by the following parametrization:

$$x\left(\zeta\right) = \sum_{n=1}^{l} a_n \sin\left(n \cdot \zeta\right), \tag{3.1}$$

$$z\left(\zeta\right) = \sum_{n=1}^{l} b_n \cos\left(n \cdot \zeta\right), \tag{3.2}$$

with $a_n$ and $b_n$ the Fourier coefficients of the $n^{th}$ order terms, $\zeta$ a parameter varying from 0 to $\pi$ and $l$ the maximum number of terms taken into account. The three dimensional shape is obtained by revolving the cross section around

the $z$-axis:

$$x\left(\zeta, \phi\right) = \sum_{n=1}^{l} a_n \sin\left(n \cdot \zeta\right) \cdot \cos\left(\phi\right), \tag{3.3}$$

$$y\left(\zeta, \phi\right) = \sum_{n=1}^{l} a_n \sin\left(n \cdot \zeta\right) \cdot \sin\left(\phi\right), \tag{3.4}$$

$$z\left(\zeta\right) = \sum_{n=1}^{l} b_n \cos\left(n \cdot \zeta\right), \tag{3.5}$$

with $\phi$ being the second parameter varying from 0 to $2\pi$. The complete surface of the vesicle can therefore be described by two parameters: $\zeta$ and $\phi$. In terms of this parametrization, all points on the surface, $\vec{r}$ are described by:

$$\vec{r} = \left(x\left(\zeta, \phi\right), y\left(\zeta, \phi\right), z\left(\zeta\right)\right). \tag{3.6}$$

A few examples of parameterized vesicles, together with their Fourier coefficients are shown in Figure 3.1.

In order to use this parametrization for the analysis of experimentally observed polymersomes, a fitting routine is needed that can fit this parametrization to an experimentally observed cross section obtained by cryo electron microscopy. In order to do so, we have developed a Matlab script that fits the parametrization (equations 3.1 and 3.2) to a collection of points positioned on the membrane surface. In short, this was achieved by loading the corresponding cryo-TEM or cryo-SEM image in Matlab, after which the symmetry axis was defined. Afterwards, numerous points on the polymersome membrane were selected. The selected points, describing the vesicle cross-section were rotated to have its symmetry axis in the vertical directions (along the z-axis). The parameters $a_n$ and $b_n$ were initially manually optimized to obtain a relative good first approximation of the shape. Next, a routine was started that minimized the distance between the selected points and the parametrized curve. This process was repeated until all parameters were optimized.

### 3.2.2 Calculating vesicle properties in terms of the parametrization

For a parameterized vesicle, geometrical properties such as surface area and volume can be calculated. The surface area of a vesicle is given by [10]:

$$A = \int_{\phi=o}^{2\pi} \int_{\zeta=0}^{\pi} J\left(\zeta, \phi\right) \cdot d\zeta \cdot d\phi, \tag{3.7}$$
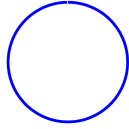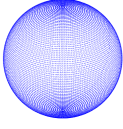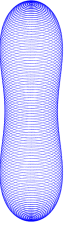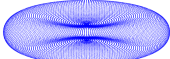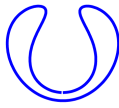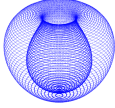
| shape | 2D (cross section) | 3D | parameterization coefficients |
|-------|--------------------|----|-------------------------------|
| sphere | | | $a = [2.5 \quad 0 \quad 0 \quad 0] \cdot 10^{-7}$ $b = [2.5 \quad 0 \quad 0 \quad 0] \cdot 10^{-7}$ |
| rod | | | $a = [1.4869 \quad 0 \quad 0.37172 \quad 0] \cdot 10^{-7}$ $b = [4.9563 \quad 0 \quad 0.24781 \quad 0] \cdot 10^{-7}$ |
| disc | | | $a = [3.1586 \quad 0 \quad -0.15793 \quad 0] \cdot 10^{-7}$ $b = [0.63171 \quad 0 \quad -0.31586 \quad 0] \cdot 10^{-7}$ |
| stomatocyte | | | $a = [1.7095 \quad -0.51286 \quad 0.85477 \quad 0.085477] \cdot 10^{-7}$ $b = [0 \quad -1.8805 \quad -0.17095 \quad -0.17095] \cdot 10^{-7}$ |

**Figure 3.1:** *Four vesicles of different shape, parameterized by equations 3.3 - 3.5. The coefficients (first 4 orders in a and b) are given for each shape.*

with $J(\zeta, \phi)$ being the Jacobian, which is defined as:

$$J(\zeta, \phi) = \left| \frac{\partial \vec{r}}{\partial \zeta} \times \frac{\partial \vec{r}}{\partial \phi} \right|. \tag{3.8}$$

Working out the Jacobian for our parametrization gives:

$$J(\zeta) = \left( \left[ \left( \sum_{n=1}^{l} n \cdot b_n \sin(n \cdot \zeta) \right) \cdot \left( \sum_{n=1}^{l} a_n \sin(n \cdot \zeta) \right) \right]^2 \right.$$
$$\left. + \left[ \left( \sum_{n=1}^{l} n \cdot a_n \cos(n \cdot \zeta) \right) \cdot \left( \sum_{n=1}^{l} a_n \sin(n \cdot \zeta) \right) \right]^2 \right)^{0.5}. \tag{3.9}$$

Equation 3.9 shows that the Jacobian depends on $\zeta$ only, since the shape is cylindrically symmetric. This simplifies equation 3.7 to:

$$A = 2\pi \int_{\zeta=0}^{\pi} J(\zeta) \cdot d\zeta. \tag{3.10}$$

The general equation to calculate the volume within any closed surface of spherical topology, described in any parametrization in $\zeta$ and $\phi$, can be written as:

$$V(\zeta, \phi) = \int_{\phi=0}^{2\pi} \int_{\zeta=0}^{\pi} z(\zeta, \phi) \cdot \left( \frac{\partial x}{\partial \zeta} \frac{\partial y}{\partial \phi} - \frac{\partial y}{\partial \zeta} \frac{\partial x}{\partial \phi} \right) \cdot d\zeta \cdot d\phi, \tag{3.11}$$

which, for our parametrization, equals:

$$V(\zeta) = 2\pi \int_{\zeta=0}^{\pi} \left( \sum_{n=1}^{l} b_n \cos(n \cdot \zeta) \right) \cdot \left( \sum_{n=1}^{l} a_n \sin(n \cdot \zeta) \right)$$
$$\cdot \left( \sum_{n=1}^{l} n \cdot a_n \cos(n \cdot \zeta) \right) \cdot d\zeta. \tag{3.12}$$

Again, this expression only depends on $\zeta$ since the parametrization is cylindrically symmetric. One can now define a reduced volume, which is the volume of
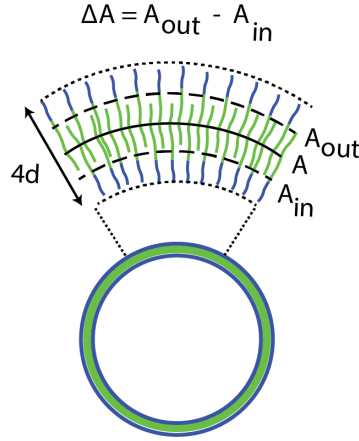


**Figure 3.2:** *Cartoon showing the midplane (solid line) that is used to calculate the surface area A. The dashed lines correspond to the midplanes of both monolayers which determine $A_{\mathrm{out}}$ and $A_{\mathrm{in}}$. All midplanes are separated by a distance d.*

the vesicle, divided by the volume of a sphere with an identical surface area:

$$v = \frac{V}{\frac{4}{3}\pi \left(\frac{A}{4\pi}\right)^{3/2}} = 6V\sqrt{\pi}A^{-3/2}.$$
(3.13)

By definition, the reduced volume must lie between 0 (no internal volume) and 1 (a sphere). The reduced volume has the advantage that it is only depending on shape and not on size.

Beside surface area $A$ and volume $V$, one can define another useful property, namely the area difference $\Delta A$. The area difference is the difference in surface area between the midplanes of the outer and inner monolayer of the membrane, as is depicted in Figure 3.2. The area difference can be calculated with [1]:

$$\Delta A = 4d \oint C \cdot dA,$$
(3.14)

with $d$ one quarter of the membrane thickness and $C$ the mean curvature. The mean curvature for any parameterized surface in $\zeta$ and $\phi$ is given by [11]:

$$C = -\frac{E \cdot N - 2 \cdot F \cdot M + G \cdot L}{2 \cdot (E \cdot G - F^2)},$$
(3.15)

with:

$$E = \frac{\partial \vec{r}}{\partial \zeta} \cdot \frac{\partial \vec{r}}{\partial \zeta},$$
(3.16)

$$F = \frac{\partial \vec{r}}{\partial \zeta} \cdot \frac{\partial \vec{r}}{\partial \phi},$$
(3.17)

$$G = \frac{\partial \vec{r}}{\partial \phi} \cdot \frac{\partial \vec{r}}{\partial \phi},$$
(3.18)

$$L = \frac{\partial^2 \vec{r}}{\partial \zeta^2} \cdot \hat{n},$$
(3.19)

$$M = \frac{\partial^2 \vec{r}}{\partial \zeta \partial \phi} \cdot \hat{n},$$
(3.20)

$$N = \frac{\partial^2 \vec{r}}{\partial \phi^2} \cdot \hat{n},$$
(3.21)

and $\hat{n}$ the unit normal vector on the membrane, which is defined as:

$$\hat{n} = \frac{\frac{\partial \vec{r}}{\partial \zeta} \times \frac{\partial \vec{r}}{\partial \phi}}{\left|\frac{\partial \vec{r}}{\partial \zeta} \times \frac{\partial \vec{r}}{\partial \phi}\right|}.$$
(3.22)

In terms of our parametrization, equations 3.16 to 3.21 can be expressed as:

$$E = \left( \sum_{n=1}^{l} n \cdot a_n \cos{(n \cdot \zeta)} \right)^2 + \left( \sum_{n=1}^{l} n \cdot b_n \sin{(n \cdot \zeta)} \right)^2. \qquad (3.23)$$

$$F = 0. \qquad (3.24)$$

$$G = \left( \sum_{n=1}^{l} a_n \sin{(n \cdot \zeta)} \right)^2. \qquad (3.25)$$

$$L = \left( \left( \sum_{n=1}^{l} -n^2 \cdot a_n \sin{(n \cdot \zeta)} \right) \cdot \left( \sum_{n=1}^{l} n \cdot b_n \sin{(n \cdot \zeta)} \right) \right.$$
$$\left. + \left( \sum_{n=1}^{l} -n^2 \cdot b_n \cos{(n \cdot \zeta)} \right) \cdot \left( \sum_{n=1}^{l} n \cdot a_n \cos{(n \cdot \zeta)} \right) \right)$$
$$\cdot \frac{\sum_{n=1}^{l} a_n \sin{(n \cdot \zeta)}}{J(\zeta)}. \quad (3.26)$$

$$M = 0. \qquad (3.27)$$

$$N = \frac{-\left( \sum_{n=1}^{l} a_n \sin{(n \cdot \zeta)} \right)^2 \cdot \left( \sum_{n=1}^{l} n \cdot b_n \sin{(n \cdot \zeta)} \right)}{J(\zeta)}. \qquad (3.28)$$

The area difference $\Delta A$ can also be normalized to make it size independent by dividing it by the area difference of a sphere with an identical surface area:

$$\Delta a = \frac{\Delta A}{16\pi d \left( \frac{A}{4\pi} \right)^{1/2}} = \frac{\Delta A}{8d\sqrt{\pi A}}. \qquad (3.29)$$

## 3.3   Magnetic properties

### 3.3.1   Magnetic energy of diamagnetic anisotropic objects

In a homogeneous magnetic field, the magnetic energy of an object is given by [12]:

$$E_{\mathrm{mag}} = -\frac{1}{2\mu_0} \chi V B^2, \qquad (3.30)$$

with $\mu_0$ the magnetic permeability in vacuum, $V$ the volume of the object, $B$ the applied magnetic field and $\chi$ the magnetic susceptibility of the material the

object is made of. For macromolecular structures or aggregates of molecules, it usually is more convenient to express the magnetic susceptibility per mole of objects:

$$E_{\mathrm{mag}} = -\frac{1}{2\mu_0 N_{\mathrm{A}}} \chi^{\mathrm{obj}} B^2, \tag{3.31}$$

with $N_{\mathrm{A}}$ Avogadro's constant and $\chi^{\mathrm{obj}}$ the magnetic anisotropy of one mole of objects, expressed in $m^3/mol$, rather than being dimensionless as in equation 3.30.

When the magnetic susceptibility of an object is anisotropic, it means that the magnetic susceptibility over the three principal axes are different. In that case, the magnetic energy along those axes is different as well, as follows from equation 3.31. In the remainder of this thesis we will only consider cylindrically symmetric structures, for which the magnetic susceptibility can be expressed by the following tensor [12]:

$$\chi^{\mathrm{obj}} = \begin{pmatrix} \chi_{\perp}^{\mathrm{obj}} & 0 & 0 \\ 0 & \chi_{\perp}^{\mathrm{obj}} & 0 \\ 0 & 0 & \chi_{\parallel}^{\mathrm{obj}} \end{pmatrix}, \tag{3.32}$$

with $\chi_{\perp}^{\mathrm{obj}}$ and $\chi_{\parallel}^{\mathrm{obj}}$ the magnetic susceptibility perpendicular and parallel to the symmetry axis respectively. This is shown schematically in figure 3.3a for a rod. The magnetic susceptibilities $\chi_{\perp}$ and $\chi_{\parallel}$ are defined in the axis frame of the object itself. To calculate the magnetic susceptibilities in the lab-frame, one has to make the following transformation:

$$\chi_x^{\mathrm{obj}} = \chi_{\parallel}^{\mathrm{obj}} \sin^2(\theta) \cos^2(\phi) + \chi_{\perp}^{\mathrm{obj}} \cos^2(\theta) \cos^2(\phi) + \chi_{\perp}^{\mathrm{obj}} \sin^2(\phi),$$
$$\chi_y^{\mathrm{obj}} = \chi_{\parallel}^{\mathrm{obj}} \sin^2(\theta) \sin^2(\phi) + \chi_{\perp}^{\mathrm{obj}} \cos^2(\theta) \sin^2(\phi) + \chi_{\perp}^{\mathrm{obj}} \cos^2(\phi), \tag{3.33}$$
$$\chi_z^{\mathrm{obj}} = \chi_{\parallel}^{\mathrm{obj}} \cos^2(\theta) + \chi_{\perp}^{\mathrm{obj}} \sin^2(\theta),$$

with $\theta$ and $\phi$ the angles that symmetry axis of the object makes with the $z$-axis and $x$-axis respectively, as is shown schematically in Figure 3.3b. Since the magnetic field is applied in the $z$-direction, the combination of equation 3.31 and 3.33 leads to:

$$E_{\mathrm{mag}} = -\frac{B^2}{2\mu_0 N_{\mathrm{A}}} \left( \chi_{\perp}^{\mathrm{obj}} + \left( \chi_{\parallel}^{\mathrm{obj}} - \chi_{\perp}^{\mathrm{obj}} \right) \cos^2(\theta) \right), \tag{3.34}$$

with $\theta$ the angle between the symmetry axis of the object and the applied magnetic field. For magnetic alignment, only the angle dependence of the magnetic

a



b
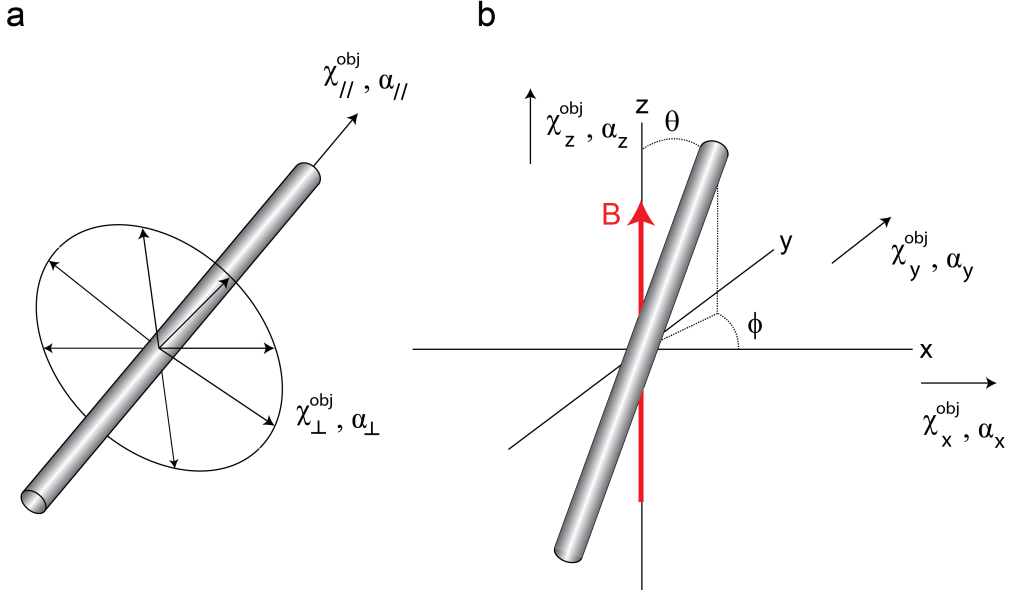
**Figure 3.3:** *(a) The magnetic susceptibilities and electric polarizabilities of a cylindrically symmetric object. (b) A cylindrically symmetric object in the lab frame (x,y,z). The magnetic field is applied in the z-direction.*

energy matters, as we will see in the next subsection. The angle dependent part of equation 3.34 can be written to:

$$E_{\mathrm{mag}}\left(\theta\right) = -\frac{1}{2\mu_0 N_{\mathrm{A}}} \Delta\chi^{\mathrm{obj}} B^2 \cos^2\left(\theta\right),$$ (3.35)

with $\Delta\chi^{\mathrm{obj}}$ the magnetic anisotropy, which is defined as:

$$\Delta\chi^{\mathrm{obj}} = \chi^{\mathrm{obj}}_{\parallel} - \chi^{\mathrm{obj}}_{\perp}.$$ (3.36)

### 3.3.2 Magnetic alignment, magnetic birefringence and the order parameter

We consider a cylindrically symmetric object such as the rod shown in Figure 3.3a. Such a structure can be aligned in a magnetic field as explained in the previous subsection. In this subsection, we will derive the optical properties of an object as function of its degree of alignment. We will assume that the object has an anisotropic electric polarizability, $\Delta\alpha$, in the molecular frame as shown in Figure 3.3a, similar to the magnetic anisotropy. This difference

in electric polarizability can be intrinsic to the material and/or be caused by its shape anisotropy. Since the refractive index of a material is proportional to the electric polarizability, the difference in refractive index, $\Delta n$, between two perpendicular directions in a material is proportional to the difference in electric polarizability between these directions [13]:

$$\Delta n \propto \Delta \alpha, \tag{3.37}$$

with:

$$\Delta \alpha = \alpha_{\parallel} - \alpha_{\perp}. \tag{3.38}$$

However, in a solution the object will have a certain orientation which depends on the angles $\theta$ and $\phi$ as shown in Figure 3.3b. This means that the polarizabilities in the molecular frame need to be transformed to the lab frame:

$$
\begin{aligned}
\alpha_{\mathrm{x}} &= \alpha_{\parallel} \sin^2(\theta) \cos^2(\phi) + \alpha_{\perp} \cos^2(\theta) \cos^2(\phi) + \alpha_{\perp} \sin^2(\phi), \\
\alpha_{\mathrm{y}} &= \alpha_{\parallel} \sin^2(\theta) \sin^2(\phi) + \alpha_{\perp} \cos^2(\theta) \sin^2(\phi) + \alpha_{\perp} \cos^2(\phi), \\
\alpha_{\mathrm{z}} &= \alpha_{\parallel} \cos^2(\theta) + \alpha_{\perp} \sin^2(\theta).
\end{aligned}
\tag{3.39}
$$

The orientation of the object is determined by the magnetic energy as was given by equation 3.35. The magnetic energy only depends on $\theta$ and therefore so does the orientation distribution $f(\theta)$. The distribution function is given by the Boltzmann equation [13, 14]:

$$f(\theta) = \frac{\exp\left(-E(\theta)/kT\right)}{\int_{\theta=0}^{\pi} \exp\left(-E(\theta)/kT\right) \cdot \sin(\theta) \cdot d\theta}. \tag{3.40}$$

The electric polarizability in the lab frame can then be expressed as:

$$
\begin{aligned}
\Delta \alpha^{\mathrm{lab}} &= \frac{\int_{\phi=0}^{2\pi} \int_{\theta=0}^{\pi} \left(\alpha_{\mathrm{z}} - \frac{\alpha_{\mathrm{x}} + \alpha_{\mathrm{y}}}{2}\right) \cdot f(\theta) \cdot \sin(\theta) \cdot d\theta \cdot d\phi}{\int_{\phi=0}^{2\pi} \int_{\theta=0}^{\pi} f(\theta) \cdot \sin(\theta) \cdot d\theta \cdot d\phi}, \\
&= \frac{2\pi \int_{\theta=0}^{\pi} \left(\frac{3\cos^2(\theta)-1}{2}\right) \cdot \left(\alpha_{\parallel} - \alpha_{\perp}\right) \cdot f(\theta) \cdot \sin(\theta) \cdot d\theta}{2\pi \int_{\theta=0}^{\pi} f(\theta) \cdot \sin(\theta) \cdot d\theta}, \\
&= \left\langle \frac{3\cos^2(\theta)-1}{2} \right\rangle \cdot \Delta \alpha
\end{aligned}
\tag{3.41}
$$

This means that the change in refractive index between directions parallel and perpendicular to the magnetic field is proportional to the order parameter [14]:

$$\Delta n^{\mathrm{lab}} = \Delta n_{\mathrm{max}} \left\langle \frac{3\cos^2(\theta)-1}{2} \right\rangle, \tag{3.42}$$

with $\Delta n_{\max}$ the maximal possible birefringence (at saturated alignment) and $\left\langle \frac{3\cos^2(\theta)-1}{2} \right\rangle$ the order parameter. The magnetic birefringence can be measured by a standard polarization modulation technique as is explained in chapter 4 (see figure 4.1).

### 3.3.3 Magnetic properties of a PEG-PS block-copolymer

As will be shown below, the magnetic anisotropy of a fully stretched PEG-PS block copolymer, $\Delta\chi^P$ (see figure 3.4), is negative, meaning that according to equation 2.7, it aligns perpendicular to an applied magnetic field. However, as we will see, the magnetic energy of one single PEG-PS polymer is not large enough to compete with thermal fluctuations, so an aggregate or an assembly of PEG-PS polymers is necessary to obtain magnetic alignment. The following initial calculation presented is only meant to give insight into the sign of the magnetic anisotropy for fully extended polymers. In that case, the magnetic anisotropy of a single PEG-PS block-copolymer, $\Delta\chi^P$, can be written in terms of the average magnetic anisotropy of a PEG or PS monomer as follows:

$$\Delta\chi^{\mathrm{P}} = n \cdot \Delta\chi^{\mathrm{PEG}} + m \cdot \Delta\chi^{\mathrm{PS}}, \tag{3.43}$$

with $n$ the number of repeating units of PEG and $m$ the number of repeating units of PS. In first instance, the anisotropy of the magnetic susceptibility $\Delta\chi$ is calculated for fully extended PEG and PS polymers. Since in reality the polymers in the membrane are coiled to some extent, the absolute value of the magnetic anisotropy will be lower than the value calculated here, which represents the maximal $\Delta\chi$ possible. The effect of coiling will be considered later.

**Diamagnetic anisotropy of PEG**

In Figure 3.5a, one monomer of PEG is shown. This monomer consists of one C-O-C and one C-C group as shown in Figure 3.5b and 3.5c [1]. The diamagnetic anisotropies of these groups (in $10^{-12}$ m$^3$/mol) are [15]:

$$\begin{aligned} \chi_{\mathrm{i}}^{\mathrm{COC}} &= \chi_{\mathrm{i}}^{\mathrm{COC}}, \\ \chi_{\mathrm{j}}^{\mathrm{COC}} &= \chi_{\mathrm{i}}^{\mathrm{COC}} + \Delta\chi_{\mathrm{ij}}^{\mathrm{COC}} = \chi_{\mathrm{i}}^{\mathrm{COC}} + 49, \\ \chi_{\mathrm{k}}^{\mathrm{COC}} &= \chi_{\mathrm{i}}^{\mathrm{COC}} + \Delta\chi_{\mathrm{ik}}^{\mathrm{COC}} = \chi_{\mathrm{i}}^{\mathrm{COC}} + 82, \end{aligned} \tag{3.44}$$

---

[1]The contributions of the C-H bonds are being neglected since they are much smaller than those of C-C and C-O bonds

and [14]:

$$
\begin{aligned}
\chi_i^{CC} &= \chi_i^{CC}, \\
\chi_j^{CC} &= \chi_i^{CC} + \Delta\chi_{ij}^{CC} = \chi_i^{CC} + 16, \\
\chi_k^{CC} &= \chi_i^{CC} + \Delta\chi_{ik}^{CC} = \chi_i^{CC} + 16.
\end{aligned}
\tag{3.45}
$$

The C-O-C frame $(i,j,k)$ coincides with the lab frame of the polymer $(x, y, z)$ and therefore:

$$
\begin{aligned}
\chi_x^{COC} &= \chi_i^{COC}, \\
\chi_y^{COC} &= \chi_j^{COC}, \\
\chi_z^{COC} &= \chi_k^{COC}.
\end{aligned}
\tag{3.46}
$$

For simplicity, we shall assume that all backbone atoms are bonded to their neighboring atoms by perfect tetrahedral symmetry. In that case, the $i$-axis of the C-C frame $(i,j,k)$ makes an angle of $35.5°$ with respect to the $x$-axis of the polymer frame $(x, y, z)$ and therefore:

$$
\begin{aligned}
\chi_x^{CC} &= \chi_i^{CC}\cos^2\left(35.5\right) + \chi_j^{CC}\sin^2\left(35.5\right) = \chi_i^{CC} + 5.4, \\
\chi_y^{CC} &= \chi_i^{CC}\sin^2\left(35.5\right) + \chi_j^{CC}\cos^2\left(35.5\right) = \chi_i^{CC} + 10.6, \\
\chi_z^{CC} &= \chi_k^{CC} = \chi_i^{CC} + 16.
\end{aligned}
\tag{3.47}
$$
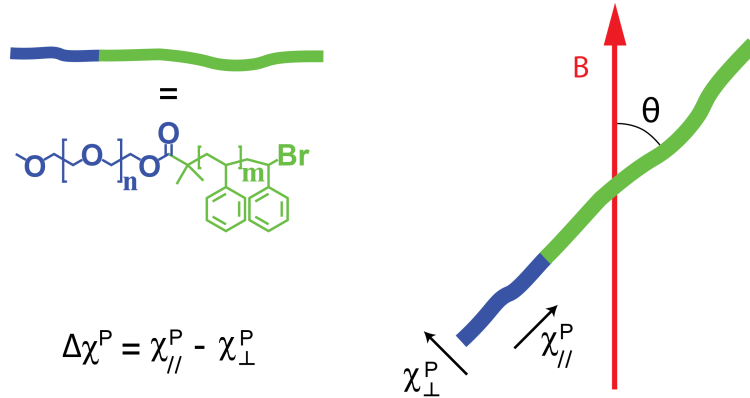


**Figure 3.4:** *A PEG-PS block copolymer in a magnetic field B. The magnetic susceptibility along the polymer chain is smaller than the magnetic susceptibility perpendicular to it, leading to a negative $\Delta\chi^P$.*

This gives a total diamagnetic susceptibility per monomer of PEG of:

$$\begin{aligned}
\chi_x^{PEG} &= \chi_i^{COC} + \chi_i^{CC} + 5.4, \\
\chi_y^{PEG} &= \chi_j^{COC} + \chi_j^{CC} + 59.6, \\
\chi_z^{PEG} &= \chi_k^{COC} + \chi_k^{CC} + 98.
\end{aligned} \tag{3.48}$$

Assuming that the polymers in the membrane are rotated along the molecular $x$-axis in random orientations, $\chi_y$ and $\chi_z$ will average out to one component perpendicular to $\chi_x$. This leads to the following magnetic anisotropy:

$$\Delta\chi^{PEG} = \chi_x^{PEG} - \frac{\chi_y^{PEG} + \chi_z^{PEG}}{2} = -73.4. \tag{3.49}$$
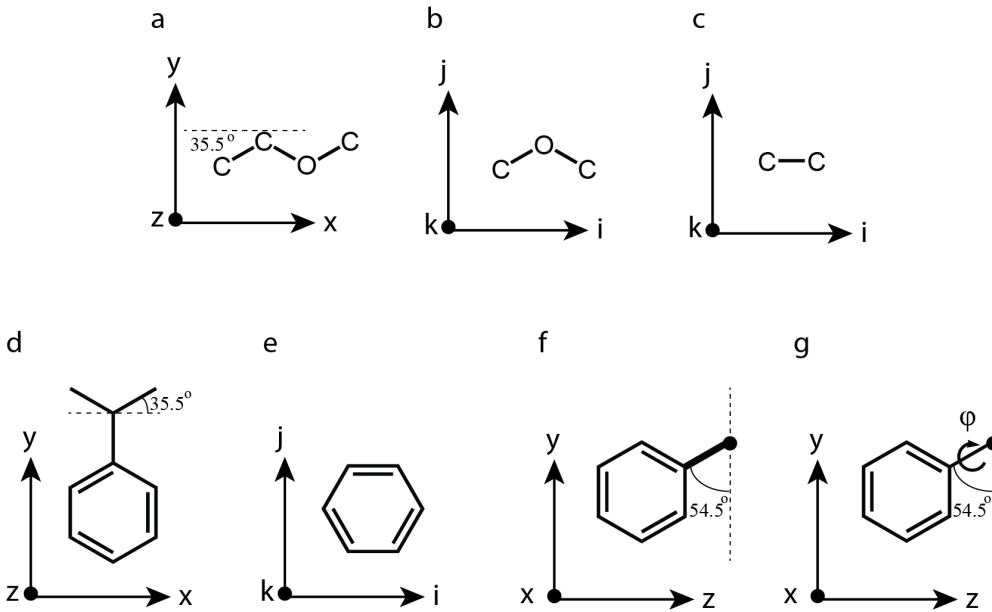


**Figure 3.5:** *(a) One monomer of PEG in the lab frame. (b) C-O-C group in the molecular frame in which $\chi^{COC}$ is defined. (c) C-C group in the molecular frame in which $\chi^{CC}$ is defined. (d) one monomer of PS in the lab frame showing the angle that the backbone C-C's make with respect to the x-axis. (e) One monomer of PS in the lab frame showing the angle of the C-C connecting the phenyl to the backbone with respect to the y-axis. (f) a phenyl group in the molecular frame in which $\chi^{Ph}$ is defined. (g) the phenyl is assumed to rotate free around the C-C bond connecting it to the PS backbone.*

So the magnetic anisotropy of one monomer of PEG when the polymer is fully extended is $\Delta\chi^{\text{PEG}} = -73.4 \cdot 10^{-12}$ m$^3$/mol.

**Diamagnetic anisotropy of PS**

In Figure 3.5d, one repeating unit of polystyrene is shown in the lab frame. It consists of one phenyl group, two C-C bonds in the backbone and one C-C bond connecting the phenyl to the backbone.

   We will consider the C-C bonds in the backbone first. The $i$-axis of the C-C frame $(i,j,k)$ makes an angle of 35.5° with respect to the $x$-axis of the polymer frame $(x, y, z)$ for both C-C bonds in the backbone. The contribution of each of these two bonds to the magnetic susceptibility of the PS monomer in the frame of the polymer can be written as:

$$
\begin{aligned}
\chi_x^{\text{CC}} &= \chi_i^{\text{CC}} + 5.4, \\
\chi_y^{\text{CC}} &= \chi_i^{\text{CC}} + 10.6, \\
\chi_z^{\text{CC}} &= \chi_i^{\text{CC}} + 16.
\end{aligned}
\tag{3.50}
$$

Now, we will consider the C-C bond connecting the phenyl to the backbone (Figure 3.5f). The $i$-axis of the C-C frame $(i,k,j)$ makes an angle of 54.5° (half of the angle between two bonds in a SP$^3$ hybridized molecule, which is 109°) with respect to the $y$-axis of the polymer frame $(x, y, z)$ and therefore:

$$
\begin{aligned}
\chi_x^{\text{CC}} &= \chi_i^{\text{CC}} + 16, \\
\chi_y^{\text{CC}} &= \chi_i^{\text{CC}} \cos^2(54.5) + \chi_j^{\text{CC}} \sin^2(54.5) = \chi_i^{\text{CC}} + 10.6, \\
\chi_z^{\text{CC}} &= \chi_i^{\text{CC}} \sin^2(54.5) + \chi_j^{\text{CC}} \cos^2(54.5) = \chi_i^{\text{CC}} + 5.4.
\end{aligned}
\tag{3.51}
$$

The three C-C bonds in a PS monomer thus give:

$$
\begin{aligned}
\chi_x^{\text{allCC}} &= 3\chi_i^{\text{CC}} + 26.8, \\
\chi_y^{\text{allCC}} &= 3\chi_i^{\text{CC}} + 31.8, \\
\chi_z^{\text{allCC}} &= 3\chi_i^{\text{CC}} + 37.4.
\end{aligned}
\tag{3.52}
$$

Assuming that the polymers in the membrane are rotated along the molecular $x$-axis in random orientations, $\chi_y$ and $\chi_z$ will average out to one component which is perpendicular to $\chi_x$. This leads to the following magnetic anisotropy:

$$
\Delta\chi^{\text{allCC}} = \chi_x^{\text{allCC}} - \frac{\chi_y^{\text{allCC}} + \chi_z^{\text{allCC}}}{2} = -7.8.
\tag{3.53}
$$

Finally, the contribution of the phenyl group needs to be considered (Figure 3.5e). The diamagnetic susceptibility of a phenyl group (in $10^{-12}$ m$^3$/mol) is:

$$\begin{aligned}
\chi_{\mathrm{i}}^{\mathrm{Ph}} &= -439, \\
\chi_{\mathrm{j}}^{\mathrm{Ph}} &= -439, \\
\chi_{\mathrm{k}}^{\mathrm{Ph}} &= -1189,
\end{aligned} \qquad (3.54)$$

with the molecular axis $i$, $j$, $k$ as defined in Figure 3.5e. The $i$-axis of the phenyl frame makes an angle of $54.5°$ with respect to the $y$-axis of the polymer frame (Figure 3.5f). Also, the phenyl group can rotate along the C-C bond that connects it to the backbone, thereby introducing an angle $\phi$ (with $\phi = 0$ corresponding to the configuration as drawn in Figure 3.5g). The diamagnetic susceptibility of the phenyl group in the polymer frame can therefore be written as:

$$\begin{aligned}
\chi_{\mathrm{x}}^{\mathrm{Ph}} &= \chi_{\mathrm{k}}^{\mathrm{Ph}} \cos^2\left(\phi\right) + \chi_{\mathrm{j}}^{\mathrm{Ph}} \sin^2\left(\phi\right), \\
\chi_{\mathrm{y}}^{\mathrm{Ph}} &= \left(\chi_{\mathrm{k}}^{\mathrm{Ph}} \sin^2\left(\phi\right) + \chi_{\mathrm{j}}^{\mathrm{Ph}} \cos^2\left(\phi\right)\right) \sin^2\left(\theta\right) + \chi_{\mathrm{i}}^{\mathrm{Ph}} \cos^2\left(\theta\right), \qquad (3.55) \\
\chi_{\mathrm{z}}^{\mathrm{Ph}} &= \left(\chi_{\mathrm{k}}^{\mathrm{Ph}} \sin^2\left(\phi\right) + \chi_{\mathrm{j}}^{\mathrm{Ph}} \cos^2\left(\phi\right)\right) \cos^2\left(\theta\right) + \chi_{\mathrm{i}}^{\mathrm{Ph}} \sin^2\left(\theta\right).
\end{aligned}$$

In Figure 3.6, $\chi_{\mathrm{x}}^{\mathrm{Ph}}$, $\chi_{\mathrm{y}}^{\mathrm{Ph}}$, $\chi_{\mathrm{z}}^{\mathrm{Ph}}$ and $\chi_{\mathrm{y,z}}^{\mathrm{Ph}}$, the average of $\chi_{\mathrm{y}}^{\mathrm{Ph}}$ and $\chi_{\mathrm{z}}^{\mathrm{Ph}}$, are plotted as function of $\phi$. $\chi_{\mathrm{x}}^{\mathrm{Ph}}$ is smaller than $\chi_{\mathrm{y,z}}^{\mathrm{Ph}}$ for angles of $0°$ to $54.7°$ and $125.3°$ to $180°$. This means that in this region the contribution of the phenyl groups leads to a perpendicular alignment of the PS relative to the magnetic field. The angle $\phi$ (or possible angles $\phi$) that the phenyl group can adopt determines the diamagnetic susceptibilities in the $x$, $y$ and $z$ directions. If the phenyl group is free to rotate, or if many phenyl rings adopt all possible orientations equally, the average contribution to the anisotropy of the diamagnetic susceptibility per phenyl is: $\Delta\chi^{\mathrm{Ph}} = -188.3 \cdot 10^{-12}$ m$^3$/mol. A freely rotating phenyl group leads to a $\Delta\chi_{\mathrm{x}}^{\mathrm{Ph}}$ which is lower than $\Delta\chi_{\mathrm{y,z}}^{\mathrm{Ph}}$ which supports the idea that the polymer aligns perpendicularly to the magnetic field. Adding to this the contribution of the backbone, we get: $\Delta\chi^{\mathrm{PS}} = -196.1 \cdot 10^{-12}$ m$^3$/mol.

The calculated $\Delta\chi$'s for PEG and PS are for maximally extended polymers, so they represent the maximum $\Delta\chi$ possible. The phenyl groups as well as the PS and PEG backbones all contribute to a negative $\Delta\chi$, which means that the polymers will align perpendicular to an applied magnetic field. The magnetic anisotropy per repeating unit is about 3 times as large for PS than for PEG. Also, in a typical PEG-PS block copolymer the number of PS units is at least 3 times as large. This means that the contribution to the magnetic anisotropy is
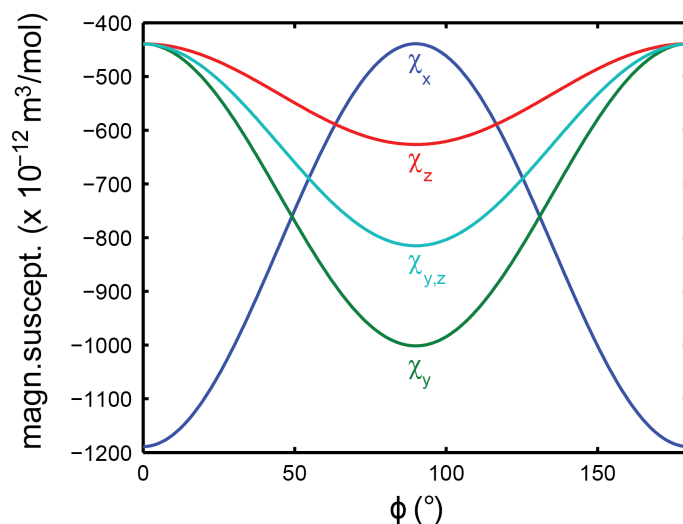
**Figure 3.6:** *The magnetic susceptibility of a phenyl group in the lab frame (x, y and z directions) as function of the angle $\phi$.*

dominated by the PS rather than the PEG. Also, in reality, the polymer chain will not be fully extended but rather be randomly coiled to some extent [16,17]. This will decrease the absolute value of $\Delta\chi$ as will be discussed next.

**The effect of coiling on the magnetic anisotropy of PS**

In a polymersome membrane the block-copolymers are not fully stretched since this configuration is statistically improbable. Rather, the block-copolymer will be coiled to some unknown extent [16, 17]. Therefore, one should investigate how the magnetic anisotropy depends on the degree of coiling. For this purpose, a Matlab script was written that calculates the magnetic anisotropy for PS as function of the degree of coiling. As an input parameter, the fraction of maximal extension is given, which determines the projection of the backbone C-C bonds on the $x$-axis. Then, all possible directions in the $y$ and $z$ directions are calculated, given the angles for certain bonds. From these possibilities, one is randomly chosen. This has no effect on the outcome of $\Delta\chi^{\mathrm{PS}}$, since the contributions in the $y$ and $z$ direction are averaged anyway. Again, the phenyl is allowed to rotate around the C-C bond connecting it to the backbone.

The result of the calculation is given in Figure 3.7a. It shows how the magnetic anisotropy per repeating unit, $\Delta\chi^{\mathrm{PS}}$ depends on the degree of polymer
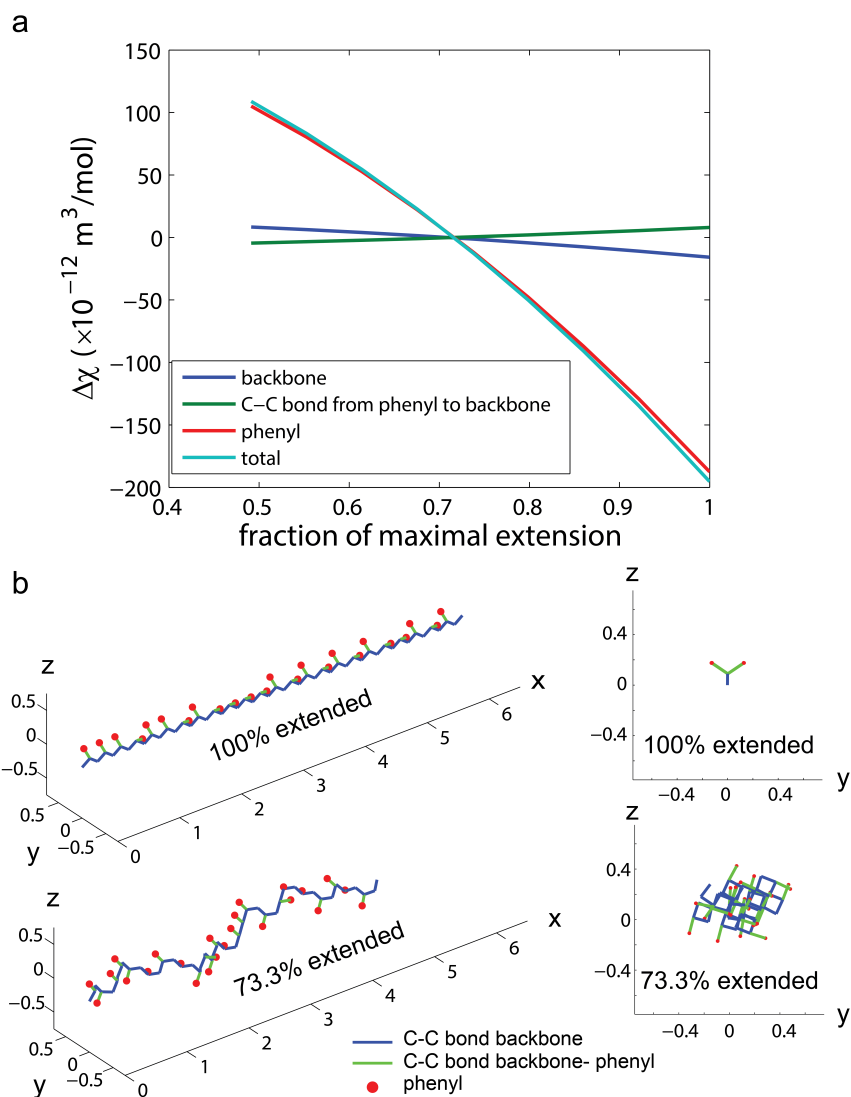
**Figure 3.7:** *(a) The magnetic anisotropy of PS (given per repeating unit) as function of extension. The largest contribution comes from the phenyl group. The phenyl is allowed to rotate freely around the C-C bond connecting it to the backbone. (b) Examples of differently extended polymers consisting of 24 PS units. The top one is fully extended while the bottom one is extended for only 73.3%. The one that is partially extended occupies more space in the yz plane. All distances are in nm.*

extension. The contributions from the individual components are also given. The plot clearly shows that the magnetic anisotropy is dominated by the contribution of the phenyl group. This is mainly because the phenyl group has a much larger magnetic anisotropy than a C-C group. Furthermore, one can see that the contribution of the C-C bond connecting the phenyl to the backbone is of opposite sign compared to the contributions of the backbone C-C's. This makes the contribution of all C-C bonds together even smaller.

If the polymer gets more extended, $\Delta\chi^{\mathrm{PS}}$ will become more negative. Coiling will lead to a conformation in which the polymer occupies less space in the $x$-direction but more space in the $yz$-plane, as can be seen in Figure 3.7b-d. The effect is that $\Delta\chi^{\mathrm{PS}}$ becomes smaller upon coiling up to a point where it is actually zero. Upon further reduction of the projection of the $x$-axis the sign of $\Delta\chi^{\mathrm{PS}}$ flips, meaning that the polymer becomes more extended in the $yz$-plane. In principle, this means that the polymer is stretched again, but this time in the $yz$-plane rather than in the $x$-direction.

### 3.3.4 Magnetic properties of a polymersome vesicle

In order to calculate the magnetic properties of a polymersome vesicle, it is necessary to transform the magnetic susceptibilities of every single polymer in the membrane (both $\chi_{\parallel}^{\mathrm{P}}$ and $\chi_{\perp}^{\mathrm{P}}$) from the polymer axes to the lab axes in which the whole vesicle will be described:

$$
\begin{aligned}
\chi_{\mathrm{x}}^{\mathrm{P}} &= \chi_{\parallel}^{\mathrm{P}} \sin^2\left(\theta_{\mathrm{N}}\right)\cos^2\left(\phi\right) + \chi_{\perp}^{\mathrm{P}}\cos^2\left(\theta_{\mathrm{N}}\right)\cos^2\left(\phi\right) + \chi_{\perp}^{\mathrm{P}}\sin^2\left(\phi\right), \\
\chi_{\mathrm{y}}^{\mathrm{P}} &= \chi_{\parallel}^{\mathrm{P}} \sin^2\left(\theta_{\mathrm{N}}\right)\sin^2\left(\phi\right) + \chi_{\perp}^{\mathrm{P}}\cos^2\left(\theta_{\mathrm{N}}\right)\sin^2\left(\phi\right) + \chi_{\perp}^{\mathrm{P}}\cos^2\left(\phi\right), \\
\chi_{\mathrm{z}}^{\mathrm{P}} &= \chi_{\parallel}^{\mathrm{P}} \cos^2(\theta_{\mathrm{N}}) + \chi_{\perp}^{\mathrm{P}}\sin^2(\theta_{\mathrm{N}}),
\end{aligned}
\tag{3.56}
$$

with $\theta_{\mathrm{N}}$ the angle between the surface normal and the $z$-axis. This is schematically shown in Figure 3.8. It can be calculated using:

$$
\theta_{\mathrm{N}} = \cos^{-1}\left(\frac{n_{\mathrm{z}}}{\hat{n}}\right),
\tag{3.57}
$$

with $n_{\mathrm{z}}$ the $z$ component of $\hat{n}$ which is given by equation 3.22. We can now calculate the magnetic anisotropy of the whole vesicle, $\Delta\chi^{\mathrm{ves}}$, by integrating $\chi_{\mathrm{z}}^{\mathrm{P}} - \frac{\chi_{\mathrm{x}}^{\mathrm{P}}+\chi_{\mathrm{y}}^{\mathrm{P}}}{2}$ over the vesicle surface:

a

b
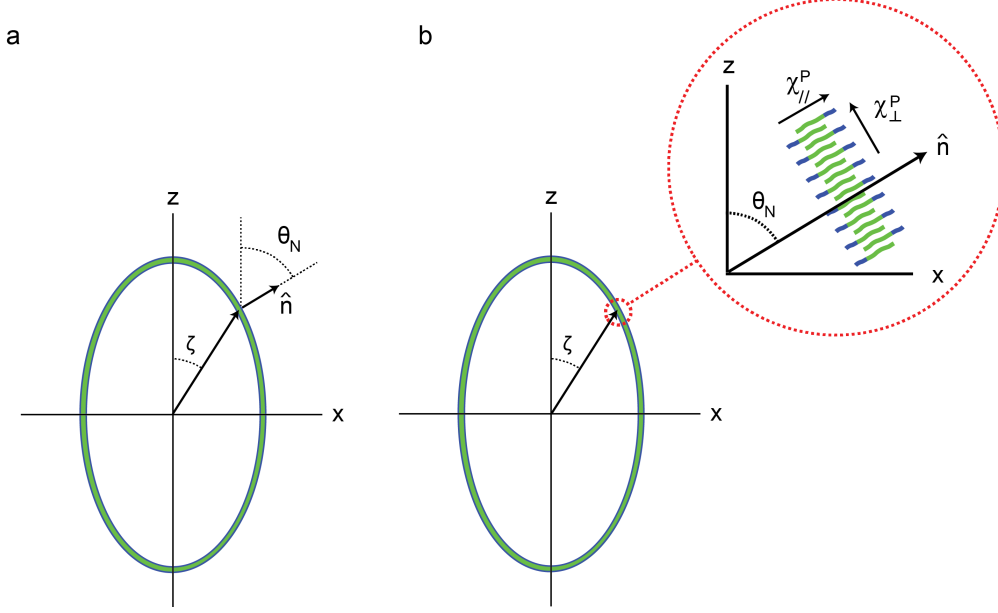


**Figure 3.8:** *(a) Cross section of a vesicle (spheroid) showing the angle $\theta_N$ that the surface normal, $\hat{n}$, makes with the z-axis. While $\zeta$ is a parameter in the parametrization of the vesicle (varying from 0 to $\pi$), $\theta_N$ is determined by the direction of $\hat{n}$ on the membrane surface. (b) Same vesicle as shown in (a) this time showing the individual polymers in the membrane making the same angle $\theta_N$ with the z-axis as the surface normal.*

$$
\begin{aligned}
\Delta\chi^{\text{ves}} &= \int_{\phi=0}^{2\pi} \int_{\theta=0}^{\pi} \left( \chi_z^{\text{P}} - \frac{\chi_x^{\text{P}} + \chi_y^{\text{P}}}{2} \right) \cdot \frac{N}{A} \cdot J(\zeta) \cdot d\zeta \cdot d\phi \\
&= 2\pi \int_{\theta=0}^{\pi} \left( \frac{3\cos^2(\theta_N) - 1}{2} \right) \cdot \left( \chi_\parallel^{\text{P}} - \chi_\perp^{\text{P}} \right) \cdot \frac{N}{A} \cdot J(\zeta) \cdot d\zeta \\
&= \left\langle \frac{3\cos^2(\theta_N) - 1}{2} \right\rangle \cdot \Delta\chi^{\text{P}} \cdot N,
\end{aligned}
\tag{3.58}
$$

with $N$ the number of polymers in the vesicle. Equation 3.58 demonstrates that the magnetic anisotropy of a vesicle depends on $\left\langle \frac{3\cos^2(\theta_N) - 1}{2} \right\rangle$, which is a shape dependent order parameter. It is calculated by the average orientation (order parameter) of all polymers. It is therefore determined by the distribution of all polymer orientations or, in other words, by the shape of the whole vesicle. To

distinguish this order parameter from the one used in the magnetic alignment of rigid structures (section 3.3.2) we will call this shape dependent order parameter just the *shape parameter* from now on, which we will define as:

$$SP = \left\langle \frac{3\cos^2(\theta_{\mathrm{N}}) - 1}{2} \right\rangle. \tag{3.59}$$

In the batches of block copolymers that are used in this research, the length of the number of PS repeating units is around 3 times larger than that of PEG. Also, the magnetic anisotropy of PS is more than 3 times larger than that of PEG. Finally, the PEG is more flexible while the PS is more confined and glassy in the interior of the membrane. Therefore, the magnetic anisotropy of a PEG-PS polymer is almost entirely dominated by the PS. We can thus approximate $\Delta\chi^{\mathrm{P}}$ by:

$$\Delta\chi^{\mathrm{P}} = m \cdot \Delta\chi^{\mathrm{PS}}, \tag{3.60}$$

with $m$ the number of PS monomers per polymer. The total number of polymers in a vesicle, $N$, can be calculated by:

$$N = \frac{A \cdot t \cdot \rho^{\mathrm{PS}}}{m \cdot M^{\mathrm{PS}}}, \tag{3.61}$$

with $A$ the surface area of the membrane, $t$ the thickness of the polystyrene part of the membrane, $\rho^{\mathrm{PS}}$ the density of polystyrene and $M^{\mathrm{PS}}$ the mass of one monomer of polystyrene. Combining equations 3.58, 3.59, 3.60 and 3.61 gives:

$$\Delta\chi^{\mathrm{ves}} = \frac{SP \cdot A \cdot t \cdot \rho^{\mathrm{PS}}}{M^{\mathrm{PS}}} \cdot \Delta\chi^{\mathrm{PS}}, \tag{3.62}$$

with $SP$ given by equation 3.59. Since, $\Delta\chi^{\mathrm{PS}}$ is defined in m$^3$/mol, $\Delta\chi^{\mathrm{ves}}$ is also expressed in m$^3$/mol, meaning that it is the susceptibility per mole of vesicles.

## 3.4 Total energy of a polymersome vesicle in a magnetic field

In the previous sections it was shown how a vesicle with any cylindrically symmetric shape can be parameterized. This parametrization was used to express the magnetic anisotropy of the whole vesicle in terms of the magnetic anisotropy of an individual block copolymer. In this section we will define all relevant energetic terms and express them in terms of our parametrization:

$$E_{\mathrm{tot}} = E_{\mathrm{mag}} + E_{\mathrm{bend}} + E_{\mathrm{osm}}. \tag{3.63}$$

The first term, which is the magnetic energy, is given by equation 3.35. The second and third terms represent the bending and osmotic energy respectively. These terms will be addressed in the next two subsections.

### 3.4.1 Bending energy

In the past, numerous models have been proposed for calculating the bending energy of a vesicle. Most of these models were proposed with phospholipid vesicles in mind [1,4]. To some extent, these models are material independent which means that they can be applied to polymersomes as well. However, one should always critically evaluate to which extent these models are valid.

The most general model nowadays is the so-called *Area Difference Elasticity* model [1,4]. In this model, the bending energy consists of two terms: the local bending energy and the non-local bending energy:

$$E_{\text{bend}} = E_{\text{bend}}^{\text{l}} + E_{\text{bend}}^{\text{nl}}. \tag{3.64}$$

The local bending energy is defined by [1,4,18]:

$$E_{\text{bend}}^{\text{l}} = \frac{\kappa}{2} \oint (2C - C_0)^2 \cdot dA, \tag{3.65}$$

with $\kappa$ the bending constant, $C$ the mean curvature as defined by equation 3.15 and $C_0$ the spontaneous curvature. The non-local bending energy can be written as [1,4,18]:

$$E_{\text{bend}}^{\text{nl}} = \frac{\alpha \pi \kappa}{8Ad^2} (\Delta A - \Delta A_0)^2, \tag{3.66}$$

with $\Delta A$ as defined by equation 3.14, $\Delta A_0$ the area difference of lowest energy (offset), $d$ a quarter of the thickness of the membrane (see Figure 3.2) and $\alpha$ a dimensionless parameter that usually is in the order of 1.

From equations 3.65 and 3.66 one can see where the designations *local* and *non-local* come from. To calculate the local bending energy, one has to square the mean curvature at every position and integrate over the surface of the vesicle. Because the mean curvature is squared, it does not matter if the difference between $C$ and $C_0$ is positive or negative. This means that one cannot alleviate stress in one part of the membrane by bending another part of the membrane in the opposite direction. In other words, if one were to divide the vesicle in a number of small pieces, the total local bending energy would be the sum of the local bending energy of each piece, hence it is local. For non-local bending this cannot be done. Since $\Delta A$ depends on the mean curvature only, the sign of $C$ does matter and one can alleviate stress in one part of the membrane by bending another part of the membrane in an opposite direction. In other words,
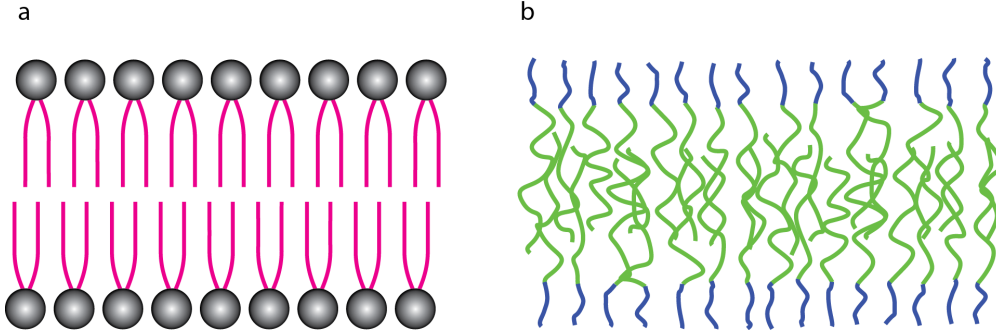
**Figure 3.9:** *(a) Schematic overview of a phospholipid membrane. The two monolayers are clearly separated. (b) In a polymersome membrane the polymers of both monolayers are entangled to some degree which does not allow for the two monolayers to move with respect to each other. The two membranes are not drawn to scale. The polymersome membrane is usually thicker than a phospholipid membrane.*

the non-local bending energy can only be calculated on the vesicle as a whole, hence it is non-local.

The non-local bending energy term was derived for bilayer vesicles and covers the extra degree of freedom one has for bilayer vesicles. It describes the lateral stresses between both monolayers [18]. However, this term is only valid if both monolayers are uncoupled, so they can move with respect to each other. In our polymersomes, the PS polymers in the membrane are entangled to a certain degree, which makes it improbable for one monolayer to shift freely with respect to the other (see Figure 3.9). Since our polymersomes do not fulfill this requirement, we will not consider non-local bending any further in this thesis.

To use the parametrization given in equations 3.3, 3.4 and 3.5 to calculate the bending energy (using equation 3.65), one must first find the minimum number of terms, $n$ to accurately describe the surface of any given vesicle. Therefore, we reproduced the shapes of minimal bending energy for different reduced volume as was calculated before by Seifert *et al.* [1, 4]. For $n = 4$, the exact same solutions could be reproduced (Figure 3.10): for reduced volumes between 0.70 and 0.95 rods were found, for reduced volumes between 0.60 and 0.65 discs were observed and for reduced volumes between 0.45 and 0.55 stomatocytes were found. This demonstrates that it is sufficient to only use the first four terms in equations 3.3, 3.4 and 3.5.
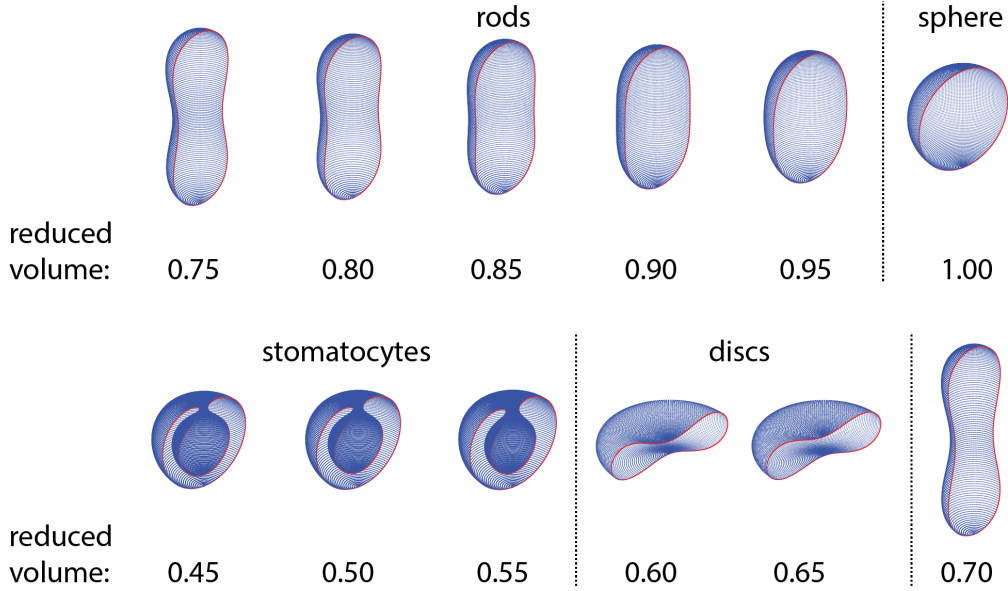
**Figure 3.10:** *Calculated shapes of lowest bending energy as function of the reduced volume v. Using the spontaneous curvature model with $C_0 = 0$, the shapes of lowest energy were calculated using the parametrization as given by equations 3.3 3.4 and 3.5 using only the first four terms in n. The calculated shapes are in full agreement with those found by Seifert et al. [1,4], demonstrating that it is sufficient to only use the first four terms in our parametrization.*

### 3.4.2 Osmotic energy

The osmotic energy plays an important role when the concentration of a chemical compound for which the membrane is relative impermeable[2] is different within the vesicle compared to the vesicle surroundings. In that case there is an osmotic pressure which has leads to the following energy:

$$E_{\mathrm{osm}} = R_{\mathrm{g}}T\left(n \cdot \ln\left(\frac{V}{V_0}\right) - c\left(V - V_0\right)\right), \qquad (3.67)$$

with $R_{\mathrm{g}}$ the gas constant, $T$ the temperature, $n$ the number of moles of molecules located within in the vesicle, $c$ the concentration of the chemical component responsible for the osmotic pressure, $V$ the inner volume of the vesicle and $V_0 \equiv n/c$.

The osmotic energy is decreased only if the difference in concentration of

---

[2]At least at time scales in which vesicle shape changes take place.

the chemical species over the membrane is decreased. Since the membrane is impermeable to the species, the osmotic energy can be lowered if the solvent is able to flow through the membrane. This means that changes in osmotic energy are accompanied by changes in the vesicle's inner volume.

## 3.5  Conclusions

In summary, we showed how the surface of any cylindrically symmetric vesicle can be described in terms of a Fourier-based parametrization. Equations to calculate vesicle properties like volume, surface area, bending energy and magnetic energy are calculated in terms of this parametrization. Furthermore we showed that the magnetic anisotropy of a vesicle scales linearly with the magnetic anisotropy of an individual polymer, the surface area of the vesicle and the shape factor, which is a shape dependent order parameter. Theoretical calculations of the magnetic properties of a single polymer show that its value strongly depends on its degree of extension.

## References

[1] U. Seifert, *Adv. Phys.*, **46**, 13 (1997)

[2] P.B. Canham, *J. Theoret. Biol.*, **26**, 61 (1970)

[3] B. Loubet, U. Seifert and M.A. Lomholt, *Phys. Rev. E*, **85**, 031913 (2012)

[4] U. Seifert, K. Berndl, and R. Lipowsky, *Phys. Rev. A*, **44**, 1182 (1991)

[5] V. Heinrich, M. Brumen, R. Heinrich, S. Svetina and B. Žekš, *J. Phys. II. France*, **2**, 1081 (1992)

[6] K. Khairy and J. Howard, *Soft Matter*, **7**, 2138 (2011)

[7] X. Li, P.M. Vlahovska and G.E. Karniadakis, *Soft Matter*, **9**, 28 (2012)

[8] G. Lim, M. Wortis and R. Mukhopadhyay, *PNAS*, **99**, 16766 (2002)

[9] R. Lipowsky, *Nature*, *349*, 475 (1991)

[10] Wolfram website. Link: http://mathworld.wolfram.com/SurfaceIntegral.html. Accessed September 2014.

[11] Wolfram website. Link: http://mathworld.wolfram.com/MeanCurvature.html. Accessed September 2014.

[12] M. Yamaguchi and Y. Tanimoto (Ed.). *Magneto-Science*, 2006, Kodansha Springer. 1st Ed. Chapter 1.

[13] J.C. Gielen, A. van Heyen, S. Klyatskaya, W. Vanderlinden, S. Höger, J.C. Maan, S. de Feyter and P.C.M. Christanen, *J. Am. Chem. Soc.*, **131**, 14134 (2009)

[14] G. Maret and K. Dransfeld, *Top. Appl. Phys.*, **57**, 143 (1985)

[15] R.R. Gupta, *Diamagnetische Suszeptibilität*, Springer, Berlin (1986)

[16] J.C.-M. Lee, M. Santore, F.S. Bates and D.E. Discher, *Macromol.*, **35**, 323 (2002)

[17] H. Bermudez, D.A. Hammer and D.E. Discher, *Langmuir*, **20**, 540 (2004)

[18] S. Svetina and B. Žekš, *Adv. Colloid Interface*, **208**, 189 (2014)

# Chapter 4

# Probing morphological changes of polymersomes during dialysis with magnetic birefringence

## Abstract

Magnetic birefringence was used to monitor *in situ* the morphological changes of diamagnetic polymersomes during shape transformation by dialysis. The birefringence was found to be very sensitive to the polymersome morphology as determined by electron microscopy. The deflation of polymersomes into disks was observed, followed by a bending and partial inflation into stomatocytes. The speed of this process could be increased significantly by performing the dialysis at higher temperatures. The kinetics of the dialysis process were found to be independent of the applied magnetic field up to 20 T, indicating that the osmotic forces are dominant.

## 4.1   Introduction

Amphiphilic block-copolymers can self-assemble in water into bilayer vesicles called polymersomes [1]. Many properties of these polymersomes, such as flexibility, permeability and functionality, can be tuned by varying the type or length of either the hydrophobic or the hydrophilic part of the block-copolymer [1] or by adding functional groups to make them stimuli responsive [2]. Flexibility and permeability can be also affected by the addition of organic solvent, such as tetrahydrofuran (THF), which acts as a plasticizer for the hydrophobic part of the polymersome membrane [3,4]. It has been previously demonstrated that polymersomes, self-assembled from poly(ethylene glycol) polystyrene (PEG-PS) in a mixture of THF, 1,4-dioxane and water, undergo shape transformations into bowl-shaped structures called stomatocytes by dialysis against pure water [5]. Also the conformation of these stomatocytes could be further manipulated by a reverse dialysis against a mixture of water, THF and dioxane [6]. This control over morphology has led to nanoparticle encapsulation by the stomatocytes [7] and their supramolecular assembly to give stomatocyte nanorockets [8,9]. These properties make polymersomes and stomatocytes very promising candidates as nanocontainers in drug delivery or nanochemistry.

Until now, the effect of dialysis on the morphology of the polymersomes or stomatocytes has been investigated by taking samples at regular intervals followed by the *ex situ* imaging of their conformations using electron microscopy. In this chapter, we demonstrate how the morphology of polymersomes during dialysis can be probed in a continuous and non-invasive way using *in situ* magnetic birefringence. These measurements clearly reveal the exact times at which the morphology of the polymersomes is changing, making it possible to take samples for electron microscopy at the crucial points of the dialysis.

Magnetic birefringence can be observed upon the alignment of molecules or aggregates. Even seemingly non-magnetic matter (such as the vast majority of polymers and biomolecules) is in fact weakly magnetic (diamagnetic). Molecules used for self-assembly are usually anisotropic in shape, leading to a magnetic response that is also anisotropic. These molecules therefore have a preferential orientation in a magnetic field. The difference in energy between two orthogonal orientations of a molecule is normally quite small and hence the alignment is largely randomized by thermal motion. However, when these molecules form aggregates or self-assemble into supramolecular structures, the total diamagnetic anisotropy can be enhanced significantly [10]. This principle has been used to orient organic nanostructures composed of a wide variety of molecules, including polymers [11–14]. The diamagnetic anisotropy, and hence the magnetic alignment, of these self-assembled structures is also related to

their overall shape. For instance, a sphere with an isotropic orientational distribution of molecules has no preferential axis of alignment. However, when the distribution of molecular orientations is anisotropic, magnetic alignment can occur. For example, a disc constructed from diamagnetic anisotropic molecules aligns with its flat side either parallel or perpendicular to the magnetic field, depending on the sign of the diamagnetic anisotropy of the molecular building blocks.

Magnetic orientation of supramolecular aggregates in solution results in a difference in the refractive index for light polarized parallel and perpendicular with respect to the magnetic field. This magnetic birefringence has been frequently measured to determine the degree of alignment of various aggregates in magnetic fields [11–14]. In this chapter, we will demonstrate how magnetic birefringence can be used to probe morphological changes of polymersomes during dialysis. Further insight into the mechanism of osmotically induced shape changes is presented.

## 4.2   Experimental details

### 4.2.1   Materials and Instrumentation

Tetrahydrofuran (THF) and 1,4-dioxane were purchased from Sigma-Aldrich. Poly (ethylene glycol)-polystyrene ($PEG_n$-$PS_m$) was synthesized by atom-transfer radical polymerization (ATRP) starting from PEG-macroinitiators as described previously [5, 6]. Two different batches were synthesized, each having its own molecular weight (MW) and polydispersity index ($PDI$): $PEG_{44}$-$PS_{133}$ (MW = 16 kDa, $PDI$ = 1.06) and $PEG_{44}$-$PS_{200}$ (MW = 23 kDa, $PDI$ = 1.05). The dialysis cell was home made by Peter Walraven at the Techno Centre of the Radboud University Nijmegen. The dialysis membranes were Spectra/Por Dialysis Membrane 4 (MWCO 12-14,000) from Spectrum Laboratories, Inc.

To explore the morphological changes we implemented a dialysis cell in a magnetic birefringence setup (Figure 4.1). For the birefringence measurements, a 1.5 mW intensity stabilized HeNe laser (1.5 mW, 632.8 nm) was used from Research Electro-Optics Inc. To increase the sensitivity of the birefringence measurements, a photo-elastic modulator (PEM) at 50 kHz was used. The flow cell with the polymersomes was placed between two crossed-polarizers, both at 45° with respect to the magnetic field. The magnetic field was applied using a Varian V-3900 2 T electromagnet or a 20 T Duplex Bitter magnet. Light of a HeNe laser was focussed on the upper chamber of a flow cell, which contained the polymersome sample. Initially the sample consisted of spherical polymersomes in pure water. A dialysis fluid consisting of 50% water, 40% THF

TOP VIEW



FRONT VIEW
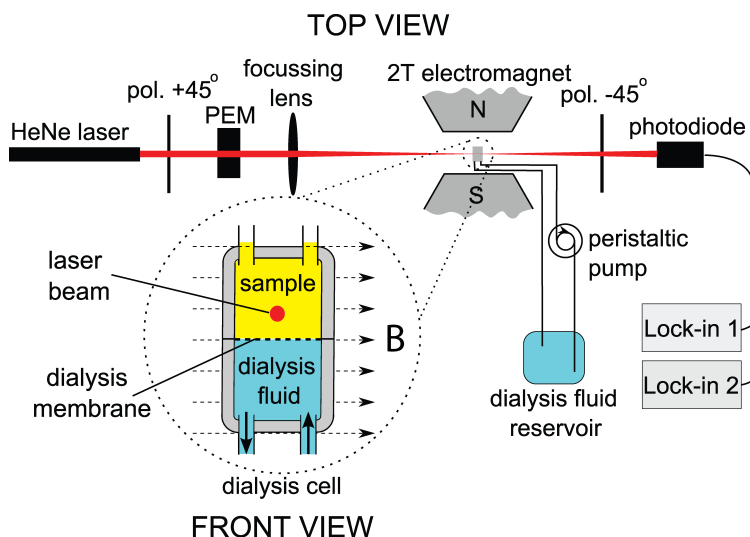
**Figure 4.1:** *Experimental setup in the 2 T electromagnet. The dialysis cell is placed between the poles of a 2 T electromagnet. The close-up of the dialysis flow cell shows how the two chambers are separated by a 12-14 kDa cut-off membrane. The laser beam is directed through the upper chamber, containing the polymersome sample. The birefringence is detected using a standard polarization modulation technique, using a photo-elastic modulator (PEM) and crossed polarizers (pol.). The magnetic field (B) lines are indicated by the dashed arrows pointing right. The dialysis fluid is refreshed continuously as indicated by the two solid arrows.*

and 10% 1,4-dioxane was pumped through the bottom chamber at a rate of 100 mL/h. The chambers were separated by a 12-14 kDa cut-off membrane. The magnetic birefringence was detected using a standard polarization modulation technique [15, 16].

(Cryo-)SEM was performed on a JEOL 6330 Cryo Field Emission Scanning Electron Microscope at an acceleration voltage of 3 kV. For Cryo-TEM a JEOL 2100 cryo-Transmission Electron Microscope was used. TEM was performed on a JEOL 1010 Transmission Electron Microscope at an accelerating voltage of 60 kV, for which 4 $\mu$L of sample was air dried on 200 Mesh carbon coated copper grids.

DLS was performed with a Malvern Zetasizer Nano S instrument and its data was analyzed with the corresponding software from Malvern Instruments.

### 4.2.2   Sample preparation

The polymersome sample that was used to perform the *in situ* dialysis experiment was prepared as follows. First, 10 mg of either $PEG_{44}$-$PS_{133}$ (16k) or $PEG_{44}PS_{200}$ (23k) powder was dissolved in a mixture of 600 $\mu$L THF and 400 $\mu$L dioxane and the solution was stirred for 30 minutes. Next, 3 mL of water was added at a rate of 1 mL/h (still under rigorous stirring). Polymersome formation was observed by the transition from a clear colorless solution to a cloudy suspension. Afterwards, the organic solvents were removed by dialysis against pure water. This was performed by placing the sample in a 12-14 kDa cutoff membrane tubing which was stirred over 48 hours in a 1 L beaker which was filled with water. During this time, the water was replenished 5 times at regular intervals. The resulting sample consisted of spherical polymersomes in pure water. A transition of polymersomes into stomatocytes during this dialysis step was prevented by performing the self-assembly step in an excess of water (75:25 water : organic solvent), rather than the 50:50 ratio that, upon dialysis against water, leads to the formation of stomatocytes. The hydrodynamic radii ($R_H$) of all samples used were measured by DLS. For the 16k sample measured at room temperature, $R_H$ = 251.7 nm with a $PDI$ of 0.134. For the 23k sample, $R_H$ = 230.7 nm with a $PDI$ of 0.100. For the 16k sample used for the temperature measurements, $R_H$ = 235.5 with a $PDI$ of 0.041. For the 16k sample measured at 20 T, $R_H$ = 254.7 nm with a $PDI$ of 0.091.

## 4.3   Measurements

### 4.3.1   Dialysis of a rigid polymersome sample

The birefringence of a rigid 16k polymersome sample was measured during dialysis over a time interval of 360 minutes (Figure 4.2a). At the beginning of the experiment, the birefringence remained zero up to 170 minutes (point 3), after which a rapid increase in the signal was observed. A maximum was reached at 230 minutes (point 5), after which the birefringence decreased. From point 7 onwards, the sample showed a small birefringence, which remained constant until the end of the measurement (point 8). At certain time points, magnetic field sweeps were performed where the magnetic field was reduced to zero and subsequently brought back to 2 T (indicated in Figure 4.2a by the colored lines I to V). The field sweeps were sufficiently rapid (about one minute) to allow the subsequent birefringence signal to remain unchanged by the continuous dialysis. The birefringence always decreased to zero when the magnetic field was brought to zero. Restoring the field to 2 T also recovered the birefringence

a



b
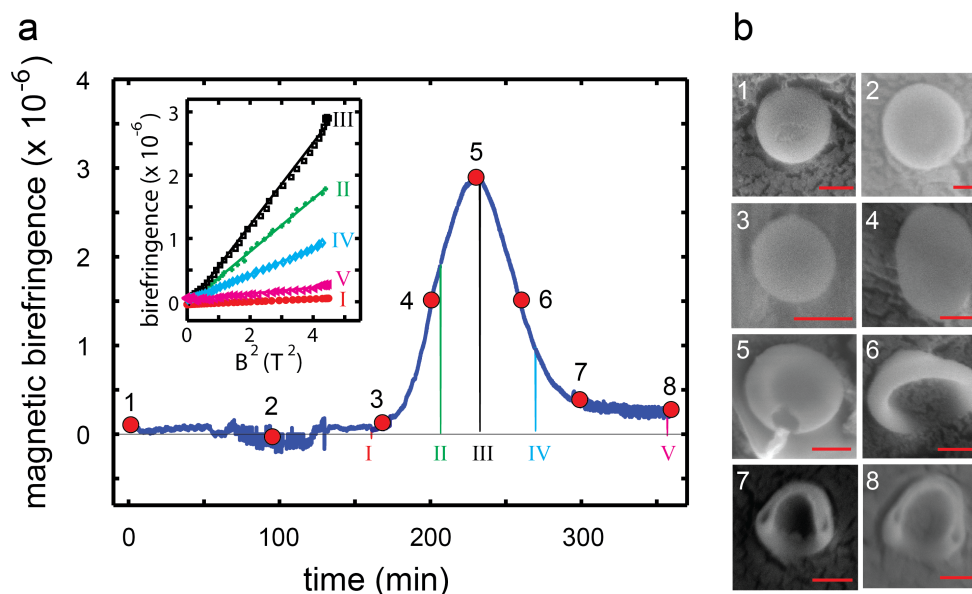


**Figure 4.2:** *(a) Magnetic birefringence during dialysis of a 16k polymersome sample at 2 T at room temperature. Several magnetic field sweeps (I to V) were performed, which are plotted against $B^2$ in the inset. Samples taken at points 1-8 were investigated by cryo-SEM, images of which are shown in (b). Note that the birefringence increases from the moment the polymersomes start to deflate and become anisotropically shaped (3-5). The decrease in birefringence occurs when the disks at point 5 fold and partly inflate to form stomatocytes (6-8). All scale bars are 250 nm.*

to the same value before the field sweep, showing that the measured signal is not caused by any drift. The inset of Figure 4.2a shows the birefringence as function of $B^2$. All curves scale quadratically with the applied magnetic field, implying a non-saturated magnetic alignment. This is usually observed in the low magnetic field regime where the competition with thermal motion tends to randomize the orientation of the molecules resulting in only partial alignment with the field.

Measuring magnetic birefringence during dialysis offers the opportunity to stop dialysis at well-defined points to take samples for further investigation by electron microscopy. In this manner, the morphology can be related to the amplitude of the birefringence signal. Samples were taken at points 1-8 as indicated by the red dots in Figure 4.2a. Cryogenic-Scanning Electron Microscopy (cryo-SEM) images of sample 1-8 are shown in Figure 4.2b. At the beginning
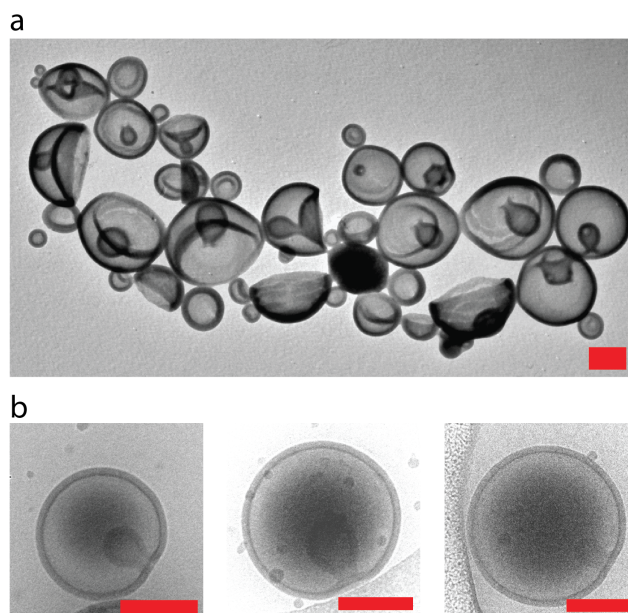
**Figure 4.3:** *(a) TEM image of the 16k sample after 20 hours of dialysis. Stomatocytes having a very small inner cavity are visible. The polymersomes are partly collapsed because of drying effects during TEM grid preparation. (b) Three cryo-TEM images of the same sample showing the stomatocytes with the small inner cavity. Here the stomatocytes are not collapsed since cryo-TEM grids are frozen instead of dried. All scalebars are 250 nm.*

of the dialysis, polymersomes were present with the expected spherical morphology (point 1) corresponding to zero birefringence. At points 2 and 3 no changes in conformation were observed, in agreement with the measured constant magnetic birefringence. At point 4 the birefringence increased to half of its maximal value. The cryo-SEM images show ellipsoidal polymersomes, which can only be explained by a partial deflation of the spherical polymersomes. When the birefringence reached a maximum (point 5), flat disks were observed under cryo-SEM. Continuation of the dialysis led to the bending of the flat discs (point 6) and the formation of stomatocytes (points 7 and 8), where the structures partly inflated again. At this point, the hydrodynamic radius of the polymersomes was decreased to 218 nm with a $PDI$ of 0.12, as determined by DLS. At all points, the magnitude of the birefringence reflects the shape of the structures. All spherical polymersomes show zero birefringence since they cannot be aligned [17]. With increasing deflation of the polymersomes the bire-

fringence amplitude increases. The largest birefringence is observed for discs, in which most of the polymers have identical orientation, perpendicular to the flat surface. The transition of disks to stomatocytes leads to a more curved conformation, and hence a smaller diamagnetic anisotropy.

Due to a small but continuous decrease in sample volume, caused by the dialysis itself, the MB could only be measured for the first 6 hours. Despite this restriction, a sample was still dialyzed for 20 hours without recording the MB using the exact same setup as shown in Figure 4.1. After 20 hours, the sample was quenched and imaged with (cryo-)TEM. The TEM images (Figure 4.3) show stomatocytes with a very small cavity. When comparing these stomatocytes with the ones found after only 4 hours of dialysis (Figure 4.2b,7), it becomes clear that the stomatocytes re-inflate during further dialysis.

### 4.3.2   Effect of polymer length on the dialysis process

To investigate the effect of polymer length on the dialysis process, the experiment was repeated for rigid polymersomes consisting of $PEG_{44}$-$PS_{200}$ instead of $PEG_{44}$-$PS_{133}$. The result is shown in Figure 4.4.

The overall trend is identical to that observed for the 16k sample. Also for the 23k sample the initially spherical polymersomes deflate into discs which subsequently fold into stomatocytes. Although the timescales for both samples are of the same order, there does seem to be a small difference between the two. To obtain some statistics, the experiment was repeated several times for both samples. The characteristic times corresponding to the begin, top and end of the peak are summarized in Table 4.1. There appears to be a small but consistent difference between the two samples. On average, the 23k sample changes its shape earlier in the dialysis process than the 16k sample. Also, the peak width is somewhat smaller for the 23k sample, indicating that the shape

|  | time (min) sample $PEG_{44}$-$PS_{133}$ | time (min) sample $PEG_{44}$-$PS_{200}$ |
|---|---|---|
| begin peak | $188 \pm 10$ | $160 \pm 6$ |
| top peak | $247 \pm 13$ | $201 \pm 6$ |
| end peak | $303 \pm 2$ | $242 \pm 5$ |
| peak width | $115 \pm 11$ | $82 \pm 8$ |

**Table 4.1:** *Characteristic times for the dialysis process on 16k and 23k polymersomes at room temperature. Begin, top and end peak are defined by points 3, 5 and 7 as shown in Figure 4.2.*

a



b



**Figure 4.4:** *(a) MB during dialysis of a 23k polymersome sample at 2 T (blue curve) at room temperature. The 16k trace from fig 4.2 is also plotted for comparison (green curve). Three samples taken at points 1-3 were investigated by SEM, images of which are shown in (b). Before the peak in the MB, the polymersomes are still spherical (2) but they eventually deflate into discs (2) and subsequently fold into stomatocytes (3). Although the trend is identical to that of the 16k sample, the dialysis process proceeds somewhat faster for the 23k sample. All scale bars are 500 nm.*

changes occur faster for the 23k sample than for the 16k sample.

### 4.3.3   Effect of temperature on the dialysis process

The effect of temperature on the dialysis process was investigated by repeating the dialysis experiment on the 16k sample at several temperatures in the interval of 25 to 60 °C. The results are presented in Figure 4.5a. The MB data clearly show that the dialysis process is accelerated when the temperature is increased. Not only do the peaks in the MB occur earlier when the temperature is raised but the peak width also decreases at higher temperatures, as can be seen in Figure 4.5c and 4.5d. SEM images were taken at crucial points in the dialysis process for the 25 and 50 °C measurements. At both temperatures, discs were observed when the MB was maximal and stomatocytes at the end of the MB
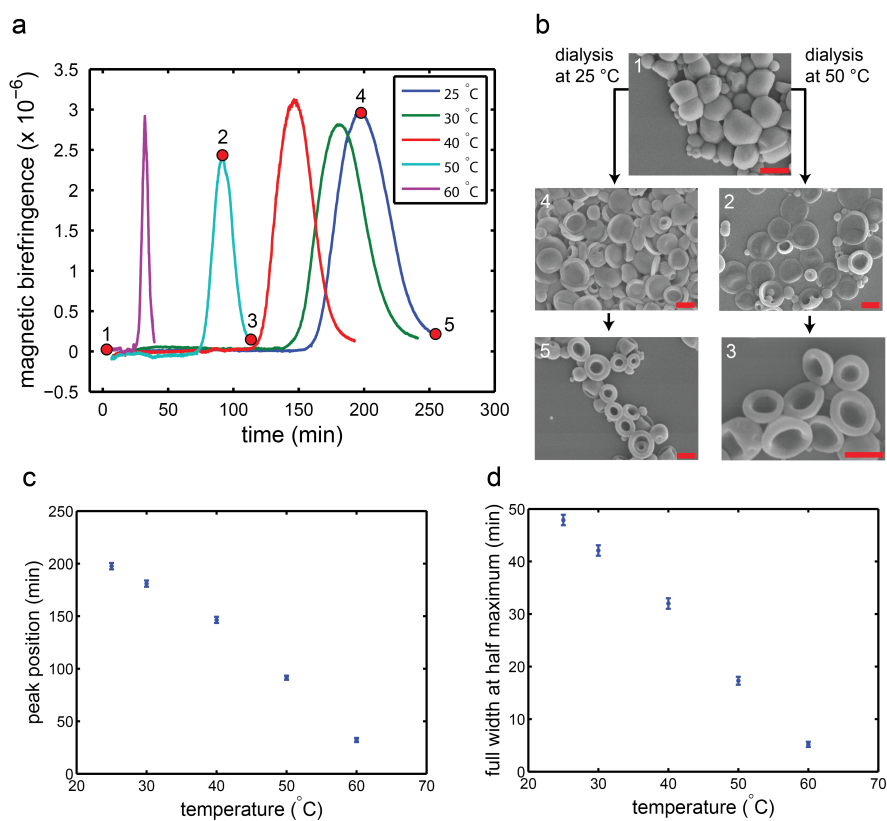
**Figure 4.5:** *(a) MB during dialysis of 16k polymersome samples at 2 T as function of temperature. The dialysis process is clearly accelerated by an increase in temperature, as can be seen by the earlier appearance of the peaks. (b) SEM images taken on at different points during a 25°C and a 50° trace as indicated by the numbers 1-5 in (a). For both traces, discs were observed at the top of the MB peak (2,4) and stomatocytes at the end of the MB trace (3,5). (c) Plot showing the time at which the maximum in the MB was observed as function of the temperature at which the dialysis was performed (d) Plot relating the width of the peaks in the MB as function of the temperature at which the dialysis was performed. All scale bars are 500 nm.*
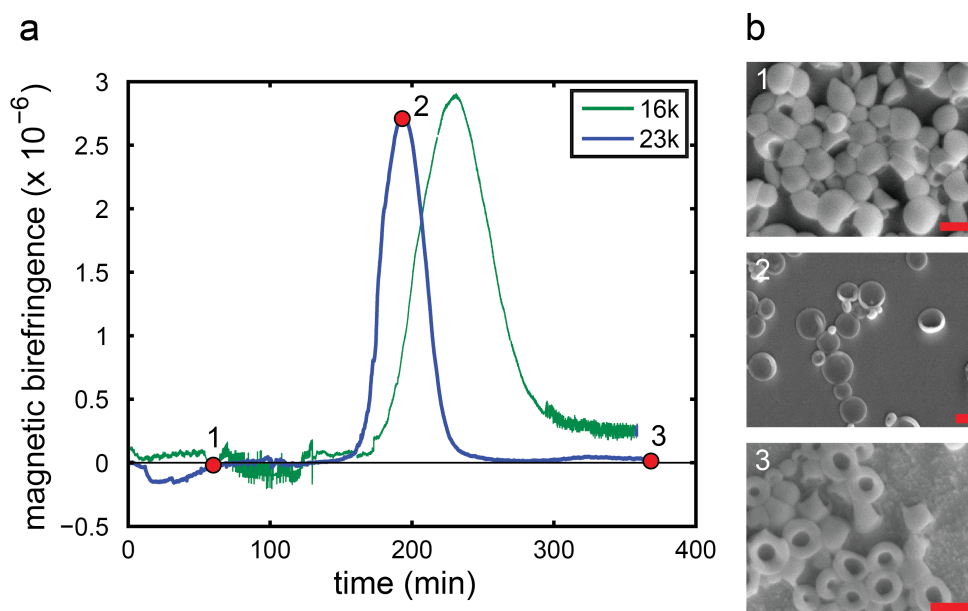
trace.
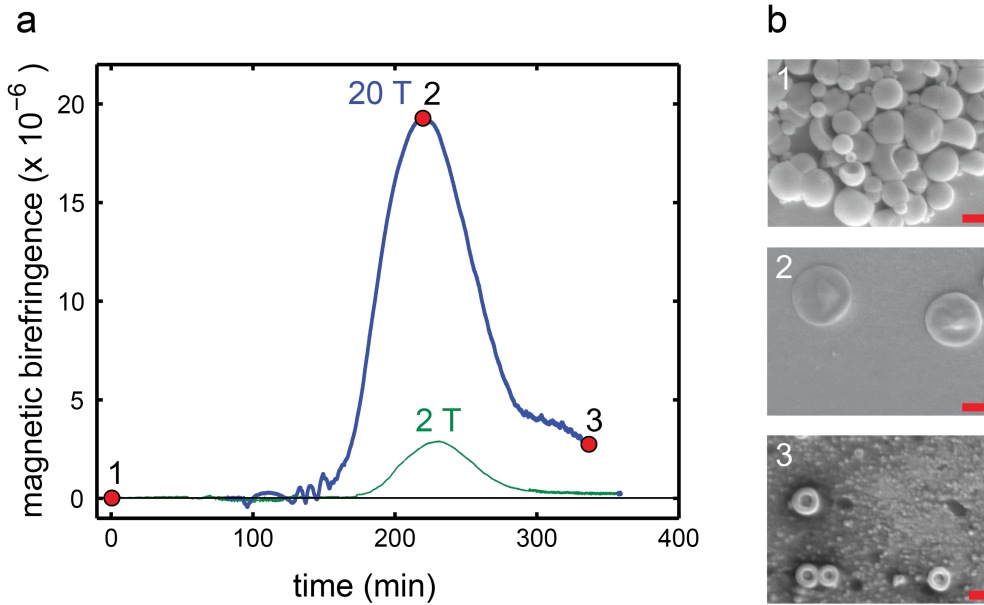
**Figure 4.6:** *(a) MB during dialysis of a 16k polymersome sample at 20 T (blue curve) at room temperature. The 16k trace measured at 2 T from fig 4.2a is also plotted for comparison (green curve). The MB signal at 20 T is much higher than at 2 T, which is due to a larger degree of alignment at higher fields. No significant changes in the characteristic dialysis times were observed. Three samples taken at points 1-3 were investigated by SEM, images of which are shown in (b). Before the experiment, the polymersomes are spherical (1) but during dialysis they deflate into discs (2) and subsequently fold into stomatocytes (3). All scale bars are 500 nm.*

### 4.3.4 Effect of the magnetic field strength on the dialysis process

To examine if high magnetic fields can influence the kinetics of the dialysis process, dialysis of a 16k sample was performed at 20 T. For experimental reasons, the first hour was performed at 0 T after which the field was brought and kept at 20 T. The result is shown in Figure 4.6. For comparison the measurement performed at 2 T is also depicted. Although there is a large difference in the size of the MB, the characteristic times of the MB are not significantly different when comparing the 20 T trace with the 2 T trace. Also for the dialysis performed at 20 T, samples taken at the top and at the end of the MB trace were quenched and imaged with SEM. The results show, again,
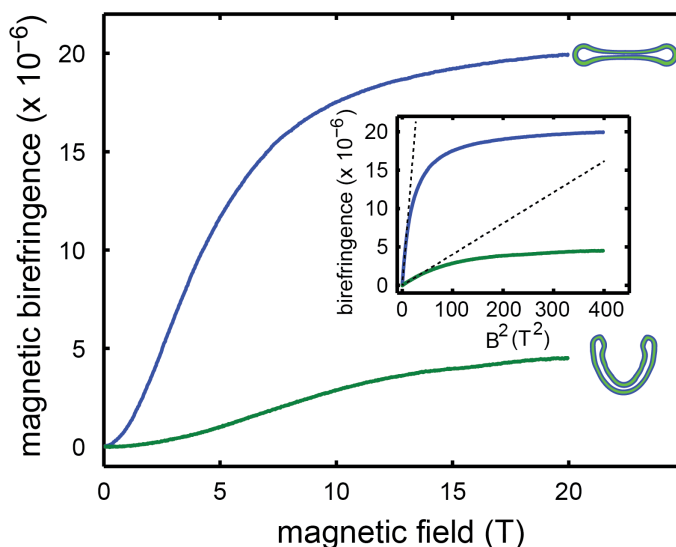
**Figure 4.7:** *Field sweeps performed at the top of the MB peak of Figure 4.6 (discs, blue curve) and after the MB peak (stomatocytes, green curve). The magnetic alignment of discs and stomatocytes both approach saturation at 20 T, although the discs clearly give the largest signal. At high fields (above 3.6 T for discs and 7 T for stomatocytes) the MB clearly deviates from its initial quadratic behavior as can be seen in the inset. The dashed lines represent the extrapolated quadratic behavior.*

the deflation of spheres into discs which subsequently fold into stomatocytes. Beside the size of the MB signal, the magnetic field does not seem to have an influence on the kinetics of the dialysis process.

The difference in the size of the MB signal is related to the degree of alignment at different fields. This was checked by measuring the MB as function of field during dialysis when the MB was maximal (discs) and at the end of the dialysis (stomatocytes). The results are shown in Figure 4.7.

The field sweep for discs is quadratic for the first few tesla, but is almost fully saturated at 20 T. While the alignment is quadratic at 2 T , this is not the case for fields up to 20 T. The effect of polymersome shape on the MB is discussed theoretically in chapter 3 and experimentally in chapter 6.

## 4.4 Shape analysis

To obtain more quantitative data about the dialysis process, samples from three points during dialysis were imaged with cryo-TEM/SEM and parameterized using the parametrization described in chapter 3. All samples were taken from the room temperature measurement on a 16k sample at 2 T. Samples were taken at the top of the peak (discs), end of the peak (deflated stomatocytes) and after 20 hours of dialysis (inflated stomatocytes). The cryo-TEM/SEM images with fittings and fitting parameters are given in the Appendix, section 4.7. From the obtained fittings, the reduced volume and reduced area difference were calculated using equations 3.13 and 3.29. These are depicted in the phase diagram as shown in Figure 4.8. This phase diagram only shows geometrical properties: the reduced volume $v$ and the reduced area difference $\Delta a$, which have been explained in chapter 3. During the first 3 hours of dialysis the shape
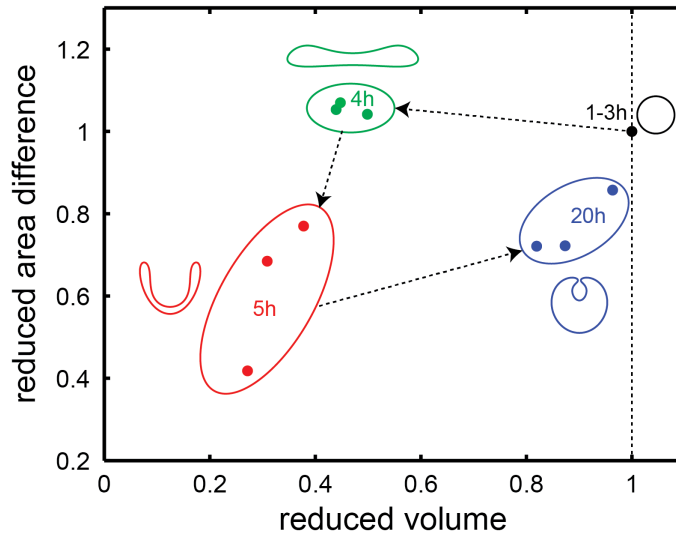


**Figure 4.8:** *Phase diagram showing the positions of the different shapes observed during dialysis at room temperature. Each dot is calculated by parametrization of an observed shape as shown in figure 4.10. Shapes observed at the same point in time are given an identical color to distinguish them from the shapes encountered at different times. The times at which these shapes are observed is indicated. The dashed arrows are a guide to the eye to indicate the order in which the transitions occur. They do not represent the actual path followed.*

was observed to remain spherical and therefore $v$ and $\Delta a$ remained equal to 1 during that time (black region). Only after 3 hours did we observe a deflation of the shapes towards discs (green region). The reduced volume is observed to drop to a value around 0.4 while the reduced area difference increases only slightly. During its folding towards stomatocytes (red region), the reduced volume is observed to decrease somewhat more (between 4 and 5 hours of dialysis) while the reduced area difference decreases drastically. This decrease in $\Delta a$ is caused by the bending of the discs, which leads to a negative curvature to the membrane positioned in the inner part of the cavity, which in turn reduces the area difference. After 5 hours, the stomatocytes begin to fill again, which leads to an increase of the reduced volume, which can be seen by the decreasing size of the stomatocytes cavity (blue region). The reduced area difference is observed to increase slightly, since amount of membrane within the cavity (having negative curvature) decreases while the amount of membrane outside the cavity (having positive curvature) increases. Indeed, the shape gets closer to that of a sphere and $v$ and $\Delta a$ are both observed to approach 1.

## 4.5   Discussion

To explain the effects of dialysis on the morphology of the polymersomes, we propose the mechanism depicted in Figure 4.9. At the starting point of the dialysis, the polymersome membrane is very rigid, due to lack of plasticizing organic solvent (a). During dialysis, the organic solvent (red dots) enters the polymersome membrane (b). At point c, enough organic solvent has entered the hydrophobic part of the polymersome membrane to make it permeable to water (blue dots). From this point on, water diffuses out of the polymersome, as a result of the concentration gradient over the membrane. The outflow of water leads to a reduced inner volume, giving rise to an elongated shape (d). Further outflow of water eventually leads to a disk, which shows the highest birefringence (e). At this point the disk begins to bend in one direction, most probably due to fluctuations in the membrane. The membrane starts to fill slowly with the mixture of water and organic solvent again (f). This process continues and stomatocytes are formed (g, h).

The results clearly demonstrate that the dialysis process is accelerated at higher temperatures. There are two effects that can contribute to this effect. First of all, at elevated temperatures the diffusion coefficients for all solvent components increase, leading to a faster exchange of water, THF and dioxane over the dialysis membrane. However, this effect is expected to be small since the diffusion coefficients scale linearly with the absolute temperature which

**Figure 4.9:** *a-h: Proposed mechanism of the dialysis of polymersomes against 50% water, 40% THF and 10% 1,4-dioxane. The morphologies correspond to those shown in Figure 4.2b. For a-c, the polymersome membrane is shown enlarged. Organic solvent acts as a plasticizer, which swells the membrane. Swollen membranes are indicated by dashed lines in Figures c-h compared to the solid lines in Figures a and b.*

only varies 12% [18–20]. Secondly, and more importantly, the polymersome membrane is expected to be more flexible and permeable at higher temperatures since it is known that polystyrene swells with increasing temperature [21]. This means that the threshold for deflation can be reached at lower concentrations of organic solvent, so at shorter dialysis times. Higher permeability and flexibility also lead to a faster outflow of solvents, which means a faster transition into discs and stomatocytes. This is in agreement with the measurements, since at elevated temperatures the peaks in the MB occur earlier while the width of

these peaks are smaller.

One might expect that the speed of the dialysis process can be influenced by a magnetic field, since the most anisotropic shapes are, at least magnetically, the most favorable. However, as Figure 4.6 shows, no such effects were observed up to fields of 20 T. The kinetics of the dialysis process measured at 20 T seems to be identical to those measured at 2 T. This indicates that the magnetic energy is too low to compete with the other energies involved, like the osmotic and bending energy. The magnetic field sweeps of discs and stomatocytes do demonstrate that the magnetic alignment of these structures approach saturation at 20 T. Pure magnetic alignment is a process in which the orientation of a vesicle in solution is altered, but where the shape of the vesicle remains unchanged. Therefore, osmotic and bending energies are not involved in the magnetic alignment of the vesicles. As explained in chapters 2 and 3, magnetic alignment has to compete with the thermal energy which tends to randomize the orientation effects of the magnetic field. This explains why an increase in field strength does not change the kinetics of the dialysis process but only increases the degree of alignment.

The fittings of the shapes observed during dialysis of the 16k sample at room temperature have led to the phase diagram shown in figure 4.8. It is striking that the deflation and inflation do not follow the same routes, instead a large hysteresis is observed. While the deflation occurs via discs that subsequently fold into stomatocytes, the inflation is observed to proceed via stomatocytes only. The reason for this behavior is explained in the next chapter, where we will show that a different procedure to induce shape changes can lead to a similar hysteresis effect.

## 4.6    Conclusions

In conclusion, we have demonstrated that magnetic birefringence in a magnetic field of only 2 T can be used as a useful tool to monitor morphological changes in polymersomes resulting from dialysis in a flow cell. This method has the advantage of being non-invasive; the morphology can be determined without disrupting the dialysis setup for sample investigation by electron microscopy. Also, because the dialysis in the flow cell is rather slow (in the order of several hours), the shape transformations can be determined at very precise points on the birefringence curve, providing samples with very specific and predictable morphologies. If necessary, the speed at which this process takes place can be increased by performing the dialysis at higher temperatures. This is most probably due to the increased permeability and flexibility of the polymersome

membrane at elevated temperatures. Using polymersomes self-assembled from block copolymers with a longer PS block also led to a reduction in dialysis time, although these effects were rather small compared to the temperature effects. The reason for this polymer length dependency is thusfar unknown. No changes in kinetics were observed when the dialysis was performed at 20 T instead of 2 T. This indicates that the forces associated with osmotic pressure are dominant over the magnetic forces.

## 4.7 Appendix

### 4.7.1 Parametrization of different shapes obtained from cryo-EM images

All encountered shapes were fitted using the parametrization as given by equations 3.3 to 3.5 (chapter 3). The fittings are shown in Figure 4.10 and the obtained fitting parameters, as well as the calculated reduced volume and reduced area difference, are listed in Table 4.2.
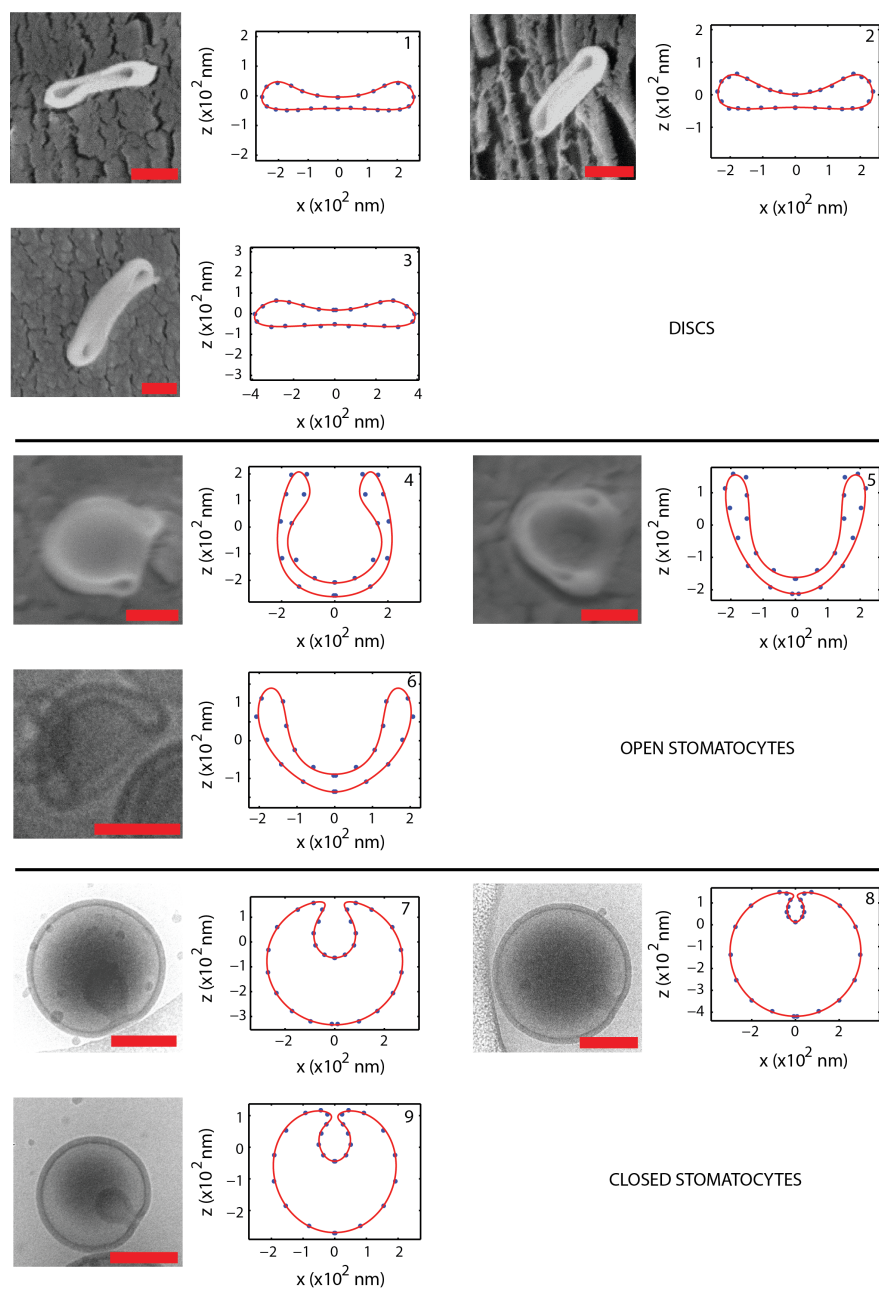
**Figure 4.10:** *Fittings of the discs, open stomatocytes and closed stomato-cytes from chapter 4. All scale bars are 250 nm.*

| fit # | $a_1$ ($\cdot 10^{-7}$) | $a_2$ ($\cdot 10^{-7}$) | $a_3$ ($\cdot 10^{-7}$) | $a_4$ ($\cdot 10^{-7}$) | $a_5$ ($\cdot 10^{-7}$) | $b_1$ ($\cdot 10^{-7}$) | $b_2$ ($\cdot 10^{-7}$) | $b_3$ ($\cdot 10^{-7}$) | $b_4$ ($\cdot 10^{-7}$) | $b_5$ ($\cdot 10^{-7}$) | v | $\Delta a$ |
|---|---|---|---|---|---|---|---|---|---|---|---|---|
| 1 | 2.461 | -0.479 | 0.157 | 0.0043 | 0 | 0.3157 | -0.3074 | -0.1246 | 0.07467 | 0 | 0.4395 | 1.0537 |
| 2 | 2.326 | 0.1056 | -0.050 | 0.063 | 0 | 0.460 | -0.117 | -0.261 | -0.073 | 0 | 0.4991 | 1.0422 |
| 3 | 3.755 | -0.4809 | 0.064 | 0.078 | 0 | 0.591 | -0.202 | -0.236 | 0.017 | 0 | 0.4474 | 1.0697 |
| 4 | 1.840 | -0.288 | 0.906 | 0.115 | 0.173 | 0.144 | -2.128 | 0.288 | -0.230 | -0.173 | 0.2713 | 0.4177 |
| 5 | 2.116 | -0.354 | 0.405 | 0.044 | 0.044 | -0.022 | -1.696 | 0.229 | -0.174 | 0.044 | 0.3087 | 0.6850 |
| 6 | 1.888 | -0.1033 | 0.030 | 0.195 | 0 | 0.451 | -1.211 | -0.2165 | 0.088 | 0 | 0.3780 | 0.7702 |
| 7 | 1.528 | -0.952 | 0.918 | -0.046 | 0 | 1.013 | -1.801 | 0.337 | -0.183 | 0 | 0.8195 | 0.7206 |
| 8 | 1.284 | -1.251 | 0.979 | -0.191 | 0 | 1.529 | -1.743 | 0.622 | -0.288 | 0 | 0.9639 | 0.8572 |
| 9 | 0.905 | -0.690 | 0.721 | -0.109 | 0 | 0.701 | -1.322 | 0.426 | -0.247 | 0 | 0.8735 | 0.7220 |

**Table 4.2:** *Fitting parameters of the fits shown in Figure 4.10.*

87

# References

[1] D.E. Discher and F. Ahmed, *Annu. Rev. Biomed. Eng.*, **8**, 323 (2006)

[2] F. Meng, Z. Zhong and J. Feijen, *Biomacromol.*, **10**, 197 (2009)

[3] S.J. Holder and N.A.J.M. Sommerdijk, *Polym. Chem.*, **2**, 1018 (2011)

[4] Y. Yu, A. Eisenberg, *J. Am. Chem. Soc.*, textbf119, 8383 (1997)

[5] K.-T. Kim, J. Zhu, S.A. Meeuwissen, J.J.L.M. Cornelissen, D.J. Pochan, R.J.M. Nolte and J.C.M. van Hest, *J. Am. Chem. Soc.*, **132**, 12522 (2010)

[6] S.A. Meeuwissen, K. Kim, Y. Chen, D.J. Pochan, and J.C.M. van Hest, *Angew. Chem. Int. Ed.*, **50**, 7070 (2011)

[7] D.A. Wilson, R.J.M. Nolte and J.C.M. van Hest, *J. Am. Chem. Soc.*, **134**, 9894 (2012)

[8] D.A. Wilson, R.J.M. Nolte and J.C.M. van Hest, *Nat. Chem.*, **4**, 268 (2012)

[9] D.A. Wilson, B. de Nijs, A. van Blaaderen, R.J.M. Nolte and J.C.M. van Hest, *Nanoscale*, **5**, 1315 (2013)

[10] R.S.M. Rikken, R.J.M. Nolte, J.C. Maan, J.C.M van Hest, D.A. Wilson and P.C.M. Christianen, *Soft Matter*, **50**, 5394 (2014)

[11] I.O. Shklyarevskiy, M.I. Boamfa, P.C.M. Christianen, F. Touhari, H. van Kempen, G. Deroover, P. Callant and J.C. Maan, *J. Chem. Phys.*, **116**, 8407 (2002)

[12] P.C.M. Christianen, I.O. Shklyarevskiy, M.I. Boamfa, J.C. Maan, *Physica B*, **346-347**, 255 (2004)

[13] J.C. Gielen, M. Wolffs, G. Portale, W. Bras, O. Henze, A.F.M. Kilbinger, W.J. Feast, J.C. Maan, A.P.H.J. Schenning and P.C.M. Christianen, *Langmuir*, **25**, 1272 (2009)

[14] J.C. Gielen, I.O. Shklyarevskiy, A.P.H.J. Schenning, P.C.M. Christianen and J.C. Maan, *Sci. Technol. Adv. Mater.*, **10**, 014601 (2009)

[15] G. Maret and K. Dransfeld, *Strong and Ultrastrong Magnetic Fields and Their Applications*, Springer-Verlag, Berlin, Chapter 4 (1985)

[16] J.C. Kemp, *Polarized Light and its Interaction with Modulated Devices A Methodology review*, HINDS International Inc., Hillsbore (1987)

[17] This indicates that the PEG-PS polymersomes are not yet deformed at 2 T. Magnetic deformation of other nanocapsules has been observed at higher magnetic fields up to 20 T: I.O. Shklyarevskiy, P. Jonkheijm, P.C.M. Christianen, A.P.H.J. Schenning, E.W. Meijer, O. Henze, F.M. Kibinger, W.J. Feast, A. Del Guerzo, J.P. Desvergne and J.C. Maan, *J. Am. Chem. Soc.*, **127**, 1112 (2005)

[18] N.C. Santos and M.A.R.B. Castanho, *Biophys. J.*, **71**, 1641 (1996)

[19] J. Pencer and F.R. Hallett, *Langmuir*, **19**, 7488 (2003)

[20] P.J. Patty and B.J. Frisken, *Appl. Optics*, **45**, 2209 (2006)

[21]  B. Erman and B.M. Baysal, *Macromol.*, **18**, 1696 (1985)

# Chapter 5

# Shaping polymersomes into predictable morphologies via out-of-equilibrium self-assembly

## Abstract

In this chapter, we demonstrate a mechanistically fully understood procedure to precisely control polymersome shape via an out-of-equilibrium process. Carefully selecting osmotic pressure and permeability initiates controlled deflation, resulting in transient vesicle shapes, followed by re-inflation of the polymersomes. The shape transformation towards stomatocytes, is probed in real-time with magnetic birefringence, permitting us to stop the process and fabricate capsules with any intermediate shape in the phase diagram. Quantitative electron microscopy analysis of the different morphologies reveals that the shape transformation proceeds via a long-predicted hysteretic deflation-inflation trajectory, which can be understood in terms of bending energy. Because of the high degree of controllability and predictability, this study provides the design rules for accessing polymersomes with all possible different shapes.

## 5.1   Introduction

For the last 15 years, there has been an increasing interest in artificial vesi-cles made from amphiphilic block copolymers, often called polymersomes [1–7]. Polymersomes have the advantage that many of their properties are tunable, simply by modifying the polymer building blocks [8, 9]. Both the hydrophilic and the hydrophobic blocks of the constituting copolymer can be adjusted to give the required surface charge, temperature sensitivity, rigidity and permeabil-ity to the vesicle. The latter two can also be tuned by adding organic solvents that plasticize the hydrophobic part of the polymersome membrane [10, 11]. Finally, polymers can easily be functionalized with (biological) molecules, mak-ing polymersomes promising candidates for medical applications such as drug delivery [12–14].

Interactions between particles such as polymersomes and cells, which are key to a range of processes such as immune regulation and cellular uptake, are strongly affected by the particle shape [15–18]. The shape of the poly-mersomes also affects their flow properties [19], as is believed to be the case for red blood cells, biconcave disc-like erythrocytes [20, 21]. Therefore, it is of great importance to obtain full control over the shape of polymersomes and to understand the mechanism of their interconversion. The number of studies on polymersome shape is still rather limited [22]. We showed that spherical poly-mersomes, assembled from poly(ethylene glycol)-polystyrene (PEG-PS), deflate into cup-shaped polymersomes called stomatocytes [23–25]. Rod-shaped poly-mersomes have been created by employing cross-linkers [26] or rehydration [27]. Bicontinuous cubic structures have been reported as well [28]. Another study showed polymersomes that deflate to form nested vesicles [29], possibly through a sequence of intermediate vesicle shapes such as prolate spheroids, discs and stomatocytes [30], which unfortunately were not observed. In chapter 4, we demonstrated how continuous dialysis of an initially rigid polymersome sample can lead to the formation of discs, which subsequently fold into stomatocytes. Furthermore, we demonstrated that magnetic birefringence (MB) is an excellent tool to probe these shape changes in real-time.

All studies mentioned above have been rather empirical in nature, despite the existence of detailed theoretical bending energy models, predicting the shape of phospholipid vesicles as a function of reduced volume and surface area difference [31]. Currently, a clear and quantitative understanding of the shape transformation of polymersomes is missing, which hampers the construction of polymeric nanostructures with tailor-made shapes.

In this chapter we describe a mechanistically fully understood new method to transform spherical PEG-PS polymersomes into a variety of shapes, such as
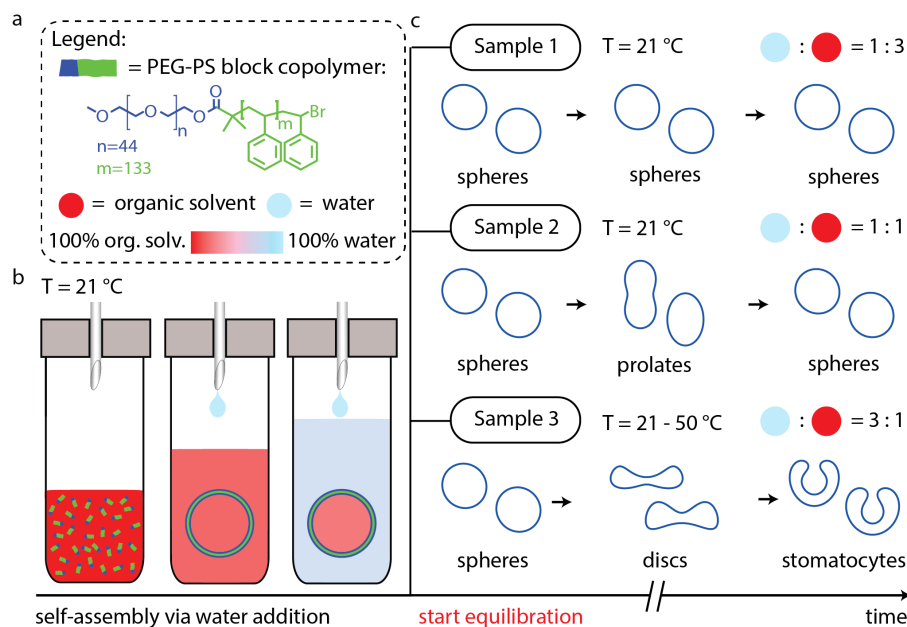
**Figure 5.1:** *Overview of the out-of-equilibrium self-assembly approach. (a) Legend, showing the structure of the poly(ethylene glycol)-polystyrene block copolymer building block and the color scale for organic solvents, water and mixtures of the two. (b) Scheme of the self-assembly process. Slow (1 mL/hour) addition of water to a solution of PEG-PS in THF:dioxane (3:2) triggers self-assembly into spherical polymersomes with identical internal and external solvent composition. Continued addition of water to the exterior lowers the permeability to water of the polymer membrane and induces osmotic pressure, creating an out-of-equilibrium situation. (c) Three samples with different final water content, showing different equilibration behavior over time. Sample 1 (25% water) remained spherical. Sample 2 (50% water) deflated into prolate shapes after which they inflated back to spheres. Sample 3 (75% water) deflated into discs after which they inflated into stomatocytes.*

prolate spheroids, discs and stomatocytes (Figure 5.1), which can be kinetically trapped at any stage of their formation. The polymersomes are initially formed by adding water to a molecularly dissolved polymer solution in a mixture of tetrahydrofuran (THF) and dioxane (Figure 5.1b, left flask). Our approach for obtaining a controlled shape transformation is based on the notion that polymersomes are only in osmotic equilibrium at the exact moment they are formed (Figure 5.1b, middle flask). By adding extra water to bring the sample to a carefully chosen final solvent composition, the polymersome solution

is pushed out of osmotic equilibrium (Figure 5.1b, right flask). After this out-of-equilibrium self-assembly, a slow re-equilibration process starts, which leads to a predictable deflation of the spherical polymersomes into any desired polymersome morphology (Figure 5.1c). The total amount of water in the solvent mixture is a crucial parameter, as it not only sets the osmotic pressure across the polymersome membrane, but, owing to the amorphous glassy nature of the PS block, it also (indirectly) modifies its flexibility and its permeability [24]. In contrast with the method described in chapter 4, this method does not require any dialysis. Instead, all parameters necessary for the shape changes (osmotic pressure, flexibility and permeability) are set during the self-assembly. The advantage of this method is that, compared with dialysis, one can control the solvent composition much better, which in turn makes it easier to understand the observed shape changes.

Because of the rather thick PS part of the polymersome membrane ($> 133$ monomers), the time scale of the shape transformations is in the order of several hours up to a few days, which enables probing the whole process carefully [25]. The long time scale also allows us to kinetically trap the observed morphologies, including the intermediates, by quickly adding an excess of water or by a fast decrease in temperature. All the resulting shapes could be extensively characterized by *ex situ* electron microscopy, providing a quantitative mathematical description of the nanocapsules in terms of the reduced volume and surface area difference. An asymmetric deflation-inflation trajectory has been observed for the first time, in full accordance with the predictions of the Seifert model on liposomes [31]. Our quantitative understanding of the shape transformation of our new equilibration method paves the way for molding polymersome nanocontainers or scaffolds in the most efficient shape, which is highly desirable for biomedical applications.

## 5.2    Experimental details

### 5.2.1    Materials

Tetrahydrofuran (THF) and 1,4-dioxane were purchased from Sigma-Aldrich and used as received. Poly(ethylene glycol)-polystyrene ($PEG_n$-$PS_m$) was synthesized by atom-transfer radical polymerization (ATRP) starting from PEG-macroinitiators as described previously [23]. For samples 1 to 3, $PEG_{44}$-$PS_{133}$ was used (MW = 16 kDa, $PDI = 1.06$). For sample 4, $PEG_{44}$-$PS_{200}$ was used instead (MW = 23 kDa, $PDI = 1.05$).

### 5.2.2 Equipment

Magnetic birefringence (MB) was measured in a Varian V-3900 2 T electro-magnet using a standard polarisation modulation technique [32]. A HeNe laser was used (1.5 mW, 632.8 nm) to probe the dispersion contained inside a 5 mm thick optical cell (Hellma) within a temperature controlled environment. (Cryo-) SEM was performed on a JEOL 6330 Cryo Field Emission Scanning Electron Microscope at an acceleration voltage of 3 kV. TEM was performed on a JEOL 1010 Transmission Electron Microscope at an acceleration voltage of 60 kV. For Cryo-TEM a JEOL 2100 cryo-Transmission Electron Microscope was used. The hydrodynamic radius was determined by Dynamic Light Scattering, performed with a Malvern Zetasizer Nano S instrument.

### 5.2.3 Sample preparation

The polymersome samples were prepared as demonstrated in Figure 5.1b. All samples were made by first dissolving 10 mg of PEG-PS in THF:dioxane 3:2 (v/v) ranging from 1 to 3 mL (Figure 5.1b, left flask). The initial concentrations of PEG-PS before the addition of $H_2O$ was 3.33 mg/mL for sample 1, 5 mg/mL for sample 2 and 10 mg/mL for sample 3. In this range, initially spherical polymersomes are formed [23, 24, 26]. Then water was slowly added (for up to 3 hours using a syringe pump) until the total volume of the mixture was 4 mL. During the preparation the samples were stirred at 750 rpm. The final amount of $H_2O$ in the samples was 25% (sample 1), 50% (sample 2) and 75% (sample 3). Self-assembly of the PEG-PS into polymersomes occurred when the ratio of water:organic solvent approached 1:4 (v/v) (Figure 4.1b, middle flask), which was observed by the solution turning cloudy. Since the final volume of all three samples were brought to 4 mL, some of the water was added after self-assembly had occurred (Figure 5.1b, right flask). The amount of water that was added after self-assembly were 0.25 mL for sample 1, 1.5 mL for sample 2 and 2.75 mL for sample 3. This is expected to set different osmotic pressures over the polymersome membrane, since after self-assembly the solvents inside the polymersomes are shielded from the exterior solution by the polymersome membrane. The extent of osmotic pressure depends on the amount of organic solvent that is used and the amount of water that is added. The addition of extra water will also make the polymersome membrane more rigid and even less permeable to water [24]. In this manner, three different samples were prepared, varying from a sample almost in equilibrium (sample 1, 25% $H_2O$) via an intermediate sample (sample 2, 50% $H_2O$) to a sample far from equilibrium (sample 3, 75% $H_2O$). See Table 5.1 for more details. After the sample preparation, the samples were divided over HPLC vials in aliquots of 450 $\mu$L, sealed and stored

| sample | hydrodynamic radius (nm) | *PDI* | water (% v/v) | THF (% v/v) | dioxane (% v/v) |
|---|---|---|---|---|---|
| Sample 1 for equilibration at room temperature | 272 ± 84 | 0.093 | 25 | 45 | 30 |
| Sample 2 for equilibration at room temperature | 265 ± 968 | 0.130 | 50 | 30 | 20 |
| Sample 2 for temperature measurements | 275 ± 86 | 0.096 | 50 | 30 | 20 |
| Sample 3 for equilibration at room temperature | 223 ± 56 | 0.062 | 75 | 15 | 10 |
| Sample 3 for temperature measurements | 231 ± 62 | 0.072 | 75 | 15 | 10 |
| Sample 3 for testing magnetic field effect | 227 ± 79 | 0.121 | 75 | 15 | 10 |
| Sample 4 for equilibration at room temperature and temperature measurements | 230 ± 71 | 0.095 | 75 | 15 | 10 |

**Table 5.1:** *Hydrodynamic radius with its PDI as determined by DLS for all samples used as determined right after self-assembly. Also given are the relative contents of the three solvents.*

at room temperature for equilibration.

Samples to be analyzed by cryo-TEM or cryo-SEM were obtained by injecting 10 µL of sample in 0.5 mL of water with a micro pipette. This led to a rapid expulsion of organic solvent from the polymersome membrane which made the polystyrene part of the membrane rigid (glassy). In this manner, all samples for further analysis were kinetically trapped, preventing any further shape changes in time.
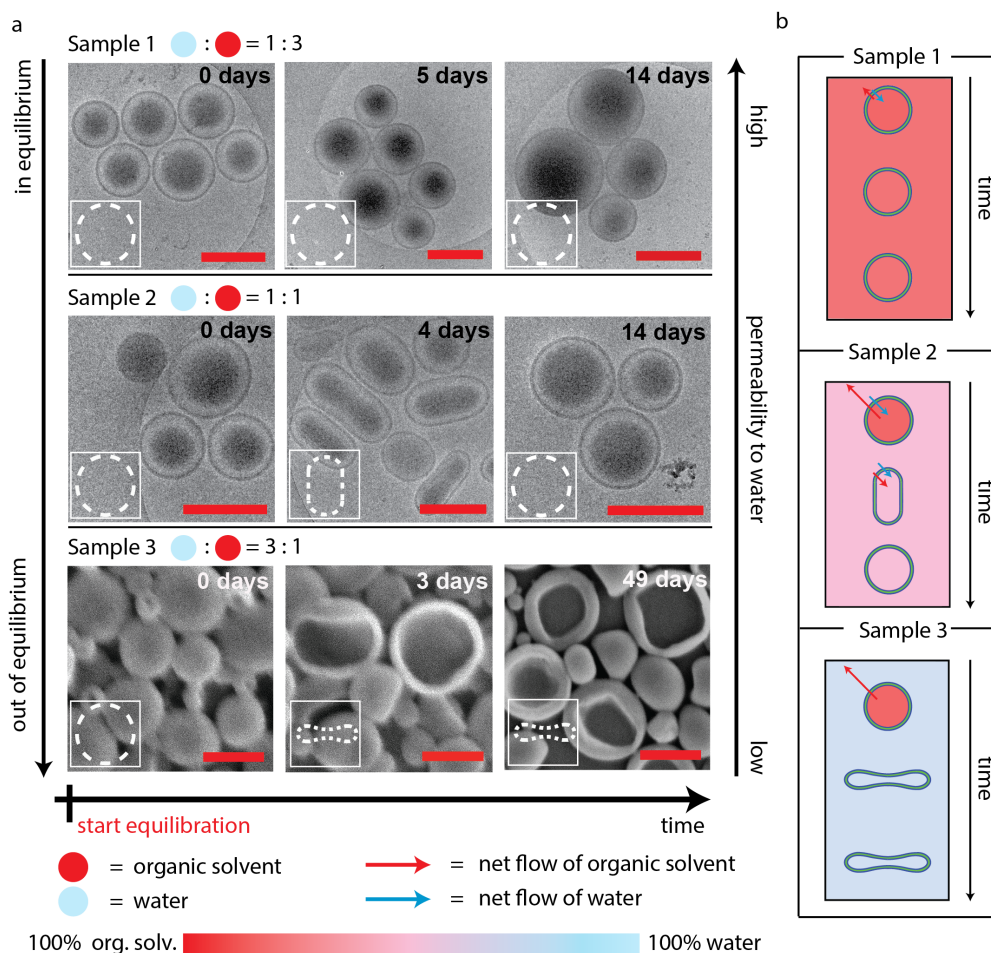
**Figure 5.2:** *Polymersome morphology over time for the three different samples. (a) Electron microscopy images. All scalebars are 500 nm. Top row: cryo-TEM images of sample 1, showing no change in morphology over time. Middle row: cryo-TEM images of sample 2, changing from spheres to a prolate morphology after 4 days and back to spheres after 14 days. Bottom row: SEM images of sample 3, changing from spheres to discs after 3 days and remaining discs after 49 days. (b) Schematic explanation. Top: Sample 1 is near osmotic equilibrium and the most permeable to water, allowing a simultaneous exchange of water and organic solvent to alleviate the small change in osmotic pressure without changing the shape. Middle: Sample 2 is more out of equilibrium than sample 1 and less permeable to water. Organic solvent flows out faster than water flows in, causing a small deflation into prolates. Subsequently, bending energy is relieved by simultaneous inflow of water and organic solvent. Sample 3 is the most out of osmotic equilibrium and impermeable to water. Therefore, these polymersomes deflate the most to form discs, and no re-inflation is possible.*

## 5.3 Results

### 5.3.1 Kinetics at room temperature

Equilibration started immediately after the sample preparation. Each sample was studied at several points in time (days) using (cryogenic) transmission and scanning electron microscopy (TEM, cryo-TEM, and SEM, Appendix, section 5.6.1, Figures 5.10, 5.11 and 5.12). Figure 5.2a gives an overview of the cryogenic transmission or scanning electron microscopy (cryo-TEM or SEM) images of samples 1, 2 and 3 taken at different points in time. The left arrow indicates the difference in solvent composition between the polymersome's interior and exterior, i.e. how far the system deviates from osmotic equilibrium. The right arrow indicates the relative change in permeability to water while the horizontal arrow indicates the direction of time. Samples were left to stand at room temperature (21 °C) to equilibrate over time. For all three samples, three key moments that coincide with morphological changes are shown.

The polymersomes of sample 1 were spherical after self-assembly and remained spherical up to 14 days (Figure 5.2 top). At intermediate days the shapes were also determined to be spherical (Appendix, section 5.6.1, Figure 5.10).

The polymersomes of sample 2 were spherical immediately after self-assembly but started changing into prolates (spheroids and rods) after the first day, with most prolates observed at day 4 (5.2 middle, Appendix, section 5.6.1, Figure 5.11)). However, from day 8 onwards all polymersomes were observed to have a spherical morphology again.

The polymersomes of sample 3 were spherical after self-assembly and remained spherical up until 2 days (Figure 5.2 bottom, Appendix, section 5.6.1, Figure 5.12). After 3 days about one third of the polymersomes had changed into discs. The same amount of discs was observed after 49 days, indicating that discs are a stable morphology under these conditions. Magnetic birefringence (MB) measurements on sample 3 were in full agreement with these EM results (Figure 5.3). MB measures the difference in refractive index of light polarized parallel or perpendicular to a magnetic field (optical anisotropy), which is induced by magnetic alignment of structures that exhibit (dia)magnetic anisotropy [25, 33]. When comparing structures composed of identical building blocks the MB signal is a measure of the anisotropy of the overall shape as was explained in chapter 3, section 3.3.4. Indeed, the MB signal increased tenfold from the background level after 3 days, which is in accordance with the observed transition of one third of the spheres into discs.

The different shape changes of the three samples can be explained in terms

of osmotic pressure and membrane permeability. Since sample 1 is close to equilibrium immediately after the self-assembly, and also the most permeable to water, the small difference in solvent composition is easily alleviated by a simultaneous outflow of organic solvent and inflow of water (Figure 5.2b). The result is that the polymersomes will not deflate and therefore retain their spherical morphology. Sample 2 is more out of equilibrium than sample 1 but also less permeable to water. Therefore, after sample preparation the organic solvent flows out faster than water can flow in (Figure 5.2b). This leads first to a net decrease of the inner volume and the polymersomes adopt a prolate morphology, lowering the osmotic pressure at the expense of bending energy. To relieve this bending energy, the polymersomes inflate again into spheres at a speed which is limited by the inflow of water.

The polymersomes in sample 3 are the most out of equilibrium and impermeable to water. Therefore, osmotic equilibrium can only be obtained by



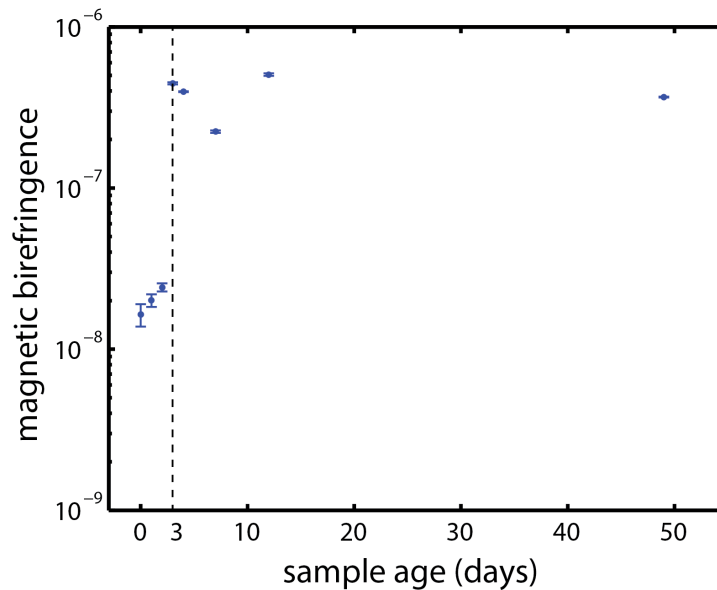**Figure 5.3:** *Magnetic birefringence of sample 3 as function of sample age. The magnetic birefringence of sample 3 was measured at room temperature over multiple days to follow the equilibration process. A sudden increase of an order of magnitude in birefringence was observed when the sample was 3 days old. These findings are in complete accordance with the EM images which show a significant increase in discs after this time.*

outflow of organic solvent. Since water cannot flow back in, the polymersomes do not re-inflate to spheres but retain their disc-like morphology. Because the polymersomes in sample 3 are more out of equilibrium than those in sample 2, they will deflate more, which is the reason for the different shapes as will be explained later. Sample 3 is not observed to go back to spheres since the permeability to water at room temperature is negligible. Also, the membrane flexibility of the polymersomes of sample 3 is low, since they contain the smallest amount of organic solvent to plasticize the membrane, making the time scales in which shape changes occur very large. We suspect that this relatively high rigidity is also the cause for two thirds of the polymersomes not to undergo the shape transformation at room temperature at all.

### 5.3.2   Kinetics above room temperature

To investigate the shape transformation of sample 3 at higher flexibility and permeability to water, the MB was also measured at higher temperatures: 35, 40 and 50 °C respectively (Figure 5.4a, Appendix, section 5.6.2, Figure 5.13). At these temperatures, the MB was observed to initially increase steeply followed by a decrease to a small, finite value. The measurements also showed that at higher temperature the changes in birefringence occurred faster and the peak value of the MB was higher. For all three measurements the shape of the polymersomes was determined by TEM or cryo-TEM and SEM at the beginning (1), top (2) and after the peak (3). The shapes at these three key points were identical for all three temperatures and a representative overview for the 40 °C measurement is given in Figure 5.4b. At the beginning of the experiment polymersomes had, as expected, a spherical morphology (1) and changed into discs at maximal birefringence (2). At the end of the experiment, the discs had transformed into stomatocytes (3). There is full agreement between EM pictures and the MB measurements. The transition from spheres to discs leads to a large increase in the MB since the polymersomes become highly anisotropic. The change from discs to stomatocytes leads to a decrease in birefringence since stomatocytes resemble more closely a sphere and are therefore much less anisotropic than discs. Interestingly, the disc morphology is maintained when quickly lowering the temperature right before the magnetic birefringence reaches a maximum, as is shown in Figure 5.4c.

The temperature treatments on sample 3 demonstrate three effects. First of all, the increase in temperature leads to a much faster transition from spheres to discs. Secondly, the maximal birefringence at elevated temperature (Figure 5.4a) is about three times as high as the birefringence obtained by equilibration at room temperature (Figure 5.3). As the shapes are identical, this indicates
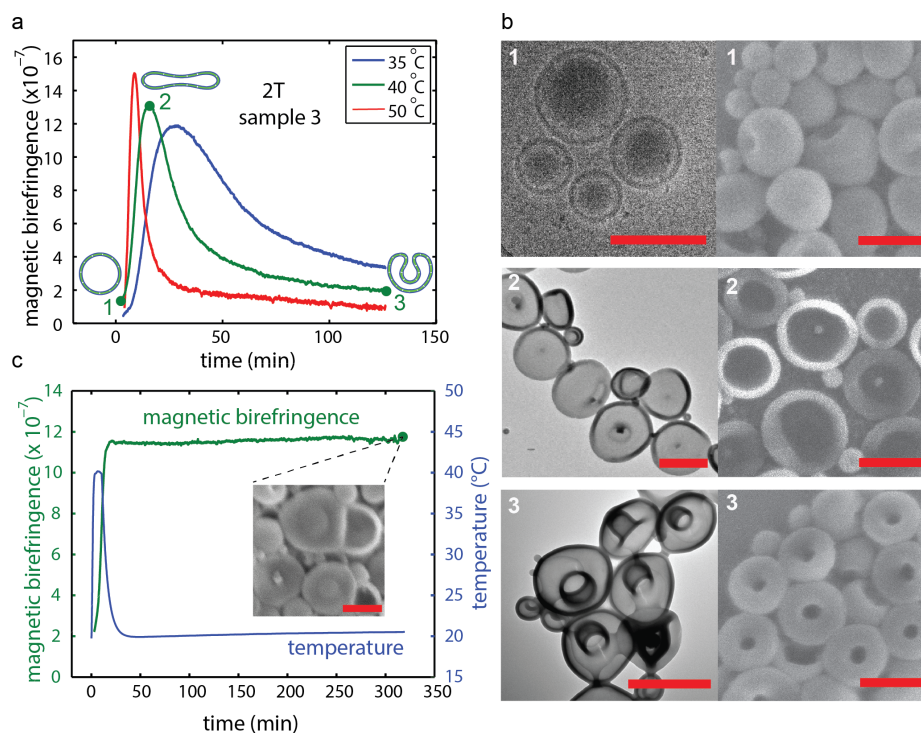
**Figure 5.4:** *Observed changes in morphology at elevated temperatures. (a) Magnetic birefringence of sample 3 (75% $H_2O$, 25% THF/dioxane) as function of time at different temperatures. At each temperature, the birefringence increases to a maximum followed by a slower decrease. The higher the temperature, the faster the changes in birefringence occur. At three characteristic points on the 40 °C trace, an aliquot of the sample was injected in water to quench the structure. (b) cryo-TEM (left, 1), TEM (left, 2 and 3) and SEM (right, 1, 2 and 3) images of the quenched samples marked in (a). For the spheres, cryo-TEM was used, as spheres tend to collapse in dry TEM. At the start of the experiment the sample consists of spheres (1) and the birefringence is almost zero. At maximal birefringence discs are observed (2). At the end of the trace the sample consists of stomatocytes (3). (c) Magnetic birefringence of sample 3 as a function of time (green line), following the temperature trajectory shown in blue. By cooling the sample right before the maximal birefringence is reached the transition from discs to stomatocytes is prevented as can be seen by the constant high birefringence and the SEM picture of the sample after 320 minutes. All scalebars are 500 nm.*

that at elevated temperatures the number of discs become close to 100%, which

is confirmed by EM microscopy. Finally, at elevated temperatures a further transition from discs to stomatocytes is observed, which was not observed by equilibration at room temperature. This demonstrates that, like the prolates, the disc is an intermediate morphology in the equilibration process, but that elevated temperatures are required to allow the shape change to complete.

The MB shown in Figure 5.4 was measured when sample 3 was 1 day old. One can also repeat this temperature experiment at different days after self-assembly when equilibration is in a different stage. Temperature measurements on sample 3 were therefore also performed at different days after self-assembly (Figure 5.5). It shows that the sample needs to equilibrate a day before the transition becomes possible. A complete smooth transition becomes possible when the initial birefringence is at least $3.5 \cdot 10^{-8}$ which is typically after 1 to 3 days. The most probable explanation for this delay is the fact that in the preparation of sample 3 the water content is increased to 75%. This large amount of water is expected to initially vitrify the polystyrene part of the membrane, thereby blocking any shape changes. Over time, organic solvent trapped in the lumen of the polymersomes diffuses into the membrane and plasticizes it sufficiently for shape changes to occur. Indeed, the addition of a large excess of water (>95%) is a standard method to permanently quench PEG-PS polymersomes by vitrification of the PS part of the membrane [22–24].

### 5.3.3 Reproducibility

All the experiments described above demonstrate how a variety of polymersome shapes can be obtained at will, by carefully setting an osmotic pressure difference during sample preparation. With magnetic birefringence and electron microscopy, the exact structure at a given moment during the shape change process can be accurately determined. All morphologies can be kinetically trapped by adding an excess of water to vitrify the polystyrene part of the membrane. Discs and stomatocytes, owing to the low concentration of organic solvent in the PS block, can also be trapped by lowering the temperature. To investigate the reproducibility of the process, we repeated the procedures used for sample 3, using a block copolymer with a PS length of 200 units instead of 133 (sample 4). We obtained the exact same results as with sample 3 as can be seen in Figures 5.6 and 5.7. This clearly demonstrates that the procedure is reproducible and robust against changes in the length of the PS block.
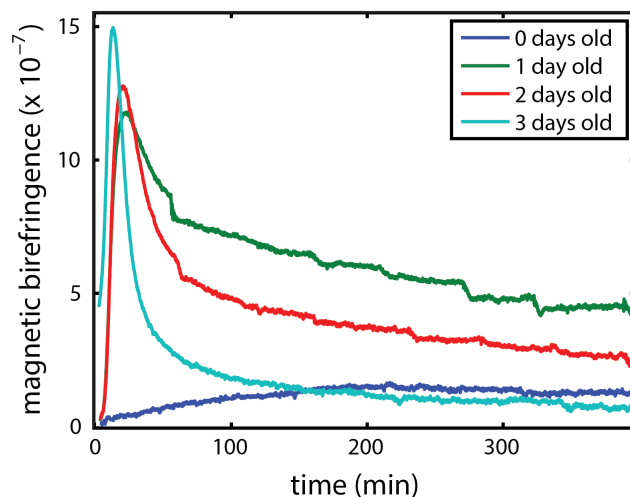
**Figure 5.5:** *Magnetic birefringence of sample 3 measured at 40 °C at 0, 1, 2 and 3 days after self-assembly. As can be seen there is almost no change in birefringence when the sample is just self-assembled (0 days old). The older the sample gets, the more easily the sample can make the transition to discs and subsequently stomatocytes. The whole transition becomes smooth and stable with temperature when the magnetic birefringence at t = 0 is at least 3% of the maximal birefringence (at the peak).*

## 5.4 Analysis and discussion

For a more quantitative description of the out-of-equilibrium shape change process, the found shapes of samples 1 to 3 were used to construct a phase diagram, which is presented in Figure 5.8. All polymersome cross sections obtained by cryo-TEM/SEM were fitted using the parametrization as formulated in chapter 3. Since all observed shapes are cylindrically symmetric (see Appendix 5.6.4, Figures 5.15 - 5.18 ), their 3D shape was reconstructed by revolving the fitted cross sections around the z-axis (Figure 5.8b,c). The results of these fittings are shown in Figure 5.8a,b and in the Appendix, section 5.6.3, Figure 5.14 and Table 5.2. The obtained parametrizations were then used to calculate the reduced volume (v) and the reduced area difference ($\Delta$a) between the outer and inner layer of the membrane, using equations 3.13 and 3.29. These two geometrical properties determine the position of each morphology in the phase diagram as is indicated by the dots in Figure 5.8d. The reduced volume (v) quantifies the amount of deflation and re-inflation and changes only slowly for our polymer-
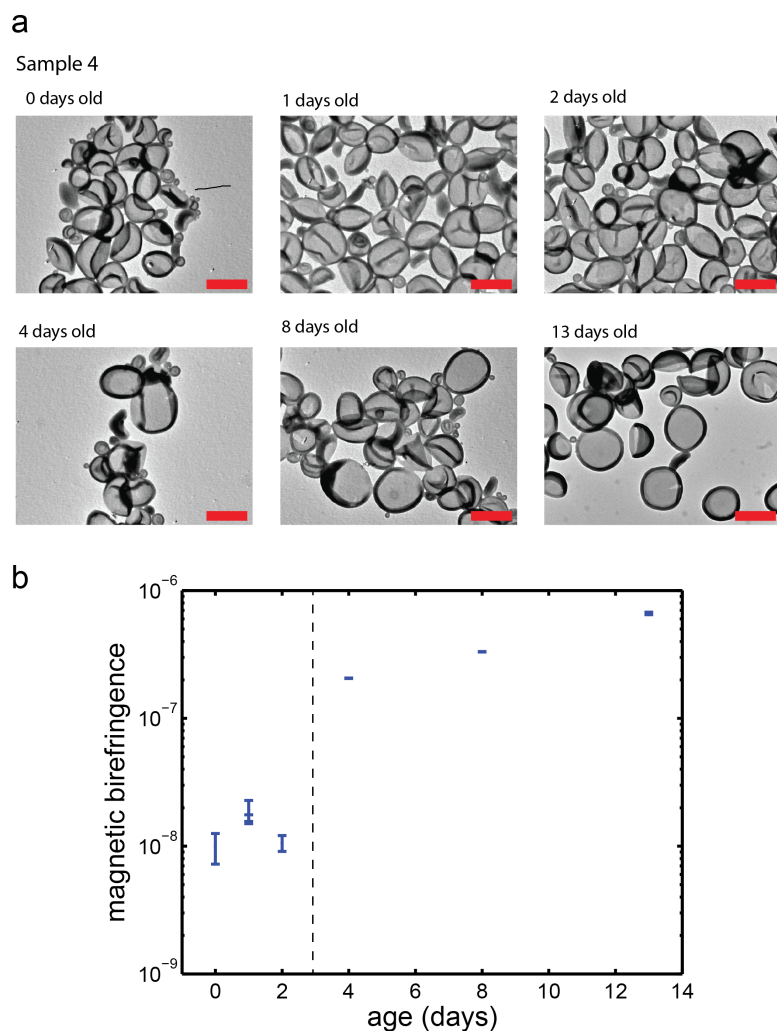
**Figure 5.6:** *Results from the equilibration experiments on sample 4. The sample was made from PEG$_{44}$-PS$_{200}$ rather than PEG$_{44}$-PS$_{133}$ while the self-assembly procedure was identical to that of sample 3. (a) In the TEM images we see that the first discs are observed when the sample was 4 days old. (b) The magnetic birefringence measurements are in agreement with the results from TEM. The observed effects and trends are very similar to those observed for sample 3, demonstrating that the experiment is quite robust to changes in the length of the PS block. All scale bars are 500 nm.*

a



c

b



**Figure 5.7:** *Overview of the results from the measurements on sample 4 at elevated temperatures. The sample was made from $PEG_{44}$-$PS_{200}$ rather than $PEG_{44}$-$PS_{133}$ while the s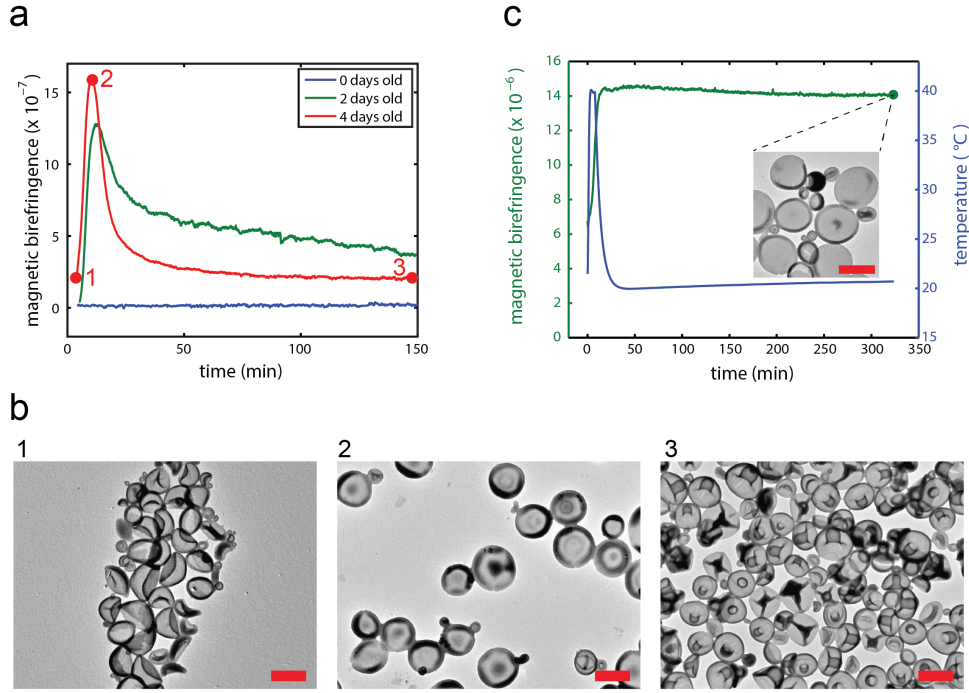elf-assembly procedure was identical to that of sample 3. (a) The magnetic birefringence measurements at $40°C$ show the same trend as sample 3 when measured over time. (b) TEM images are in agreement with the changes in magnetic birefringence. At point 1 the morphology is spherical (collapsed by drying), while point 2 shows discs and point 3 shows stomatocytes. (c) Also for sample 4 it was possible to thermally quench the discs by lowering the temperature right before the magnetic birefringence reached a maximum. These trends are all identical to the ones observed for sample 3. All scale bars are 500 nm.*

somes; $\Delta a$ is a geometrical parameter we use to identify the different shapes. The color scale in the background indicates the bending energy as calculated by the spontaneous-curvature model with zero spontaneous curvature (see section 3.4.1) [31, 34]. Trajectories of local minima as function of v are indicated with solid lines. The lines corresponding to discs and stomatocytes end when there is no longer a local minimum, which occurs for discs below v = 0.52 and for stomatocytes above v = 0.66 (Figure 5.9) [31, 34]. Sample 2 consists of prolates, and indeed, the shapes encountered in this sample are located very closely to
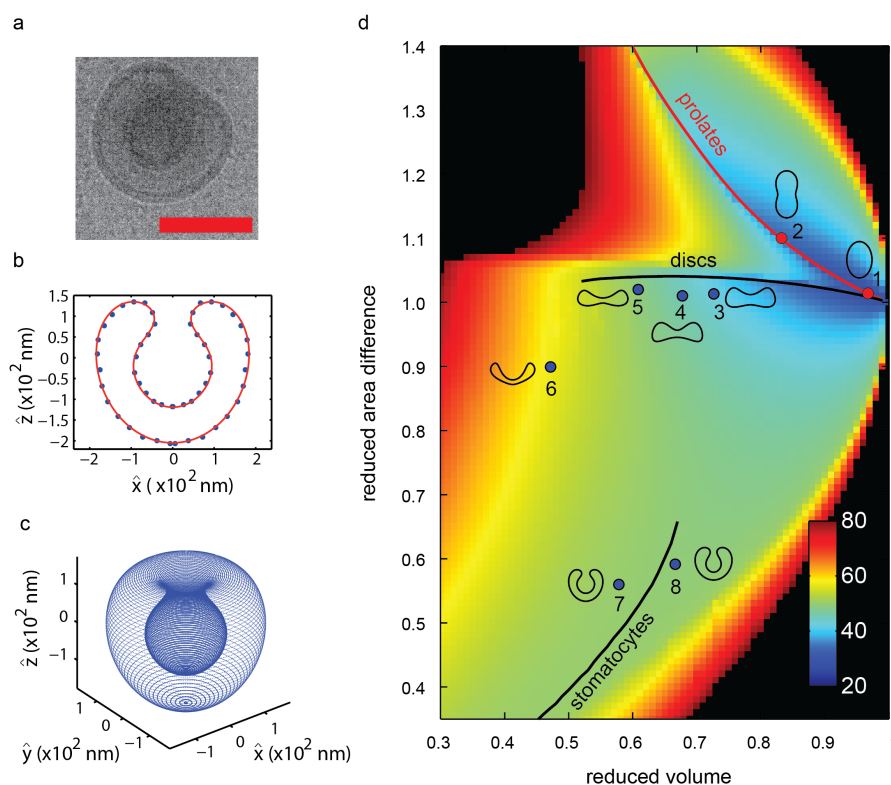
**Figure 5.8:** *Analysis of the observed shape transitions. All observed cross sections of the shapes that were captured with cryo-TEM and cryo-SEM were parameterized in order to calculate vesicle properties. (a) Cryo-TEM image of a stomatocyte found in sample 3 after heating to 35 °C. Scalebar is 250 nm. (b) Parametrization of the stomatocyte shown in (a). Points on the membrane surface are indicated by the blue dots. The red line corresponds to the parametrization that fits the data best. (c). After parametrization of the cross section, the 3D structure is obtained by revolving the fit around the z-axis since all observed structures are axisymmetric [35]. For every fitted shape, the reduced area difference and the reduced volume are calculated. (d) Phase diagram showing the positions of all observed shapes of sample 2 (red dots) and 3 (blue dots). The colorscale in the phase diagram indicates the bending energy ($E_{\text{bend}}/\kappa$). The lines drawn correspond to the calculated local minima for prolates (red line), discs (black middle line) and stomatocytes (black bottom line). The observed shapes are very close to the calculated local minima.*

the local minimum of prolates. Sample 3 consists of discs and stomatocytes, both of which are located close to the lines corresponding to the local minima of these two shapes. An intermediate between discs and stomatocytes (shape 6) was found at a reduced volume for which a disc is no longer a local minimum and where a stomatocyte is lower in energy. This strongly suggests that local bending is the driving force for discs to fold into stomatocytes when the reduced volume has decreased below v = 0.52 (Figure 5.9). Sample 2 was observed to deflate via prolates while sample 3 was observed to deflate via discs. Assuming zero spontaneous curvature ($c_0 = 0$), the difference in bending energy between discs and prolates is very small, in favor of prolate morphologies. It is however likely that the difference in solvent composition of the polymersome interior and exterior leads to a negative spontaneous curvature, which is larger for sample 3 than for samples 1 and 2 and which explains the preference for deflation via either prolates or discs. To understand why spheres deflate via prolates in sample 2 and via discs in sample 3 one should take into account that the solvent composition in the polymersome interior is different from the exterior after sample preparation. Since the interior contains a larger amount of organic solvent than the exterior, one would expect the membrane to be more swollen on the polymersome interior than on the exterior. In the spontaneous curvature model this can be described by the introduction of a negative spontaneous curvature which is largest for sample 3 and smallest for sample 1. For a reduced spontaneous curvature between 0 and -1.18, the prolates are still lowest in energy when deflating from a sphere. For $c_0 <$ -1.18 the discs will be lower in energy when deflating from a sphere [34]. This is indeed what we experimentally observe: sample 3 deflates via discs while sample 2 deflates via prolates. The energy associated with osmotic pressure is up to two orders of magnitude larger than the bending energy (Appendix, section 5.6.5). Therefore, osmotic pressure will quickly be relieved through an outflow of organic solvent, causing deflation, which will lower v. The morphology and the corresponding $\Delta$a at each value of v is then determined by the minimum bending energy. During this deflation, the osmotic energy will decrease but the bending energy will slightly increase. After the osmotic pressure has been alleviated, the polymersomes can re-inflate by a simultaneous inflow of water and organic solvent in order to decrease the bending energy while maintaining osmotic balance. In case of sample 2, the polymersomes are slightly permeable to water, allowing inflow of both water and organic solvent. Indeed, inflation of prolates into spheres was observed. In case of sample 3, the permeability to water is almost absent at room temperature. Therefore, the discs are not observed to re-inflate back to spheres. At elevated temperatures, the discs deflate further into stomatocytes. Once stomatocytes are formed, they re-inflate as stomatocytes, but only marginally. The
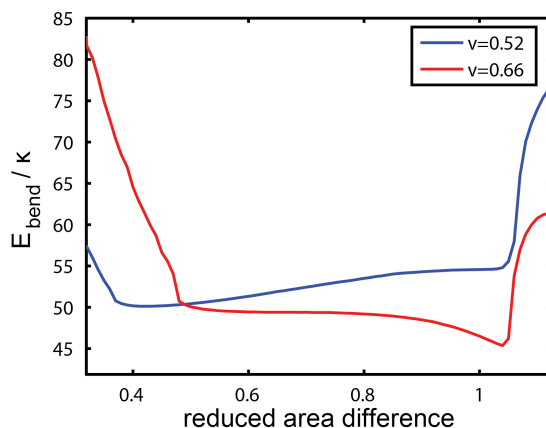
**Figure 5.9:** *Minimized bending energy as function of reduced area difference for a reduced volume of 0.52 (blue) and 0.66 (red). At v = 0.52 (and lower) the disc is no longer a local minimum, but the stomatocyte is (at a reduced area difference of 0.42) . At v = 0.66 (and higher) the stomatocyte shape is no longer in a local minimum but the disc is (at a reduced area difference of 1.04).*

decrease in bending energy for inflating stomatocytes is very small compared to inflating discs or rods which might explain why stomatocytes re-inflate only marginally. However, it is striking how the deflation and inflation of sample 3 occur via different routes. This hysteresis was also observed during the *in situ* dialysis as described in chapter 4. One explanation for this hysteresis can be found in the spontaneous curvature model itself. One of its characteristics is that shape transitions between rods and discs and between discs and stomatocytes are discontinuous [31, 34–37], and the shapes can be trapped in local minima. Another explanation can be found in the fact that folding of a disc into a stomatocyte requires the reorganization of the individual polymers which is accompanied by friction, which breaks down microscopic reversibility. Energetic costs associated with this reorganization can be accounted for by the release of osmotic energy during deflation. During inflation, the reorganization of the polymers might be too costly energetically, which would prevent the stomatocyte from folding back into a disc. The latter explanation is supported by the fact that elevated temperatures are required to allow sample 3 to transform all the way to stomatocytes.

The asymmetry between deflation and inflation of vesicles far out-of- equilibrium is unique for polymersomes. Since phospholipid vesicles are much more

flexible, the energetic barriers are much smaller and their shape changes are indeed observed to be totally symmetric. These differences make polymersomes more versatile than phospholipid vesicles since their shapes can be directed and trapped in different positions in the phase diagram. Another difference between polymersomes and phospholipid vesicles is the effect of temperature on the morphology. The effect of temperature on phospholipid vesicles has been investigated before and a theory was developed that explains shape changes in terms of an asymmetric thermal coefficient of expansion between the outer and inner layer of the vesicle membrane [31,38]. There are several reasons why this mechanism is unlikely to apply to our polymersome system. Firstly, the asymmetry in the coefficient of thermal expansion only has to be very small (0.2%) for phospholipid vesicles to explain a deflation into discs and subsequently into stomatocytes. But since this effect scales with $R/d$, when $R$ is the vesicle radius and $d$ the thickness of the membrane, the asymmetry has to be around 20% to explain the effect for our polymersomes. Furthermore, the model only predicts deflation upon heating while sample 3 shows an initial deflation (into folded discs) followed by inflation into stomatocytes. Finally, the theory does not take into account any osmotic forces which dominate the changes in inner volume. Instead, for polymersomes one can explain the temperature effects more easily in terms of permeability and flexibility. An increase in temperature will make the membrane more permeable and more flexible. A higher permeability will lead to a faster equilibration, which is indeed observed. A higher flexibility will lead to a lower bending energy, which will lower any energetic barrier that might exist between a disc and a stomatocyte. This will allow a disc to fold into a stomatocyte at temperatures above 35 °C, whereas it will remain trapped as a disc at room temperature.

## 5.5 Conclusions

In summary, we have demonstrated the manipulation of polymersomes into different shapes in a controllable manner using out-of-equilibrium self-assembly. To the best of our knowledge, this is the first time that different shapes via different routes were observed, all by starting from the same spherical morphology. The high rigidity and small permeability of the polymersomes leads to slow kinetics, allowing to carefully monitor shape changes in time spans varying from a few hours to many days. Parametrization of the observed shapes enabled us to place all morphologies in a phase diagram and calculate their geometrical properties. The shapes obtained can be explained by a simple model based on osmotic and bending energy. The ability to vitrify the membrane by adding an

excess of water makes it possible to trap all observed morphologies, including all of the intermediates. Discs can even be obtained by thermal quenching. This provides us with the possibility to prepare large batches of low-polydispersity polymersomes with well defined and predictable shapes, such as spheres, prolates, discs and stomatocytes, at any desirable reduced volume. These differently shaped polymersomes are promising candidates for nanocontainers and scaffolds, or as building blocks for assembly of larger and more complicated architectures.

## 5.6  Appendix

### 5.6.1  Additional TEM and SEM images of samples 1, 2 and 3

Additional TEM and SEM images were taken at multiple moments during equilibration of samples 1, 2 and 3. The images are shown in Figures 5.10, 5.11 and 5.12.
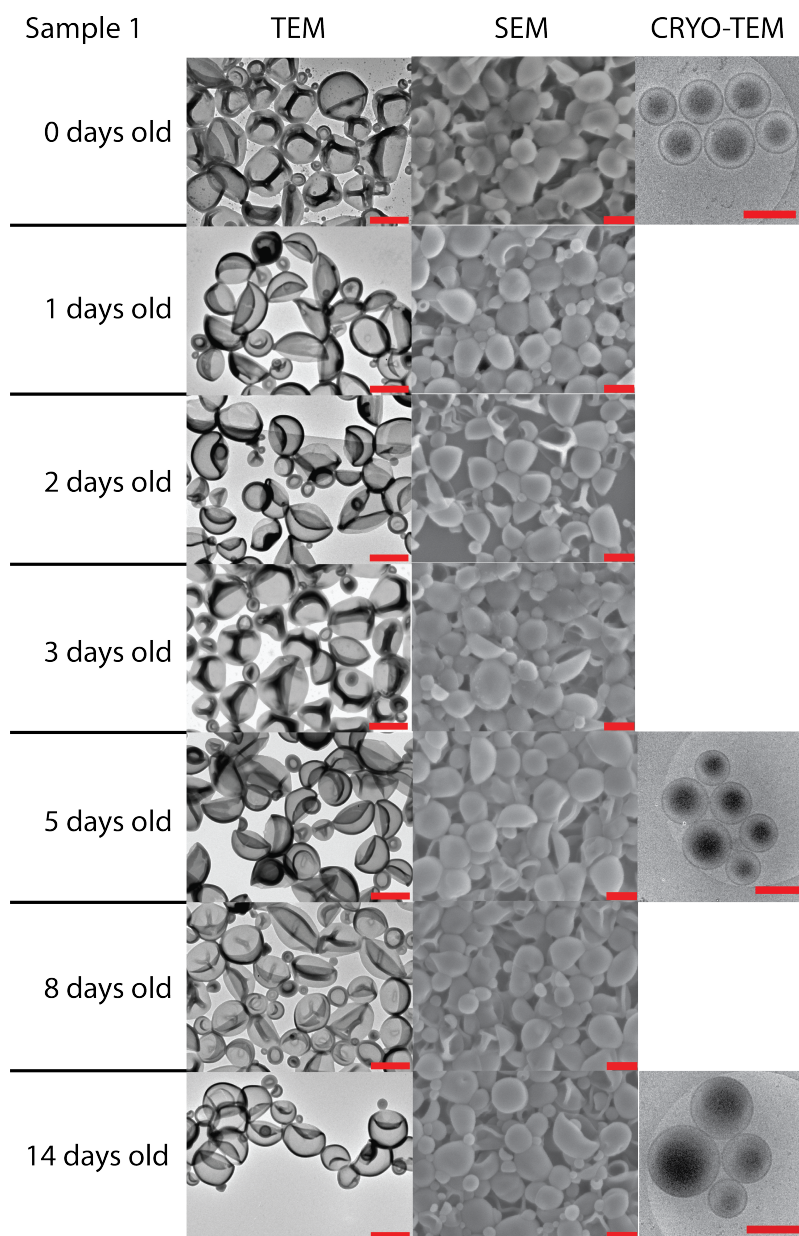
**Figure 5.10:** *TEM and SEM images of sample 1 at seven different days after self-assembly. Cryo-TEM (right) clearly shows that the morphology remains spherical over time. The indented structures, due to drying, in normal TEM (left) can still be identified as spheres. All scale bars are 500 nm.*

**Figure 5.11:** *TEM and SEM images of sample 2 at six different days after self-assembly. Cryo-TEM is shown on the right. As can be seen, the morphology changed from spherical to prolate after 1 day with the number of prolates increasing when the sample is 3 and 4 days old. After 8 and 14 days only spheres were observed. All scale bars are 500 nm.*

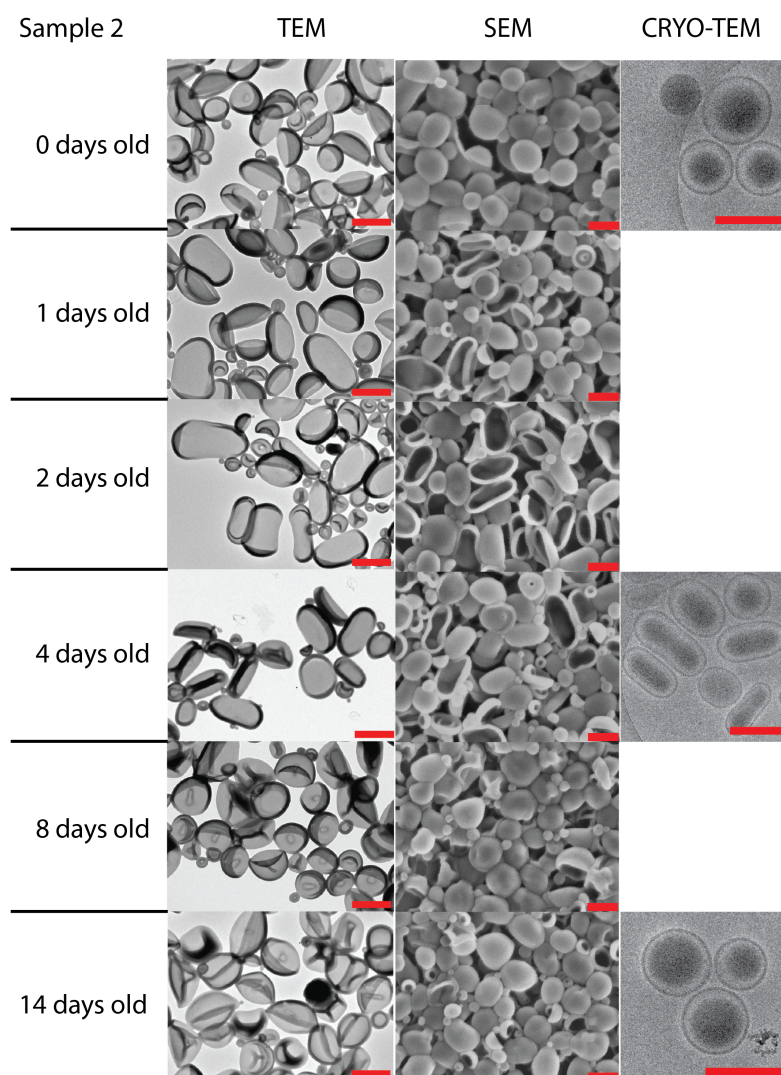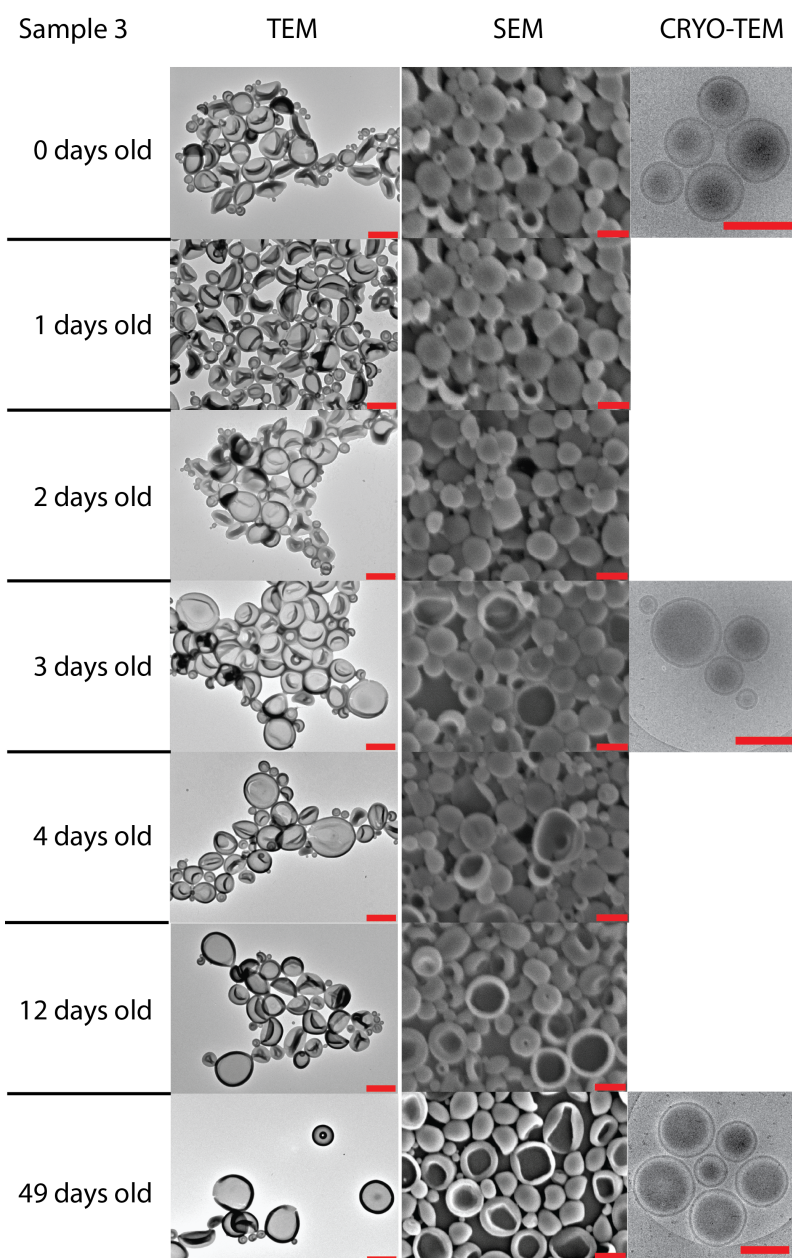**Figure 5.12:** *TEM and SEM images of sample 3 at seven different days after self-assembly. Cryo-TEM is shown on the right. As can be seen, the morphology changed from spherical to disc for about one third of the sample. All scale bars are 500 nm.*

### 5.6.2 Magnetic birefringence

To prove that the magnetic field of 2 T did not influence the experiment by inducing magnetic deformation [33] or by changing the rate at which the shape changes occur, the MB measurement at 50 °C was repeated at 0.5 T for comparison (Figure 5.13). The amplitude of the 0.5 T curve was multiplied with a factor of 16 since it was observed that, up to 2 T, the MB scales with $B^2$. After this scaling, no difference in amplitude or transition rate was observed between the two, indicating that a magnetic field of 2 T can be used to probe polymersome morphologies in sample 3.
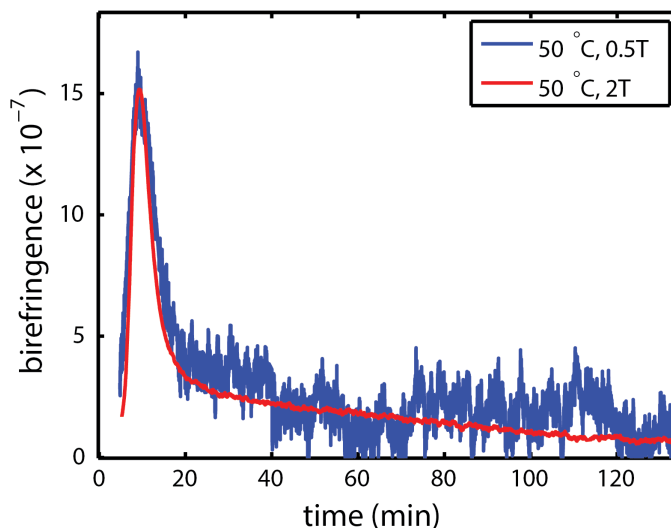


**Figure 5.13:** *Magnetic field dependence of sample 3 at 50 °C. The magnetic birefringence of sample 3 at 50 °C measured once at 0.5 T and once at 2 T. For comparison the amplitude of the 0.5 T measurement is scaled to a 2 T measurement by multiplication with 16, since the magnetic birefringence was observed to scale with $B^2$ up to 2 T . The two curves overlap indicating that the magnetic field does not accelerate or decelerate the rate at which the changes in morphology occur. Therefore a 2 T magnetic field can be used for probing sample 3.*

### 5.6.3 Parametrization of different shapes obtained from cryo-EM images

All encountered shapes were fitted using the parametrization as given by equations 3.3 to 3.5 (chapter 3). The fittings are shown in Figure 5.14 and the obtained fitting parameters are listed in Table 5.2.
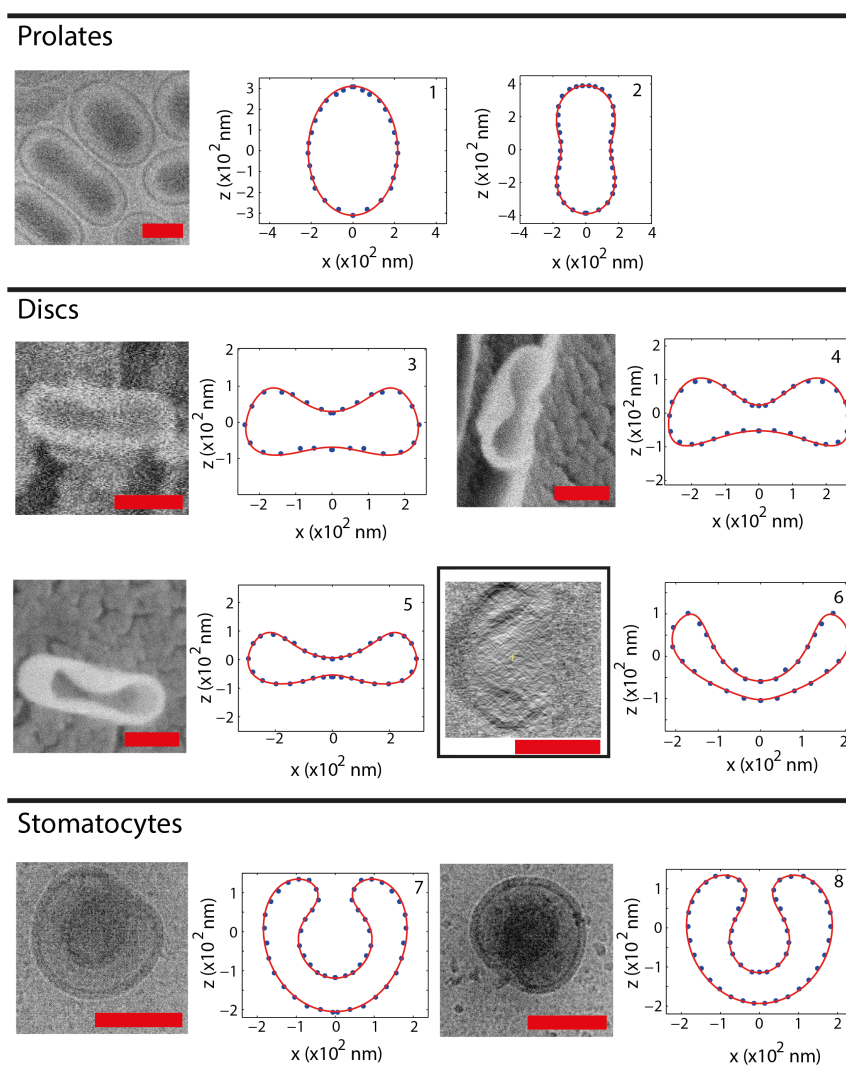


**Figure 5.14:** *Fittings of the prolates (rods and spheroids), discs and stomatocytes from chapter 5. All scale bars are 250 nm.*

| fit # | $a_1$ ($\cdot 10^{-7}$) | $a_2$ ($\cdot 10^{-7}$) | $a_3$ ($\cdot 10^{-7}$) | $a_4$ ($\cdot 10^{-7}$) | $b_1$ ($\cdot 10^{-7}$) | $b_2$ ($\cdot 10^{-7}$) | $b_3$ ($\cdot 10^{-7}$) | $b_4$ ($\cdot 10^{-7}$) | v | $\Delta$a |
|---|---|---|---|---|---|---|---|---|---|---|
| 1 | 2.15 | 0 | 0 | 0 | 3.1 | 0 | 0 | 0 | 0.9672 | 1.0139 |
| 2 | 1.995 | 0 | 0.50625 | 0 | 3.4 | 0 | 0.5 | 0 | 0.8323 | 1.1003 |
| 3 | 2.25 | -0.15 | -0.075 | 0.075 | 0.882 | -0.195 | -0.39 | 0 | 0.7266 | 1.0132 |
| 4 | 2.76 | 0 | -0.15 | 0.15 | 0.75 | -0.23625 | -0.45 | 0 | 0.6085 | 1.02 |
| 5 | 2.55 | -0.315 | -0.075 | 0 | 0.882 | -0.125 | -0.5 | -0.015 | 0.6776 | 1.0102 |
| 6 | 1.936 | -0.055 | -0.05775 | 0.165 | 0.495 | -0.77 | -0.275 | -0.033 | 0.4718 | 0.8993 |
| 7 | 1.1925 | -0.4275 | 0.72 | -0.07442 | 0.009 | -1.35 | 0.42 | -0.27 | 0.5784 | 0.5597 |
| 8 | 1.1 | -0.53 | 0.7 | -0.072 | -0.0252 | -1.32 | 0.42 | -0.22 | 0.6666 | 0.5914 |

**Table 5.2:** *Fitting parameters of the fits shown in Figure 5.14.*

### 5.6.4 Determining the symmetry axis of the vesicles

To determine the symmetry axis of every shape encountered, we recorded cryo-TEM images of all shapes at 3 different angles to obtain more information about their 3D shape and direction of symmetry axis. For the equilibration experiments at room temperature of samples 1, 2 and 3, these images are shown in Figures 5.15, 5.16 and 5.17 respectively. For the temperature experiments on sample 3, the cryo-TEM images are shown in Figure 5.18.

It was observed that rods always lie with their symmetry axis in-plane, as is shown in Figure 5.16. Discs lie with their symmetry axis out-of-plane (Figure 5.17). To parameterize a shape, its symmetry axis must lie in-plane. Therefore, we used cryo-SEM to obtain the cross-sections of some discs instead. This was done by breaking a frozen disc sample in two and only look for those discs that lie perpendicular in the ice and that are broken in half to show their cross section. The cryo-TEM images do show that the discs are cylindrically symmetric, so the symmetry axis can be drawn parallel to the plane of symmetry of the cross-section found in SEM.

When performing cryo-TEM, the stomatocytes were found to lie either with their symmetry axis in-plane or out-of-plane as can be seen in Figure 5.18. The ones that lie in-plane can be parameterized. The stomatocytes that lie with their symmetry axis out-of-plane do show that the stomatocytes are completely cylindrically symmetric.

Sample 1

|       | -45°  | 0°    | +45°  |



**Figure 5.15:** *Angle-dependent cryo-TEM on sample 1. The sample at day 0, 5 and 14 are shown under 3 different angles: -45, 0° and 45°. At all days, we see circular structures under all angles, proving that the 3D shape of the vesicle remains spherical over time. All scale bars are 500 nm.*
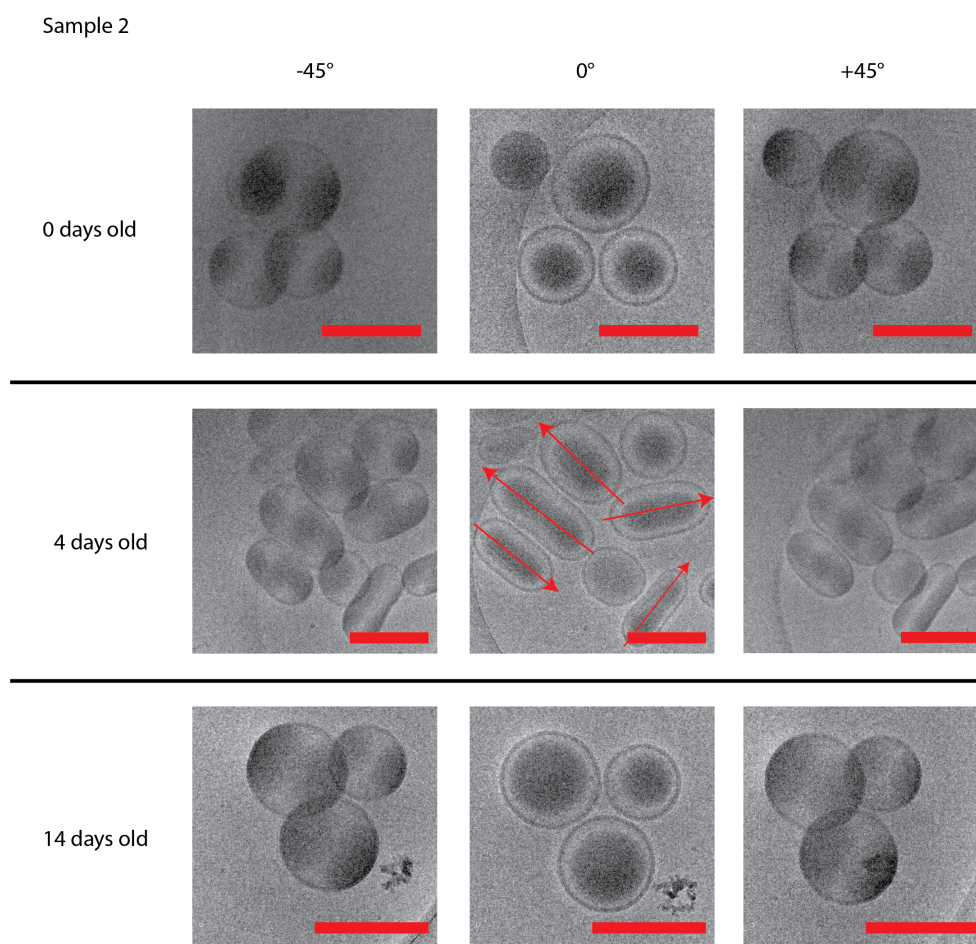
**Figure 5.16:** *Angle-dependent cryo-TEM on sample 2. The samples at day 0, 4 and 14 are shown under 3 different angles: -45, 0° and 45°. At day 0 and 14 we see circular structures under all angles, proving that the 3D shape of the vesicles at these times is indeed spherical. At day 4 we see prolates. The images recorded at -45° and 45° look similar and show a shorter aspect ratio. The largest aspect ratio was observed at 0°, suggesting that the prolates are lying with their symmetry axis in-plane as indicated by the red arrows. All scale bars are 500 nm.*
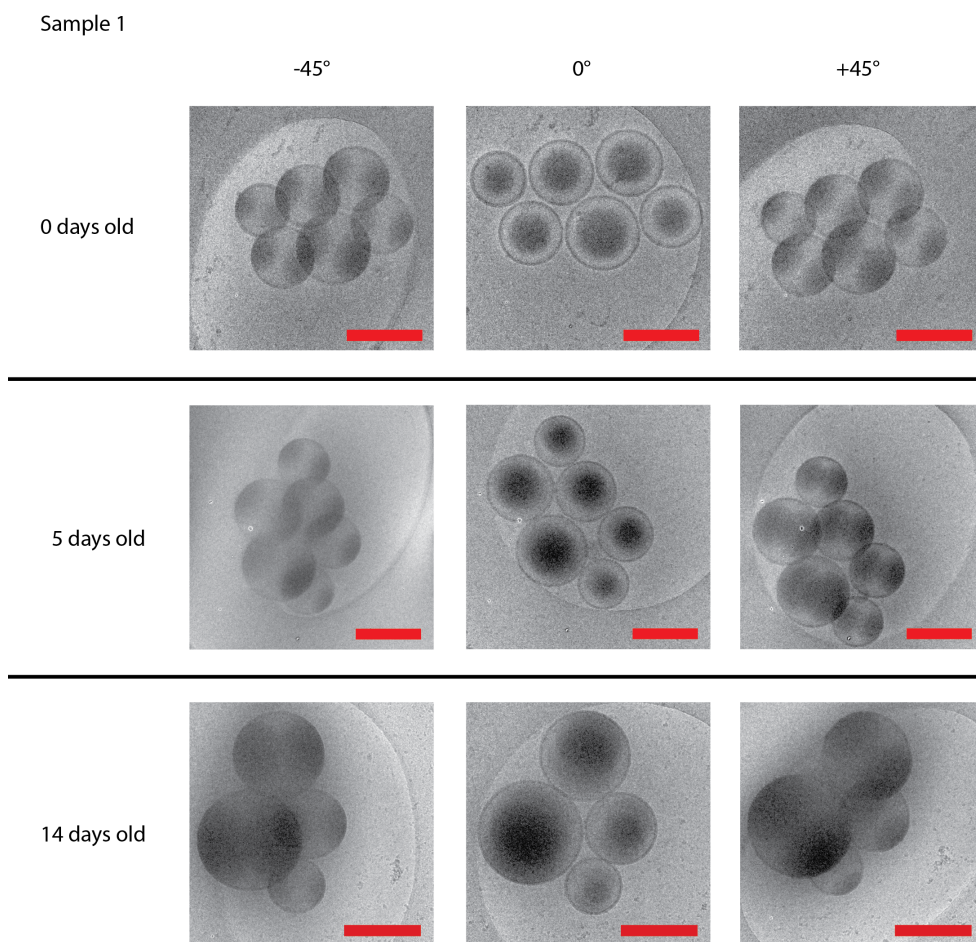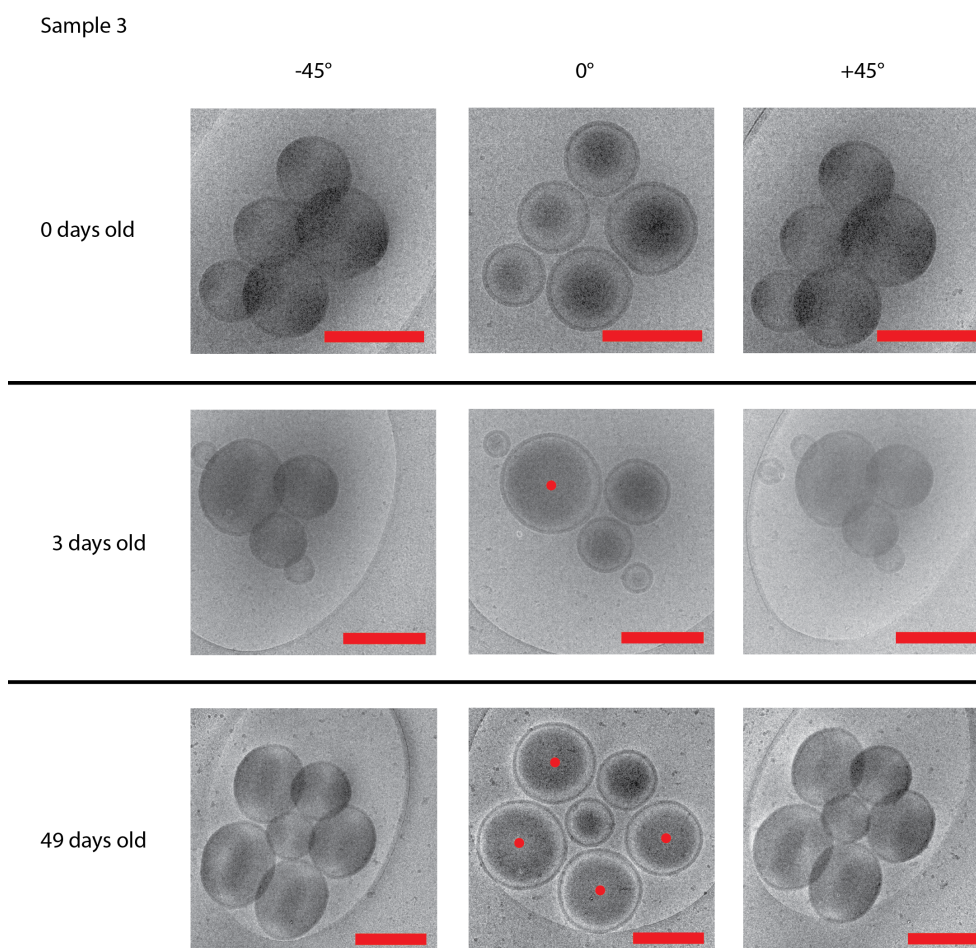
Sample 3



**Figure 5.17:** *Angle-dependent cryo-TEM on sample 3. The samples at day 0, 3 and 49 are shown under 3 different angles: -45, 0° and 45°. At day 0 we see circular structures under all angles, proving that the 3D shape of the vesicles at these times is indeed spherical. At day 3 and 49 we see that there are also structures which look dented and not circular when looked at under -45° or 45°. These disc-shaped polymersomes are lying with their symmetry axis out-of-plane, since they are only circular when viewed from the top (0°. Some structures remain spherical however as can be seen by their circular representation at all different angles. For the discs, the symmetry axes are indicated by the red dots (out-of-plane arrrow). All scale bars are 500 nm.*
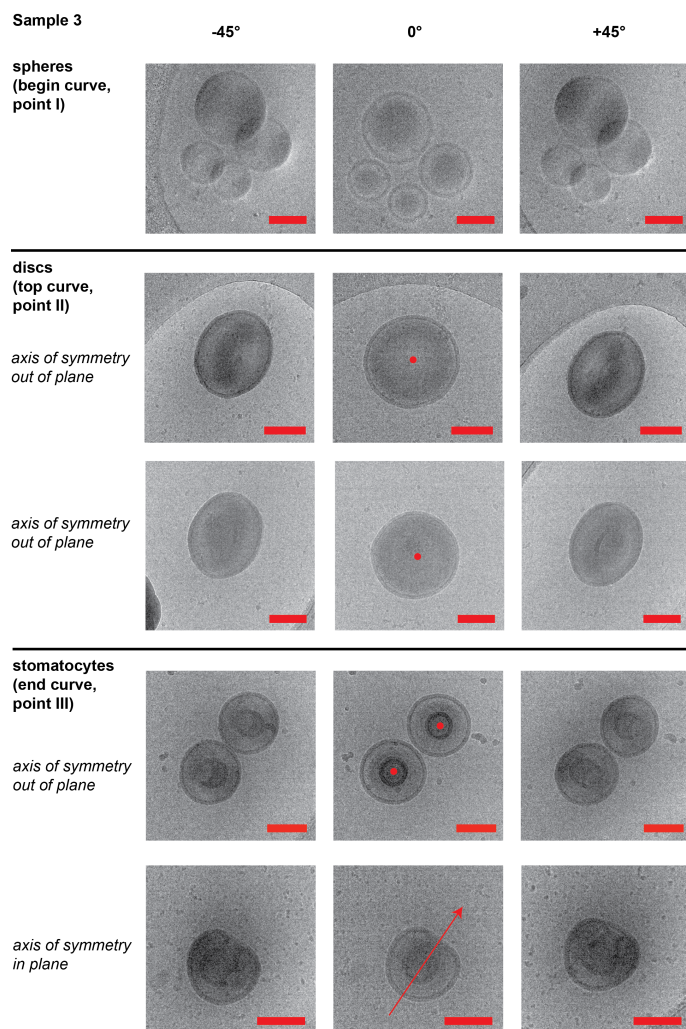
**Figure 5.18:** *Angle-dependent cryo-TEM on sample 3 at elevated temperatures (35-40°). Before heating, (point 1 in MB curve of figure 5.4), the shape is spherical. At point 2 of the MB curve in figure 5.4, only discs were observed. The symmetry axis is out-of-plane (indicated with red dot) since the discs only look circular when imaged at 0°. The stomatocytes observed at the end of the experiment (point 3 in the MB curve of figure 5.4) are found either with their symmetry axis out-of-plane (red dot) or with their symmetry axis in-plane (red arrow). Those found with their symmetry axis in-plane can be used for parametrization. All scale bars are 500 nm.*

### 5.6.5 Energetic calculations

**Osmotic pressure**

The concentrations of solvents range between 1.17 M (for dioxane in sample 3) and 41.67 M (for water in sample 3). The concentration differences are therefore in the order of ten mole. When taking a vesicle of radius 250 nm (which is the average radius), the osmotic energy, $E_{\text{osm}}$, is in the order of $10^{-16}$ J.

**Bending energy**

Depending on the flexibility of the polymersome membrane, which also depends on the amount of organic solvent present, the bending constant $\kappa$ is usually in the order of 10-100 $kT$; with longer polymer chains even higher than 100 $kT$ [9, 39]. Since the bending energy, $E_{\text{bend}}$, of a sphere is $4\pi\kappa$, the bending energy of polymersomes is in the order of $10^{-18}$ J. So there is 2 orders of magnitude difference between the bending energy and the osmotic energy. Since $E_{\text{osm}}$ is around two orders of magnitudes larger than $E_{\text{bend}}$, one can assume that shape changes will not occur if they induce a large osmotic pressure difference.

## References

[1] B.M. Discher, Y.-Y. Won, D.S. Ege, J.C.-M. Lee, F.S. Bates, D.E. Discher and D.A. Hammer, *Science*, **284**, 1143 (1999)

[2] D.E. Discher and A. Eisenberg, *Science*, **297**, 967 (2002)

[3] J.A. Opsteen, J.J.L.M. Cornelissen and J.C.M. van Hest, *Pure Appl. Chem.*, **76**, 1309 (2004)

[4] G. Srinivas, D.E. Discher and M.L. Klein, *Nat. Mater.*, **3**, 638 (2004)

[5] D.E. Discher, N. Bhasin, and C.P. Johnson, *P. Natl. Acad. Sci. USA*, **103**, 7533 (2006)

[6] C. LoPresti, H. Lomas, M. Massignani, T. Smart and G. Battaglia, *J. Mater. Chem.* , **19**, 3576 (2009)

[7] Y.Y. Mai and A. Eisenberg, *Chem. Soc. Rev.*, **41**, 5969 (2012)

[8] J.F. Le Meins, O. Sandre and S. Lecommandoux, *Eur. Phys. J. E*, **34** (2011)

[9] R. Rodríguez-García, M. Mell, I. López-Montero, J. Netzel, T. Hellweg and F. Monroy, *Soft Matter*, **7**, 1532 (2011)

[10] S.J. Holder, and N.A.J.M. Sommerdijk, *Polym. Chem-Uk*, **2**, 1018 (2011)

[11] Y.S. Yu and A. Eisenberg, *J. Am. Chem. Soc.*, **119**, 8383 (1997)

[12] S.F.M. van Dongen, M. Nallani, S. Schoffelen, J.J.L.M. Cornelissen, R.J.M. Nolte and J.C.M. van Hest, *Macromol. Rap. Comm.*, textbf29, 321 (2008)

[13] R.P. Brinkhuis, F.P.J.T. Rutjes and J.C.M. van Hest, *Polym. Chem-Uk*, **2**, 1449 (2011)

[14] M.F. Debets, W.P.J. Leenders, K. Verrijp, M. Zonjee, S.A. Meeuwissen, I. Otte-Holler and J.C.M. van Hest, *Macromol. Biosci.*, **13**, 938 (2013)

[15] S.C. Balmert and S.R. Little, *Adv. Mater.*, **24**, 3757 (2012)

[16] P. Kolhar, A.C. Anselmo, V. Gupta, K. Pant, B. Prabhakarpandian, E. Ruoslahti and S. Mitragotri, *P. Natl. Acad. Sci.*, **110**, 10753 (2013)

[17] R.A. Petros and J.M. DeSimone, *Nat. Rev. Drug Discov.*, **9**, 615 (2010)

[18] J.L. Perry, K.P. Herlihy, M.E. Napier and J.M. DeSimone, *Accounts Chem. Res.*, **44**, 990 (2011)

[19] J.R. Rothenbuhler, J.-R. Huang, B.A. DiDonna, A.J. Levine and T.G. Mason, *Soft Matter*, **5**, 3639 (2009)

[20] C. Uzoigwe, *Med. Hypotheses.*, **67**, 1159 (2006)

[21] N. Doshi, A.S. Zahr, S. Bhaskar, J. Lahannand and S. Mitragotri, *P. Natl. Acad. Sci.*, **106**, 21495 (2009)

[22] H.Y. Chang, Y.J. Sheng and H.K. Tsao, *Soft Matter*, **10**, 6373 (2014)

[23] K.T. Kim, J. Zhu, S.A. Meeuwissen, J.J.L.M. Cornelissen, D.J. Pochan, R.J.M. Nolte and J.C.M. van Hest, *J. Am. Chem. Soc.*, **132**, 12522 (2010)

[24] S.A. Meeuwissen, K.T. Kim, Y. Chen, D.J. Pochanand and J.C.M. van Hest, *Angew. Chem. Int. Edit.*, **50**, 7070 (2011)

[25] R.S.M. Rikken, H.H.M. Kerkenaar, R.J.M. Nolte, J.C. Maan, J.C.M. van Hest, P.C.M. Christianen and D.A. Wilson, *Chem. Commun.*, **50**, 5394 (2014)

[26] M.C.M. van Oers, F.P.J.T. Rutjes and J.C.M. van Hest, *J. Am. Chem. Soc.*, **135**, 16308 (2013)

[27] J.D. Robertson, G. Yealland, M. Avila-Olias, L. Chierico, O. Bandmann, S.A. Renshaw and G. Battaglia, *ACS Nano*, **8**, 4650 (2014)

[28] Y. La, C. Park, T.J. Shin, S.H. Joo, S. Kang and K.T. Kim, *Nat. Chem.*, **6**, 534 (2014)

[29] R. Salva, J.-F. Le Meins, O. Sandre, A. Brûlet, M. Schmutz, P. Guenoun and S. Lecommandoux, *ACS Nano*, **7**, 9298 (2013)

[30] D.H.W. Hubert, M. Jung, P.M. Frederik, P.H.H. Bomans, J. Meuldijk and A.L. German, *Langmuir*, **16**, 8973 (2000)

[31] U. Seifert, K. Berndl and R. Lipowsky, *Phys. Rev. A*, **44**, 1182 (1991)

[32] G. Maret and K. Dransfeld, *Top. Appl. Phys.*, **57**, 143 (1985)

[33] P.G. van Rhee, R.S.M. Rikken, L.K.E.A. Abdelmohsen, J.C. Maan, R.J.M. Nolte, J.C.M. van Hest, P.C.M. Christianen and D.A. Wilson, *Nat. Commun.*, **5**, 5010 (2014)

[34] U. Seifert, *Adv. Phys.*, **46**, 13 (1997)

[35] V. Heinrich, M. Brumen, R. Heinrich, S. Svetina and B. Žekš, *J. Phys. II France*, **2**, 1081 (1992)

[36] U. Seifert and R. Lipowsky, *Handbook of Biological Physics Vol. 1*, Ch. 8, Elsevier Science B.V., (1995)

[37] M. Jarić, U. Seifert, W. Wintz and M. Wortis, *Phys. Rev. E*, **52**, 6623 (1995)

[38] K. Berndl, J. Käs, R. Lipowsky, E. Sackmann and U. Seifert, *Europhys. Lett.*, **13**, 659 (1990)

[39] H. Bermúdez, D.A. Hammer and D.E. Discher, *Langmuir*, **20**, 540 (2004)

# Chapter 6

# Determining the magnetic anisotropy of an individual polymer in polymersomes self-assembled from PEG-PS

## Abstract

We determined the average magnetic anisotropy of PEG-PS inside a polymersome membrane by measuring the shape factors, surface areas and magnetic birefringence of both disc-shaped and stomatocyte-shaped polymersomes. From this, we have estimated the contribution of a single polystyrene repeating unit to the total magnetic anisotropy, $\Delta\chi^{PS}$. The value obtained, $(-2.5 \pm 0.4)\cdot10^{-12}$ m$^3$/mol, is negative which proves that an individual polymer aligns perpendicularly to an applied magnetic field. This $\Delta\chi$ value is considerably smaller than that of fully extended chains, which is attributed to the coiling of the polymer. We predict that fully extended polymers would boost the magnetic response of polymersomes, which would be highly advantageous for practical applications.

## 6.1 Introduction

Diamagnetic materials are promising for numerous applications in magnetic fields [1]. For instance, they are the only type of materials that can be levitated stably in all three dimensions in an inhomogeneous magnetic field [2–4]. When the diamagnetic susceptibility of an object is anisotropic, the object will have a preferential direction in a magnetic field, which leads to magnetic alignment [1,5]. Several examples of diamagnetic alignment have already been discussed in chapter 2. The origin of diamagnetic anisotropy can be found in the chemical properties of the materials [5]. For a large number of chemical bonds or chemical groups, the magnetic anisotropy has already been determined [5–9]. In macromolecules the total diamagnetic anisotropy also depends heavily on their conformation, in other words the orientations of all the bonds and groups with respect to each other [5]. Also in crystals, the diamagnetic anisotropy is found to dependent on their chemical structure [10].

In order to align diamagnetic materials with magnets readily available, the diamagnetic anisotropy needs to be sufficiently high. For polymersomes self-assembled from poly(ethylene glycol)-polystyrene (PEG-PS), we have already demonstrated partial magnetic alignment of differently shaped polymersomes in magnetic fields of only 2 T in chapters 4 and 5. However, these studies were rather qualitative. For a full quantitative understanding of the behavior of PEG-PS based polymersomes in magnetic fields, the exact value of the magnetic anisotropy, $\Delta\chi$, of a single PEG-PS polymer has to be determined. Although the magnetic anisotropy of polystyrene in an assembly of block copolymers has been determined before [11], the found value applies only to the investigated lamellar mesophase assembled from poly(styrene-b-4-vinyl pyridine). The magnetic anisotropy of PEG-PS within in a polymersome could very well be different because of the differences in chemical composition of the block copolymer, and its surroundings, and the morphology of the assembly (a polymersome being a bilayer vesicle rather than a lamellar mesophase).

Over the last decades, several techniques have been developed that can be used to determine the diamagnetic anisotropy of a material or sample. The preferred technique heavily depends on the properties of the material and the size of the sample. The diamagnetic anisotropy of a variety of relative large (macroscopic) crystals have been determined by oscillating them in a static magnetic field, using either fibers for suspension [12–14] or micro-gravity [15–17] to keep the crystals in place. Diamagnetic anisotropies have also been detected during phase transitions by magnetically levitating a sample while heating or cooling it [18, 19]. Nuclear Magnetic Resonance (NMR) has been used to determine diamagnetic anisotropies of single bonds or small chemical

groups [20, 21]. For small molecular aggregates in solution, the diamagnetic anisotropy can be determined by measuring the degree of alignment as function of the applied magnetic field, often by using optical techniques such as magnetic birefringence (MB) [5] or polarized absorbance [22]. MB has been used to determine the magnetic alignment of a wide variety of biological [23–27] and organic [28–32] structures.

For molecular aggregates in solution, such as our polymersomes, the first two mentioned techniques are not always well suited. Molecular aggregates are usually too small to measure with the magnetic oscillation technique, while NMR usually focuses strongly on individual chemical bonds or groups. For our polymersomes, a technique is preferred to measure the magnetic anisotropy of a polymersome vesicle as a whole, which in turn can be related to that of a single polymer. Therefore, MB seems to be the most preferred technique.

In this chapter we will demonstrate how the average magnetic anisotropy of a PEG-PS polymer in a polymersome can be determined by measuring the MB of several differently shaped rigid polymersomes samples (spheres, stomatocytes and discs). By using high fields it was possible to (partly) saturate the magnetic alignment of some of the shapes. This allowed the MB curves to be fitted using equations 3.35, 3.40 and 3.42 of chapter 3. For all samples, the shapes obtained by cryo-EM were fitted to the parametrization first introduced in chapter 3 (equations 3.1 and 3.2). This provided the quantitative information about size and shape which was needed to express the magnetic anisotropy of a whole vesicle in terms of the magnetic anisotropy of a single repeating unit of polystyrene. We will show that the magnetic anisotropy of the polymer is only a fraction of what it potentially could be, which can be explained by the polymers being coiled rather than being entirely stretched. Controlling the magnetic properties of a polymersome by changing the extension of the polymers within the polymersome membrane could therefore be a promising new method to tune the magnetic anisotropy and therefore its response to magnetic fields.

## 6.2 Experimental details

### 6.2.1 Instrumentation

MB was measured using a standard polarization modulation technique as described in chapter 4. A 1.5 mW intensity stabilized HeNe laser (1.5 mW, 632.8 nm) from Research Electro-Optics Inc was used. To increase the sensitivity of the birefringence measurements, a photo-elastic modulator (PEM) at 50 kHz was used. A 33 T Florida-Bitter magnet was used at the High Field Magnet Laboratory (HFML). (Cryo-)SEM was performed on a JEOL 6330 Cryo

Field Emission Scanning Electron Microscope at an acceleration voltage of 3 kV. For Cryo-TEM a JEOL 2100 cryo-Transmission Electron Microscope was used. TEM was performed on a JEOL 1010 Transmission Electron Microscope at an accelerating voltage of 60 kV, for which 4 $\mu$L of sample was air dried on 200 Mesh carbon coated copper grids. DLS was performed with a Malvern Zetasizer Nano S instrument and its data was analyzed with the corresponding software from Malvern Instruments.

### 6.2.2  Sample preparation

We used $PEG_{44}$-$PS_{178}$ block-copolymers to prepare three batches of rigid polymersomes, each having a different shape. Samples 1 to 3 consisted of spheres, discs and stomatocytes respectively. The preparation of each batch started by self-assembly of spherical and flexible polymersomes, by dissolving 10 mg of $PEG_{44}$-$PS_{178}$ in a mixture of 600 $\mu$L THF and 400 $\mu$L dioxane. Then, 3 mL of MilliQ was added at a rate of 1 mL/h to induce self-assembly. For the spherical polymersomes, this fresh sample was dialyzed against MilliQ for 48 hours with 5 changes of water to remove all organic solvents, thereby trapping the spherical morphology. The discs were made by using the method described in chapter 5, where the spherical flexible polymersomes were equilibrated at 40 °C until the magnetic birefringence was at a maximum (and almost all polymersomes deflated into discs). The sample was quenched at that point by injecting it in an excessive amount of MilliQ. This solution was subsequently spin-filtrated multiple times to remove the remaining organic solvents and to increase the concentration back to its initial value. Stomatocytes were made by applying the solvent addition method to the rigid spherical polymersomes as described in ref. [33].

## 6.3  Results and analysis

The measured MB curves for all samples are shown in Figure 6.1a. The sample consisting of spheres shows zero MB up to 29 T, compared to the background (water). This is to be expected since spheres are completely isotropic with no preferred direction of alignment. The stomatocytes have a small anisotropy, which is confirmed by the small, even up to 29 T, MB. The largest signal is obtained by the most anisotropic shapes (discs) which is observed to saturate, indicating that the magnetic alignment is almost complete at 29 T. Cryo-TEM and cryo-SEM were used to image all polymersome samples. A representative image for every shape is shown in Figure 6.1b.

a



b
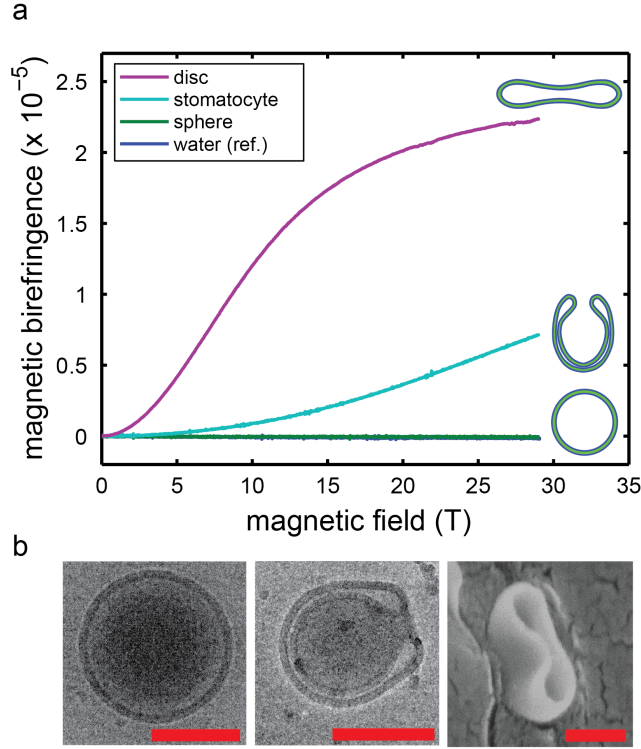


**Figure 6.1:** *(a) Results of the magnetic birefringence measurements for discs, stomatocytes, spheres and water. (b) Representative Cryo-EM images of a sphere (left, cryo-TEM), a stomatocyte (middle, cryo-TEM) and a disc (right, cryo-SEM). All scale bars are 250 nm.*

Cryo-TEM images were used to estimate the thickness, $t$, of the membrane for all shapes. It was found to be independent of the vesicle's shape and was determined to be $26 \pm 3$ nm.

To obtain quantitative information about the shape and size of the discs and the stomatocytes, we fitted five different vesicles for each shape, using the parametrization postulated in chapter 3. All individual fittings and fitting parameters are given in the Appendix (section 6.6). For every fit we calculated the value of $SP \cdot A$, which is the surface parameter multiplied with the surface area of the vesicle. In chapter 3, the surface parameter $SP$ was defined as:

$$SP = \left\langle \frac{3\cos^2(\theta_\mathrm{N}) - 1}{2} \right\rangle, \tag{6.1}$$

with $\theta_N$ the angle between a patch of membrane on the vesicle and the vesicle's symmetry axis. This means that the product of $SP$ and $A$ ($SP \cdot A$) can be calculated by integrating $\frac{3\cos^2(\theta_{\mathrm{N}})-1}{2}$ over the surface of the vesicle. For the discs, the average value of $SP \cdot A$ obtained from these fits is $39 \cdot 10^{-14}$ m$^2$ with a spread of $7 \cdot 10^{-14}$ m$^2$. For the stomatocytes, the average value of $SP \cdot A$ is $-6.0 \cdot 10^{-14}$ m$^2$ with a spread of $1.6 \cdot 10^{-14}$ m$^2$. Since the surface area is always positive, it follows that the $SP$ of discs and stomatocytes are opposite in sign. This is due to the fact that in stomatocytes most of the polymers are directed perpendicularly to the vesicle's symmetry axis, while in discs most of the polymers are oriented parallel to the vesicle's symmetry axis. This is shown schematically in Figure 6.2a. Because of this, the alignment of the discs and stomatocytes in a magnetic field must occur in different directions: one shape will align with its symmetry axis parallel to the magnetic field while the other must align with its symmetry axis perpendicular to the magnetic field. The sign of $\Delta\chi^{\mathrm{PS}}$ determines the orientation of the symmetry axis relative to the direction of the magnetic field, as is shown in Figure 6.2b. $\Delta\chi^{\mathrm{PS}}$, and its sign, will be determined by the fittings of the MB curves in the next subsection.

### 6.3.1 Parametrization of vesicle shapes

### 6.3.2 Fittings of MB curves

In order to obtain $\Delta\chi^{\mathrm{PS}}$, the MB curves of the discs and the stomatocytes were fitted using equations 3.35, 3.40 and 3.42 of chapter 3. In chapter 3, we explained that almost all contribution to $\Delta\chi$ is expected to be caused by the PS rather than the PEG. The reason for this is threefold. First of all, the intrinsic magnetic anisotropy of PS is much larger than that of PEG (at least three times or more). Secondly, the length of the PS is at least three to four times larger than that of PEG. Thirdly, the PEG is solvated by the surrounding water, which randomizes its orientation and therefore reduces its magnetic anisotropy even further. Because of this, the value of $\Delta\chi^{\mathrm{obj}}$ in equation 3.35 was substituted by equation 3.62, so that we could directly fit the value of $\Delta\chi^{\mathrm{PS}}$ to the MB data with the following function:

$$\Delta n = \Delta n_{\max} \cdot \frac{\int_{\theta=0}^{\pi} \left(\frac{3\cos^2(\theta)-1}{2}\right) \cdot f(\theta) \cdot \sin(\theta) \cdot d\theta}{\int_{\theta=0}^{\pi} f(\theta) \cdot \sin(\theta) \cdot d\theta}, \tag{6.2}$$

with $f(\theta)$ defined as:

$$f(\theta) = \frac{\exp(-E(\theta)/kT)}{\int_{\theta=0}^{\pi} \exp(-E(\theta)/kT) \cdot \sin(\theta) \cdot d\theta}, \tag{6.3}$$
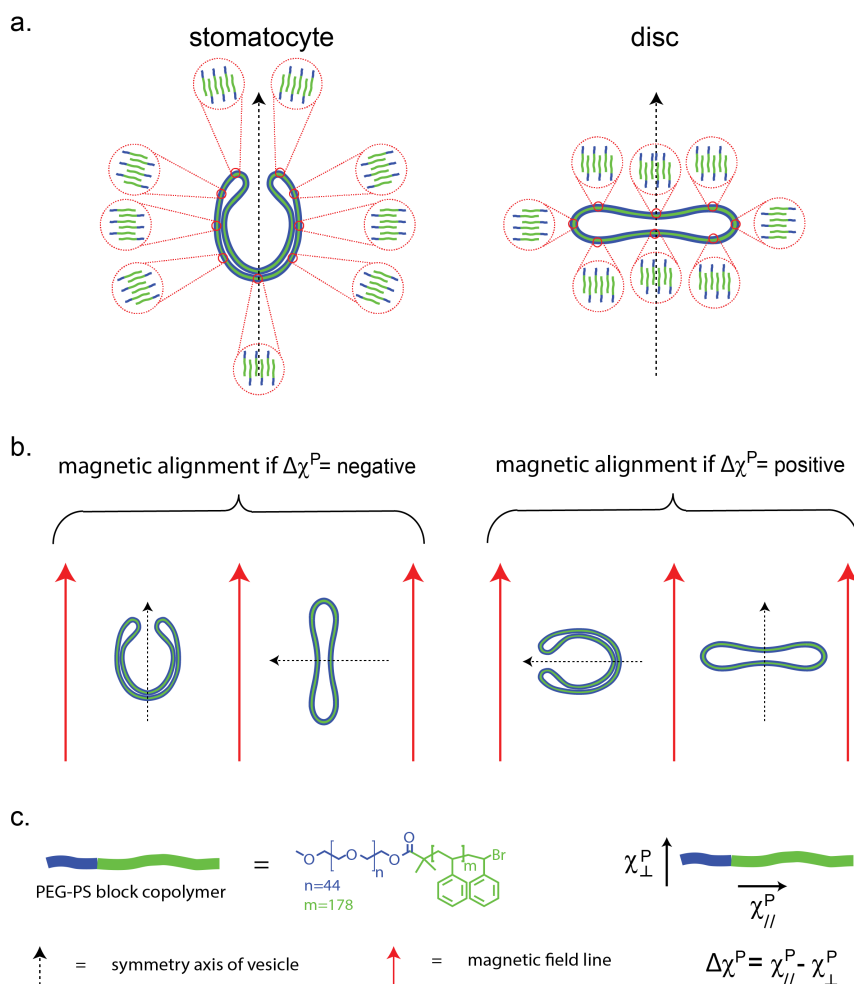
**Figure 6.2:** *(a) Schematic picture showing the orientations of polymers in a stomatocytes and a disc-shaped polymersomes. A stomatocyte has most of its polymers are oriented perpendicular to its symmetry axis (dashed arrow). A disc has most of its polymers oriented parallel to its symmetry axis. Because of this difference, the direction of alignment will be opposite for stomatocytes and discs. (b) The alignment of stomatocytes and a discs in a magnetic field in case $\Delta\chi^P$ is negative (left) or positive (right). If $\Delta\chi^P$ is negative (positive), the individual polymers will tend to align perpendicularly (parallel) to the magnetic field and therefore the stomatocytes and discs will align with their symmetry axis parallel (perpendicular) and perpendicular (parallel) to the magnetic field respectively. (c) Legend to (a) and (b).*

and $E(\theta)$ given by:

$$E(\theta) = -\frac{SP \cdot A \cdot t \cdot \rho^{\text{PS}}}{2\mu_0 \cdot M^{\text{PS}}} \Delta\chi^{\text{PS}} \cdot B^2 \cdot \cos^2(\theta). \tag{6.4}$$

Constants that are needed to perform the fit are $SP \cdot A$, $t$, the density of the polystyrene, $\rho^{\text{PS}}$, and the mass of a repeating unit of polystyrene, $M^{\text{PS}}$. The values of $SP \cdot A$ and $t$ have already been determined in the previous subsection. The density of polystyrene is known from literature to be 1055 kg/m$^3$ [34] and the mass of a single repeating unit of polystyrene was calculated to be 104.15 Da or $1.73 \cdot 10^{-25}$ kg. Since the samples are polydisperse, the MB curves were fitted with a Gaussian spread in $SP \cdot A$, as was obtained from the parametrization of the vesicles in the previous subsection. The only parameter to be fitted to the MB data was $\Delta\chi^{\text{PS}}$ Each MB curve was fitted twice: once with a positive $\Delta\chi^{\text{PS}}$ and once with a negative $\Delta\chi^{\text{PS}}$. The fittings are shown in Figure 6.3 and the corresponding values of $\Delta\chi^{\text{PS}}$ obtained are listed in Table 6.1. Figure 6.3 clearly shows that the quality of the fits is best when using a negative $\Delta\chi^{\text{PS}}$. This is especially true for the MB fit of the discs. Also, when fitting a negative $\Delta\chi^{\text{PS}}$, one obtains values of $\Delta\chi^{\text{PS}}$ which are identical for both the discs and the stomatocytes. This is a necessity since both vesicles are made out of identical polymers which are both in the same glassy state. Fittings with a positive $\Delta\chi^{\text{PS}}$ clearly leads to significantly different values which is not realistic. Therefore, we can conclude that $\Delta\chi^{\text{PS}}$ is negative and has an error weighted average of $(-2.6 \pm 0.4) \cdot 10^{-12}$ m$^3$/mol.

| Sign of $\Delta\chi^{\text{PS}}$ | Fitted $\Delta\chi^{\text{PS}}$ for stomatocytes ($\cdot 10^{-12}$ m$^3$/mol) | Fitted $\Delta\chi^{\text{PS}}$ for discs ($\cdot 10^{-12}$ m$^3$/mol) |
|---|---|---|
| Negative | $-2.5 \pm 0.3$ | $-2.6 \pm 0.4$ |
| Positive | $0.52 \pm 0.06$ | $3.9 \pm 0.5$ |

**Table 6.1:** *Results from the fittings of the MB curves of the disc and stomatocyte samples when forcing a negative or a positive value of $\Delta\chi^{\text{PS}}$. The obtained values of $\Delta\chi^{\text{PS}}$ are only identical when the value is negative.*

## 6.4 Discussion

In chapter 3, we calculated the theoretical value of $\Delta\chi^{\text{PS}}$ as function of the fraction of maximal extension of the PS polymer in the membrane, assuming the phenyls are free to rotate around the bonds connecting them to the PS
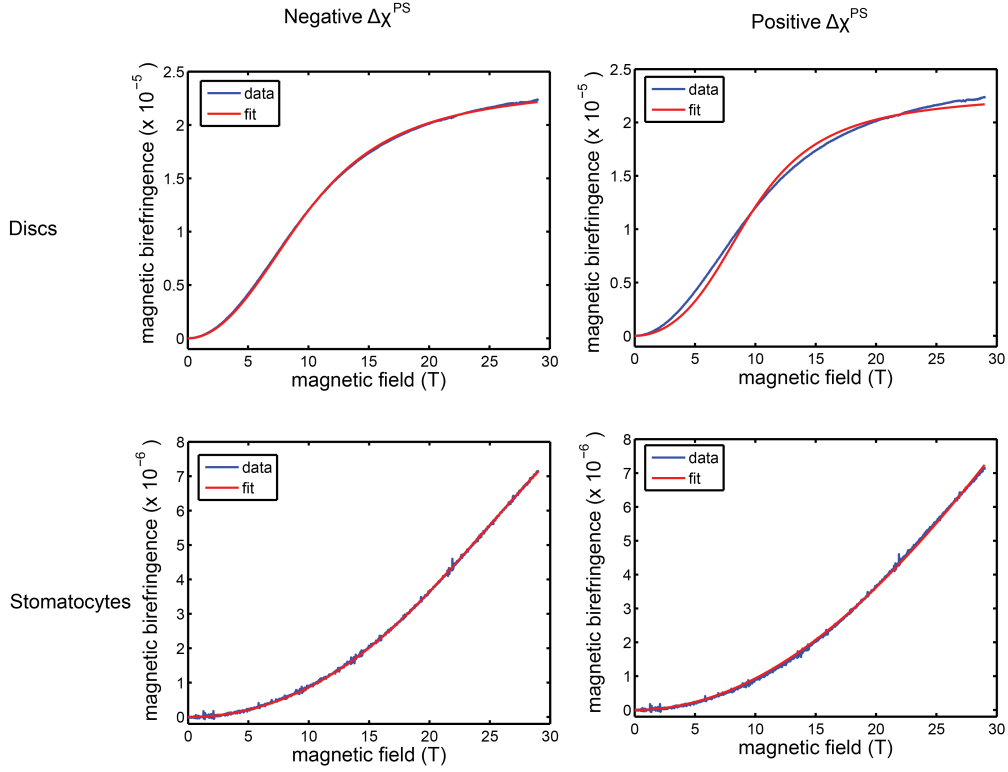
**Figure 6.3:** *Fittings of the MB curves for the stomatocytes (bottom) and the discs (top). Both curves have been fitted twice: once with a negative $\Delta\chi^{PS}$ (left) and once with a positive $\Delta\chi^{PS}$ (right). The values of $\Delta\chi^{PS}$ obtained are listed in Table 6.1. The quality of the fits is optimal when using a negative $\Delta\chi^{PS}$.*

backbone. The value we determined experimentally corresponds to an average extension of 72% as can be seen in Figure 6.4.

Two major observations can be made when comparing the experimentally found value with the results obtained from the theoretical calculations. First of all, an increase in the extension of the polymers would significantly enhance $\Delta\chi^{PS}$. When fully extended, the magnetic anisotropy increases by a factor of 75. Secondly, if the polymers would contract even a little bit, the magnetic anisotropy would flip sign since the experimentally determined magnetic anisotropy is very close to zero. These results strongly suggest that the magnetic response of polymersomes can be tuned by controlling the ordering of the polymers in the polymersome membrane. By creating polymersomes consisting of
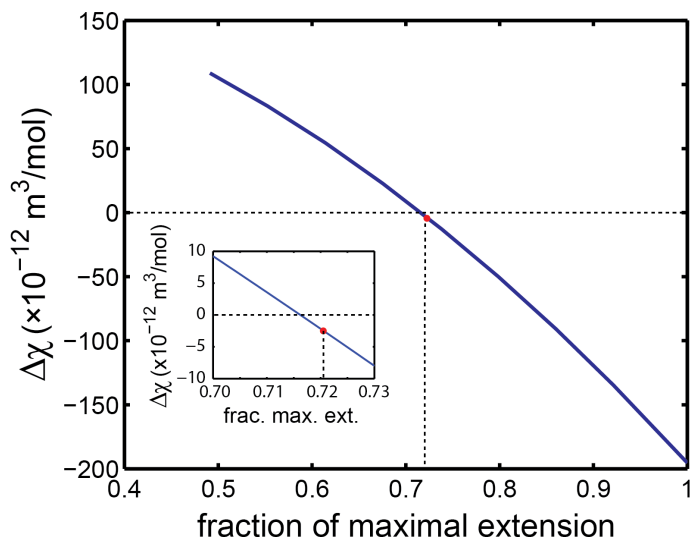
**Figure 6.4:** *Theoretical value of $\Delta\chi^{PS}$ as function of the extension of the polystyrene in the membrane. The experimentally determined value of $\Delta\chi^{PS}$ is indicated with a red dot. The inset is a magnification of the region around the red dot. The experimentally determined value is only a fraction of what can be obtained when fully stretching the polystyrene chains within the polymersome membrane.*

strongly extended polymers one would greatly lower the required magnetic field to align them. For instance, when the polymers are fully extended, fields of less than 1 T would already be sufficient to fully align a disc-shaped polymersome. This would make applications more realistic since these kinds of fields can easily be generated with permanent magnets. Also, contraction of the polymers could lead to a change in sign of $\Delta\chi^{PS}$, which would give control over the direction of alignment (parallel or perpendicular to the applied magnetic field).

When comparing the diamagnetic anisotropy of polystyrene within PEG-PS polymersomes with that of polystyrene found in lamellar mesophases assembled from poly(styrene-b-4-vinyl pyridine), it is striking how similar the values are. The value of $\Delta\chi^{PS}$ found in the lamellar mesophase was $-1.6 \cdot 10^{-8}$ in dimensionless SI units [11]. The value of PS found in this research is $(-2.6 \pm 0.5) \cdot 10^{-8}$ when expressed in the same dimensionless SI units. First of all, both experimentally values of $\Delta\chi^{PS}$ have the same sign, showing that both assemblies align in such a way that most of the polystyrene chains are aligned with their backbones perpendicular to the applied magnetic field. Furthermore, the ab-

solute values themselves also do not differ much, indicating that the structure and degree of coiling of PS is rather similar in both self-assembled structures.

## 6.5 Conclusions

We demonstrated that it is possible to determine the average magnetic anisotropy of a single repeating unit of polystyrene by measuring the MB of two differently shaped polymersomes, which are self-assembled from the same batch of PEG-PS block copolymers. Necessary information for the MB fittings are the shape factor, surface area and membrane thickness, which can all be determined by cryo-EM and parametrization of the obtained cross sections. For vesicles self-assembled from $PEG_{44}$-$PS_{178}$ polymers we determined that the magnetic anisotropy of a single repeating unit of polystyrene is $(-2.6 \pm 0.4) \cdot 10^{-12}$ m$^3$/mol, which is far from the maximum that can be obtained by fully stretching the polymers within the membrane. Comparisons with the theoretical calculation also showed that the sign of $\Delta\chi^{PS}$ can be flipped by even a small contraction of the polymers. Further research on how to control the extensiveness of the block copolymers in a membrane could therefore lead to new methods that allow one to control the strength and/or direction of the magnetic response.

## 6.6 Appendix

### 6.6.1 Parametrization of different shapes obtained from cryo-EM images

All encountered shapes were fitted using the parametrization as given by equations 3.3 to 3.5 (chapter 3). The fittings are shown in Figure 6.5 and the obtained fitting parameters are listed in Table 6.2.
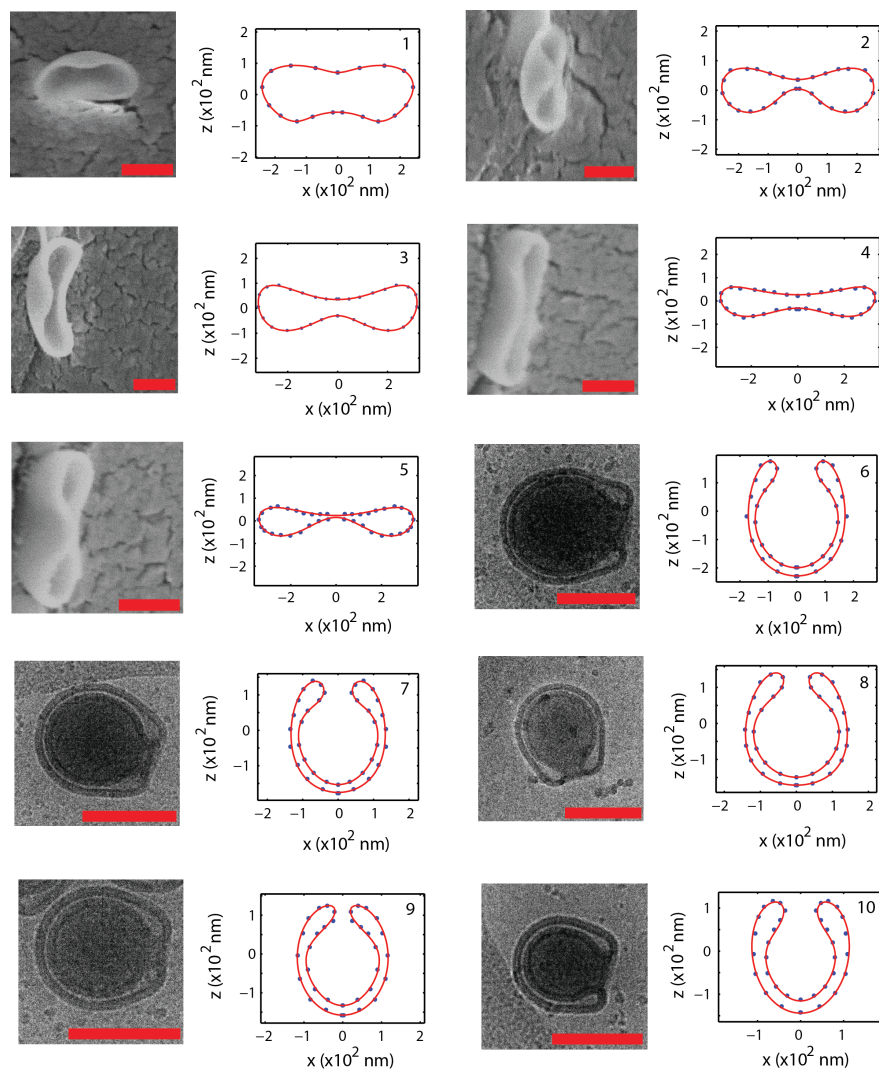
**Figure 6.5:** *Fittings of the discs and stomatocytes from chapter 6. All scale bars are 250 nm. The obtained fitting parameters are listed in Table 6.2.*

| fit # | $a_1$ ($\cdot10^{-7}$) | $a_2$ ($\cdot10^{-7}$) | $a_3$ ($\cdot10^{-7}$) | $a_4$ ($\cdot10^{-7}$) | $a_5$ ($\cdot10^{-7}$) | $b_1$ ($\cdot10^{-7}$) | $b_2$ ($\cdot10^{-7}$) | $b_3$ ($\cdot10^{-7}$) | $b_4$ ($\cdot10^{-7}$) | $b_5$ ($\cdot10^{-7}$) | $SP \cdot A$ ($\cdot10^{-13}\mathrm{m}^2$) |
|---|---|---|---|---|---|---|---|---|---|---|---|
| 1 | 2.1385 | 0.1676 | -0.1728 | -0.1591 | 0 | 0.9436 | 0.1059 | -0.3093 | -0.0370 | 0 | 2.13 |
| 2 | 2.1213 | 0.5918 | -0.1452 | -0.1222 | 0 | 0.4845 | 0.3580 | -0.3229 | -0.1589 | 0 | 2.55 |
| 3 | 3.0176 | 0.3561 | -0.1184 | 0.0298 | 0 | 0.7837 | 0.0497 | -0.4598 | -0.0241 | 0 | 4.00 |
| 4 | 3.2319 | 0.1119 | -0.0888 | 0.0470 | 0 | 0.5795 | -0.0724 | -0.2907 | 0.0491 | 0 | 5.37 |
| 5 | 3.1649 | 0.5080 | -0.0941 | -0.0228 | 0 | 0.4011 | 0.2411 | -0.3582 | -0.0488 | 0 | 5.49 |
| 6 | 1.4515 | -0.1631 | 0.7525 | 0.0776 | 0.0478 | 0.0997 | -1.8945 | 0.1776 | -0.2429 | -0.1324 | -1.20 |
| 7 | 1.0529 | -0.1408 | 0.6231 | 0.0700 | 0.0078 | 0.1055 | -1.4522 | 0.1443 | -0.1906 | -0.1388 | -0.568 |
| 8 | 1.0675 | -0.1715 | 0.6920 | 0.0914 | 0.0345 | 0.1371 | -1.4682 | 0.1001 | -0.1342 | -0.1271 | -0.412 |
| 9 | 0.8132 | -0.0521 | 0.5862 | -0.1376 | -0.0067 | -0.1873 | -1.2300 | 0.3174 | -0.2222 | -0.0065 | -0.371 |
| 10 | 0.8653 | -0.1414 | 0.4641 | -0.0751 | -0.0099 | -0.1482 | -1.1066 | 0.3026 | -0.1917 | -0.0122 | -0.425 |

**Table 6.2:** *Fitting parameters of the fits shown in Figure 6.5.*

# References

[1] R.S.M. Rikken, R.J.M. Nolte, J.C. Maan, J.C.M. van Hest, D.A. Wilson and P.C.M. Christianen, *Soft Matter*, **10**, 1295 (2014)

[2] M.V. Berry and A.K. Geim, *Eur. J. Phys.*, **18**, 307 (1997)

[3] E. Beaugnon and R. Tournier, *Nature*, **349**, 470 (1991)

[4] M.D. Simon and A.K. Geim, *J. Appl. Phys.*, **87**, 6200 (2000)

[5] G. Maret and K. Dransfeld, *Top. Appl. Phys.*, **57**, 143 (1985)

[6] M.A. Lasheen, *Acta Cryst.*, **24**, 289 (1968)

[7] D.L. Worcester, *Proc. Natl. Acad. Sci.*, 75, 5475 (1978)

[8] L. Pauling, *Proc. Natl. Acad. Sci.*, 76, 2293 (1979)

[9] R.R. Gupta, *Diamagnetische Suszeptibilität*, Springer, Berlin (1986)

[10] K. Lonsdale and K.S. Krishnan, *Proc. R. Soc. A*, **156**, 597 (1936)

[11] Y. Rokhlenko, M. Gopinadhan, C.O. Osuji, K. Zhang, C.S. O'Hern, S.R. Larson, P. Gopalan, P.W. Majewski and K.G. Yager, *Phys. Rev. Lett.*, **115**, 258302 (2015)

[12] G.B. Tul'chinskaya and N.V. Fedorchenko, *Sov. Phys. J*, **20**, 1192 (1977)

[13] C, Uyeda, A. Tsuchiyama, T. Yamanaka and M. Date, *Phys. Chem. Minerals.*, **20**, 83 (1993)

[14] C. Uyeda, T. Takeuchi, A. Yamagishi, A. Tsuchiyama, T. Yamanaka and M. Date, *Phys. Chem. Minerals*, **20**, 369 (1993)

[15] C. Uyeda, K. Hisayoshi and S. Kanou, *J. Phys. Soc. Jap.*, **79**, 064709 (2010)

[16] C. Uyeda, K. Tanaka, R. Takashima, *Jpn. J. Appl. Phys.*, **42**, L1226 (2003)

[17] C. Uyeda, M. Mamiya, R. Takashima, T. Abe, H. Nagai and T. Okutani, *Jpn. J. Appl. Phys.*, **45**, L124 (2006)

[18] K. Takahashi, C. Umeki, I. Mogi, K. Koyama, S. Awaji, M. Motokawa and K. Watanabe, *Physica B*, **346-347**, 277 (2004)

[19] H. Ezure, T. Kimura, S. Ogawa and E. Ito, *Macromol.*, **30**, 3600 (1997)

[20] M.J. McGlinchey and K. Nikitin, *J. Orgmet. Chem.*, **751**, 809 (2014)

[21] J.H. Goldstein and G.S. Reddy, *J. Chem. Phys.*, **36**, 2644 (1962)

[22] I.O. Shklyarevskiy, P.C.M. Christianen, E. Aret, H. Meekesm E. Vlieg, G. Deroover, P. Callant, L. van Meervelt and J.C. Maan, *J. Phys. Chem. B*, **108**, 16386 (2004)

[23] J. Torbet and M.J. Dickens, *FEBS*, **173**, 403 (1984)

[24] J. Torbet and M.-C. Ronziere, *Biochem. J.*, **219**, 1057 (1984)

[25] J. Torbet, *TIBS*, **12**, 327 (1987)

[26] C. Martin, H. Kramer, C. Johner, B. Weyerich, J. Biegel, R. Deike, M. Hagenbüchle and R. Weber, *Macromol.*, **28**, 3175 (1995)

[27] W. Bras, G.P. Diakun, J.F. Díaz, G. Maret, H. Kramer, J. Bordas and F.J. Medrano, *Biophys. J.*, **74**, 1509 (1998)

[28] G. Weill and G. Maret, *Polymer*, **23**, 1990 (1982)

[29] T. Kimura, M. Yamato, W. Koshimizu, M. Koike and T. Kawai, *Langmuir*, **16**, 858 (2000)

[30] J.C. Gielen, I.O. Schklyarevskiy, A.P.H.J. Schenning, P.C.M. Christianen and J.C. Maan, *Sci. Technol. Adv. Mater.*, **10**, 014601 (2009)

[31] B. Frka-Petesic, J. Sugiyama, S. Kimura, H. Chanzy and G. Maret, *Macromol.*, **48**, 8844 (2015)

[32] R.S.M. Rikken, H.H.M. Kerkenaar, R.J.M. Nolte, J.C. Maan, J.C.M. van Hest, P.C.M. Christianen and D.A. Wilson, *Chem. Commun.*, **50**, 5394 (2014)

[33] L.K.E.A. Abdelmohsen, M. Nijemeisland, G.M. Pawar, G.-J. Janssen, R.J.M. Nolte, J.C.M. van Hest and D.A. Wilson, *ACS Nano*, **10**, 2652 (2016)

[34] H. Kahler and B.J. Lloyd Jr., *Science*, **114**, 34 (1951)

## Chapter 7

# Changing polymersome shapes by pipetting: rod formation and the subsequent relaxation to spheres.

### Abstract

*Using magnetic birefringence and transmission electron microscopy, we demonstrate that rod-shaped polymersomes are formed by pipetting a flexible spherical polymersome sample with a glass Pasteur pipette. Subsequently, these rods were observed to equilibrate back to spheres. The recovery time was found to depend on polymer length, with the fastest recovery rates being measured for the longest polymers. Not only does this study provide a new means to create rod-shaped polymersomes, it also proves that sample handling can be a very delicate process.*

## 7.1   Introduction

Over the last 20 years, a variety of different methods to induce shape changes in polymersomes have been reported. Many of these methods rely on an osmotic shock to induce a deflation [1–5], and has led to the formation of stomatocytes, rod-shaped polymersomes, nested vesicles and discs. Other methods, that have led to the formation of tubular polymersomes, include thermal quenches [6], the addition of a cross-linking chemical that covalently connects adjacent polymers together [7] or the incorporation of biological membrane components [8]. Techniques to create more exotic structures, such as bicontinuous vesicles [9] or onion-like vesicles [10] have been reported as well. However, to the best of our knowledge, there has been no mention of shape changes induced by forces such as shear force or increasing or decreasing air pressure.

Beside the above mentioned methods for introducing shape changes in polymersomes, we have recently observed a shape change in spherical polymersomes after transferring a sample with a glass Pasteur pipette. Although such sample handling effects have already been observed before for biological systems such as erythrocytes [11–14], these effects have not been discussed with regard to polymersomes so far.

In polymersome research, samples often have to be transferred from one container to the other, for instance when loading a cuvette or small container for analysis [15, 16]. Therefore it is of great importance to know the influence of a transferring process has on the morphology of polymersomes. To further investigate the effect of different pipetting methods on the shape of flexible polymersomes, transmission electron microscopy (TEM) images were taken of the sample right before and after they were transferred from their original container to a quartz cuvette. For some methods, we observed a shape change from spherical to rod-shaped polymersomes. The tube shaped polymersomes were followed over time using magnetic birefringence measurements. The rod-shaped polymersomes were found to re-inflate to their original spherical morphology. Since this re-inflation was measured in real-time by MB, its rate constant could be determined by fitting the MB curves with a single-exponential function. The experiments were repeated for polymersomes assembled from three PEG-PS polymers, each having a different PS-block length. The results clearly show that the polymersomes with the longest PS block re-inflate the fastest.

## 7.2 Experimental details

### 7.2.1 Instrumentation

Glass Pasteur pipettes were purchased from Brand GmbH + Co., 150 mm length, Cat. No.:747715, inner diameter at the tip: 1 mm. Plastic Pasteur pipettes were purchased from Kartell S.p.a., 3 mL, Cat. No.: 88337, inner diameter at the tip: 2.2 mm. Syringes were obtained from Henke-Sass, Wolf GmbH, 1 mL NORM-JECT, Luer, Cat. No.: 4010.200V0. The needles used were obtained from B. Braun, Sterican 0.80x50 mm BL/LB, 21Gx2", Cat. No.: 4665503, inner diameter at the tip: 0.5 mm.

Magnetic birefringence was measured using a standard polarization modulation method as was already explained in chapter 4. The temperature of the sample was kept constant at 21 °C. Transmission electron microscopy (TEM) was performed on a JEOL 1010 TEM. Dynamic light scattering (DLS) was performed on a Malvern Zetasizer Nano S.

### 7.2.2 Sample preparation

The following three batches of $PEG_n$-$PS_m$ block copolymers were synthesized by atom-transfer radical polymerization (ATRP) starting from PEG-macro initiators as described previously [2,3]: $PEG_{44}$-$PS_{139}$ (MW = 16.5 kDa), $PEG_{44}$-$PS_{178}$ (MW = 20.5 kDa) and $PEG_{44}$-$PS_{200}$ (MW = 23 kDa). All polymersome samples were made by dissolving 10 mg of $PEG_n$-$PS_m$ in 2 ml of organic solvent mixture, consisting of THF and dioxane in a 3:2 ratio. The solution was left to stand for half an hour while stirring at 750 rpm. Afterwards, 2 mL of water was added at a rate of 1 mL/h, using a syringe pump, while still stirring at 750 rpm. This initiated the self-assembly and brought the total sample volume

| sample | hydrodynamic radius (nm) | $PDI$ |
|---|---|---|
| 16.5 kDa batch 1 | 245 ± 71 | 0.082 |
| 16.5 kDa batch 2 | 215 ± 80 | 0.137 |
| 20.5 kDa batch 1 | 221 ± 44 | 0.088 |
| 20.5 kDa batch 2 | 203 ± 64 | 0.098 |
| 23 kDa batch 1 | 189 ± 36 | 0.036 |

**Table 7.1:** *Hydrodynamic radius and PDI of all samples used, measured immediately after self-assembly by DLS. All samples are in 50% water, 30% THF and 20% dioxane.*

a



b
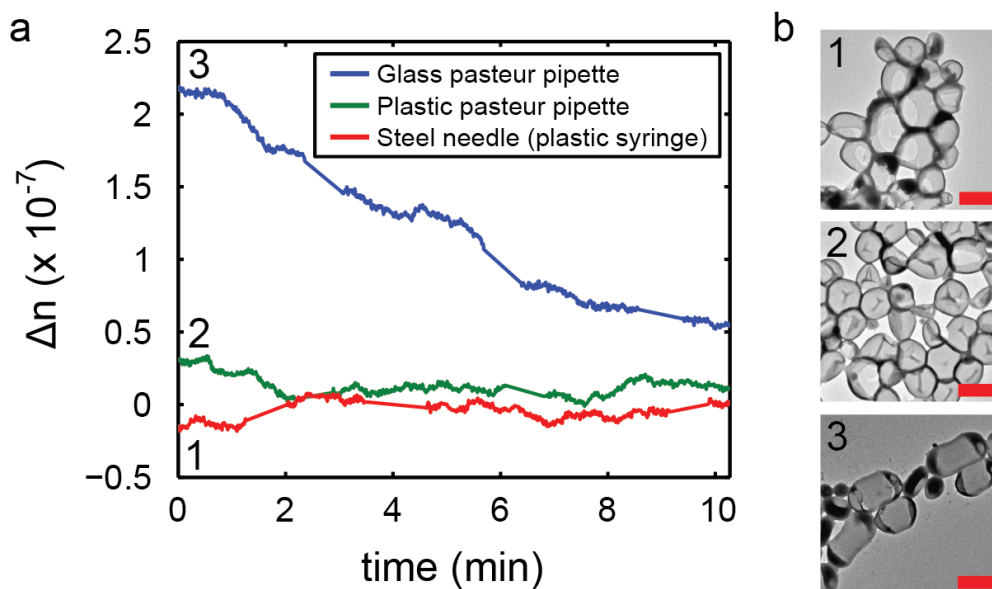
**Figure 7.1:** *(a) MB measurements on a 20.5k polymersome sample right after transferring the sample into a cuvette using different tools. Using a glass Pasteur pipette (3), the birefringence starts off at a significant non-zero birefringence (which decayed to zero over time). A plastic pipette (2) and a syringe (1) lead to a negligible MB (b) TEM images of the sample quenched immediately after pipetting the sample in the cuvette (corresponding to t=0 in (a)). Using a plastic Pasteur pipette or a syringe with steel needle leads to spheres, which is in agreement with a non-zero MB. A glass Pasteur pipette results in a large fraction of rods, which is in agreement with a non-zero MB. The MB decreases over time, which indicates that the shape becomes less anisotropic (see also Figure 7.3). All scale bars are 500 nm.*

to 4 mL. Afterwards, the samples were divided over 8 HPLC vials, filling each with 450 $\mu$L of sample. These vials were left to stand for 3 to 5 days, to let the samples equilibrate, before using them in the experiments. The hydrodynamic radii of these samples, as measured by DLS, are given in Table 7.1.

## 7.3 Measurements

### 7.3.1   Effect of transferring methods on shape

To test which methods can induce a shape change, we used a 20.5k polymersome batch and transferred it from its container directly into a quartz cuvette using either a glass Pasteur pipette, a plastic Pasteur pipette and a syringe with steel needle. Right after transferring the sample, an aliquot of the sample was quenched by injecting it in an excess of water using a micro-pipette with a plastic tip. The cuvette was then closed and placed in the 2 T magnet to measure the MB over time. The quenched samples were imaged with TEM. The results are shown in Figure 7.1.

A non-zero MB was measured only when the sample was transferred using a glass Pasteur pipette. The signal however was observed to decay over time as can be seen in Figure 7.1a, blue curve. The samples that were transferred with a plastic Pasteur pipette or a syringe with steel needle did not show a significant MB. The corresponding TEM images correspond very well with the MB data. The sample that was transferred with the plastic Pasteur pipette and the plastic syringe with steel needle showed spherical polymersomes which indeed should not give any signal in the MB. The sample that was transferred with a glass Pasteur pipette showed many prolate structures (rods) which indeed can be aligned in a magnetic field, as was already shown in chapter 4, leading to a non-zero MB. The fact that the MB decreases over time suggests that the rods are not stable and transform into a less anisotropic shape. Therefore, we quenched the sample right before and after pipetting it into the cuvette using the glass Pasteur pipette. A third quench was performed when the MB had decayed to zero. These three samples were imaged by TEM and the results are shown in Figure 7.2. As can be seen, the shapes are initially spherical, but after pipetting the sample into the cuvette, rod-shaped polymersomes are observed. After several minutes, when the MB has decayed to zero, all polymersomes had recovered their spherical morphology.

These measurements suggest that somewhere during the pipetting, the polymersomes change their shapes from spheres to rods. To investigate the effect of the pipetting further, we repeated the MB measurement with the glass Pasteur pipette but varied the number of times the sample was pipetted, from 1 time to 10 times (Figure 7.3) [1]. The results obtained by MB clearly show that both the relaxation time and the initial birefringence increase when the sample is pipetted up and down more often. The TEM images show that both the number of rods and their aspect ratio increase with amount of times the sample is pipetted up and down.

---

[1]A single pipetting activity involves both the uptake and the release of a sample.

a



b
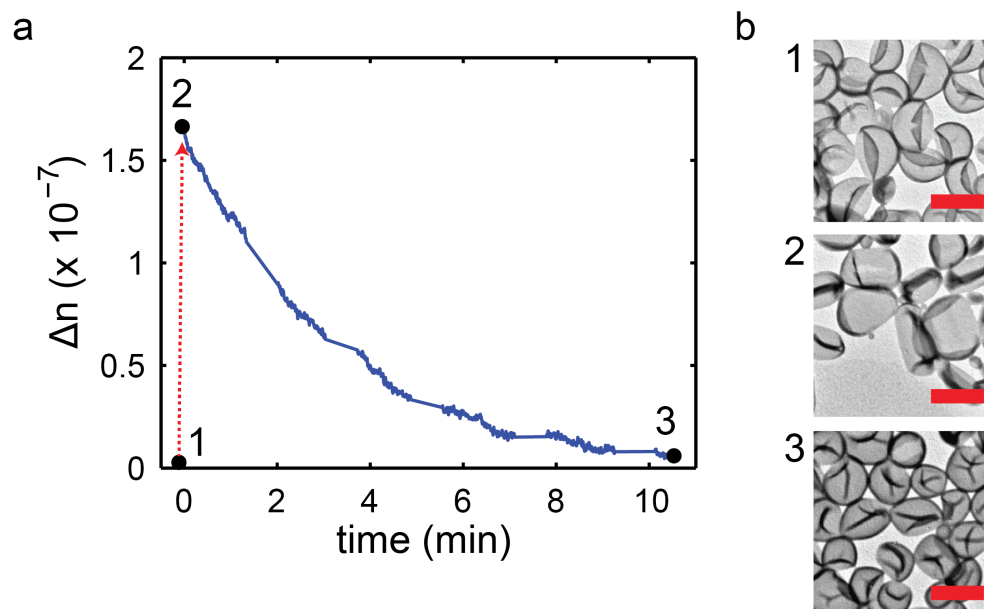


**Figure 7.2:** *(a) MB measurements on a 20.5k polymersome sample. The red dashed arrow represents the transfer of the sample into the cuvette by the glass Pasteur pipette, after which the MB was measured. (b) Corresponding TEM images of the sample quenched at different points in time as indicated in the MB curve. The first TEM image shows the sample before it is transferred into the cuvette (therefore not indicated in Figure (a)). The polymersomes all look spherical. The second image shows the sample right after pipetting it into the cuvette. Most polymersomes have adopted a rod-like morphology. The last TEM image is taken when the MB was back at zero. The image shows spherical polymersomes again, indicating that the rod-shaped polymersomes re-inflate over time to obtain their original spherical morphology. All scale bars are 500 nm.*

### 7.3.2 Effect of polymer length

The effect of polymer length on the observed shape transformation induced by pipetting was investigated by repeating the experiments with polymersomes assembled from block copolymers of three different lengths (16.5 kDa, 20.5 kDa and 23 kDa, from here-on named 16.5k, 20.5k and 23k). All samples were pipetted only one time to transfer the sample from the HPLC vial to the cuvette. Care was taken to keep the procedure as constant as possible in order to make all measurements comparable.

a



b



c
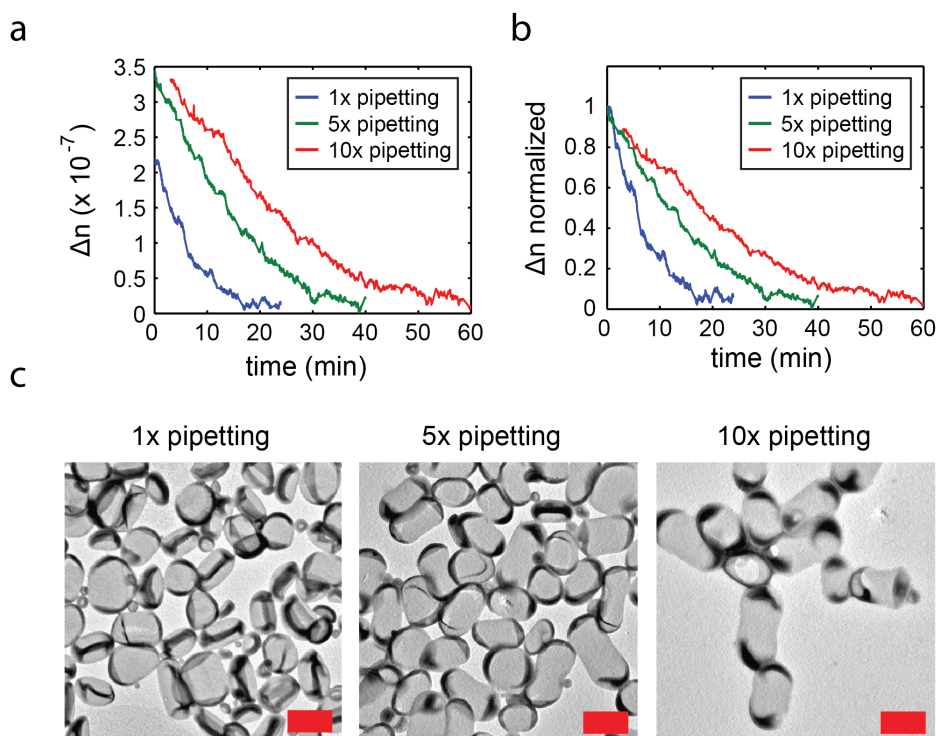


**Figure 7.3:** *MB measurements on a 20.5k polymersome sample after transferring the sample into a cuvette 1, 5 or 10 times using a glass Pasteur pipette. (a) the measured MB traces. The measurement performed after 10 times pipetting was started 3 minutes later than the other two, which explains why the first 3 minutes are missing. (b) Normalized MB traces. The MB value and the relaxation time clearly increase with the number of times the sample has been pipetted. (c) TEM images of the sample right after pipetting it 1, 5 or 10 times. After pipetting the sample 1 time, about half of the polymersomes are observed to have adapted a rod-like morphology. After 5 times pipetting almost all of the polymersomes have adapted a rod-like morphology. The aspect ratio of the rods also seems to increase with the number of times it has been pipetted with the largest being observed after 10 times pipetting. Both observations are in agreement with the observed increase in MB. All scale bars are 500 nm.*

The 23k sample could not be measured at 2 T since the signal to noise ratio was too low to obtain a clear signal. Also, TEM did not show a very clear effect of the pipetting, showing mostly spherical polymersomes. The 16.5k and 20.5k

**Figure 7.4:** *MB curves measured at 2 T of 16.5k and 20.5k samples after pipetting them into a cuvette 1 time. (a) Actual measured MB curves. The 16.5k sample has a larger initial MB but also decays slower than the 20.5k sample. The difference in decay times become extra apparent when normalizing all curves to 1 at t=0 (b). (c,d) The natural logarithm of the MB seems to depend linearly on time, meaning that the MB itself decays exponentially.*

samples gave clear signals at 2 T (Figure 7.2, Appendix, section 7.6, Figure 7.7). For both of these polymer lengths, two different batches of polymersomes were prepared which were all measured at 2 T several times. The results are shown in Figure 7.4.

All curves of the 16.5k sample begin at higher values than those of the 20.5k samples. Also the decay time of the 16.5k sample seemed to be larger than that of the 20.5k sample. The effect on the decay time became more clearly visible when normalizing the MB curves (Figure 7.4b). The relative changes between individual measurements of similar samples were clearly much smaller than the differences between measurements of different samples. To check if the data can be expressed as a single exponential, we also plotted the natural logarithm
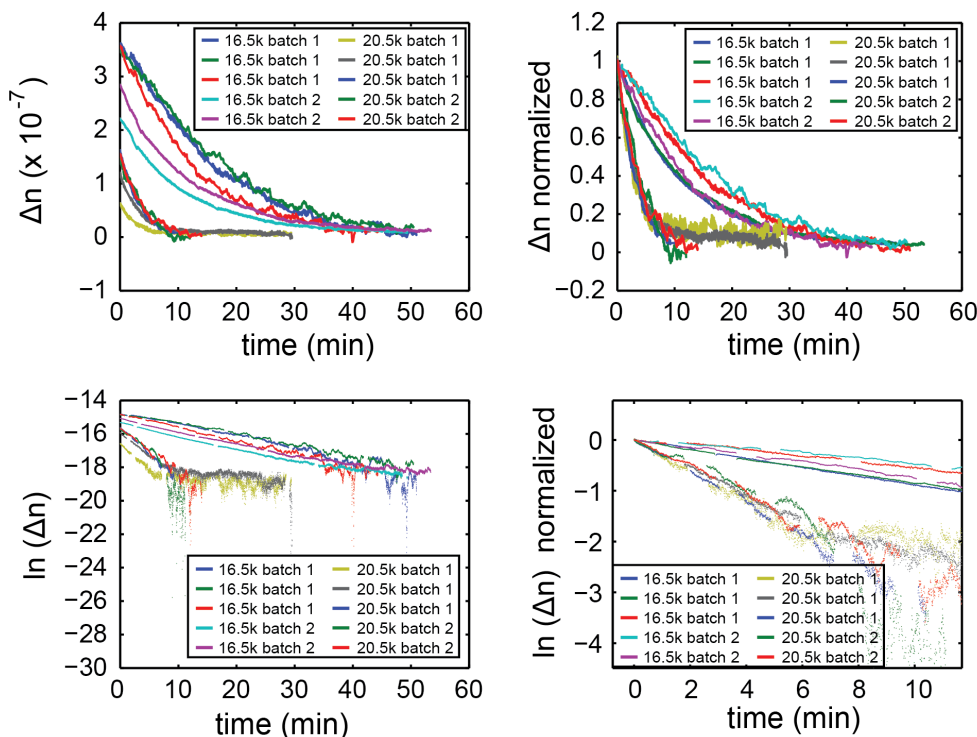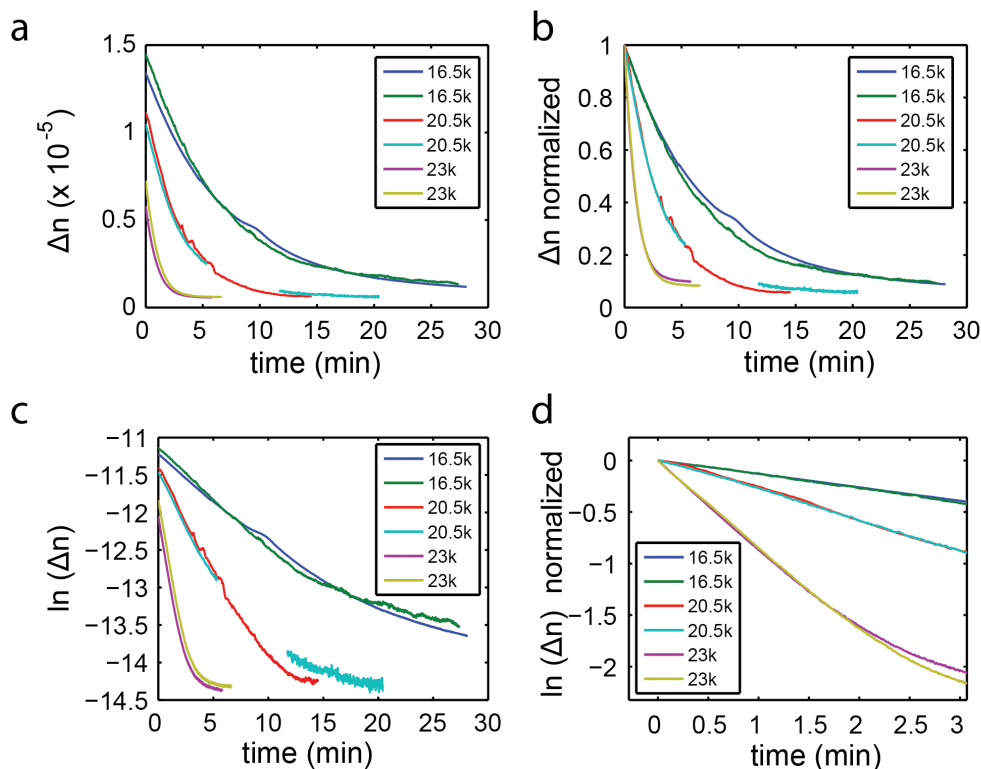
**Figure 7.5:** *MB curves measured at 20 T of 16.5k, 20.5k and 23k samples after pipetting them into a cuvette 1 time. (a) Actual measured MB curves. Both the initial MB and the decay time increase with decreasing polymer length. The difference in decay times become apparent when normalizing all curves to 1 at t=0 (b). (c,d) Initially, the natural logarithm of the MB depends linearly on time, but the very last part of the curve shows a clear deviation from this linear behavior. The gap in one of the two measurements performed on the 20.5k sample was caused by an overload in the Lock-in.*

of the MB as function of time (Figure 7.4c,d). The relation is linear, up to at least the first half of the measured MB curves.

The 16.5k, 20.5k and 23k samples were also measured at 20 T. The results are shown in Figure 7.5. The signal to noise is much larger at 20 T, which is due to a larger degree of alignment. The 23k was observed to give a clear signal as well, in contrast with the measurements performed at 2 T where the 23k could not be measured. The data clearly shows that both the size of the MB and the relaxation time increase with decreasing PS length. When plotting the

natural logarithm against time (Figure 7.5c,d), we again see an initial linear dependence, as was the case for the measurements performed at 2 T.

### 7.3.3 Fittings of the MB curves

To compare the differences between the three different samples in a more quantitative manner, the MB curves were fitted with a single exponential:

$$\Delta n\left(t\right) = A\exp\left(-t/\tau\right), \tag{7.1}$$

or:

$$\ln\left(\Delta n\left(t\right)\right) = A - t/\tau, \tag{7.2}$$

with $A$ the offset in the MB at $t = 0$ and $\tau$ the decay constant of the MB signal. For the 16.5k samples, only the first 25 minutes were taken into account. For the 20.5k sample this range was limited to the first 6 minutes. For the 23k sample only the first 1.5 minutes were taken into account. The fits themselves are shown in the Appendix, section Figures 7.8 and 7.9. The results of the fits are shown in Table 7.2 and Figure 7.6. The measurements of the 16.5k sample performed at 20 T could not be fitted over the same time interval as the ones measured at 2 T (see Figure 7.9a,b), indicating that the alignment at 20 T becomes significantly different (out of the quadratic regime). This was not the case for the 20.5k sample. Most probably this is due to the fact that the 16.5k samples showed the largest aspect ratio's and therefore have the largest magnetic anisotropy, leading to a saturation in the alignment at relative lower fields than is the case for the 20.5k and the 23k samples. For the 16.5k samples, the average decay time and its spread was therefore calculated using the 2 T measurements only, leading to an average value of $\tau$ of (14.2 $\pm$ 2.1) minutes. For the 20.5k samples, all measurements were taken into account since no deviations at 20 T in the alignment behavior were observed. The average value of $\tau$ was determined to be (3.6 $\pm$ 0.5) minutes. For the 23k, only the 20 T measurements were used since no values could be obtained at 2 T, as was explained before. For this sample, an average value for $\tau$ of (1.182 $\pm$ 0.010) minutes was obtained. These values all differ significantly and show that polymer length clearly influences the decay rate of the MB.

## 7.4 Discussion

The observation that shape changes in polymersomes can be induced just by transferring the sample from one container to the other might be the beginning of a whole new approach in controlling polymersome morphologies. For now,

| Sample | measured at | Figure fit (Appendix) | $\tau$ (min) | average $\tau$ (min) |
|---|---|---|---|---|
| 16.5k, batch 1 | 2 T | 7.8a | 12.8 | |
| 16.5k, batch 1 | 2 T | 7.8b | 13.7 | |
| 16.5k, batch 1 | 2 T | 7.8c | 15.7 | $14.2 \pm 2.1$ |
| 16.5k, batch 2 | 2 T | 7.8d | 16.8 | |
| 16.5k, batch 2 | 2 T | 7.8e | 12.0 | |
| 20.5k, batch 1 | 2 T | 7.8f | 3.2 | |
| 20.5k, batch 1 | 2 T | 7.8g | 3.7 | |
| 20.5k, batch 1 | 2 T | 7.8h | 3.2 | |
| 20.5k, batch 2 | 2 T | 7.8i | 4.5 | $3.6 \pm 0.5$ |
| 20.5k, batch 2 | 2 T | 7.8j | 3.4 | |
| 20.5k, batch 2 | 20 T | 7.9c | 3.7 | |
| 20.5k, batch 2 | 20 T | 7.9d | 3.6 | |
| 23k, batch 1 | 20 T | 7.9e | 1.175 | |
| 23k, batch 1 | 20 T | 7.9f | 1.880 | $1.182 \pm 0.010$ |

**Table 7.2:** *Results obtained from fitting the MB curves for all three samples. The final average result with error are given in the last column.*
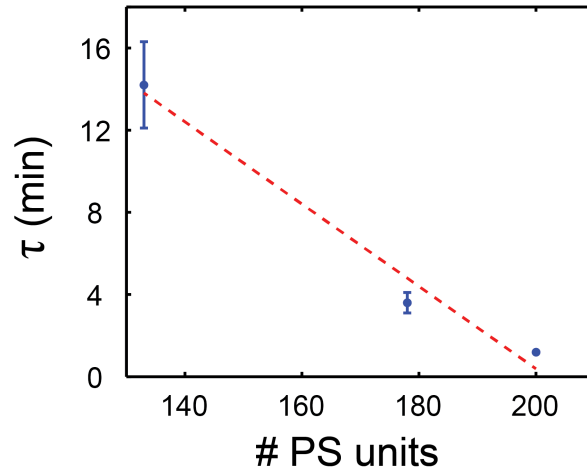


**Figure 7.6:** *Experimentally determined recovery times ($\tau$) as function of the PS length. The red dashed line represents a linear fit.*

the observed shape changes are limited to the formation of rods, but there might be combinations of solvent compositions and pipettes that could lead to other morphologies as well. Compared to dialysis and equilibration processes, this method has the advantage that it works very fast, usually within half a minute.

On the other hand, the results described in this chapter should also be considered as a warning. Often such effects are not expected and can then easily be missed or falsely assumed to be caused by any other effect. The data presented in this chapter clearly demonstrates that it is the pipetting itself which is causing the shape transformation from spheres into rods. It is striking that this shape transformation is only observed when using a glass Pasteur pipette. Until now, the reason for this is not clear. It is possible that the shape changes are caused by shear forces that arise during pipetting of the sample. The openings of the three tools also have different diameters, which could also influence the shear force when the sample is being taken in. It is very well possible that the material of the pipette is related. The glass Pasteur pipette is the only tool made out of glass, while the other two are of plastic and/or steel, which could also effect the shear force. The Pasteur pipette might also be the only tool which sucks up the solution the most violently, thereby creating a fast and strong pressure drop above the sample solution. This would then lead to a fast equilibration by evaporation of solvents, which in turn would lead to an osmotic pressure over the polymersome membrane. It is even possible that this leads the polymersomes membranes to burst or crack.

The polymersomes assembled from the largest polymers are affected the least when pipetting them with a glass Pasteur pipette (lowest MB, lowest aspect ratio). This is expected since longer polymers are expected to give the membrane a higher rigidity. The effect of polymer length on the relaxation time is unexpected however. The polymersomes assembled from the longest polymers recover the fastest after pipetting. This could be explained by the fact that the bending constant $\kappa$ is highest for the polymersomes made from the longest polymersomes. Therefore the absolute change in the bending energy between spheres and rods increases when the polymer length increases. The larger change in energy might therefore be linked to faster kinetics and thus a shorter relaxation time. It might also be the case that polymersome membranes made from longer polymers might show more small cracks and imperfections, allowing water to flow through more easily. Diffusion studies, for instance by NMR, are necessary to determine if the observed differences in relaxation time are really caused by differences in diffusion rates.

So far, these shape changes have only been observed for polymersomes prepared in 1:1 water: organic solvent ratio's, and only when transferring it with a

glass Pasteur pipette. In the research described in all previous chapters, these effects have not been observed since pipetting was either performed by plastic pipettes, or because samples were too rigid to be effected. The combination of electron microscopy and MB has proven to be a good set of tools to check for such effects.

## 7.5  Conclusions

Beside providing some interesting effects and a potential new method to make rods, the experiments in this chapter also pose a clear warning. It has become apparent that pipetting methods can change the morphology of polymersomes, depending on the solvent composition and the pipetting method. In this chapter we have shown that, using a glass Pasteur pipette, we can change the morphology of a polymersome sample from spheres to rods. The reason for this shape transformation is not yet clear, however, the effects are reproducible. Factors that need to be studied in more depth are the influence of the opening diameter of the glass pipettes and the speed at which the sample is being taken up by the pipette. The rod-shaped polymersomes were also observed to inflate back to their original spherical morphology. A clear dependence on polymer length was found, with the polymersomes assembled from the longest polymers being ones that inflate fastest. Diffusion studies over the membrane, by NMR for example, might provide new insights in the polymer length dependence on the inflation rate. For now, this study should be regarded as a critical overview of polymersome sample handling. We advise to always check for shape changes after transferring a polymersome sample from one container to another.

## 7.6 Appendix
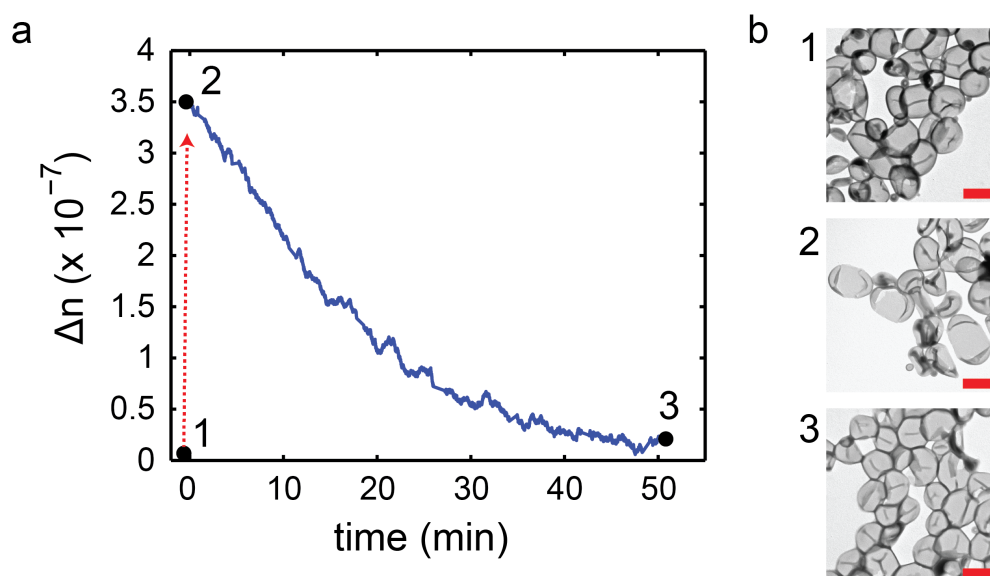


**Figure 7.7:** *(a) MB measurements on a 16.5k polymersome sample. The red dashed arrow represents the transfer of the sample into the cuvette by the glass Pasteur pipette, after which the MB was measured. (b) Corresponding TEM images of the sample quenched at different points in time as indicated in the MB curve. The first TEM image shows the sample before it is transferred into the cuvette (therefore not indicated in Figure (a)). The polymersomes all look spherical. The second image shows the sample right after pipetting it into the cuvette. Most polymersomes have adopted a rod-like morphology. The last TEM image is taken when the MB was back at zero. The image shows spherical polymersomes again, indicating that the rod-shaped polymersomes re-inflate over time to obtain their original spherical morphology. All scale bars are 500 nm.*

**Figure 7.8:** *Single-exponential fits (red line) performed on the MB curves (blue line) for the 16.5k and 20.5k samples which were measured at 2 T. For the 16.5k samples, only the first 25 minutes of the curves are fitted since data points measured later become to noisy. For the 20.5k samples the first 6 minutes were fitted for the very same reasons. The results of the fits are given in Table 7.2.*
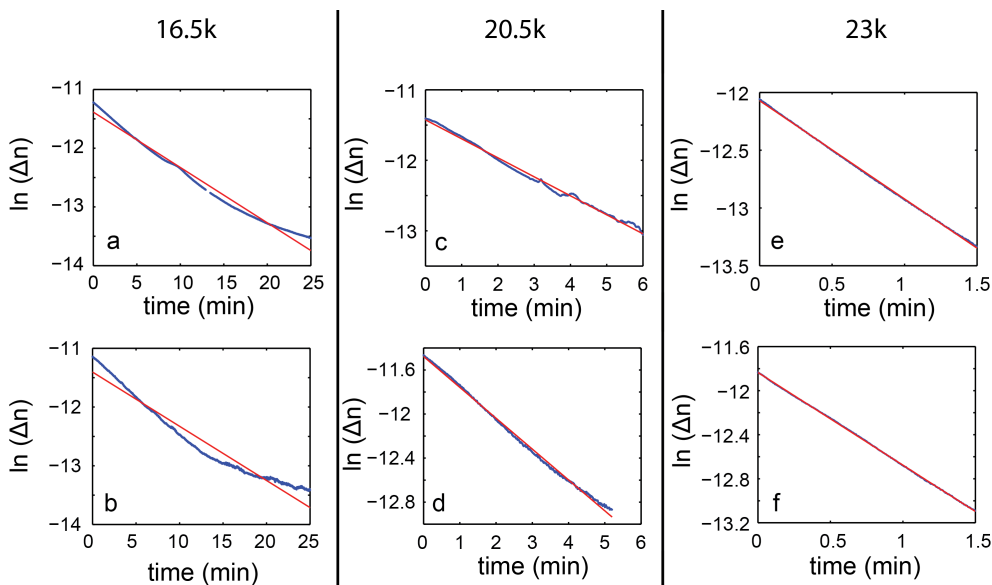
**Figure 7.9:** *Single-exponential fits (red line) performed on the MB curves (blue line) for the 16.5k, 20.5k and 23k samples which were measured at 20 T. For the 16.5k samples, the first 25 minutes of the curves are fitted since this was also done for the data obtained at 2 T. However, for the MB curves measured at 20 T we clearly see that the fits are not correct and that the decay is not single-exponential over this time interval. The results of the fittings of the 2 T and 20 T measurements can therefore not be compared. For the 20.5k samples the first 6 minutes were fitted as was the case for the 2 T measurements. For this sample, the decay is also mono-exponential at 20 T over the same time interval as the 2 T measurement. The 23k sample has been fitted over the first 1.5 minutes. No reference with 2 T measurements were possible since the signal to noise was too low too obtain a usable MB curve. However, based on the size of the MB, the aspect ratio of 23k rods will be even smaller than that of the 20.5k rods, and therefore the values obtained at 20 T would probably be similar to those at 2 T if they were measurable.*

# References

[1] B.M. Discher, Y.-Y. Won, D.S. Ege, J.C.-M. Lee, F.S. Bates, D.E. Discher, D.A. Hammer, *Science*, **284**, 1143 (1999)

[2] K.T. Kim, J. Zhu, S.A. Meeuwissen, J.J.L.M. Cornelissen, D.J. Pochan, R.J.M. Nolte and J.C.M. van Hest, *J. Am. Chem. Soc.*, **132**, 12522 (2010)

[3] S.A. Meeuwissen, K.T. Kim, Y. Chen, D.J. Pochanand and J.C.M. van Hest, *Angew. Chem. Int. Edit.*, **50**, 7070 (2011)

[4] R.S.M. Rikken, H.H.M. Kerkenaar, R.J.M. Nolte, J.C. Maan, J.C.M. van Hest, P.C.M. Christianen and D.A. Wilson, *Chem. Commun.*, **50**, 5394 (2014)

[5] R. Salva, J.-F. Le Meins, O. Sandre, A. Brûlet, M. Schmutz, P. Guenoun and S. Lecommandoux, *ACS Nano*, **7**, 9298 (2013)

[6] A.A. Reinecke and H.-G. Döbereiner, *Langmuir*, **19**, 605 (2003)

[7] M.C.M. van Oers, F.P.J.T. Rutjes and J.C.M. van Hest, *J. Am. Chem. Soc.*, **135**, 16308 (2013)

[8] J.D. Robertson, G. Yealland, M. Avila-Olias, L. Chierico, O. Bandmann, S.A. Renshaw and G. Battaglia, *ACS Nano*, **8**, 4650 (2014)

[9] B.E. McKenzie, J.F. de Visser, H. Friedrich, M.J.M. Wirix, P.H.H. Bomans, G. de With, S. J. Holder and N.A.J.M. Sommerdijk, *Macromol.*, **46**, 9845 (2013)

[10] S. Burke, H. Shen and A. Eisenberg, *Macromol. Symp.*, **175**, 273 (2001)

[11] A.W.L. Jay, *Biophys. J.*, **13**, 1166 (1973)

[12] G.M. Artmann, K.-L. Paul Sung, T. Horn, D. Whittemore, G. Norwich and S. Chien, *Biophys. J.*, **72**, 1434 (1997)

[13] P. Wong, *J. Theor. Biol.*, **233**, 127 (2005)

[14] L.E. Göran Eriksson, *Biochim. Biophys Acta*, **1036**, 193 (1990)

[15] M. Felice, M. Marzá-Pérez, N.S. Hatzakis, R.J.M. Nolte and M.C. Feiters, *Chem. Eur. J.*, **14**, 9914 (2009)

[16] I.M. Henderson and W.F. Paxton, *J. Polym. Sci. B Polym. Phys.*, **53**, 297 (2015)

# Chapter 8

# Towards dynamic light scattering in high magnetic fields

## Abstract

*In this chapter we describe the design and development of a new insert for measuring dual-angle dynamic light scattering in a Bitter magnet of the HFML. A design is presented based on the theoretical prediction that the anisotropic diffusion coefficients of an anisotropically shaped particle can be determined by magnetically aligning these particles. A first version of the insert has been constructed and tested on a variety of differently shaped polymersomes, including spheres, discs and tubes. The setup is demonstrated to work up to 23.5 T, above which deviations are observed which are most probably caused by coupling of the insert itself to the strong magnetic field. Up to 23.5 T, clear changes in the measured diffusion coefficients between the different samples are observed which are in accordance with theory for the higher scattering angles but not for the lower scattering angles. Suggestions for possible improvements are given to increase sensitivity and decrease magnetic interference.*

## 8.1 Introduction

Over the last few decades, DLS has become a routine technique for particle characterization in the fields of soft matter and nanomaterials [1, 2]. In most cases polarized DLS is used, where only the light with an identical polarization as the incoming light is analyzed. This type of DLS provides translational diffusion coefficients, which can easily be translated to a hydrodynamic radius via the Stokes-Einstein relation [3, 4]. It is also possible to analyze only that light which is polarized perpendicular to the polarization of the incoming light. This configuration is called depolarized DLS, and is used to obtain rotational diffusion coefficients [5–9].

By measuring depolarized DLS in a magnetic field, one basically determines the degree of alignment, since full magnetic alignment will stop rotation along one axis altogether. However, the degree of alignment can already be accurately be measured with magnetic birefringence as was demonstrated in chapters 4, 5 and 6. Also, measuring depolarized DLS in a magnetic field is practically impossible because it is extremely sensitive to small changes in the polarization of the light [7]. In a magnetic field, the polarization will undoubtedly be altered to a certain extent because of Faraday rotation, making depolarized DLS in a magnetic field practically impossible. Polarized DLS however should be much easier to perform in a magnetic field, since it is much less sensitive to small changes in polarization. Also, polarized DLS provides translational diffusion coefficients which can be related to linear translational motion. Since linear motion cannot be measured with magnetic birefringence, it is therefore a useful complementary technique.

So far, DLS measurements in high magnetic fields are scarce. The ability to measure DLS in high magnetic fields would be beneficial for two reasons. First of all, it provides the possibility to determine the size of nanoparticles in high magnetic fields. Phenomena like aggregation and self-assembly can then be studied *in situ*. Also the work on magnetically induced growth of lipid vesicles, as reported by Ozeki [10], might benefit from *in situ* DLS. Second of all, it may even be possible to measure magnetic alignment on anisotropically shaped particles by measuring the diffusion coefficients parallel and perpendicular to the magnetic field. Research in the field of soft matter in high magnetic fields would benefit greatly from such a technique. Also with respect to the investigation of polymersomes, DLS in magnetic fields could significantly add to the understanding of motion of polymersomes in a magnetic field, since it is the translational diffusion coefficient that is being measured [11].

Measuring (polarized) DLS at high magnetic fields has been reported once before by Challa *et al.* [12]. They reported the investigation of liquid crystal

director fluctuations up to 25 T by measuring DLS in a split-coil magnet of the National High Magnetic Field laboratory in Tallahassee, Florida. This magnet has many openings around the field center where a laser beam can enter and scattered light can exit, allowing a light scattering setup to be built around rather than inside the magnet. The magnets at the High Field Magnet Laboratory (HFML) in Nijmegen do not have these openings, so in order to measure DLS in one of these magnets, one has to place most optics inside the magnet.

In this chapter we will describe our progress with the development of a new DLS insert (polarized DLS geometry) for the 32 T wide-bore Bitter magnet of the HFML. We will start by reciting the standard well-known theoretical equations for DLS after which we will extend these equations to include magnetically aligned structures. This will be quite different from the theory described by Challa *et al.* since we would like to describe the free diffusion of magnetically aligned nanostructures rather than the alignment of liquid crystals. From there, we will discuss the design of the DLS insert and present the first results obtained with this setup. We will conclude with some suggestions for improvements.

## 8.2 Theory

To derive the equations for DLS in high magnetic fields, we will first start by reciting the basic theory for DLS in case of isotropic diffusion (no magnetic alignment) as has been published many times before [1–4,13–18]. Following this, we will extend this theory to include anisotropic diffusion caused by magnetic alignment.

### 8.2.1 Isotropic diffusion

When light encounters an object with a refractive index which is different from its surroundings, it is known to scatter. For a point particle (an object much smaller than the wavelength of the light) the intensity of the scattered light is identical in all directions. If the object is of the same dimensions (or larger) than the wavelength of the light, one must consider the object to consist of many scattering point particles, meaning one has to integrate the scattered light over the volume of the particle. Interference of the scattered light from different positions of the object will cause the intensity of the scattered light to be angle dependent. For these large particles, the intensity of the scattered light decreases with increasing scattering angle. In dynamic light scattering, we only consider elastic scattering, which means that the absolute value of the wavevector $k$ remains unchanged after scattering. The direction however

does change as is shown in Figure 8.1a for a specific scattering angle $\delta$. The scattering vector is then defined as $\vec{q} = \vec{k}_{in} - \vec{k}_{out}$, which is equal to [3, 4, 14, 15]:

$$|q| = \frac{4\pi \cdot n_{\text{solv}}}{\lambda} \sin\left(\frac{\delta}{2}\right), \qquad (8.1)$$

with $n_{\text{solv}}$ the refractive index of the solvent and $\lambda$ the wavelength of the light. The scattering vector $\vec{q}$ is shown graphically in Figure 8.1b.

The electric field component of the scattered light, and hence the intensity of the scattered light, is only constant if the particles do not move. This is not the case in a solution where the particles diffuse. The diffusion is described by Fick's second law, which, in q-space, is given by [1, 16]:

$$\frac{\partial}{\partial t} F_{\text{s}}(\vec{q}, t) = -q^2 D \cdot F_{\text{s}}(\vec{q}, t), \qquad (8.2)$$
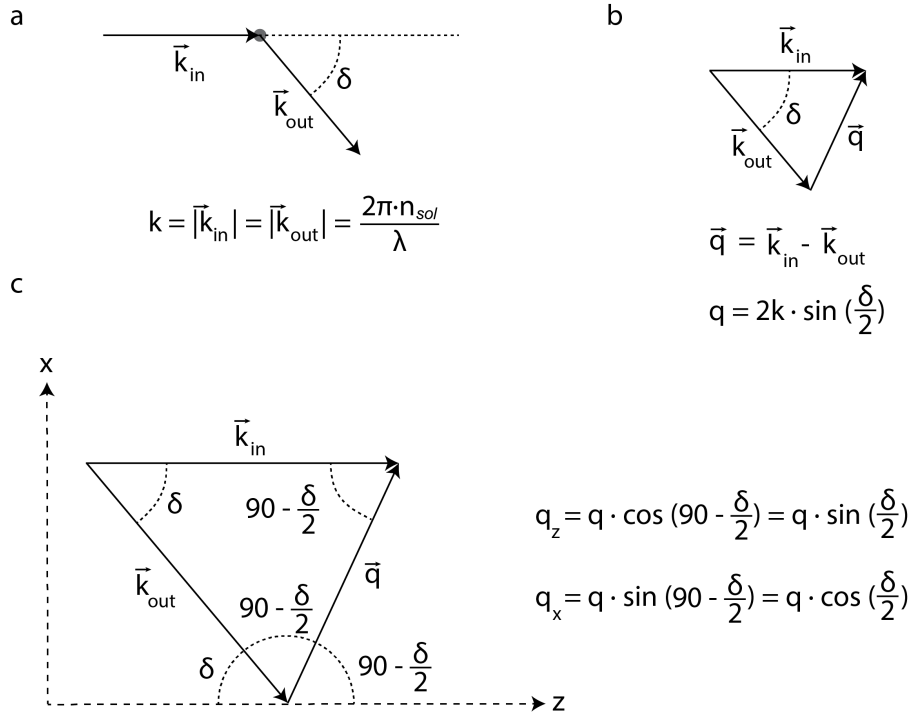


**Figure 8.1:** *(a) Scattering of light on a single particle. The incoming and outgoing wavevectors are shown. (b) The scattering vector $\vec{q}$ and its relation to the scattering angle $\delta$ and the size of the wavevector $k$. (c) The scattering vector $\vec{q}$ can be composed in x and z components as is shown here.*

where $F_{\rm s}\left(\vec{q}, t\right)$ is the Fourier transform of the probability distribution function [1]. Equation 8.2 is a first order differential equation and has the following solution:

$$F_{\rm s}\left(q, t\right) = e^{\left(-|q|^2 D \cdot t\right)}. \tag{8.3}$$

The diffusion of particles causes fluctuations in the amplitude of the electric field $E$ of the scattered light. This is normally given in a so-called first order autocorrelation function $g^{(1)}\left(q, \tau\right)$, which is defined as [1, 17]:

$$g^{(1)}\left(\vec{q}, \tau\right) = \frac{\langle E\left(t\right) \cdot E^*\left(t + \tau\right) \rangle}{\left\langle E\left(t\right)^2 \right\rangle} = \left\langle e^{i\vec{q} \cdot \left(\vec{r}(t+\tau) - \vec{r}(t)\right)} \right\rangle. \tag{8.4}$$

In case of normal Brownian diffusion, one can show that $g^{(1)}\left(\vec{q}, \tau\right) = F_{\rm s}\left(q, \tau\right)$ [1]. The first order autocorrelation function can therefore be written as [1, 18]:

$$g^{(1)}\left(q, \tau\right) = e^{-D|q|^2 \tau}. \tag{8.5}$$

During a scattering experiment, one measures the intensity of the light rather than the electric field component of it. Therefore, it is only possible to determine the second order autocorrelation function, which is defined as [15, 17]:

$$g^{(2)}\left(\vec{q}, \tau\right) = \frac{\langle I\left(t\right) \cdot I\left(t + \tau\right) \rangle}{\left\langle I\left(t\right)^2 \right\rangle}. \tag{8.6}$$

The first and second order autocorrelation function are related via the so-called Siegert relation [14, 15, 17, 18]:

$$g^{(2)}\left(q, \tau\right) = 1 + \beta \left| g^1\left(q, \tau\right) \right|^2, \tag{8.7}$$

where $\beta$ is a factor which defines the coherence area [2]. Ideally, this factor is equal to 1. Substituting equation 8.5 in equation 8.7 and rearranging gives [15]:

$$g^{(2)}\left(q, \tau\right) - 1 = \beta e^{-2|q|^2 D \cdot \tau}. \tag{8.8}$$

Equation 8.8 applies only to monodisperse samples where all particles are incidental and therefore have the same diffusion coefficient $D$. In case the sample is polydisperse, one can expand equation 8.8 with a higher order term to give [17]:

$$g^{(2)}\left(q, \tau\right) - 1 = \beta e^{-2|q|^2 D \cdot \tau} \cdot \left(1 + \frac{\mu_2}{2!} \cdot \tau^2\right)^2, \tag{8.9}$$

where $\mu_2$ is related to the spread in the diffusion coefficient. An often used parameter for this spread is the polydispersity index, or $PDI$, which is defined as [13]:
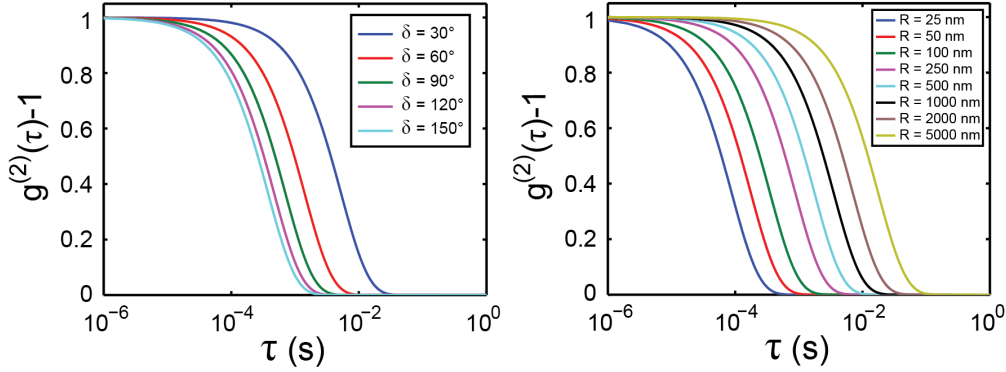
$$PDI = \frac{\mu_2}{q^4 D^2}. \tag{8.10}$$

**Figure 8.2:** *Left: effect of the scattering angle $\delta$ on the second order auto-correlation. The curves are calculated for spherical particles of 200 nm radius dispersed in water. The higher the scattering angle, the faster the autocorrelation drops down to zero. Right: the effect of particle size on the the second order autocorrelation. All curves are calculated for a scattering angle of 90°. The larger the particle, the slower the autocorrelation drops down to zero since larger particles diffuse slower and remain relatively longer in the focus of the laser. For spherical particles, its radius is related to its diffusion coefficient by equation 8.24.*

For a perfect monodisperse sample, the $PDI$ is equal to zero. The higher the $PDI$, the larger the inhomogeneity. The effect of particle size and scattering angle on the second order autocorrelation curve is shown in Figure 8.2. In figure 8.2a one can see the effect of scattering angle, $\delta$, on the autocorrelation curve: the larger the scattering angle the slower the decay. In figure 8.2b, one can see the effect of particle size on the autocorrelation curve. The larger the particle, the slower it diffuses and the slower the decay.

### 8.2.2 Anisotropic diffusion

For a (partly) aligned anisotropic particle the diffusion coefficient parallel to the magnetic field is expected to differ from that perpendicular to the magnetic field. In the following derivation, we will assume that the magnetic field is directed along the $z$-direction in the lab-frame and that the particle can diffuse independently in all three dimensions. In other words, there is no coupling between diffusion along the $x$, $y$ or $z$ direction. In that case, one can write $F_\mathrm{s}\left(q,t\right)$ as a product of three functions, one for each dimension:

$$F_\mathrm{s}\left(q,t\right) = F_\mathrm{s,x}\left(q_\mathrm{x},t\right) \cdot F_\mathrm{s,y}\left(q_\mathrm{y},t\right) \cdot F_\mathrm{s,z}\left(q_\mathrm{z},t\right), \qquad (8.11)$$

with $\vec{q} = (q_x, q_y, q_z)$. Separation of variables then leads to a set of three independent equations:

$$
\begin{aligned}
\frac{\partial}{\partial t} F_{s,x}(q_x, t) &= D_x \cdot q_x^2 \cdot F_{s,x}(q_x, t), \\
\frac{\partial}{\partial t} F_{s,y}(q_y, t) &= D_y \cdot q_y^2 \cdot F_{s,y}(q_y, t), \\
\frac{\partial}{\partial t} F_{s,z}(q_z, t) &= D_z \cdot q_z^2 \cdot F_{s,z}(q_z, t),
\end{aligned}
\tag{8.12}
$$

which have the following solutions:

$$
\begin{aligned}
F_{s,x}(q_x, t) &= e^{-q_x^2 D_x \cdot t}, \\
F_{s,y}(q_y, t) &= e^{-q_y^2 D_y \cdot t}, \\
F_{s,z}(q_z, t) &= e^{-q_z^2 D_z \cdot t},
\end{aligned}
\tag{8.13}
$$

where $D_x$, $D_y$ and $D_z$ are the diffusion coefficients in the $x$, $y$ and $z$ directions respectively. $F_s(q, \tau)$ can therefore be written as:

$$
\begin{aligned}
F_s(q, \tau) &= F_{s,x}(q_x, \tau) \cdot F_{s,y}(q_y, \tau) \cdot F_{s,z}(q_z, \tau), \\
&= e^{-\left(D_x q_x^2 + D_y q_y^2 + D_z q_z^2\right) \cdot \tau}.
\end{aligned}
\tag{8.14}
$$

If we define the $xz$-plane as the scattering plane, we can write:

$$
q_x^2 = |q|^2 \cdot \cos^2\left(\frac{\delta}{2}\right),
\tag{8.15}
$$

$$
q_y^2 = 0,
\tag{8.16}
$$

$$
q_z^2 = |q|^2 \cdot \sin^2\left(\frac{\delta}{2}\right).
\tag{8.17}
$$

The definitions of $q_x$, $q_y$ and $q_z$ are shown graphically in Figure 8.1c. Substituting equations 8.15, 8.16 and 8.17 in equation 8.14 gives:

$$
F_s(q, \tau) = e^{-|q|^2 D_{\text{obs}} \cdot \tau},
\tag{8.18}
$$

with $D_{\text{obs}}$ the observed diffusion coefficient, which is defined as:

$$
D_{\text{obs}} = D_z \sin^2\left(\frac{\delta}{2}\right) + D_x \cos^2\left(\frac{\delta}{2}\right).
\tag{8.19}
$$

For the second order autocorrelation function we obtain:

$$
g^{(2)}(q, \tau) - 1 = \beta e^{-2|q|^2 D_{\text{obs}} \cdot \tau},
\tag{8.20}
$$

for a monodisperse sample, and:

$$g^{(2)}\left(q,\tau\right) - 1 = \beta e^{-2|q|^2 D_{\mathrm{obs}} \cdot \tau} \cdot \left(1 + \frac{\mu_2}{2} \cdot \tau^2\right)^2, \qquad (8.21)$$

for a polydisperse sample. Equations 8.19 and 8.21 show that the measured diffusion coefficient depends heavily on the scattering angle $\delta$ in case $D_{\mathrm{z}} \neq D_{\mathrm{x}}$. If $\delta = 0°$, one measures only $D_{\mathrm{x}}$. If $\delta = 180°$, one measures only $D_{\mathrm{z}}$. At all angles in between, the measured diffusion coefficient is a combination of the two. In the limiting case where $D_{\mathrm{z}} = D_{\mathrm{x}} = D$, equation 8.21 becomes equal to equation 8.9 as should be expected. In principle, one does not have to measure exactly at $0°$ or $180°$ to obtain $D_{\mathrm{z}}$ and $D_{\mathrm{x}}$. Since $D_{\mathrm{obs}}$ is related to $D_{\mathrm{z}}$ and $D_{\mathrm{x}}$ via equation 8.19, one can solve for $D_{\mathrm{z}}$ and $D_{\mathrm{x}}$ by measuring $D_{\mathrm{obs}}$ at two different angles. If one measures $D_{\mathrm{obs1}}$ at $\delta_1$ and $D_{\mathrm{obs2}}$ at $\delta_2$ one can calculate $D_{\mathrm{z}}$ and $D_{\mathrm{x}}$ by:

$$D_{\mathrm{z}} = \frac{D_{\mathrm{obs2}} \cos^2\left(\frac{\delta_1}{2}\right) - D_{\mathrm{obs1}} \cos^2\left(\frac{\delta_2}{2}\right)}{\cos^2\left(\frac{\delta_1}{2}\right) - \cos^2\left(\frac{\delta_2}{2}\right)}, \qquad (8.22)$$

$$D_{\mathrm{x}} = \frac{D_{\mathrm{obs2}} \sin^2\left(\frac{\delta_1}{2}\right) - D_{\mathrm{obs1}} \sin^2\left(\frac{\delta_2}{2}\right)}{\sin^2\left(\frac{\delta_1}{2}\right) - \sin^2\left(\frac{\delta_2}{2}\right)}. \qquad (8.23)$$

How $D_{\mathrm{z}}$ and $D_{\mathrm{x}}$ depend on the shape and the degree of alignment will be derived in the next subsection.

### 8.2.3 Shape dependency of the diffusion coefficients

#### 1. No magnetic alignment

For a sphere, the diffusion coefficient is related to its radius, $R$, via the Stokes-Einstein equation [3, 4, 18]:

$$D_{\mathrm{sphere}} = \frac{kT}{6\pi\eta R}, \qquad (8.24)$$

with $k$ the Boltzmann constant, $T$ the temperature and $\eta$ the viscosity of the solvent. Since a sphere is perfectly isotropic, the diffusion coefficient is isotropic as well. This is not the case for cylindrically symmetric particles. For such particles the diffusion coefficient parallel to the symmetry axis is different from that perpendicular to the symmetry axis, as is shown in Figure 8.3. For all cylindrically symmetric structures $D_\parallel$ can be expressed in terms of $D_\perp$ by introducing the scaling constant $a$:

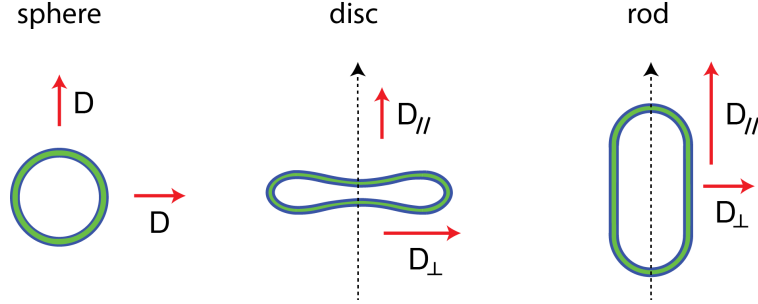$$D_\parallel = a \cdot D_\perp, \qquad (8.25)$$

**Figure 8.3:** *Cartoon showing the diffusion coefficients for a sphere, disc and a rod. The diffusion coefficient of a sphere is isotropic. A disc and a rod are both cylindrically symmetric structures. The symmetry axes (axes of rotation) are indicated by the dashed arrows. The diffusion coefficient parallel and perpendicular to the symmetry axes are defined as $D_\parallel$ and $D_\perp$ respectively. For a disc $D_\parallel = \frac{2}{3}D_\perp$ while for the rod $D_\parallel = 2D_\perp$ [19].*

where both $a$ and $D_\perp$ are determined by the exact shape. Without any magnetic alignment, all structures tumble around randomly and the diffusion coefficients in all three directions average out to:

$$D_{\mathrm{av}} = \frac{2 \cdot D_\perp + D_\parallel}{3} = \frac{2 + a}{3} D_\perp. \tag{8.26}$$

For spheres, $a = 1$ and $D_\perp = D_{\mathrm{sphere}}$ and hence $D_{\mathrm{av}} = D_{\mathrm{sphere}}$, as given by equation 8.24. Rothenbuhler *et al.* showed theoretically that $a = 2$ for rods with high aspect ratio (infinite long rods) and $a = 2/3$ for discs with very low aspect ration (infinite flat discs) [19]. This is shown schematically in Figure 8.3. From this it follows that $D_{\mathrm{av}} = \frac{4D_\perp}{3}$ for rods and $D_{\mathrm{av}} = \frac{8D_\perp}{9}$ for discs. As mentioned before, $D_\perp$ is shape dependent. For rods $D_\perp$ is given by [19, 20]:

$$D_\perp = \frac{kT}{4\pi\eta L} \ln\left(\frac{L}{b}\right), \tag{8.27}$$

with $L/b$ the aspect ratio. For discs, $D_\perp$ is given by [19]:

$$D_\perp = \frac{3kT}{16\eta V^{1/3}} \left(\frac{\pi L}{4b}\right)^{1/3}, \tag{8.28}$$
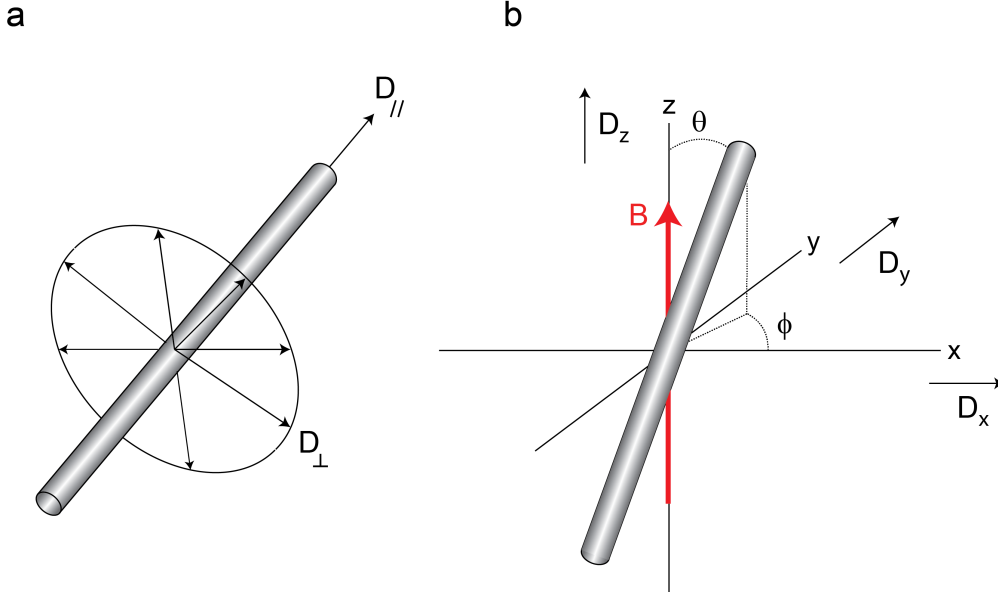
with $V$ the volume of the disc.

a

b



**Figure 8.4:** *(a) The diffusion coefficients of a cylindrically symmetric object. (b) A cylindrically symmetric object in the lab frame. (x,y,z). The magnetic field is applied in the z-direction.*

## 2. Magnetic alignment

In the previous subsection, we defined the diffusion rates for cylindrically symmetric objects in terms of $D_\parallel$ and $D_\perp$. Without magnetic alignment, the structures tumble around randomly and the diffusion coefficients average out in all three spatial dimensions in the lab-frame $(x,y,z)$. In this subsection, we will derive the diffusion coefficients in case of (partial) magnetic alignment. We will choose the magnetic field direction to be along the $z$-axis. The object will have a certain orientation with respect to the applied magnetic field by angles $\theta$ and $\phi$ as is shown in Figure 8.4. The diffusion coefficients in the lab-frame $(x,y,z)$ depend on the orientation of the cylindrically symmetric structure $(\theta, \phi)$ by the following transformation:

$$D_\mathrm{x}\left(\theta, \phi\right) = D_\parallel \sin^2\left(\theta\right) \cos^2\left(\phi\right) + D_\perp \cos^2\left(\theta\right) \cos^2\left(\phi\right) + D_\perp \sin^2\left(\phi\right),$$
$$D_\mathrm{y}\left(\theta, \phi\right) = D_\parallel \sin^2\left(\theta\right) \sin^2\left(\phi\right) + D_\perp \cos^2\left(\theta\right) \sin^2\left(\phi\right) + D_\perp \cos^2\left(\phi\right), \quad (8.29)$$
$$D_\mathrm{z}\left(\theta\right) = D_\parallel \cos^2(\theta) + D_\perp \sin^2(\theta).$$

disc:            rod:
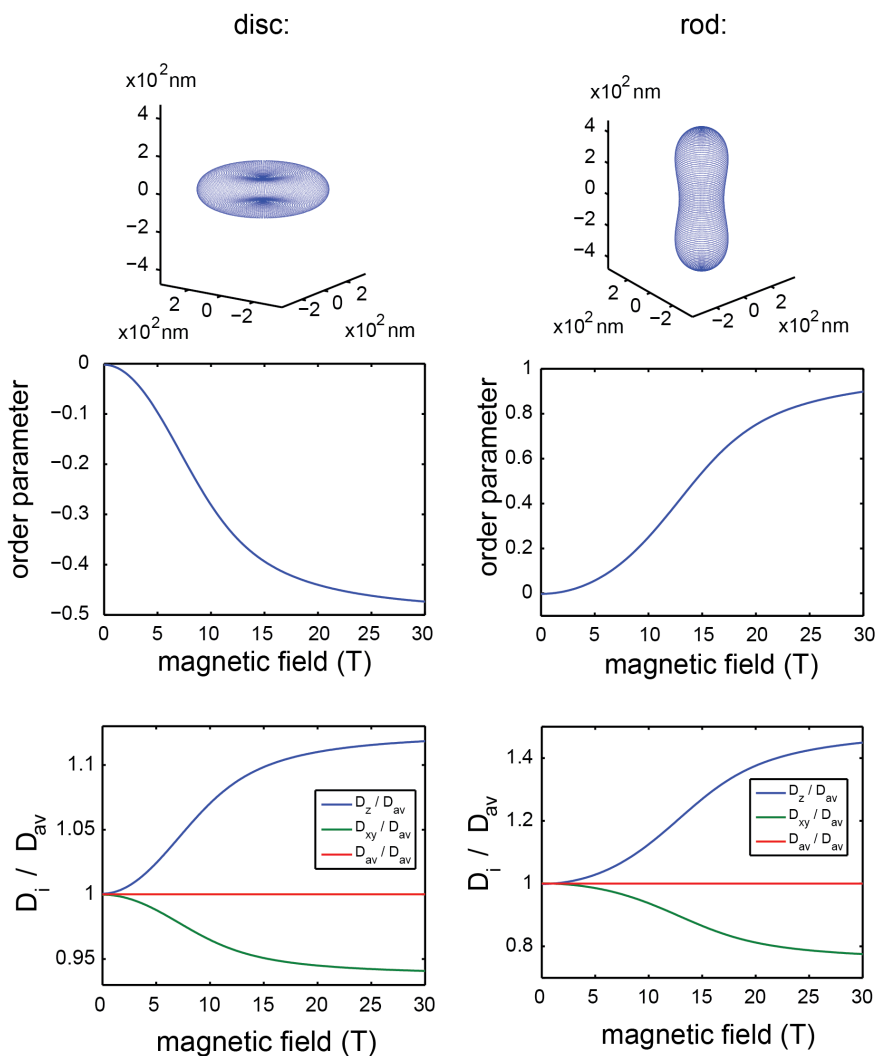


**Figure 8.5:** *Top: plots of a disc and a rod with equal surface area ($A = 4\pi R^2$ with $R = 250$ nm), using the $\Delta\chi$ obtained in chapter 6. Middle: The calculated order parameters for both discs and rods as function of the applied magnetic field. Both structures are almost fully aligned at 30 T. Bottom: The normalized diffusion coefficients along the z and xy direction as function of the applied magnetic field. The average diffusion coefficient is given for comparison. The magnetic field is applied along the z-direction. For both discs and rods, the largest change is predicted to occur along the z-direction.*

Equation 8.25 allows equations 8.29 to be written in terms of $D_\perp$ only:

$$D_x(\theta, \phi) = a \cdot D_\perp \sin^2(\theta) \cos^2(\phi) + D_\perp \cos^2(\theta) \cos^2(\phi) + D_\perp \sin^2(\phi),$$

$$D_y(\theta, \phi) = a \cdot D_\perp \sin^2(\theta) \sin^2(\phi) + D_\perp \cos^2(\theta) \sin^2(\phi) + D_\perp \cos^2(\phi), \quad (8.30)$$

$$D_z(\theta) = a \cdot D_\perp \cos^2(\theta) + D_\perp \sin^2(\theta).$$

Because partially aligned structures can still rotate around the magnetic field lines (along the $\phi$ direction), the diffusion in the $x$ and $y$ directions are therefore equal when averaged over time. Therefore, $\overline{D_x}(\theta, \phi) = \overline{D_y}(\theta, \phi) = D_{xy}(\theta)$, with:

$$D_{xy}(\theta) = \frac{1}{2} a \cdot D_\perp \sin^2(\theta) + \frac{1}{2} D_\perp \cos^2(\theta) + \frac{1}{2} D_\perp. \quad (8.31)$$

When a magnetic field is applied in the $z$-direction, the structures will start to align. The degree of alignment follows a Boltzmann distribution, as was already explained in chapter 3, section 3.3.2. We can therefore express the magnetic field dependency of the average diffusion coefficients in the $z$ and $xy$ direction by:

$$\overline{D_i}(B) = \frac{\int_{\theta=0}^{\pi} D_i(\theta) \cdot f(\theta) \cdot \sin(\theta) \cdot d\theta}{\int_{\theta=0}^{\pi} f(\theta) \cdot \sin(\theta) \cdot d\theta}, \quad (8.32)$$

with i being either $xy$ or $z$ and $f(\theta)$ the Boltzmann distribution function as given earlier in chapter 3 (equation 3.40). To gain more insight in how $D_z$ and $D_{xy}$ depend on the applied magnetic field for various polymersome shapes, we plotted equation 8.32 for both a polymersome disc and a polymersome rod. Figure 8.5 shows the degree of alignment as function of field (the order parameter, see chapters 3 and 6) and the normalized diffusion coefficients $D_z/D_\perp$ and $D_{xy}/D_\perp$ as function of magnetic field for both a disc and a rod. For both shapes, $D_z/D_\perp$ and $D_{xy}/D_\perp$ are identical to $D_{av}/D_\perp$ at zero field since there is no orientational order. As the magnetic field increases, the degree of alignment increases and the diffusion coefficients in the $z$ and the $xy$ direction start to differ. For both a polymersome disc and a polymersome rod, the largest changes occur in the $z$-direction, which is only 12.5% for discs and 50% for rods.

In a DLS measurement, one measures the scattered light at an angle between 0° and 180°. According to equation 8.19 the diffusion coefficient that is measured is a mix between $D_z$ and $D_{xy}$ and depends on the scattering angle. In case of (partial) magnetic alignment, $D_z$ and $D_{xy}$ are not equal and therefore the observed diffusion coefficient is strongly depending on the scattering angle, as was already shown by equation 8.19. Figure 8.6 shows how the normalized observed diffusion coefficient, $D_{obs}/D_{av}$, depends on both the magnetic field and the scattering angle for both the polymersome discs and the polymersome
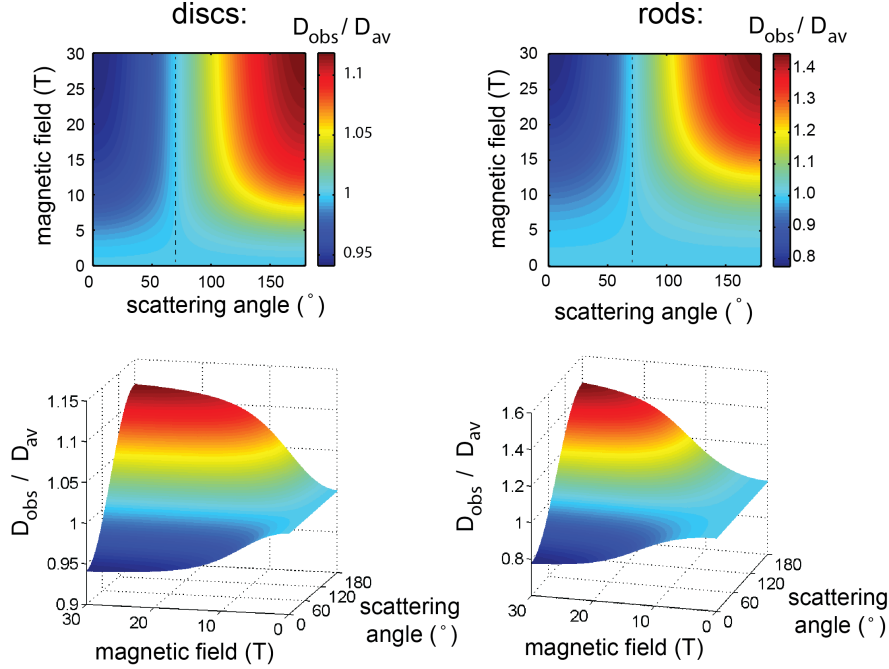
**Figure 8.6:** *The normalized observed diffusion coefficient ($D_{\mathrm{obs}}/D_{\mathrm{av}}$) as function of magnetic field and scattering angle for discs (left) and for rods (right) shown both as a color and 3D plot. For all shapes the observed diffusion coefficient at 0 T is independent from the scattering angle. This is not the case at non-zero magnetic fields. Since the degree of alignment increases with increasing field, the diffusion coefficients along the z-direction and xy directions will become increasingly different and therefore the observed diffusion coefficient will start to depend the scattering angle, according to equation 8.19. Only at a scattering angle of 70.5°, indicated by the dashed lines, the observed diffusion coefficient will equal the average diffusion coefficient independent of the degree of alignment.*

rods. Similar calculations for tubes and cross-linked tubes are given in the Appendix, figure 8.14. At 0 T the observed diffusion coefficient of both shapes is clearly independent of the scattering angle. This is due to the fact that there is no orientational order and thus the diffusion coefficients in the xy plane and the z-direction are equal to the average diffusion coefficient for discs and rods respectively. The stronger the magnetic field, the larger the difference between $\overline{D_{\mathrm{z}}}$ and $\overline{D_{\mathrm{xy}}}$, until saturation occurs. This will cause the observed diffusion coefficient to depend more and more on the scattering angle, as follows from

equation 8.19. For both the discs and the rods the observed diffusion coefficient decreases with increasing magnetic field at scattering angles below 70.5° degrees. Above this angle, the observed diffusion coefficient increases with increasing magnetic field. At 70.5° the observed diffusion coefficient equals the average diffusion coefficients at all magnetic field strengths for both discs and rods. This is no coincidence, since all cylindrically symmetric structures show this behavior at this particular angle. To prove this we use equations 8.19, 8.26, 8.30 and 8.31 and calculate the scattering angle at which the observed diffusion coefficient equals the average diffusion coefficient:

$$
\begin{aligned}
D_{\mathrm{av}} &= D_{\mathrm{obs}} \\
\frac{2+a}{3} D_{\perp} &= D_{\mathrm{z}}\left(\theta\right) \sin^{2}\left(\frac{\delta}{2}\right) + D_{\mathrm{xy}}\left(\theta\right) \cos^{2}\left(\frac{\delta}{2}\right), \\
\frac{\frac{2+a}{3} D_{\perp} - D_{\mathrm{xy}}\left(\theta\right)}{D_{\mathrm{z}}\left(\theta\right) - D_{\mathrm{xy}}\left(\theta\right)} &= \sin^{2}\left(\frac{\delta}{2}\right) \\
\frac{\frac{1}{3}\left(a-1\right) + \frac{1}{2}\left(1-a\right)\sin^{2}\left(\theta\right)}{\left(a-1\right) + \frac{3}{2}\left(1-a\right)\sin^{2}\left(\theta\right)} &= \sin^{2}\left(\frac{\delta}{2}\right), \\
\frac{1}{3} &= \sin^{2}\left(\frac{\delta}{2}\right) \\
\delta &= 2 \cdot \sin^{-1}\left(\frac{1}{\sqrt{3}}\right) \approx 70.53°. \quad (8.33)
\end{aligned}
$$

As can be seen, the scattering angle $\delta$ at which $D_{\mathrm{obs}} = D_{\mathrm{av}}$ is not a function of $\theta$ or $a$. Instead, it is constant for all cylindrically symmetric structures.

Figure 8.6 also shows that the largest changes in the observed diffusion coefficient occur at the largest scattering angle. Therefore, it will be best to measure DLS at the largest scattering angle possible. Measuring at large angles has also an additional benefit, namely that disturbances caused by dust particles is minimal at high scattering angles [18,21]. This is due to the fact that the scattering intensity drops with increasing scattering angle. The rate at which the intensity decreases with increasing scattering angle depends heavily on the size of the particles: the larger the particles, the faster the drop in intensity. Since dust particles are relatively large compared to the particles to be investigated, the contribution of contaminants will therefore be minimal at the highest possible scattering angle. Finally, the unwanted effect of multiple scattering is also at a minimum at 180° [21, 22]. So also for this reason, measuring at the largest possible scattering angle is recommended.

## 8.3   Setup design

In section 8.2, we have shown that the measured diffusion coefficient, $D_{obs}$, is angle dependent as long as the magnetic field lines lie within the scattering plane. In that case, by measuring under different angles one obtains different values of $D_{obs}$, each consisting of a different combination of $D_z$ (parallel to the magnetic field) and $D_{xy}$ (perpendicular to the magnetic field) as is given by equation 8.19. If the magnetic field would be applied perpendicular to the scattering plane one would only measure $D_{xy}$, independent of the scattering angle. Thus, by having the magnetic field lines within the scattering plane, one can obtain more information, especially when measuring at multiple angles. We therefore have chosen to apply this geometry to our DLS insert.

### 8.3.1   The DLS insert

The design of the insert is shown in Figure 8.7. To fixate the optical alignment, we use a single mode fiber to couple in the laser light in the insert. This has the advantage that the optical alignment will be maintained, even when the insert is taken out of the magnet. The light is focused by a small lens into the center of a cubical cuvette. A polarizer is placed between the lens and the cuvette to ensure that the light has the correct polarization when entering the cuvette. Some rotation of polarization is to be expected in the cuvette at high magnetic field due to Faraday rotation. To minimize this effect, we made the cuvette as small as possible (5x5x5 mm$^3$) and we placed analyzers before the detection fibers (a polarizer with the same orientation as the first polarizer) to only select the light with the correct polarization.

Since the space in the radial direction is very limited we have chosen to use small adjustable mirrors to reflect the scattered light along the axis of the magnet where we have much more working space. Two rotatable mirrors on movable rods are used to select a specific scattering angle. The scattering angle can be increased or decreased by shifting the rod up or down respectively. After fixating the rod at a certain position, the mirror can be rotated in order to reflect the scattered light towards the detection fiber, which brings it to a single photon detector that is connected to an autocorrelation system. For both channels, any scattering angle between 60° and 117° can be selected. Outside this range, the mirrors cannot couple the light in the detectors anymore.

Where possible, the components of the insert were made from non-ferromagnetic materials to reduce interactions between the insert and the magnetic field. The four rods on which the discs are mounted were made of carbon fiber. All discs containing the optical components were made from aluminum as were
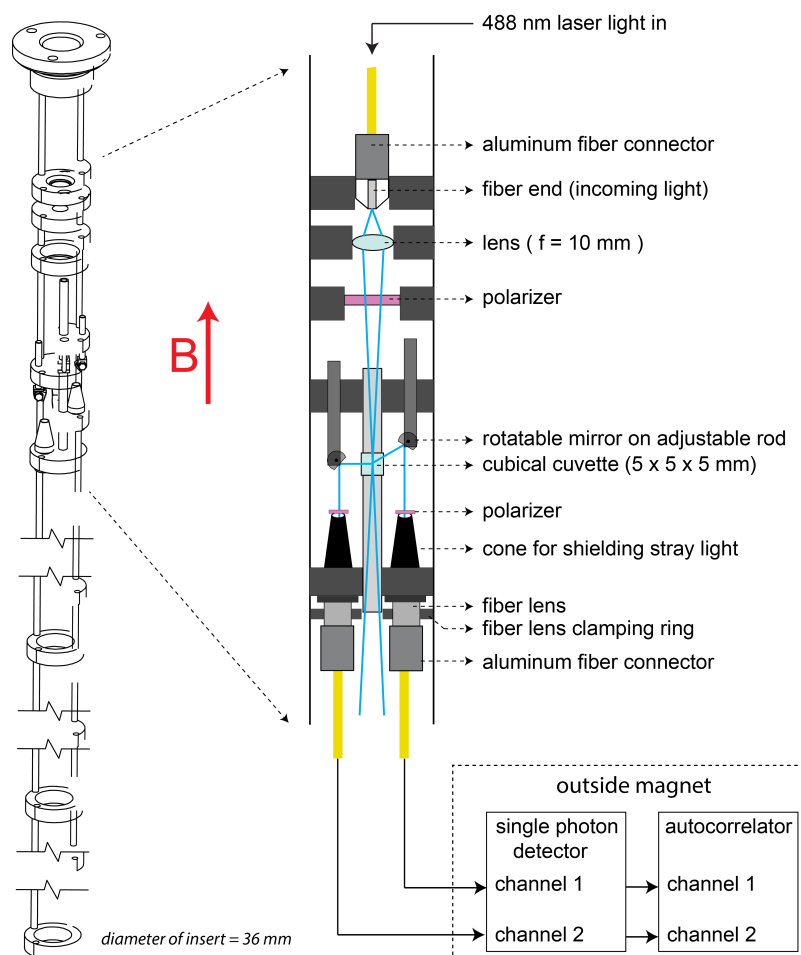
**Figure 8.7:** *Drawings of the DLS insert. Left: the design of the entire insert by Michel Peters. Right: schematic picture showing all components within the DLS insert. The positions of the individual discs containing the optical components can all be shifted separately in the vertical direction. This allows DLS to be measured at different positions in the magnet and the optical alignment to be performed for every component separately. The scattered light is directed to a single photon detector and is analyzed by an autocorrelator which are both placed at least 4 meters from the magnet.*

the holder of the cuvette and the rods containing the mirrors. The connectors that are normally mounted at the end of an optical fiber are very magnetic and therefore we replaced them by home-made aluminum connectors. In the final

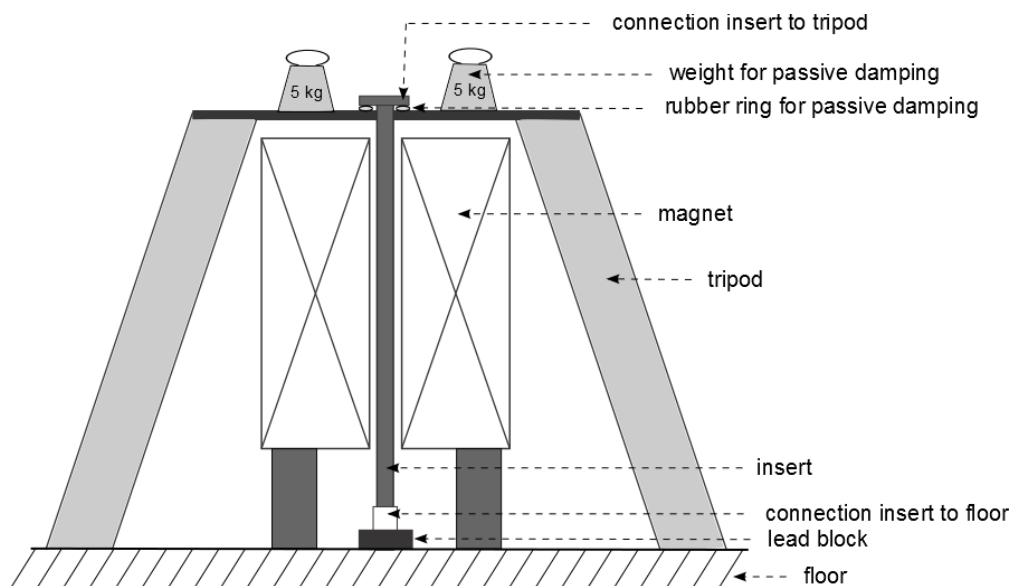**Figure 8.8:** *Schematic picture showing the placement of the insert within the magnet. There is no direct contact between the magnet and the insert. Transfer of vibrations via the tripod has been reduced by passive damping via rubber rings and the addition of extra weight on the tripod.*

design, only the two fiber lenses (made from stainless steel) were still slightly ferromagnetic. These two lenses were therefore clamped very tightly by two discs to make sure they could not shift, twist or turn in a magnetic field.

### 8.3.2 Placement in the magnet

The Bitter magnet has an inner diameter of 50 mm. Inside, a temperature tube is placed that will stabilize the temperature of the insert and the sample. This will reduce the working diameter to 40 mm. The Bitter magnet is cooled by 135 L/s of water which introduces significant vibrations in the magnet. To prevent the transfer of these vibrations from the magnet to our DLS insert, we have chosen to decouple the complete insert from the magnet. The insert was designed to have a diameter of 36 mm to ensure a 2 mm wide gap between the insert and the temperature tube. The upper part of the insert was fixed to the tripod which is not connected to the magnet but is standing on the floor. This is shown schematically in Figure 8.8. The insert is connected to the tripod via flexible rubber rings which reduces the transfer of vibrational noise. Heavy sandbags were placed on top of the tripod to damp any vibrations that were

transferred from the ground to the tripod. The bottom of the insert was fixed to the floor by a special holder mounted to a heavy block made of lead. In this way, there was no direct contact between the magnet and the insert which should minimize vibrational noise.

## 8.4 Proposed measurements and experimental details

As mentioned in the introduction, DLS in a magnetic field might be used to measure two different kinds of systems: 1) the aggregation or self-assembly of particles and 2) the alignment of anisotropic particles. In case of aggregation or self-assembly, the changes in the diffusion coefficient will be much larger than in case of alignment. For alignment of anisotropic particles, the largest change in $D_{\mathrm{obs}}$ is to be expected for rods at the largest scattering angle possible (115°) where the difference between no alignment and full alignment equals a factor of 1.2 (see Figure 8.6). For a system where aggregation takes place, the diffusion coefficient can easily change with a factor of 5 or even more, depending on the ratio of radii of the aggregate and the individual colloids. However, for the research described in this thesis, the alignment of anisotropic polymersomes are the most interesting to test. First of all, because the effects are expected to be small, as was described in section 8.2.3, they are ideal samples with which to test the sensitivity of the insert. Second of all, DLS in high magnetic fields is a complementary technique to magnetic birefringence, meaning it can provide extra information about the anisotropy of the shapes and/or the direction of alignment.

Polymersome particles of different shapes were used to measure changes in the observed diffusion coefficient ($D_{\mathrm{obs}}$) as function of the applied magnetic field. The samples included spheres, discs, rods, tubes and cross-linked tubes. Spherical polymersomes were made using the same procedure as described in chapter 4. Discs-shapes polymersomes were made by the out-of-equilibrium method described in chapter 5. Cross-linked tubes were made by a previously reported method [23]. The rods and tubes (non cross-linked) were made by a new method in which PEG was added to a flexible polymersome sample (spheres) to induce a positive spontaneous curvature, which in turn led to the formation of rods or tubes. In short, 10 mg of $PEG_{44}$-$PS_{230}$ was dissolved in a mixture consisting of 0.75 mL THF and 0.25 mL of dioxane. A total of 0.5 mL of water was added at 1 mL/h to initiate self-assembly to spherical polymersomes. Rods and

tubes were created by an addition of 0.13 mg or 1 mg of PEG respectively. All polymersome samples were made rigid by an extensive dialysis against water to remove all organic solvents.

All shapes were measured at the highest scattering angle possible (104-117°) to measure the largest possible effect. The samples which show the largest changes with increasing magnetic field were also measured around 70,5°, which is the angle where no changes in $D_{obs}$ are to be expected. Calibration of the scattering angle was performed as follows. For every sample to be measured with the DLS insert, the hydrodynamic radius was first determined by a commercial DLS machine (Malvern Zetasizer). These results were then used to calibrate the scattering angle of the DLS insert. First, the angle was set at roughly the desired angle, using a triangle ruler. The exact angle was then determined by performing a DLS measurement with the insert (outside the magnetic field), using a sample of which the hydrodynamic radius had already been determined with the Malvern Zetasizer. By fitting the autocorrelation curve, and inserting the known hydrodynamic radius, the scattering angle was determined. This procedure was performed for every sample separately. To check if this method led to accurate values, we imaged the detection path by coupling the laser in the detector fiber (see figure 8.15). The observed angles were in agreement with the experimentally determined value, which validates the calibration technique.

## 8.5 Results

### 8.5.1 Polymersome sample characterization

As mentioned in the previous subsection, five different polymersome samples were acquired for testing the sensitivity of the DLS insert for changes in the diffusion coefficients due to magnetic alignment: spheres, discs, rods, tubes and cross-linked tubes. These samples have first been characterized by standard DLS to obtain the hydrodynamic radius at zero field (using a Malvern Zetasizer DLS). The results are given in Table 8.1. As mentioned in the previous section, these values were used to calibrate the scattering angle of the DLS insert.

To test whether the samples align, and to what degree, in magnetic fields up to 29 T, we also measured all samples with magnetic birefringence (MB). These results are given in Figure 8.9a. The amplitudes of the curves cannot be compared since the concentrations of the samples are slightly different due to different assembly methods. However, the shape of the curves do show that the discs, rods, tubes and cross-linked tubes all start to saturate around 25 T. The spheres show zero birefringence as is to be expected since they are
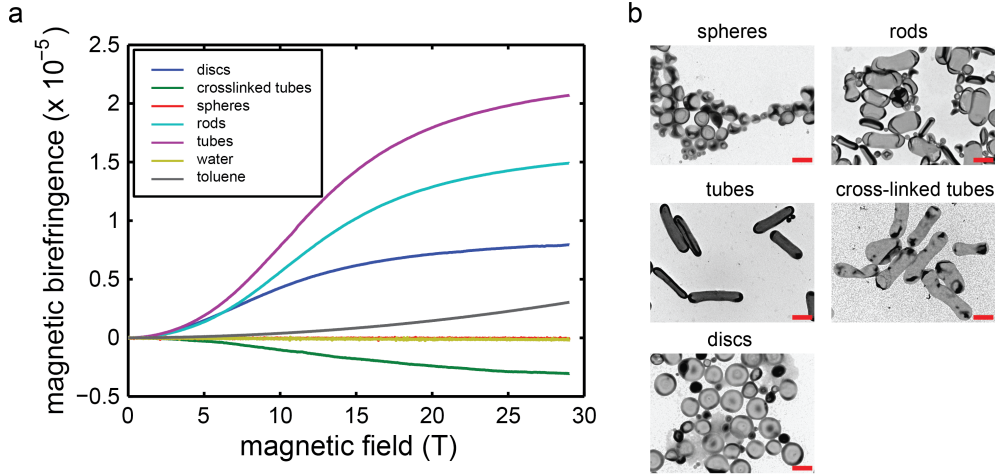
**Figure 8.9:** *Characterization of polymersome samples used in the DLS experiments. (a) Magnetic birefringence of all samples. The amplitude of the curves cannot be compared since the concentrations in each sample was different due to different assembly methods. However, the fact that the curves of the discs, rods, tubes and cross linked tubes are almost saturated at 29 T does demonstrate that alignment is nearly complete at this field. The spheres do not align as is to be expected. The fact that the MB of the cross-linked tubes is of opposite sign compared to the normal tubes and rods suggests that the cross-linked tubes align with their symmetry axis perpendicular to the magnetic field instead of parallel as is the case for the non-cross-linked tubes and rods. (b) TEM images of all samples. All scalebars are 500 nm.*

| Sample | $R_{\mathrm{h}}$ (nm) | $D_{av}$ ($\cdot 10^{-12}$ m$^2$/s) | $PDI$ |
|---|---|---|---|
| spheres | $207 \pm 53$ | $1.17 \pm 0.30$ | 0.065 |
| discs | $201 \pm 59$ | $1.21 \pm 0.36$ | 0.086 |
| rods | $232 \pm 69$ | $1.05 \pm 0.32$ | 0.089 |
| tubes | $232 \pm 77$ | $1.05 \pm 0.35$ | 0.109 |
| cross-linked tubes | $284 \pm 77$ | $0.85 \pm 0.23$ | 0.073 |

**Table 8.1:** *Overview of the hydrodynamic radii ($R_{\mathrm{h}}$) and the average diffusion coefficients ($D_{\mathrm{av}}$) of the polymersome samples to be measured with the DLS insert. Diffusion coefficients are given for dispersions in water and at 22 °C. The errors given in the hydrodynamic radius and diffusion coefficient are directly related to the polydispersity of the sample.*

fully isotropic and cannot be aligned. The MB of the stomatocytes does not saturate up to 29 T as was already found in chapter 6. The discs, rods and tubes are much more anisotropically shaped than the stomatocytes, which is confirmed by their MB saturating around 25 T. The findings of rods and discs is also in agreement with the theoretically calculated curves in figure 8.5, where the magnetic anisotropy of PEG-PS was used that was obtained in chapter 6. Interestingly, the MB of the cross-linked tubes is of opposite sign compared to all the other samples. This hints at the possibility that the cross-linked tubes align with their symmetry axis perpendicular to the magnetic field, in contrast to the normal tubes which align with their symmetry axis parallel to the magnetic field. If so, this difference in alignment between the two tube samples should become visible by the DLS experiments at high magnetic field. The normal tubes should show an increasing $D_{obs}$ with increasing magnetic field when measured in the range of 104-117° as was predicted by the theoretical results shown in Figure 8.6. If the cross-linked tubes align perpendicular to the magnetic field, this trend should be opposite. In that case, $D_{obs}$ should decrease with increasing magnetic field when measured in the range of 104-117°. TEM pictures of all samples are shown in Figure 8.9b.

## 8.5.2 Results at high scattering angle

With all samples, we started by measuring the intensity of the scattered light as function of the applied magnetic field. All samples show an oscillating behavior in the intensity, as is shown in Figure 8.10a for the spheres. The data for all other shapes are given in the Appendix (Figure 8.16). The period of the oscillation is about 6 tesla for all samples and is caused by Faraday rotation of the incoming laser light in the optical fiber. The polarization of the incoming light is set to match that of the first polarizer in order to get an optimal throughput. When the polarization of the incoming light in the fiber starts to rotate with increasing magnetic field, more and more light is blocked by the first polarizer until, around 6 tesla, the intensity reaches a local minimum where the polarization of the incoming light is perpendicular to that of the polarizer. At this point the scattering intensity is not zero, indicating that the laser light in the fiber is not 100 percent polarized. When the magnetic field increases even more, the polarization of the laser light rotates further and starts to match the direction of the polarizer again, leading to an increase in scattering intensity. The fact that the up-sweep and the down-sweep completely overlap suggest that this Faraday rotation is completely reproducible. Beside the oscillating trend of the Faraday rotation, there is also a clear overall trend that shows the scattering intensity dropping with increasing magnetic field. At present, it

is not completely known what is causing this. Although the firstly mentioned oscillatory trend (by Faraday rotation) is observed for all samples, the shape of the overall downwards trend is different for different samples (see Appendix, Figure 8.16).
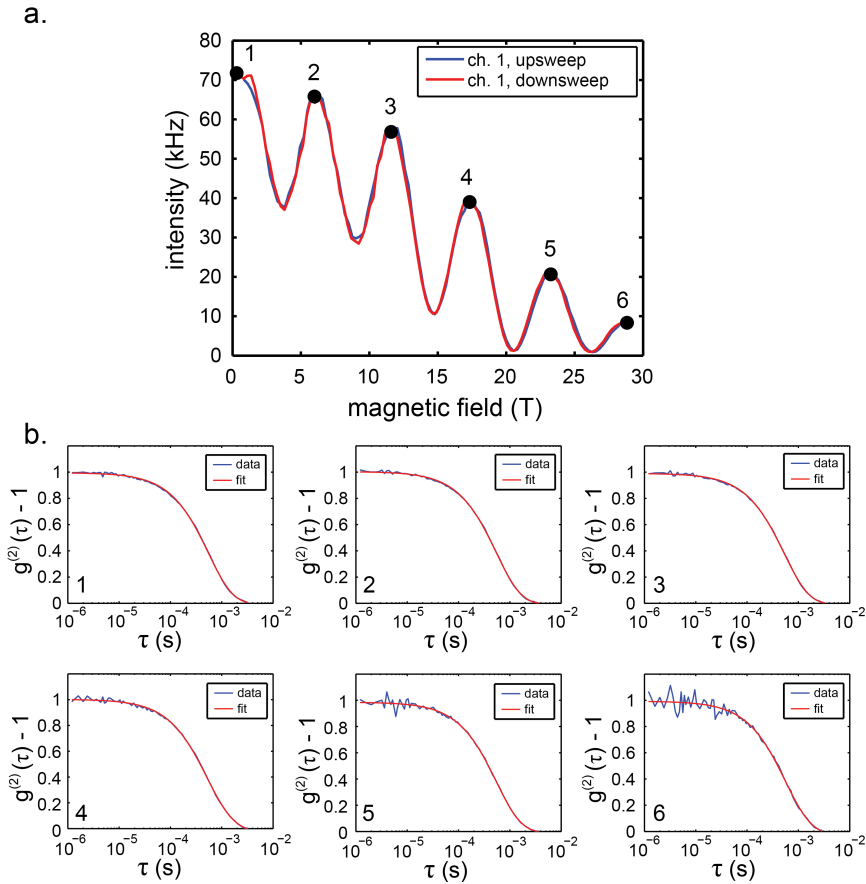


**Figure 8.10:** *(a) Intensity of the scattered light for spheres, measured at channel 1 at 106.5°. As can be seen, there is an oscillating trend while the overall signal also decreases at increasing field. The up-sweep and down-sweep are completely overlapping. DLS was measured at local maxima in the scattering intensity, indicated by roman numbers 1 to 6. (b) Examples of autocorrelation curves (blue) measured at point 1 to 6 as indicated in (a). All autocorrelation curves were measured over 15 seconds. The fits are shown in red. As can be seen, the lower the scattering intensity, the more noisy the acquired autocorrelation curves. The final diffusion coefficients were derived by measuring and fitting 20 curves at each point and averaging the obtained results.*

The best signal-to-noise ratio is obtained for the highest scattering intensity and therefore we only measured at those fields where the scattering intensity had a local maximum (around 0, 6.25, 12.5, 17.75, 23.5 and 29 T), as indicated by points 1 to 6 in Figure 8.10a. The autocorrelation curves were fitted (using equation 8.21) and from these fits the average diffusion coefficient and their errors were determined. Some measured autocorrelation curves and their fits, at points 1 to 6, are shown in Figure 8.10b. These examples clearly show the decrease in signal-to-noise with increasing scattering intensity. The obtained results for data for spheres, rods, tubes, cross-linked tubes and discs, measured in the high angle scattering regime (104-117°), are shown in Figure 8.11.

For the spheres (Figure 8.11a) we see no significant change in $D_{\mathrm{obs}}$ up to 29 T. This is to be expected since spheres, being totally isotropic, cannot be aligned and always show the same diffusion coefficients in all directions. The rods (Figure 8.11b) show a completely different trend. Up to 23.5 T $D_{\mathrm{obs}}$ increases with increasing field as is to be expected. However, above 23.5 T $D_{\mathrm{obs}}$ starts to decrease again. This decrease in $D_{\mathrm{obs}}$ is unexpected and it is thought that these high magnetic fields might interfere with the setup, perhaps by slightly modifying the optical alignment. The up-sweep and down-sweep show the same trend which does indicate that these interferences are reversible. The value of $D_{\mathrm{obs}}$ is observed to increase, maximally, by a factor in the range of 1.08 to 1.15 at 23.5 T. According to theory (Figure 8.6) the changes in $D_{\mathrm{obs}}$ at these scattering angles are maximally a factor of 1.20. The same trend is found for tubes, which have a larger aspect ratio than the rods. Also here, the results start to differ from expectations above 23.5 T due to a sudden drop in the value of $D_{\mathrm{obs}}$. For the tubes, $D_{\mathrm{obs}}$ is observed to increase, maximally, by a factor in the range of 1.15 to 1.24 at 23.5 T. This maximal increase is larger for tubes than for rods, which makes sense since the theoretical curves for rods are calculated assuming maximal aspect ratio. Since the tubes have the largest aspect ratio, it is only logical that the changes in $D_{\mathrm{obs}}$ are largest for the tubes.

The cross-linked tubes show a complete different effect than the rods or the tubes in DLS. For the cross-linked tubes (Figure 8.11d), the values of $D_{\mathrm{obs}}$ only seem to go down with increasing field. This is indeed what is expected for tubes that align with their symmetry axis perpendicular to the applied magnetic field as was explained before. However, the change is very small (only a factor of 0.975 at 23.5 T). The difference with the non-cross-linked tubes is striking though.

For the discs (Figure 8.11e), the same deviations above 23.5 T are observed as for the rods en tubes. There seems to be a slight increase in $D_{\mathrm{obs}}$ up to 23.5 T of about 1.04. The theoretical calculations did predict a small increase in $D_{\mathrm{obs}}$ with increasing magnetic field (Figure 8.6) which is indeed expected to be
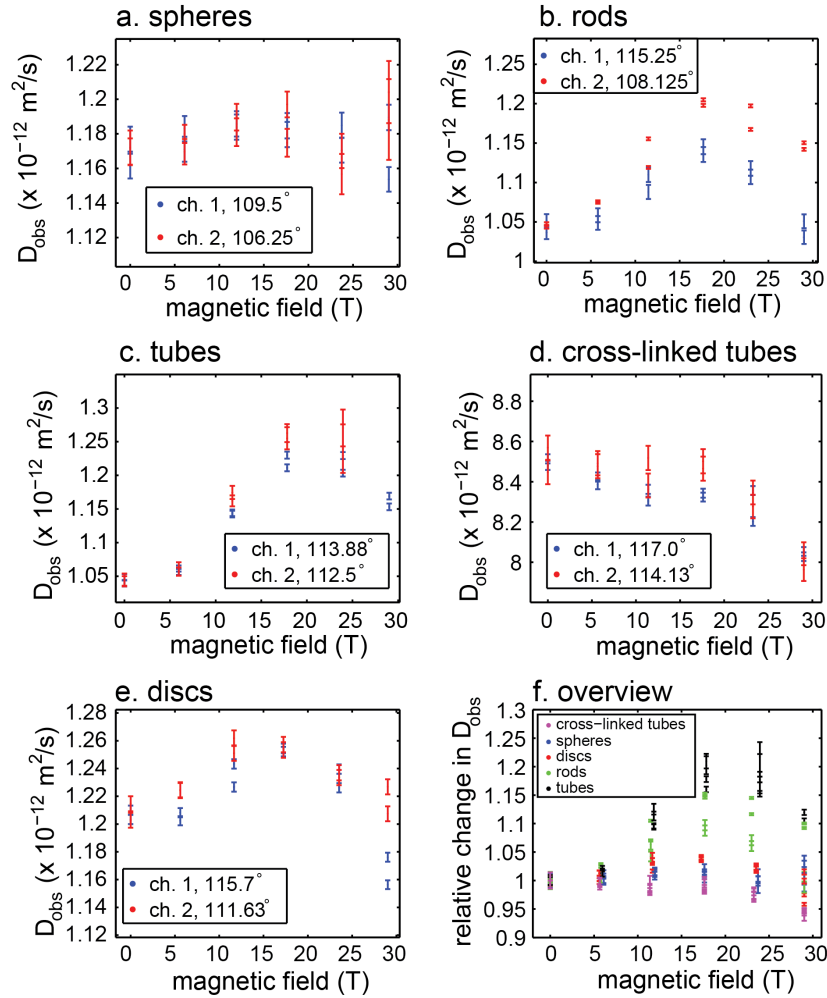
**Figure 8.11:** *The observed diffusion coefficients obtained from the autocorrelation fits for (a) spheres, (b) rods, (c) tubes, (d) cross-linked tubes and (e) discs at high angle scattering (104°-117°). For spheres, $D_{obs}$ remains constant with increasing field as is to be expected. The rods, tubes and discs show an initial increase in $D_{obs}$ up to 17 T as is to be expected. Data above 17 T start to deviate from expectations, probably due to magnetic interference. Only for the cross-linked tubes $D_{obs}$ is found to decrease with increasing field, indicating that these structures align with their symmetry axis perpendicular to the magnetic field. All data is compared in (f) where the relative changes in $D_{obs}$ are shown.*

smaller than that of rods or tubes. However, considering the error bars, the observed changes in $D_{\mathrm{obs}}$ are still quite close to the fluctuations observed for the spheres.

The relative changes in $D_{\mathrm{obs}}$ for all the samples measured in the high angle scattering regime (104-117°) are plotted in Figure 8.11f. In this plot, the differences between the different samples become more clear. The trends up to 23.5 T are matching the predictions from theory: $D_{\mathrm{obs}}$ increases for tubes, rods and discs whereas it decreases for cross-linked tubes. The tubes give the largest increase, followed by rods and then by discs, which is also to be expected. The deviations at 29 T are especially clear for tubes and discs.

### 8.5.3  Results at low scattering angle

According to the theory, at a scattering angle of 70.5°, all cylindrically symmetric samples are expected to show a constant $D_{\mathrm{obs}}$, regardless of the strength of the applied magnetic field. To test this hypothesis, we have chosen to measure the spheres and the tubes around this angle (65-75°). The spheres are not expected to give any variation in $D_{\mathrm{obs}}$ at any scattering angle, as was already demonstrated for the high scattering angle regime. The tubes showed the largest change in $D_{\mathrm{obs}}$ with increasing magnetic field in the high scattering angle regime which makes it a good sample to test the setup at low scattering angles.

Both the spheres and the tubes were measured at low scattering angles in two different runs to obtain better statistics. The result are shown in Figure 8.12. Figures 8.12a,b show the results for the spheres. Up to a 23.5 T, $D_{\mathrm{obs}}$ is observed to remain constant. Only at 29 T the value of $D_{\mathrm{obs}}$ is found to increase. Since spheres should always show the same $D_{\mathrm{obs}}$, regardless of scattering angle or the strength of the applied magnetic field, this suggests that there are factors involved which are interfering with the setup at these high fields, as was the case for the measurements performed at the higher scattering angles.

Although the spheres show a constant $D_{\mathrm{obs}}$ up to 23.5 T, the $D_{\mathrm{obs}}$ of the tubes steadily increases with increasing magnetic field (Figure 8.12c,d), which is not in accordance with theoretical predictions. At 23.5 T, $D_{\mathrm{obs}}$ has increased by a factor in the range of 1.13 to 1.19, which is slightly less then observed at the high scattering angles. The relative changes in $D_{\mathrm{obs}}$ with increasing magnetic field for both spheres and tubes are shown in Figure 8.12e. The differences between the spheres and the tubes are clearly significant.
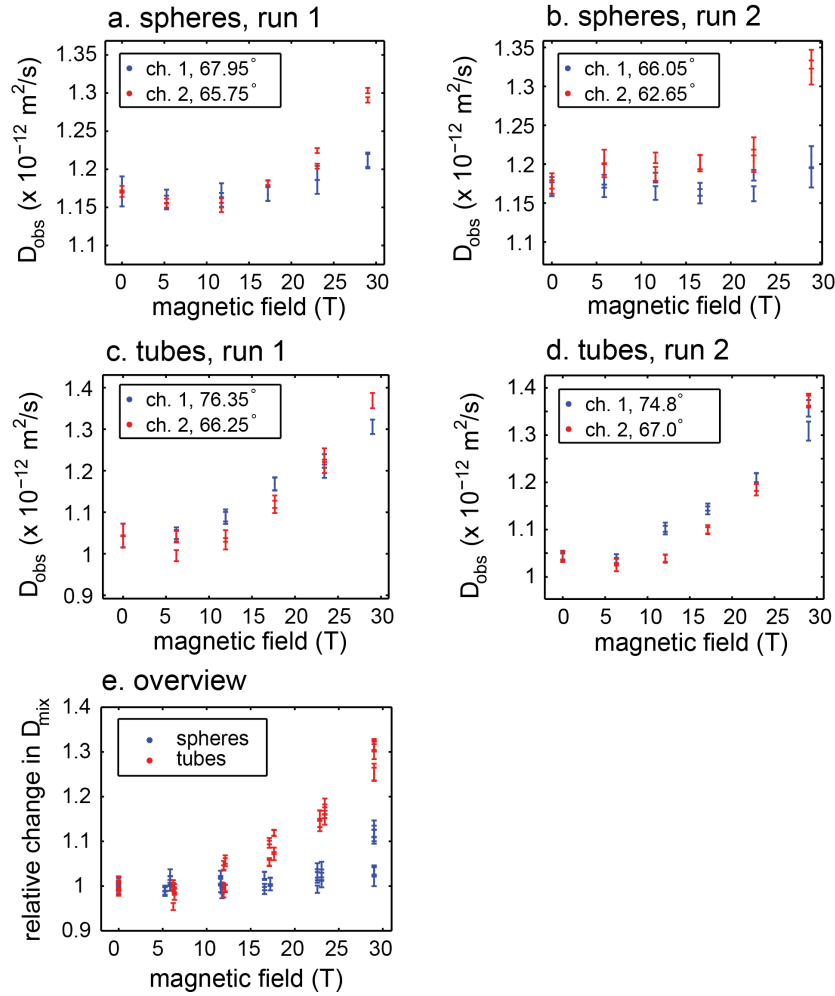
**Figure 8.12:** *The observed diffusion coefficients obtained from the autocorrelation fits for (a,b) spheres and (c,d) tubes at low angle scattering (66°- 76°). For spheres, $D_{obs}$ remains constant with increasing field up to 17 T, above which there are some deviations, especially in channel 2. This might be caused by magnetic interference. For the tubes, $D_{obs}$ is found to increase with increasing field, although not as rapidly as at high scattering angles (8.11c). All data is compared in (e) where the relative changes in $D_{obs}$ are shown.*

## 8.6 Discussion and possible improvements

The results of the measurements performed on the polymersome samples indicate that the setup works in magnetic fields up to 23.5 T and at high scattering

angles. At higher fields, there seem to be significant deviations which are most probably caused by disruptions in the optical alignment, as a result of a strong coupling between the insert and the magnetic field. The data up to 23.5 T shows, at high scattering angle, exactly the trend that was expected. Most striking is the difference between the tubes and the cross-linked tubes which not only shows a different sign in the magnetic birefringence, but also shows a different sign in the changes in $D_{\mathrm{obs}}$, which indicates that the cross-linked tubes indeed align with their symmetry axis parallel to the magnetic field.

The data recorded at the low scattering angles also show a clear difference between the spheres and tubes, although this difference was not theoretically predicted. Although the change in $D_{\mathrm{obs}}$ with increasing magnetic field is not zero for the tubes, it is somewhat smaller than when measured at the high scattering angles. The data seems consistent however and the effect could be reproduced. This suggests that some of the assumptions in the theory might not hold in practice. The theory was derived assuming that all orientations around the symmetry axis (angle $\phi$ in Figure 8.4) occur equally since they have identical energy in a magnetic field. Averaged over time or over many particles, this assumption is certainly true, however, it might not hold perfectly on the very small time scales in which a particle diffuses through the excitation volume. Then again, the autocorrelation curves are determined over time scales of seconds to minutes, so many particles are expected to diffuse through the excitation volume.

The data show clear differences in the relative change in $D_{\mathrm{obs}}$ with increasing magnetic field for the different samples. The changes at the high scattering angles were slightly larger than those at the low scattering angles. It is expected that at full backscattering, these changes are even larger, since at full backscattering, $D_{\mathrm{obs}}$ will equal $D_{\mathrm{z}}$ when measuring DLS at 180°. It is recommended that a newly improved DLS insert also allows one to measure DLS at almost full backscattering, perhaps at angles of 170°. Challenges involved with such designs are the large amounts of laser light that is reflected at the glass cuvette wall, which needs to be shielded from the light scattered by the particles in solution. However, for the rods the changes in $D_{\mathrm{obs}}$ at full alignment are then expected to be around a factor of 1.5 instead of 1.2. At the moment, the largest changes in the autocorrelation curves, induced by the magnetic field, were observed for rods at highest scattering angle. These changes were still rather small as can be seen in Figure 8.13a. The maximal expected change in the autocorrelation curve is shown in Figure 8.13b, which is the calculated change for a rod that is fully aligned. These changes are still rather small, especially when comparing these with those accompanied by a growing sample (see Figure 8.2). This demonstrates that DLS is much less sensitive in detecting magnetic
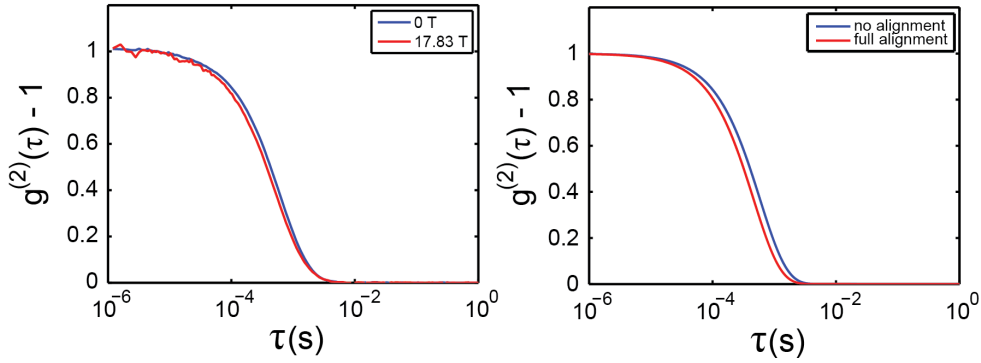
**Figure 8.13:** *Comparison between the maximal changes in the autocorrelation curves observed due to magnetic alignment of tubes (left) and the maximal changes theoretical possible for tubes (right) at a scattering angle of 113.5°. The changes in the autocorrelation due to magnetic alignment are expected to be small, especially when comparing them to changes caused by increasing particle size (see Figure 8.2), which explains the low sensitivity to magnetic alignment.*

alignment compared to growing samples, such as aggregation.

Although the Faraday rotation in the optical fiber does not pose a severe problem on our measurements, it does limit the fields at which one can measure DLS. In the future, the rotation can be counteracted by placing a half-lambda plate after the laser to rotate the polarization before it enters the fiber. In this manner, the polarization direction can be adjusted to match the first polarizer independent of the applied magnetic field. This however does not change the fact that above 23.5 T the intensity starts to drop significantly and severe deviations in the results are found. Apparently the magnetic field interferes with the DLS insert in such a way that both the scattering intensity starts to drop and the results of the autocorrelation starts to deviate. Although care was taken in designing the DLS insert using non-magnetic materials, some components were still slightly magnetic. The fiber lenses were commercially bought and were by default fixated in slightly magnetic holders. Even though they were tightly clamped by two aluminum discs which prevented them to turn or twist, at 29 T it could still pose a problem. All the optical components in the insert were tightened by tiny screws which were also slightly magnetic. Where possible, custom made fiber lens holders and screws might diminish any unwanted magnetic interferences.

## 8.7   Conclusions

In this chapter we have shown our progress in the development of a DLS insert for a 32 T Bitter magnet at the HFML. We provided a theoretical background from which we designed some first experiments on anisotropic polymersomes. Preliminary measurements performed with this new setup already show some clear differences between differently shaped polymersomes, among which a significant difference between cross-linked and non-cross-linked tubes which hints at magnetic alignment along different axes. However, this work is still far from complete. Both from a theoretical and an experimental point of view, there are still many improvements to be made. At high scattering angles, the experimentally determined trends in the diffusion coefficient are following theoretical predictions for all the samples measured. However, at low scattering angles this is not the case, the reason of which is not totally clear at this point. Nevertheless, the observed effects are reproducible.

At the moment the setup works up to fields of 23.5 T. Above this field, severe deviations become apparent which are most likely caused by magnetic interference on the setup itself. Improvements on the setup can focus either on diminishing magnetic interferences on the setup or at increasing the sensitivity of the measurements, for instance by adjusting the setup to be able to measure at even higher scattering angles. Both should lead to significant improvements of the quality of the results.

The changes in the diffusion coefficients induced by magnetic alignment are typically much smaller than the changes caused by increasing particle size. We therefore predict that the DLS insert might be even more sensitive to investigate samples that grow or aggregate over time. We suggest the current setup to be tested on such a growing system as well before developing a new and improved insert.
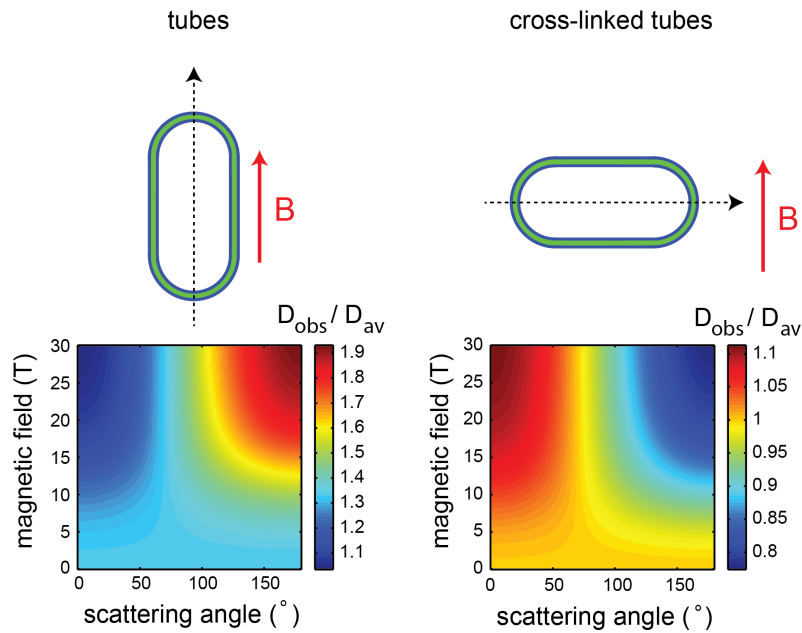
## 8.8 Appendix



**Figure 8.14:** *Theoretical prediction on the relative changes in $D_{obs}$ as function of scattering angle and magnetic field for normal tubes (left) and cross-linked tubes (right). Since cross-linked tubes are expected to align with their symmetry axis (dashed arrow) perpendicular to the magnetic field (red solid arrow), the angle dependence of $D_{obs}$ is expected to be opposite to that of a normal tube which aligns with its symmetry axis parallel to the magnetic field. For instance, at high scattering angle (104-117°) $D_{obs}$ increases with increasing magnetic field for the normal tubes while the opposite is true for the cross-linked tubes.*

Channel 1  Channel 2

High scattering
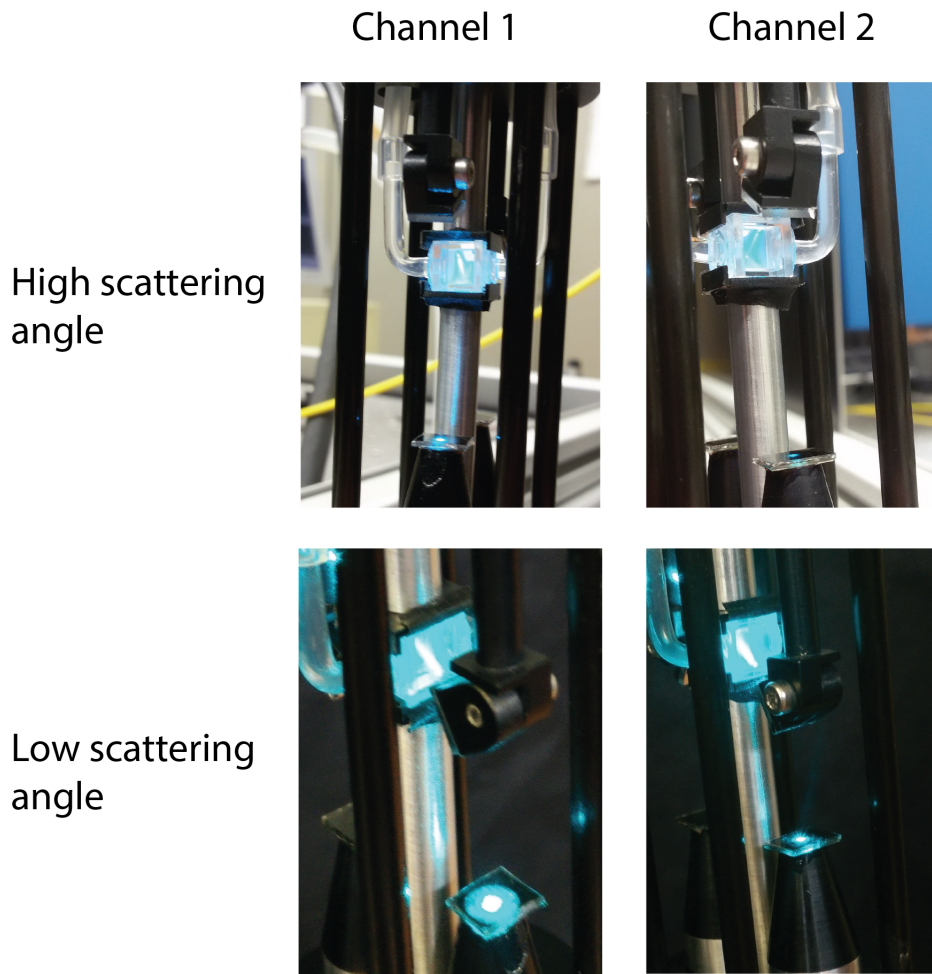angle

Low scattering
angle



**Figure 8.15:** *Photo's showing the detection path for the high angle scattering and the low angle scattering regime for both channels. The angles observed are in agreement with the theoretically determined values.*

**Figure 8.16:** *Overview of the scattering intensity as function of the applied magnetic field, measured in the high angle scattering regime (104-117°) for (a) spheres, (b) rods, (c) tubes, (d) cross-linked tubes and (e) discs. For all these samples, a oscillating pattern is observed with a period of about 6.25 T which is caused by Faraday rotation in the optical fiber as explained in the main text. On top of that, the spheres, tubes, rods and discs showed an overall decrease in scattering intensity with increasing magnetic field. Only for the cross-linked tubes this overall trend is not visible. (f) Legend to (a)-(e).*
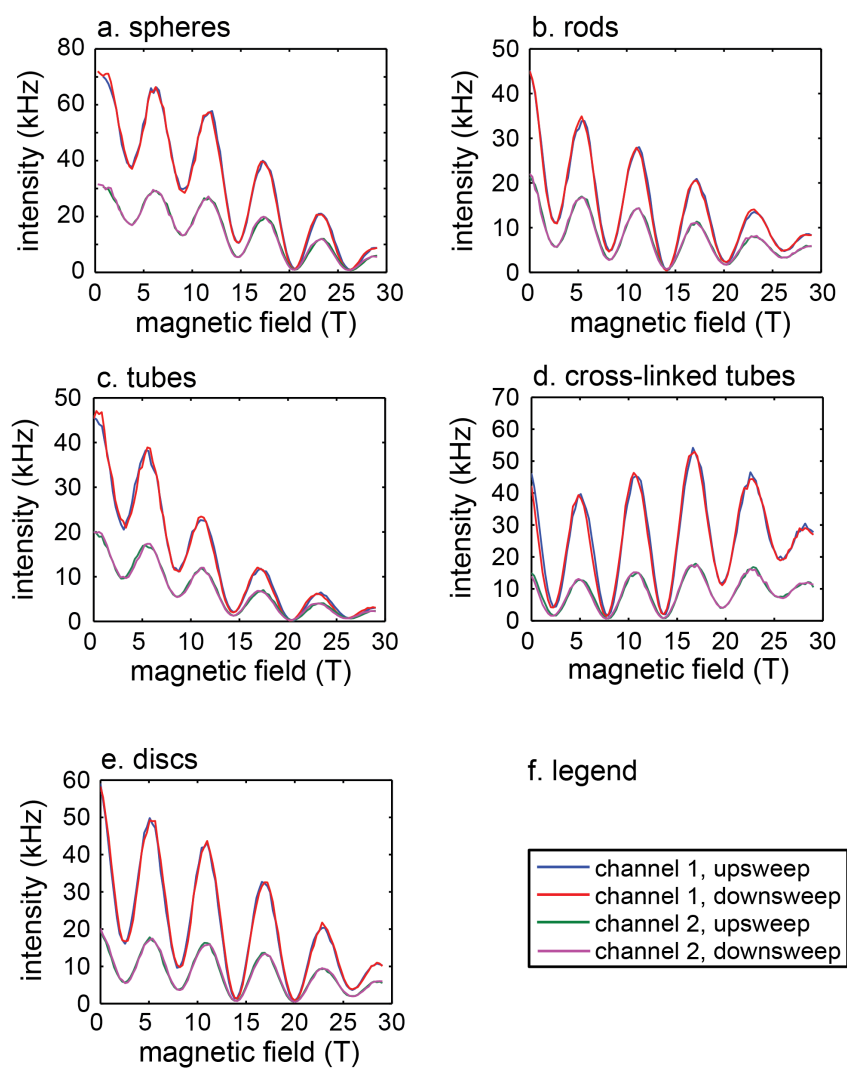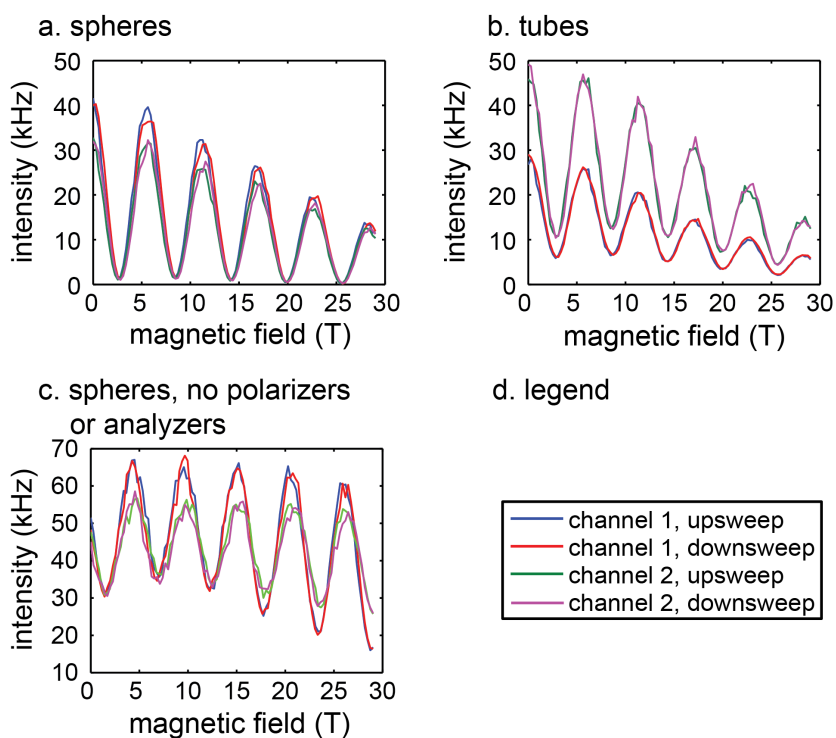
**Figure 8.17:** *Overview of the scattering intensity as function of the applied magnetic field, measured in the low angle scattering regime (65-76°) for (a) spheres and (b) rods. For both samples, an oscillating pattern is observed with a period of about 6.25 T which is caused by Faraday rotation in the optical fiber as explained in the main text. On top of that, the spheres, tubes, rods and discs showed an overall decrease in scattering intensity with increasing magnetic field as was the case for the high angle scattering measurements. A control measurement was performed with spheres when all polarizers and analyzers were removed from the setup (c). The same oscillation in the scattering intensity was observed. However the reason for this is not the blocking of light by the polarizer but the change in scattering intensity by differently polarized light. Overall the intensity does not seem to decrease significantly. (d) Legend to (a)-(c).*

# References

[1] B.J. Berne and R. Pecora, *Dynamic Light Scattering: with Applications to Chemistry, Biology and Physics.* John Wiley, 2nd Edition (1990)

[2] K.S. Schmitz, *An Introduction to Dynamic Light Scattering.*, Academic Press (1990)

[3] N.C. Santos and M.A.R.B. Castanho, *Biophys. J.*, **71**, 1641 (1996)

[4] J. Pencer and F.R. Hallett, *Langmuir*, **19**, 7488 (2003)

[5] A. Wada, N. Suda, T. Tsuda and K. Soda, *J. Chem. Phys.*, **50**, 31, (1969)

[6] D.R. Bauer, J.I. Brauman and R. Pecora, *Ann. Rev. Phys. Chem.*, **27**, 443 (1976)

[7] P.S. Russo, M.J. Saunders and L.M. DeLong, S. Kuehl, K.H. Langley and R.W. Detenbeck, *Anal. Chim. Acta*, **189**, 69 (1986)

[8] S. Badaire, P. Poulin, M. Maugey and C. Zakri, *Langmuir*, **20**, 10367 (2004)

[9] M. Glidden and M. Muschol, *J. Phys. Chem. C*, **116**, 8128 (2012)

[10] S. Ozeki, H. Kurashima and H. Abe, *J. Phys. Chem.*, **104**, 5657 (2000)

[11] R.S.M. Rikken, R.J.M. Nolte, J.C. Maan, J.C.M. van Hest, D.A. Wilson and P.C.M. Christanen, *Soft Matter*, **10**, 1295 (2014)

[12] P.K. Challa, O. Curtiss, J.C. Williams, R. Twieg, J. Toth, S. McGill, A. Jákli, J.T. Gleeson and S.N. Sprunt, *Phys. Rev. E*, **86**, 011708 (2012)

[13] Y. Zhao, W. Chen, D. Hair, J. Xu, C. Wu and C.C. Han, *Eur. Polym. J.*, **41**, 447 (2005)

[14] U. Kätzel, *Dynamic Light Scattering for the Characterization of Polydisperse Fractal Systems by the Example of Pyrogenic Silica*, PhD thesis, Dresden (2007)

[15] W.I. Goldburg. *Am. J. Phys.*, **67**, 1152 (1999)

[16] R. Borsalo and R. Pecora (Ed.), *Soft-Matter Characterization*, Springer (2008)

[17] B.J. Frisken, *Appl. Optics*, **40**, 4087 (2001)

[18] P.J. Patty and B.J. Frisken, *Appl. Optics*, **45**, 2209 (2006)

[19] J.R. Rothenbuhler, J.-R. Huang, B.A. DiDonna, A.J. Levine and T.G. Mason, *Soft Matter*, **5**, 3639 (2009)

[20] R. Vasanthi, S. Bhattacharyya and B. Bagchi, *J. Chem. Phys.*, **116**, 1092 (2002)

[21] V. Patravale, P. Dandekar and R. Jain. *Nanoparticle Drug Delivery.* Woodhead Publishing, 1st Ed, (2012)

[22] A. Michna, Z. Adamczyk, B. Siwek and M. Ocwieja. *J. Coll. Interf. Sci.*, **345**, 187 (2010)

[23] M.C.M. van Oers, F.P.J.T. Rutjes and J.C.M. van Hest, *J. Am. Chem. Soc.*, **135**, 16308 (2013)

# Chapter 9

# Outlook

All experiments described in this thesis were performed on polymersomes assembled from poly(ethylene glycol)-polystyrene (PEG-PS) block copolymers. The reason for choosing this particular block copolymer is that polymersomes assembled from PEG-PS are glassy (rigid) in water but can be made flexible by the addition of plasticizing solvents like THF. Flexible polymersomes of any shape can therefore be kinetically trapped (quenched) by injecting it in an excess of water. This allows for *ex situ* shape analysis by electron microscopy. In this thesis, we also showed that the relatively large magnetic and optical anisotropy of PS allow polymersome shape changes to be probed *in situ* by magnetic birefringence. These properties make PEG-PS polymersomes an ideal model system for the investigation polymersome shape changes in general.

**Biological compatibility**
Although PEG-PS polymersomes are an ideal model system to work with, polystyrene is not biologically compatible, and therefore polymersomes assembled from biologically more suitable polymers are needed for medical applications. However, since we found that the observed shape changes can be described in terms of Seifert's bending energy model [1], the findings presented in this thesis should be easily transferable to polymersomes assembled from other polymers. This is because *relative* changes in bending energy between different shapes are independent of the bending constant $\kappa$, and, therefore, of the material used.

**Fine tuning of shapes via spontaneous curvature**
In chapter 5 we described two possible pathways in which a spherical polymersome can deflate: via oblates or via prolates. These pathways most probably also exist for polymersomes assembled from other block copolymers. Indeed we

have very recently observed both pathways in polymersomes assembled from poly(ethylene glycol)-polylactide [2]. However, for every different type of polymer used, one will still need to determine how to select either the oblate or the prolate deflation pathway. Seifert's theory suggest that this can be done by introducing either a positive or negative spontaneous curvature. This could be done by introducing differences in the solvent composition between the interior and exterior of the polymersomes, as was demonstrated in chapter 5. Furthermore, the attachment of bulky groups on the outside or inside of the polymersomes could also prove to be a useful method to introduce a positive or negative spontaneous curvature.

**Permeability**

Although the shapes at a given reduced volume are determined by the bending energy, the reduced volume is set by the osmotic pressure. In a solvent mixture where multiple components are present (such as a water/THF/dioxane mixture), the actual degree of deflation also depends on the relative permeabilities of these co-solvents. Osmotic pressures can thus be relieved by the out-flow of one solvent but also by the inflow of another. The relative change in permeability of the membrane with regard to all solvents determines how far the polymersome will deflate. Further studies could therefore also include NMR to investigate how the permeability changes as function of solvent composition.

**Salt addition**

In most cases, polymersome shape changes are initiated by introducing an osmotic shock. In the research described in chapters 4 and 5, this osmotic shock was introduced by a change in solvent composition between the polymersome's interior and its surroundings. In principle, this osmotic shock could be greatly enhanced by adding salts. Indeed, our preliminary experiments in which europium nitrate was added to flexible polymersome samples led to reduced volumes of almost zero. It was observed that with the addition of this salt, polymersomes deflate via stomatocytes which in turn fuse into nested vesicles (see figure 9.1). The europium is known for its properties in forming complexes with the oxygens in poly(ethylene glycol) [3–5], which seems to facilitate fusion of the membrane at the opening of the stomatocyte, allowing a nested vesicle to be formed. Although nested vesicles have been encountered before for other polymersome systems [6], this was the first time that the nested vesicles, together with their intermediate structures, were observed for PEG-PS polymersomes. The processes governing the formation of new shapes based on fission and fusion of the membrane are still not very well understood and more research is needed to explore these new vesicle shapes.
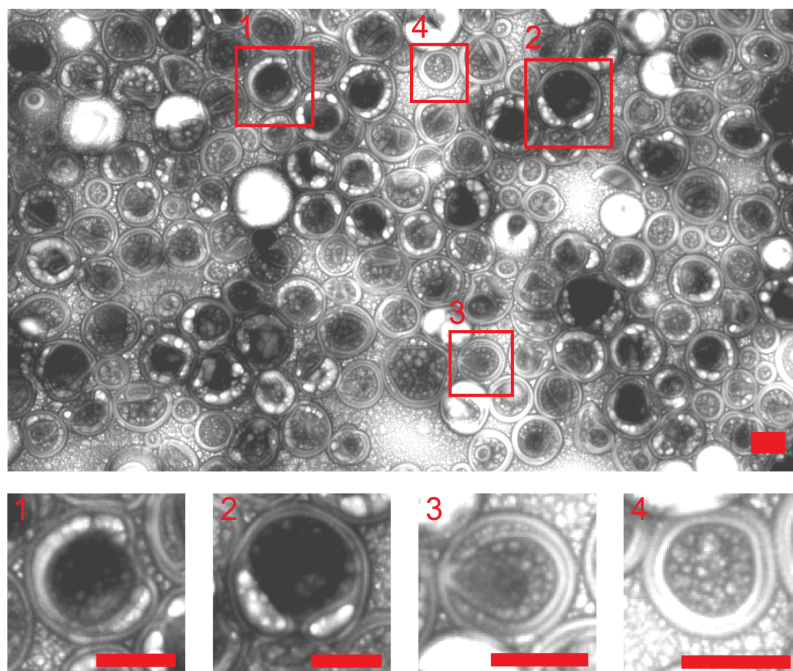
**Figure 9.1:** *Top: full TEM image of a polymersome sample to which europium nitrate was added (10 mM). A mixture of shapes are observed from stomatocytes to nested vesicles. Bottom: a selection of shapes that illustrate the transition from an open stomatocyte to a nested vesicle . An open stomatocyte (1) first has to close (2), decreasing the size of its opening, after which the membrane at the stomatocyte opening starts to fuse. The outer membrane is shown to fuse first (3). After the inner membrane has fused as well a nested vesicle is formed (4). All scale bars are 250 nm.*

**Magnetic deformation**

There is also still more to learn about the effects of high magnetic fields on the morphology of flexible polymersomes. In the experiments described in this thesis, magnetic fields were used to align anisotropically shaped polymersomes. No deformation by the magnetic field itself was measured. We previously have already demonstrated that high magnetic fields can deform flexible polymersomes self-assembled from form PEG-PS block copolymers [7]. Rod equilibration processes at 20 T, described in chapter 7 also showed that the MB does not go entirely to zero, indicating that the final shape at 20 T is not fully spherical.

Magnetic deformation of differently shaped polymersomes is still very poorly understood and more research is needed to differentiate between magnetic alignment and magnetic deformation.

**Nanomotors**
Magnetic fields can also be potentially used to study the motion of the stomatocyte nanomotor. It was previously shown that these nanomotors can be created by adding a catalyst, that produces oxygen gas by consumption of a chemical fuel, to the stomatocyte interior [8–10]. When the catalyst is trapped inside a stomatocyte, the oxygen that is produced can only escape via the mouth of the stomatocyte, leading to propulsion of the stomatocyte. It would be interesting to investigate the movement of these nanomotors in high magnetic fields, since high magnetic fields (partially) align the stomatocytes. By investigating the magnetic alignment of these nanomotors at different fuel concentrations one could find out if the magnetic alignment changes at different velocities. So far, we have demonstrated that stomatocytes can only be partially aligned at fields up to 30 T. However, it is not said that this is also the case when stomatocytes are moving at much higher velocities. Without a catalyst, the stomatocytes move according to normal diffusion (Fick's laws) while the stomatocyte nanomotors move by actual propulsion. The development of the dynamic light scattering insert that is described in chapter 8 could be a valuable tool to measure the movement of stomatocyte nanomotors, since propulsion leads to faster movement which would translate to a larger "apparent" diffusion coefficient.

**Boosting the magnetic response**
The largest challenge left is probably the boosting of the magnetic anisoptropy of the polymers within the polymersome membrane. In chapter 6 we demonstrated that the magnetic anisotropy of the PEG-PS block copolymers is only a fraction of what it could possibly be. This is due to the random coiling of the polymers, which severely limits the magnetic anisotropy. By stretching the polymers in the membrane one introduces a higher degree of order which should also enhance the magnetic anisotropy significantly. We predict that the magnetic anisotropy can be increased maximally by a factor of 75. This would bring the required field strength necessary for full alignment down from 30 tesla to fields small enough to be applied by a single permanent magnet (1 tesla or less). This certainly would make magnetic manipulation of polymersomes accessible to a wider community.

# References

[1] U. Seifert, K. Berndl and R. Lipowsky, *Phys. Rev. A*, **44**, 1182 (1991)

[2] L.K.E.A. Abdelmohsen, D.S. Williams, J. Pille, S.G. Ozel, R.S.M. Rikken, D.A. Wilson and J.C.M. van Hest, *J. Am. Chem. Soc.*, **138**, 9353 (2016)

[3] C.J.R. Silva and M.J. Smith, *Electrochim. Acta*, **40**, 2389 (1995)

[4] V. Bekiari, G. Pistolis and P. Lianos, *Chem. Mater.*, **11**, 3189 (1999)

[5] J. Tang, C.K.S. Lee and L.A. Belfiore, *J. Polym. Sci. B: Polym. Phys.*, **41**, 2200 (2003)

[6] R. Salva, J.-F. Le Meins, O. Sandre, A. Brûlet, M. Schmutz, P. Guenoun and S. Lecommandoux, *ACS Nano*, **7**, 9298 (2013)

[7] P.G. van Rhee, R.S.M. Rikken, L.K.E.A. Abdelmohsen, J.C. Maan, R.J.M. Nolte, J.C.M. van Hest, P.C.M. Christianen and D.A. Wilson, *Nat. Commun.*, **5**, 5010 (2014)

[8] D.A. Wilson, R.J.M. Nolte and J.C.M. van Hest, *Nat. Chem.*, **4**, 268 (2012)

[9] D.A. Wilson, R.J.M. Nolte and J.C.M. van Hest, *J. Am. Chem. Soc.*, **134**, 9894 (2012)

[10] L.K.E.A. Abdelmohsen, M. Nijemeisland, G.M. Pawar, G.-J.A. Janssen, R.J.M. Nolte, J.C.M. van Hest and D.A. Wilson, *ACS Nano*, **10**, 2652 (2016)

# Summary

Vesicles self-assembled from amphiphilic block copolymers (known as polymersomes) are ideal candidates for bio-medical applications such as drug delivery and antigen-presenting scaffolds. Polymersomes have many adjustable properties, such as their rigidity and permeability, which makes it relative easy to alter their properties to optimize their function. In the research described in this thesis we have used polymersomes assembled from poly(ethylene glycol)-polystyrene (PEG-PS) block copolymers to investigate polymersome shape changes. These polymersomes have ideal properties that make it an ideal model system for investigating polymersome shape changes. First of all, polystyrene has the advantage that its flexibility can be tuned by the addition of organic solvent such as tetrahydrofuran and dioxane. When in water, PEG-PS polymersomes are rigid because the PS is in a glassy state. However, with the addition of organic solvents, the polymersome membrane becomes flexible and shape changes become possible. By injecting a flexible polymersome sample in water, the organic solvent is expelled from the polymersome membrane and the morphology is kinetically trapped. This very useful property of PS makes it possible to trap any polymersome sample of any shape at any moment for further analysis with electron microscopy. Secondly, PS has a relative large magnetic and optical anisotropy, which allows anisotropically shaped PEG-PS polymersomes to be aligned in a magnetic field. This magnetic alignment leads to a anisotropic refractive index, which is known as magnetic birefringence, and can be used to probe polymersome shape changes in a non-invasive manner.

In chapter 2, we summarize the possible different combinations one can make with the different types of magnetic materials (ferro-, para- and diamagnets) and the different types of magnetic fields (homogeneous, inhomogeneous, rotating or oscillating). Beside the necessary physics, we also provide the reader with ample examples from literature where these combinations have been employed to induce motion in structures on the micro- and nanoscale.

A theoretical framework necessary to mathematically describe different vesicle shapes is given in chapter 3. Using a Fourier-based parametrization, we are

able to describe any kind of shape as long as it is cylindrically symmetric. This allows experimentally acquired polymersome shapes to be described mathematically and many of their properties, such as bending energy, volume, surface area, area difference and magnetic anisotropy, to be calculated. Furthermore, a theoretical background for magnetic alignment and the relation with magnetic birefringence are presented.

In chapter 4 we demonstrate how we can use magnetic birefringence to probe shape changes in polymersomes. The shape changes are induced by dialyzing rigid polymersomes (in water) against a mixture of water, THF and dioxane. This dialysis is performed in a small cuvette shaped dialysis cell which could be placed inside a 2 T electromagnet and a 20 T Bitter magnet to probe the magnetic birefringence during dialysis. Magnetic birefringence is based on the magnetic alignment of anisotropically shaped polymersomes, which in turn leads to a small difference in refractive index for light polarized parallel and perpendicular to the applied magnetic field. This change in refractive index was found to depend heavily on the anisotropy of the shape as is confirmed by electron microscopy. Shape changes from spheres to discs and subsequently to stomatocytes were observed.

A different method to induce shape changes is described in chapter 5. Here we show that by an out-of-equilibrium self-assembly process, we can accurately set an osmotic pressure over the polymersome membrane which leads to a certain degree of deflation. Using this method we can let initially spherical polymersomes deflate via prolates (spheroids and rods) or oblates (discs). Disc are observed to fold and inflate into stomatocytes, which shows that deflation and inflation follow two different pathways. This hysteresis was first predicted by Seifert in his spontaneous curvature model. Also, all observed shapes follow local minima in the bending energy which proves the validity of Seifert's spontaneous curvature model for our polymersome system.

The magnetic properties of the polymersomes and their polymer constituents are experimentally determined in chapter 6. By applying magnetic fields up to 29 T to disc- and stomatocyte-shaped polymersomes, we were able to bring the magnetic alignment towards saturation. Shape dependent parameters were determined from cryo-TEM and cryo-SEM, which enabled us to fit the magnetic birefringence curves to directly obtain the magnetic anisotropy of a single polystyrene repeating unit. The combination of two different shapes allowed us to determine the sign of the magnetic anisotropy. Comparison with our theoretical calculations shows that the experimental value is only a fraction of what it potentially could be, due to the coiling of the polymers in the membrane. We predict that the required field for alignment can be decreased significantly by stretching the polymers in the membrane.

Chapter 7 describes how the pipetting of an initially spherical polymersome sample from one container to the other can induce a shape change towards rods. This change in morphology is only observed when using a glass Pasteur pipette. The reason for this shape change is not yet clear, but the results do demonstrate that a sample transfer is not always as non-invasive as one might believe. After pipetting, the rod-shaped polymersomes are observed to re-inflate back to spheres. The rate at which this inflation occurs depends on the polymer length. Polymersomes assembled from the longest polymers are found to equilibrate fastest, which might indicate that this inflation is driven by bending energy, since the membranes assembled from the longest polymers are expected to have the largest bending constant. However, no such conclusion can be made at present with the data forehand.

Magnetic birefringence is an *in situ* technique that measures the degree of alignment. It only gives static information about the sample and cannot be used to probe movement of small (aligned) particles. A technique that can measure diffusion of particles is dynamic light scattering (DLS). In chapter 8 we describe our progress in the development of an insert that allows us to measure dual-angle DLS in magnetic fields up to 30 T. A theoretical framework for DLS in high magnetic fields is derived, after which a design of the insert is presented. Preliminary data on differently shaped polymersomes are shown afterwards. The insert currently works best at high scattering angles and magnetic fields below 23 T. Suggestions for improvements are given at the end of the chapter.

To conclude this thesis, an outlook and promising possibilities for future work are described in chapter 9.

Summary

# Samenvatting

Blaasjes zelf-geassembleerd uit amfifiele blokcopolymeren (beter bekend als polymersomes) zijn ideaal voor biomedische toepassingen zoals het gecontroleerd transporteren van medicijnen. Polymersomes hebben vele eigenschappen die gemakkelijk te tunen zijn, zoals de stevigheid of permeabiliteit, wat belangrijk is met het oog op mogelijke toepassingen. Voor het onderzoek wat beschreven staat in dit proefschrift hebben we gebruik gemaakt van polymersomes die geassembleerd zijn uit polyethyleenglycol-polystyreen (PEG-PS) om hiermee vervolgens allerlei vormveranderingen in polymersomes te onderzoeken. Polymersomes van PEG-PS zijn een ideaal modelsysteem hiervoor. Ten eerste kan de flexibiliteit van het PEG-PS membraan getuned worden door toevoeging van organisch oplosmiddelen zoals tetrahydrofuran (THF) en dioxaan. In zuiver water zal het membraan rigide zijn omdat polystyreen in zuiver water glasachtig is. Organisch oplosmiddelen zoals THF en dioxaan maken het polystyreen zacht en flexibel waardoor vormveranderingen in PEG-PS polymersomes mogelijk worden. Door deze flexibele polymersomes in zuiver water te injecteren zal het organisch oplosmiddel uit het membraan diffunderen waardoor het membraan, en dus ook de polymersomes, weer rigide worden. Hierdoor kan de vorm van elke PEG-PS polymersome ingevangen worden zodat deze later met elektronen microscopie zichtbaar gemaakt kan worden. Een tweede voordeel van polystyreen is dat het een relatief grote magnetische en elektrische anisotropie heeft. Dit maakt het mogelijk om anisotroop gevormde polymersomes uit te lijnen in een magneetveld wat weer leidt tot een anisotrope brekingsindex (magnetische dubbelbreking). Aangezien deze magnetische dubbelbreking sterk van vorm afhangt kan deze techniek prima gebruikt worden om vormveranderingen in polymersomes te volgen over tijd zonder het systeem te moeten verstoren.

In hoofdstuk 2 zullen we alle mogelijke combinaties tussen magnetische materialen (ferro- para- en diamagnetisch) en verschillende typen magneetvelden (homogeen, inhomogeen, roterend of oscillerend) bespreken. Naast de natuurkundige theorie zullen ook meerdere voorbeelden besproken worden om beweging in micro- en nanostructuren te induceren met behulp van magneetvelden.

Het theoretische framewerk wat nodig is voor het vervolg van dit proefschrift wordt behandeld in hoofdstuk 3. Door middel van een Fourier-gebaseerde paramterizatie zijn we in staat allerlei verschillende vormen te beschrijven, zolang deze maar cilindrisch symmetrisch zijn. Dit maakt het mogelijk om experimenteel gevonden vormen wiskundig te beschrijven, zodat allerlei eigenschappen, zoals buigingsenergie, volume, oppervlakte, en magnetische anisotropie, berekend kunnen worden. Verder zullen ook de theoretische achtergronden van het magnetisch uitlijnen, en de relatie met magnetische dubbelbreking, behandeld worden.

In hoofdstuk 4 laten we zien hoe we magnetische dubbelbreking kunnen gebruiken om vormveranderingen in polymersomes te volgen in tijd. Deze vormveranderingen zijn geinduiceerd door dialyse van rigide polymersomes (in water) tegen een mengsel van water, THF en dioxaan. De dialyse is uitgevoerd in een kleine dialysecel die geplaatst werd in een 2 T elektromagneet of een 20 T Bittermagneet, zodat de magnetische dubbelbreking tijdens de dialyse gevolgd kon worden. Magnetische dubbelbreking is gebaseerd op het principe dat magnetisch uitlijning van anisotrope deeltjes leidt tot een klein maar meetbaar verschil in de brekingsindex tussen de richtingen loodrecht en parallel aan het aangelegde magneetveld. In dit hoofdstuk laten we zien dat de grootte van de magnetische dubbelbreking direct te relateren is aan de anisotropie van de polymersomes, zoals blijkt uit de verkregen elektronen microscopie opnamen. Door het dialyseproces veranderen de bollen achtereenvolgens is schijven (discs) en kommetjes (stomatocytes).

Een andere methode om vormveranderingen in polymersomes te induceren staat beschreven in hoofdstuk 5. In dit hoofdstuk laten we zien dat we door de zelf-assemblage buiten evenwicht uit te voeren een osmotische druk over het membraan van de polymersomes aangelegd wordt, wat weer leidt tot een deflatie van de blaasjes. Via deze methode kunnen we ronde polymersomes gecontroleerd laten leeglopen naar cilinders (rods) of schijven (discs). De schijven vouwen zich op hun beurt weer tot kommetjes (stomatocytes) en lopen vervolgens weer vol, wat aantoont dat de deflatie en inflatie via twee aparte wegen in het fasediagram verlopen. Deze hysterese was al eerder voorspelt door Seifert in zijn sponteneous curvature model. De gevonden vormen in dit experiment liggen allemaal erg dicht bij lokale minima in de buigingsenergie, wat de bruikbaarheid van Seifert's model voor onze polymersomes duidelijk aantoont.

De magnetische eigenschappen van de polymersomes, en de polymeren waaruit de polymersomes zijn opgebouwd, zijn experimenteel bepaald in hoofdstuk 6. In magneetvelden t/m 29 T kon de magnetische uitlijning van schijf- en komvormige polymersomes naar verzadiging worden gebracht. Via cryogene elektronen microscopie konden vormsafhankelijke parameters worden bepaald

die ons in staat stelden om de magnetische anisotropie per repeterende eenheid van polystyreen direct te fitten aan de gemeten magnetische dubbelbreking. De combinatie van twee totaal verschillende vormen stelde ons in staat om ook het teken van de magnetische anisotropie experimenteel te bepalen. De vergelijking van de verkregen waarde met theoretische voorspellingen laten zien dat de experimenteel bepaalde waarde slechts een fractie is van wat deze maximaal zou kunnen zijn. Dit kan verklaard worden door het feit dat de polymeren niet uitgestrekt zijn maar enigszins willekeurig gewikkeld zijn, waardoor de magnetische anisotropie afneemt. We voorspellen daarom dat de sterkte van het magneetveld nodig om de polymersomes uit te lijnen drastisch verlaagd kan worden door de polymeren in het membraan verder uit te strekken.

In hoofdstuk 7 laten we zien hoe bolvormige polymersomes van vorm kunnen veranderen door deze vanuit het ene potje naar het andere te pipetteren. Na pipetteren zijn de polymersomes cilindervormig en deze vormverandering lijkt zich alleen voor te doen wanneer er gebruik gemaakt wordt van een glazen Pasteur pipet. De oorzaak voor deze vormverandering is nog niet geheel duidelijk, maar de resultaten laten duidelijk zien dat het overhevelen van polymersomes niet altijd even onschuldig is. Na het pipetteren lopen de cilindervormige polymersomes weer vol tot bollen. De snelheid waarmee dit gebeurt lijkt sterk af ta hangen van de polymeerlengte. Polymersomes die zijn opgebouwd uit lange polymeren lopen sneller vol dan polymersomes opgebouwd uit korte polymeren. Dit lijkt erop te wijzen dat de inflatie gedreven wordt door buigingsenergie, omdat membranen gemaakt van de langste polymeren ook de grootste buigingsconstante zullen hebben. Echter, met de data gepresenteerd in dit hoofdstuk kan vooralsnog geen harde conclusies hierover worden getrokken.

Magnetische dubbelbreking is een *in situ* techniek waarmee de mate van magnetische uitlijning gemeten kan worden. Het geeft dus alleen statische informatie en kan daarom dus niet gebruikt worden om de beweging van magnetisch uitgelijnde structuren te meten. Een bekende techniek waarbij de diffusie van deeltjes in oplossing wordt gemeten is dynamische lichtverstrooiing. In hoofdstuk 8 beschrijven we ons werk aan een opstelling die ons in staat stelt om via twee kanalen tegelijk dynamische lichtverstrooiing te meten in magneetvelden t/m 30 T. Vergelijkingen voor lichtverstrooiing aan uitgelijnde structuren zijn afgeleid, waarna een ontwerp voor de opstelling wordt gepresenteerd. De opstelling is getest met polymersomes en tot nu toe werkt de opstelling het beste bij grote lichtverstrooiingshoeken en magneetvelden onder de 23 T. Het hoofdstuk wordt afgesloten met enkele suggesties voor verbeteringen.

In hoofdstuk 9 zal ter afsluiting van dit proefschrift een aantal veelbelovende onderzoeken besproken worden die de kennis over polymersomes kan helpen vergroten in de nabije toekomst.

# Nawoord

Nu mijn promotietraject erop zit, rest mij alleen nog het schrijven van een dankwoord. Ik had mijn promotie niet kunnen volbrengen zonder de hulp en ondersteuning van zóveel mensen, dat het bijna ondoenlijk is ze allemaal op te noemen. Ik ga het toch proberen.

Ten eerste wil ik het team van directe begeleiders bedanken: Peter, Daniela, Jan en Hans. Ik had me geen beter team van begeleiders kunnen wensen. Peter, je bent altijd erg betrokken geweest bij mijn project en kwam regelmatig langslopen om te vragen of er nieuwe resultaten waren. Je hebt me enorm gestimuleerd en geholpen om het beste uit mezelf en uit het project te halen. Je bent altijd ontzettend duidelijk en gestructureerd, en je weet altijd alles in perspectief te plaatsen. Bedankt voor je dagelijkse begeleiding!

Daniela, when I just started my PhD, I had no clue on how to perform all the lab work that was required for this project. During my first weeks you have taught me how to use the DLS, the electron microscopes, how to perform the self-assembly of polymersomes and much more. During the following years you have always been available for discussions and advice, which I have always appreciated a lot. It was also very nice to have seen your group develop from only one PhD student to a nice group of postdocs, PhD students and undergraduate students.

Jan, bij onze project meetings was ik altijd erg onder de indruk van jouw expertise en kennis. Je wist altijd erg bruikbare tips en suggesties te geven tijdens onze meetings. Ook wist je me altijd te enthousiasmeren over het project en nieuwe experimenten.

Hans, jij bent halverwege mijn promotietraject betrokken geraakt bij mijn onderzoek, wat tot veel nuttige inzichten en ontwikkelingen heeft geleid. Vooral je suggestie voor een geschikte parameterizatie is ontzettend waardevol gebleken voor dit werk. Ik vond het erg leuk om met jou aan het model te werken in Matlab. Verder vond ik het ook erg leuk om met jou naar Matsumoto te hebben mogen gaan voor de Magneto-Science conferentie.

Naast de directe begeleiders zijn er vele andere mensen op de universiteit die een zeer belangrijke rol hebben gespeeld in de afgelopen vier jaar. Ten eerste wil ik hier noemen Jan Kees. Jij wilde garant voor mij staan toen ik de financiering voor m'n promotie via de Graduate School van het IMM nog niet helemaal rond had. Daardoor had ik toch de zekerheid op een volledige promotieplek waardoor ik toestemming kreeg om te beginnen. Hartelijk dank hiervoor en ook voor al het vertrouwen wat je in me hebt gesteld.

Roeland, tijdens de wekelijkse groupmeetings bij chemie kwam je vaak met zeer nuttige suggesties en ideeën. Bedankt voor je support!

Loai, jij was altijd mijn beste maatje bij chemie. Als er een nieuw polymeer of molecuul gemaakt moest worden dan kon ik altijd op jou rekenen. We hebben samen aan meerdere projecten gewerkt en ook hebben we een aantal bachelorstudenten samen begeleid waarbij jij het chemische deel op je nam en ik het fysische. Ik heb het altijd ontzettend fijn gevonden om met jou samen te werken. Je bent ontzettend enthousiast en gedreven en een erg goede chemicus. We hebben ook heel wat afgelachen de afgelopen jaren en ik zal erg goede herinneringen overhouden aan onze samenwerking. Ik ben dan ook erg blij en vereerd dat jij mijn paranimf wil zijn.

Op technisch vlak heb ik de afgelopen jaren ontzettend veel samengewerkt met verscheidene technici op het HFML en het Techno Centrum. Jullie ondersteuning was onmisbaar voor het voltooien van dit werk. Michel, jij hebt de insert voor de DLS gemaakt, wat uiteindelijk begonnen is met niets meer dan een ruwe eerste schets. Ook heb je een nieuwe birefringence insert gemaakt waardoor ik veel stabielere metingen heb kunnen verrichten. Wat betreft de optica en lasers kon ik altijd bij Peter Albers terecht. Bedankt voor alle ondersteuning de afgelopen jaren! De metingen in magneten vroegen om custom-made glaswerk en cuvetjes waarvoor ik Peter Walraven hartelijk wil bedanken. De flowcell die je voor ons hebt gemaakt was een daverend succes! Hung, jij hebt op het gebied van computers en software ervoor gezorgd dat ik nooit iets tekort kwam. Bedankt Hung! Verder wil ook alle overige technici en installation managers op het HFML bedanken voor alle ondersteuning met de installatie: Lijnis, Frits, Arjan, Frans, Martin, Tom, Andries, Jos P, Jos R, Jos van V, Gideon, Matthias, Edwin, Tim, Chris, Gerben, Jef en Arno. Bedankt jongens!

Voor alle administratieve zaken kon ik altijd bij Ine en Thera (HFML) of bij Marieke (Bio-Organic Chemistry) terecht. Of het nu voor een bestelling was, het opnemen van verlof of het laten inschrijven van een nieuwe stagiair, jullie stonden altijd klaar. Dank jullie wel!

Peter van Rhee, jij hebt me geholpen om de magnetic birefringence opstelling onder de knie te krijgen. Hierdoor kon ik 1 maand na de start van mijn promotie al de eerste metingen in de magneet verrichten. Peter, bedankt voor

al je hulp, en vooral je geduld, als ik weer eens met een vraag bij jou aankwam.

I had a great time co-organizing the Christmas-Quiz editions of 2014 and 2015 with Laurens, Thomas, Peter Robinson and Salvo. Laurens, according to you, the Quiz had to become much bigger and funnier: more glitter, a wheel of fortune, photoshopped pictures of everybody, movies, a full sound system with soundboard and funny hats. We made it happen! Thanks guys for all the laughing. It was great fun!

Many thanks also to my former office mates, Thomas, Andreas, Jonas, Suruchi, Andrès, Peter Robinson, Mariana, Maryam, Dima, Ineke en Mariëlle. I'm very glad to have had such fun office mates. Mariana, you just arrived a year ago, but we chatted regularly between work (it helps if your desks are right next to each other right?). I am very happy that you are willing to be my paranimf!

Also thanks to the rest of the HFML and the Bio-Organic Chemistry group for all the nice moments during lab work, breaks, borrels and lab trips.

Ik heb ook het genoegen gehad om een aantal studenten te mogen begeleiden. Harmen, jij was mijn allereerste student. Ik sta nog steeds versteld dat we jouw resultaten al hebben kunnen publiceren toen je nog maar halverwege je stage was. Het werk beschreven in hoofdstuk 4 is dan ook voor een groot deel jouw verdienste. Je hebt een eigen opstelling ontworpen en aan de praat gekregen. Door jouw werk zagen we al snel in dat 2 tesla voldoende was om vormsveranderingen te proben *in situ*, wat we in het vervolg veelvuldig zijn blijven gebruiken.

Irene, in een korte tijd heb jij ontzettend veel parameters onderzocht die mogelijk een invloed zouden kunnen hebben op de vorm van de polymersomes. Jouw voorwerk heeft ons erg goed geholpen in alles wat volgde, met name het werk beschreven in hoofdstukken 5 en 7. Ik nog altijd onder de indruk van de hoeveelheid werk die je in een korte tijd hebt verzet.

Britt en Arno, jullie hebben allebei gewerkt aan het boosten van $\Delta\chi$ door het toevoegen van magnetisch anisotrope moleculen of paramagnetische zouten. Het werk heeft helaas niet geleid tot de gewenste resultaten, hoewel jij Britt een interessante nieuwe morfologie hebt gevonden: de nested vesicle, wat in hoofdstuk 9 toch nog een plekje heeft gekregen.

Claudius en Thom, jullie hebben allebei hard gewerkt aan de equilibratie van rod-shaped polymersomes. Het vergde vele metingen om een beeld te krijgen wat er nu eigenlijk aan de hand was, maar dat bleek voor jullie allebei geen enkel probleem. Claudius, jij bent theoretisch erg sterk, wat ook bleek uit het feit dat je alle afleidingen die voor jouw project belangrijk waren wilde bestuderen of herproduceren. Thom, jij was altijd prima in staat om naast de vele vakken

die je nog volgde al je metingen zó in te plannen dat aan het einde van de week toch alles was gedaan. Ik was hiervan erg onder de indruk. De belangrijkste resultaten van jullie beiden zijn ondergebracht in hoofdstuk 7.

Olav, jij was mijn laatste student en hebt me enorm goed geholpen met het testen van de DLS insert. Aangezien deze testen in hoog magneetvelden plaatsvonden was het voor mij erg prettig om iemand bij me te hebben ter ondersteuning. Je bekeek altijd alles kritisch en nam nooit iets zonder meer aan, wat mij ook weer scherp hield.

Uiteraard wil ik ook mijn directe familie bedanken: Pap, Mam, Jordi, Alwin, Barbara, Jacqueline en Bas. Het is fijn om een familie te hebben die je steunen en in alles wat je doet en probeert te bereiken. Niet alleen de afgelopen vier jaar maar ook tijdens de vele jaren van studie die hier vooraf zijn gegaan. Ik kan oprecht zeggen dat ik ontzettend veel geluk heb gehad met alle steun die ik van jullie heb ontvangen en denk ook niet dat ik zover was gekomen zonder jullie.

Ten slotte natuurlijk Gerlinda. Wij leerden elkaar kennen op vakantie in Peru, toen ik halverwege m'n promotie was. Ik ben blij jou ontmoet te hebben en kan me een leven zonder jou al niet meer voorstellen. Je bent ontzettend geduldig geweest als ik weer eens een meetweek had of met iets anders druk was op het werk. Bedankt voor al jouw steun.

Roger Rikken
juli 2016

# List of Publications

- R.S.M. Rikken, H.H.M. Kerkenaar, H. Engelkamp, R.J.M. Nolte, J.C. Maan, J.C.M. van Hest, P.C.M. Christianen and D.A. Wilson, The effect of polymer length, temperature and magnetic field on the kinetics of polymersome shape changes induced by dialysis, *paper in preparation* (2016)

- R.S.M. Rikken, L.K.E.A. Abdelmohsen, H. Engelkamp, R.J.M. Nolte, J.C. Maan, J.C.M. van Hest, D.A. Wilson and P.C.M. Christianen, Determining the magnetic anisotropy of an individual polymer in polymersomes self-assembled from PEG-PS, *paper in preparation* (2016)

- L.K.E.A. Abdelmohsen, R.S.M. Rikken, P.C.M. Christianen, J.C.M. van Hest and D.A. Wilson, Shape Characterization of Polymersome Morphologies via Light Scattering Techniques, *Polymer*, **in press**, (2016)

- R.S.M. Rikken, H. Engelkamp, R.J.M. Nolte, J.C. Maan, J.C.M. van Hest, D.A. Wilson and P.C.M. Christianen, Shaping polymersomes into predictable morphologies via out-of-equilibrium self-assembly, *Nat. Commun.*, **7**, 12606 (2016)

- L.K.E.A. Abdelmohsen, D.S. Williams, J. Pille, S.G. Ozel, R.S.M. Rikken, D.A. Wilson and J.C.M. van Hest, Formation of well-defined, functional nanotubes via osmotically induced shape transformation of biodegradable polymersomes, *J. Am. Chem. Soc.*, **138**, 9353 (2016)

- P.G. van Rhee, R.S.M. Rikken, L.K.E.A. Abdelmohsen, J.C. Maan, R.J.M. Nolte, J.C.M. van Hest, P.C.M. Christianen and D.A. Wilson, Polymersome magneto-valves for reversible capture and release of nanoparticles, *Nat. Commun.*, **5**, 5010 (2014)

- R.S.M. Rikken, H.H.M. Kerkenaar, R.J.M. Nolte, J.C. Maan, J.C.M. van Hest, P.C.M. Christianen and D.A. Wilson, Probing morphological chan-

ges in polymersomes with magnetic birefringence, *Chem. Commun.* **50**, 5394 (2014)

- R.S.M. Rikken, R.J.M. Nolte, J.C. Maan, J.C.M. van Hest, P.C.M. Christianen and D.A. Wilson, Manipulation of micro- and nanostructure motion with magnetic fields, *Soft Matter* **10**, 1295 (2014)

# About the author

Roger Rikken was born on the $19^{\text{th}}$ of October 1984 in Nijmegen. He went to secondary school (VWO) at Canisius College in Nijmegen, where he graduated in 2002. He studied to become a teacher in physics at HAN University of Applied Sciences, where he received his BEd *cum laude* in 2007. He went on to study Natural Sciences at the Radboud University, where he received both his BSc and MSc *cum laude* in 2010 and 2012 respectively. Roger did his first research internship in the High Field Magnet Laboratory and the Molecular Materials department of the Radboud University where he investigated the activity of enzymes in magnetic fields. His second research internship was performed at the Scanning Probe Microscopy department, where he worked on the templating of porphyrin molecules on a molecular monolayer. After graduation, Roger joined the Graduate School for Molecules and Materials, where he obtained a grant for a PhD position. He performed the research for his PhD at the Soft Condensed Matter and Nanomaterials group of the High Field Magnet Laboratory (HFML) and the Bio-Organic Chemistry group of the Institute of Molecules and Materials (IMM), where he focused on polymersome shape changes in magnetic fields. At present, Roger is teaching physics at the Fontys Leraren Opleiding Tilburg (FLOT), which is part of the Fontys University of Applied Science.